POLITECNICO DI TORINO

Collegio di Ingegneria Meccanica, Aerospaziale, dell'Autoveicolo e della Produzione

Corso di Laurea Magistrale
in Ingegneria Aerospaziale

Tesi di Laurea Magistrale

Numerical assessment of the plasma properties in an Inertial Electrostatic Confinement device

Relatore
prof. Lorenzo Casalino

Candidato
Francesco Mazza

Marzo 2018

To Gabriele, Luisa and Valeria

To Alice

Abstract

Inertial Electrostatic Confinement (IEC) is a technique developed in the 1950s to produce, confine and heat a plasma by means of a steady-state electric field. Despite the original design being aimed at a nuclear fusion concept for power generation, IEC have been proposed and effectively employed for a number of technology applications, ranging from portable neutron sources to space propulsion. The conceivable design of an electric thruster based on IEC technology is motivated by the experimental observation of a jet extracted from the confined plasma under suitable operating conditions. Furthermore, the use of IEC in a space propulsion system as the appealing feature of scaling with the power provided to the device: IEC thrusters could be the bridging technology between low-power applications and high power designs for deep-space exploration, such as fusion rockets.

The thesis work reported here is set within the framework of IEC research, undertaken at the Institut für Raumfahrtsysteme (IRS), Stuttgart, since 2009. This research is aimed at deepening the comprehension of the plasma physics underlying the ionisation process and the subsequent plasma confinement and jet extraction. As a matter of fact, a thorough description of the plasma behaviour in an IEC device, operating in non-fusion mode, is necessary to the effective design of an IEC thruster. Hence, the work carried out was focused on the numerical simulation of the device built and tested at IRS, aiming at the assessment of the most significant plasma parameters, with particular emphasis on the electrostatic potential and plasma density.

At a first instance, the development of a one-dimensional solver for the numerical simulation of the core plasma is undertaken. On the basis of a pre-existing code developed at IRS a novel plasma model, referred to as "thermal" model, is implemented: this work allows to enrich the previous simulations - based on the "mono-energetic" and "rectangular" models- accounting for the effect of particle collisions in the confined plasma. The resulting numerical tool is employed to simulate the operations of the investigated IEC device. The outcome is consistent with the data found in the literature and underlines the inconsistency of the observed plasma behaviour with the physical theory employed to this day to explain the plasma confinement.

The research focus is therefore shifted to a more detailed assessment of the electrostatic filed produced by the electrodes in a typical gridded configuration. A numerical solver is this developed, capable of assessing the exact three-dimensional topology of the eternally applied field for a however complex electrode geometry.

In the light of experimental observations, realised in the IRS test facility, and the outcome of both the one-dimensional plasma simulation and the numerical assessment of the topology for the applied electrostatic field, a novel plasma model is proposed, basing on the concept of spherical double layer (SDL). A double layer is an electrostatic structure that is found to arise in a variety of plasmas and it can be thought of as localised non-neutral plasma structure, characterised by an own, inner electric field. In the proposed IEC-SDL model, a spherical double layer is thus theorised to ensue in the core plasma inside the device's cathode. On the basis of a circuital analogy, the SDL is simulated over a range of operating conditions for the investigated IEC device: the two-fluid modelling of the confined plasma allows for the numerical evaluation of the core density.

In conclusion, the developed IEC-SDL promise to provide a thorough, self-consistent theoretical background to frame the whole set of plasma phenomena observed in an operating IEC device. Further research on this topic should first provide an experimental validation of the spherical double layer. Subsequently the inclusion of the jet extraction mechanism in the framework of IEC-SDL would provide a valuable tool to the design of an effective plasma thruster.

Contents

List of Figures

List of Tables

Nomenclature

I_{S}	=	Specific impulse
$\dot{m}$	=	Mass flow rate
u_{e}	=	Exhaust velocity
$\vec{E}$	=	Electric field
$\vec{B}$	=	Magnetic field
ε_0	=	Vacuum permittivity
μ_0	=	Vacuum permeability
I	=	Electric current
$\vec{J}$	=	Electric current density
ϕ	=	Electrostatic potential
q	=	Electric charge
T	=	Temperature
p	=	Pressure
k	=	Boltzmann constant
$\vec{v}$	=	Particle velocity
W	=	Particle mechanical energy
L	=	Particle angular momentum
n	=	Particle number density
σ	=	Particle cross section
λ_{mfp}	=	Mean free path
λ_{D}	=	Debye length
ρ	=	Space-charge density
r_{a}	=	Anode radius
r_{c}	=	Cathode radius
V_{a}	=	Anode voltage
V_{c}	=	Cathode voltage
∇V	=	Applied electrode voltage
I_{PS}	=	Power supply current
η_{g}	=	Electrode geometric transparency
δ	=	Dirac's delta function
H	=	Heaviside's step function
G	=	Green's function
ϕ_{ion}	=	Ionisation potential
ϕ_{DL}	=	Electrostatic potential on the double layer
r_{DL}	=	Radius of the spherical double layer
t_{DL}	=	Thickness of the double layer
R	=	Electrical resistance

Chapter 1

Introduction

1.1 Electric propulsion

The idea of electric propulsion for spacecrafts dates back to the beginning of the 20th century when R. Goddard and K. Ė. Ciolkovskij independently wrote about the concept of an "electric rocket", in 1906 and 1911 respectively [1], [2]. Nonetheless, was only in 1929 that soviet engineer V. P. Glushko demonstrated the first electric thruster at the Gas Dynamic Laboratory, in Leningrad, while the first successful operations, for electric thrusters, in space missions were first accomplished in 1960s, with the U.S. SERT 1 and the USSR Zond 2 missions.

According to Prof R. G. Jahn, from Princeton University, electric propulsion is defined as:

"*The acceleration of gases for propulsion by electrical heating and/or by electric and magnetic body forces.*" [2]

This is clearly a very broad definition, including very different mechanisms for the thrust generation; a common classification for electric thrusters is then based on the different kind of force employed for the propellant acceleration:

1. Electrothermal propulsion employs electrical power to heat the propellant, which is then accelerated in a suitable nozzle, like in common chemical rockets.
2. Electrostatic propulsion employs electric body forces to directly accelerate the ionized propellant.
3. Electromagnetic propulsion accelerates an ionized propellant stream, by external and internal electromagnetic fields, with electric currents driven through the stream itself.

The fashion in electric propulsion lies in the highly efficient utilisation of propellant mass: due to the extremely high exhaust velocities typically attained by these acceleration mechanisms, indeed, electric thrusters allow for missions inaccessible to common chemical rockets, e.g. planetary missions. In Tab. 1.1, some of the most employed electric propulsion technologies are reported, along with typical values for the supplied power and specific impulse, an extremely important performance parameter, defined as the ratio of thrust to the rate of propellant usage by-the-sea weight:

$$I_s \doteq \frac{\dot{m} u_e}{\dot{m} \mathrm{g}_0} = \frac{u_e}{\mathrm{g}_0} \tag{1.1}$$

Where $\dot{m}$ is the propellant mass flowrate,
u_e is the exhaust velocity from thruster,
g_0 is the sea-level gravitational acceleration.

Whichever the mechanism driving the propellant acceleration, in an electric thruster the propellant itself is typically a plasma, thus, its operating principle and performances are closely related to plasma physics. The term plasma identifies the fourth state of matter and can be defined as a quasi-neutral gas of charged and neutral particles, which exhibits collective behaviour [3]. Plasmas are often participating in different physical phenomena and are produced by the ionisation of a gas: hence, the comprehension of the mechanism underlying the ionisation of a gas is fundamental to the description of any electric propulsion system.

Table 1.1 Most employed electric thrusters [1]

Thruster	Power range $[W]$	Specific impulse $[s]$
Electrothermal		
Resistojet	$\sim 10^2$	$300 \div 400$
Arcjet		
Hydrazine	$\sim 10^3$	$500 \div 600$
Hydrogen	$\sim 10^4$	$900 \div 1200$
Ammonia	$\sim 10^3 \div 10^4$	$600 \div 800$
Electrostatic		
Gridded Ion Engines	$\sim 10^3 \div 10^5$	$2000 \div 10000$
Stationary Plasma Thrusters (SPT)	$\sim 10^2 \div 10^4$	$1000 \div 2500$
Thruster with Anode Layer (TAL)	$\sim 10^2 \div 10^4$	$1000 \div 4000$
Electromagnetic		
Magnetoplasmadynamic (MPD)		
Pulsed	$\sim 10^3$	$1000 \div 4000$
Steady-state	$\sim 10^5 \div 10^6$	$3000 \div 7000$
Pulsed Plasma Thruster (PPT)	$\sim 10^1 \div 10^2$	$1000 \div 1500$
Pulsed Inductive Thruster (PIT)	$\sim 10^4$	$3000 \div 5000$
Electron Cyclotron Thruster	$\sim 10^3 \div 10^4$	$2000 \div 4000$

A collision between particles -being they molecules, atoms, ions or electrons- in a gaseous medium may result in various outcomes such as scattering (i.e. deflection through a certain angle), dissociation, and ionisation and so on: the probability associated with a specific process that can occur in collisions is commonly quantified by means of its cross-section[1]. The cross-section associated to a possible outcome of the collision between a given particle and others can be defined as the ratio of the probability of such an outcome (per unit time) to the particle flux density [4]. Consider a number of particles "a" (e.g. electrons), incident upon a slab of area A and thickness dx containing n_n particles "b" (e.g. neutral atoms) per unit volume, these are thus imagined to be opaque spheres of cross-sectional area σ: that is, every time an electron comes within the area blocked by the atom, the specific collision phenomenon ensue. Hence, since the both the dimension and the density of the slab are known quantities, it is possible to estimate the fraction of incident particles involved in the collisional process and, thus, assess the rate of the particle flux density, which decreases along the slab's thickness. Therefore, if a flux Γ_0 of electrons is incident on the slab, the flux emerging on the other side -not being interested in the collisional process- is:

$$\Gamma = \Gamma_0 e^{-n_n \sigma x} \equiv \Gamma_0 e^{-\frac{x}{\lambda_m}} \tag{1.2}$$

Where λ_m is the *mean free path* for the specific output collisions, defined as

$$\lambda_m \doteq \frac{1}{n_n \sigma} \tag{1.3}$$

Hence, the mean free path can be thought of as the distance by which the incident particles flux density is decreased to $1/e$ of its initial value [3].

[1] Since the cross-section in the definition is specified as a function of some final-state variable, it should be more properly denoted as "*differential cross-section*". On the other hand, when a cross section is integrated over all possible scattering angles (and possibly other variables), it is called a "*total cross section*".

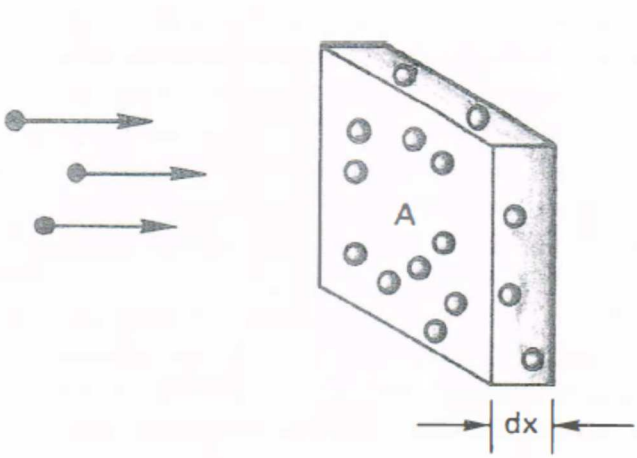

Figure 1.1 Particles incident on a slab

Of all possible outcomes arising after a collision involving a particle of the neutral gas, particular attention should be paid to the ionization collision phenomenon. Imagine having a particle incident on a neutral gas molecule (or atom for a monoatomic propellant), if the particle's kinetic energy is high enough it is possible that an amount of energy is transferred to a bounded electron sufficient to overcome its electromagnetic interaction with the nucleus, such an energy threshold is commonly known as "*ionising potential*". This mechanism is the very basis of the *electric discharge* phenomenon in gases: when an electrostatic field is applied to a finite volume of a neutral gas, free electrons -produced by the interaction of cosmic rays with the gas itself- are accelerated along the lines of the field and engage in ionising collision with the neutrals, thus generating an ion-electron pair. The additional electrons originated in this manner are in turn accelerated and become involved in further collisions, so that an avalanche multiplication of free charge carriers arises: this mechanism was named "*Townsend discharge*", after Irish physicist John Sealy Townsend who first discovered it. A voltage threshold does exist -called "*breakdown voltage*"- at which the gas must be considered as a conductive plasma, such a condition is referred to as *glow discharge* and will be detailed at a later time.

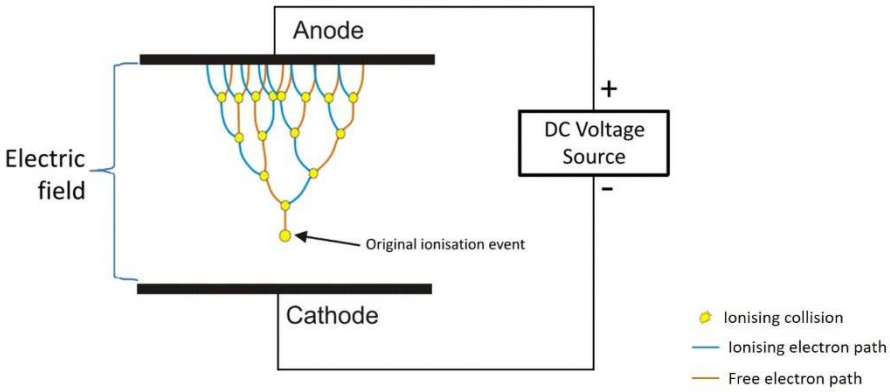

Figure 1.2 Townsend avalanche discharge phenomenon

1.2 Inertial electrostatic confinement

The present essay is going to describe work performed at the Institut für Raumfahrtsysteme (IRS), in Stuttgart, on the numerical simulation of the plasma inside an inertial electrostatic confinement device. Inertial electrostatic confinement (IEC) refers to a technique developed since the late 1950s in order to produce, confine and heat a plasma to fusion condition. Its paternity is, to some extent, unclear since,

while T. J. Dolan traces the original concept back to 22 June 1950, in Soviet physicist O. A. Lavrent'ev's work [5], the first device exploiting such a physical principle -called "fusor"- was patented in 1966 by American inventor P. T. Farnsworth [6].

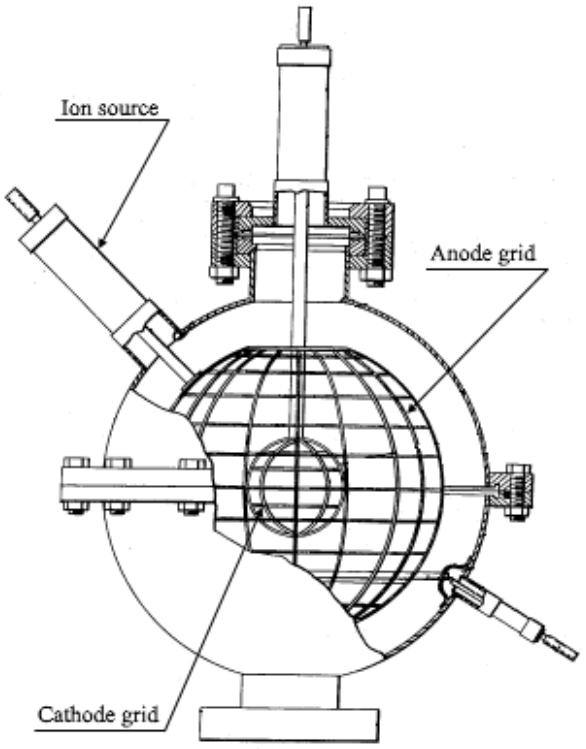

Figure 1.3 Schematic of the Hirsch-Meek fusor

An IEC device is essentially made up of two or more electrodes, upon which a high differential voltage is imposed by a power supply. Although many different geometrical layouts have been proposed for the electrodes, the most common design is the gridded-IEC where the device is composed of two concentric mesh grids: an outer anode, which is usually grounded, and an inner cathode, placed at a negative voltage. The system is then complemented by a vacuum chamber, the device is placed in, and either a gas feed subsystem or an external ion source (e.g. RF antenna ion source). In fusion applications, the main issue hindering the breakeven condition (i.e. a power output greater than the input power required for the IEC device to operate) is the scattering dominating over fusion reaction [7], which make IEC difficult to be an ideal energy source. On the contrary, for smaller neutron source and, possibly, space propulsion applications, the needed ions are produced in the glow discharge plasma, inside the gridded electrodes: a certain background neutral gas pressure is here required, in order to grant a proper rate for the ion reaction with the neutral gas. The idea of employing inertial electrostatic confinement for the development of a novel electric propulsion system -for space applications- is motivated by the experimental observation of a plasma jet escaping confinement under suitable operating conditions, in particular, if an asymmetry in the topology of confining field is provided [7]. In Tab. 1.2 an estimate of the typical propulsion performance parameters is provided, according to Prof. G.H. Miley, form University of Illinois at Urbana–Champaign, for an IEC-based electric propulsion system.

Table 1.2 Propulsion performance of a Xenon IEC ion thruster [7]

Parameter		Performance
Specific Impulse	[s]	3000
Thrust	[mN]	34
Jet Power	[W]	500
Net Accelerating Potential	[V]	600
Beam Current	[mA]	832
Input Power	[W]	$\sim 750 \div 800$
Thruster Efficiency	[%]	$62 \div 68$

The focus, in the inertial electrostatic confinement method, is the inertia of the recirculating ions in the electrostatic field, engendered inside the device's electrodes. According Earnshaw's theorem [8], a stable plasma configuration cannot be provided by an electrostatic field alone: this is conceptually straightforward if a steady-state situation is considered[2]. On the other hand, if a dynamic-state plasma is considered, the ions are electrostatically attracted by the inner cathode and, due the high transparency of this, they are most likely not to be neutralized rather they are involved in a recirculating motion through the inner electrode grid. In such a dynamic equilibrium, a positive electrostatic potential builds up at the centre of the device, which is in turn responsible for the confinement of electrons.

In a glow-discharge IEC device, the Townsend avalanche phenomenon is employed to obtain the ionisation of the neutral gas provided to the system as a "fuel": the high negative voltage applied to the inner cathode drives then the ions, in the discharge plasma, toward the device's centre at fusion-relevant energies. The ion beams, passing through the cathode grid holes, are then supposed to collide in the centre yielding a fusion reaction; otherwise, they move across the grid against the electrostatic field until the point the maximum potential energy is reached and they are accelerated back, in a loop process. The resulting recirculating motion would finally lead to the ion fusion if loss were not considered. These includes:

- Scattering with background neutrals.
- Change-exchange reaction, wherein a fast ion and slow neutral change identity, according to Eq. 1.8 [2].

$$\tilde{A}^{+} + A \rightarrow A^{+} + \tilde{A} \tag{1.8}$$

- The ions intercepting the grid wires hence being neutralised.

All in all, the confined ions have a low mean free path and a scattering cross section higher than the fusional one, hence, they are more likely to undergo ion-neutral interactions rather than a ion-ion fusion reactions. Moreover, the occurrence of charge-exchange reactions is a severe issue for an IEC device as it yields high-energy neutrals and low-energy ions, which are most likely to accelerate towards the cathode grid and are thus responsible for the electrode wire sputtering.

The presence of these loss mechanisms prevented the IEC technology, for fusion energy production, to achieve the breakeven condition so far. Nevertheless, the overcoming of some of these drawback (e.g. by employing ion guns to reduce background pressure in the reactor [9], carbon nanotubes for the grid manufacturing [10] or magnetically-generated virtual electrodes [11]), could allow for a longer confinement time and extremely high plasma density in the "core" region inside the IEC device.

[2] Consider, as an example, a positively-charged electrode placed at the edge of a plasma in the attempt to confine ions: due to its electrostatic potential it will attract electrons and, as they move to neutralise the potential, the entire plasma will be lost [8].

The achievement of a high-density core plasma in the IEC centre is possible, in a spherical geometry, thanks the three-dimensional compression effect and negligible background pressure in a device employing external ion sources. This was, indeed, the first designed ever proposed for a device exploiting the concept of inertial electrostatic confinement: the Farnsworth-Hirsch fusor. Its operating principle is based on the theory of "virtual electrodes": along the line of the reasoning exposed for the plasma confinement inside the IEC, it could be argued that, if the recirculating ions are focused inside the cathode grid, there a positive electrostatic potential yields, confining the electron population. Hence, the charged particles confined at the fusor centre would act like a virtual cathode, attracting and focusing the ion in a self-similar shell structure, as in Fig. 1.4.

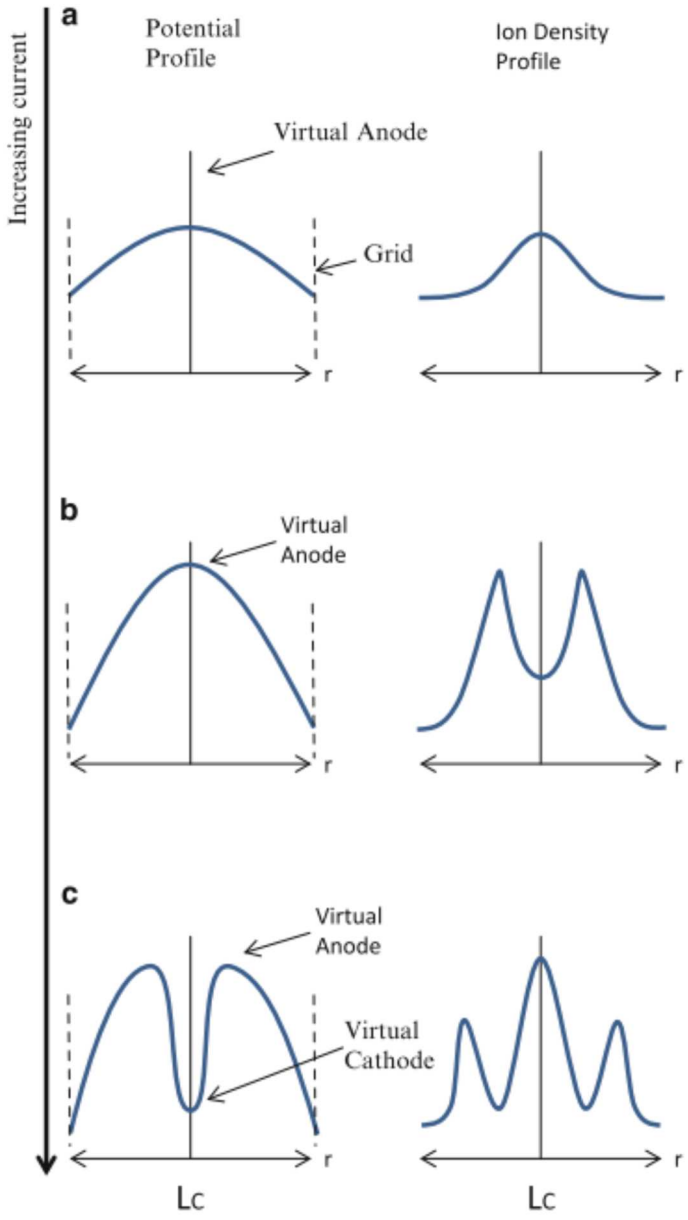

Figure 1.4 Inception of multiple electrostatic potential wells in a IEC device, for increasing circulating current, provided by the system's power source

The inception of multiple shell structures for the electrostatic field at the IEC centre (known in literature as "multiple well"), is the very point motivating the proposal of inertial electrostatic confinement as a possible fusion technology: the concentric virtual electrodes are able to confine the radially flowing ion population and focus the particles in an ultra-high density plasma core. A wealth of

numerical and experimental studies have been conducted on the physical conditions allowing for a stable establishment of multiple potential wells (e.g. in [9, 12, 13]). Numerical simulations took advantage of the high degree of symmetry in the most common geometrical layouts, for the IEC electrodes, to simplify the underlying mathematical model, solving then a one-dimensional plasma model [9, 14, 15]. All in all, except for some peculiar design (e.g. K.S. Murali's High Pressure IEC concept [16]), the multiple-well theory represents the conceptual framework to IEC fusion. Nevertheless, it is critical to observe that both numerical simulations and experimental observations disclosed the severe stability issues affecting the when the particles' recirculating motion and collisional processes are accounted for [14]. As a matter of fact, several experiments have failed to identify concentric electrostatic well structures [13, 17] and the only presence of a virtual anode in the converged core region was observed [18]. Furthermore, it is arguable that such an inconsistency between the multiple-well model and the experimentally observed plasma behaviour is all the more true in the case of a device operating a non-fusion regime, where the confined ions are not provided by external sources, but generated in the electron-impact ionisation process.

1.3 Spherical double layer model

If a glow-discharge IEC is considered, in which the recirculating ions are produced in the electric discharge between the gridded electrodes, a certain background neutral gas pressure is needed for the discharge to occur: this entails the ion-neutral interactions[3] being the dominant process in the IEC device. According to G.H. Miley and K.S. Murali:

> "*This greatly changes the plasma physics of the IEC as opposed to the idea of potential well with «zero» background pressure.*" [8]

Recently, Y.A. Chan and G. Herdrich, from the Institut für Raumfahrtsysteme in Stuttgart, have developed an alternative theory to explain plasma generation and confinement in an IEC device, basing on the concept of double layer [19]. A double layer (or "DL") is an electrostatic structure, which can arise in a current-carrying plasma, sustaining a non-negligible net potential difference [20]. The double layer - as a whole- typically has no net charge and the surrounding plasma has no significant electric field. Nonetheless, within the double layer two adjacent opposite space-charge regions can be identified: locally, the charge-neutrality condition is not give. Therefore, a significant internal potential difference ϕ_{DL} ensues across the DL thickness: the resulting electrostatic interaction with the charged particles in the surrounding plasma determines an accelerated flow, which carries the electric current I (although the occurrence of current-free DLs is given). Hence, from a circuit point of view, the double layer acts like an inertial[4] resistance, as it converts the electric power $\phi_{DL}I$ into kinetic energy for the accelerated particles. Double layers play a critical role in many physical phenomena -particularly in astrophysics (e.g. an early-suggested application is to solar flares [20]) - and, despite the common nature, can take various forms: in Chapter 4, a brief review of the most relevant kinds of DL is provided.

The double layer model for the IEC core plasma will particularly refer to one of the best-characterised double layers, known in literature as Langmuir DL [19]. B. Song *et al.* derived a stability criterion for such a double layer [21] and used it to investigate the dynamic of an exploding DL, i.e. to describe the time evolution of the nearly-spherical plasma region (also referred as "fireball") engendered in correspondence of a biased disk anode, once inserted in a steady-state plasma [22]. Y.A. Chan and G. Herdrich extended this spherical double layer (SDL) model to the core plasma in an IEC device, operating

[3] Including fusion reaction, scattering, charge-exchange reactions, etc. [101]

[4] On the contrary of common circuital load (i.e. ohmic resistance), in a double layer the balance of total mechanical energy, for charged particles in the plasma, at least as far as the Joule effect can be neglected: hence, the term "inertial" to qualify the resistance effect.

in non-fusion condition. An in-depth depiction of the IEC SDL model is provided in Chapter 4 of the present essay, for the purpose of this introductive section it will suffice to register that the proposed model offers both an efficient ionisation and plasma confinement mechanism [19].

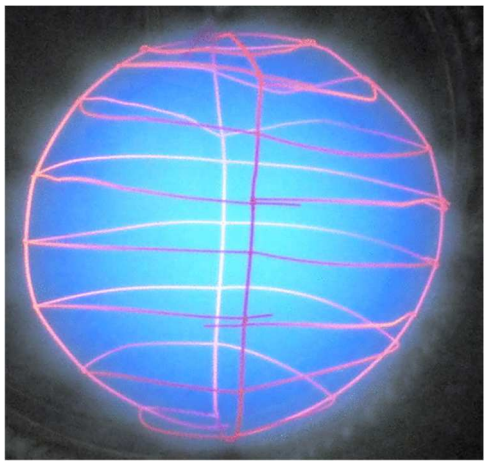

Figure 1.5 Inverted fireball in Argon plasma

In conclusion, the research work carried out at the Institut für Raumfahrtsysteme on the topic of inertial electrostatic confinement will be presented, in the present dissertation, according to the following organisation. First of all, insights on the operating principle for an IEC device and its possible applications -ranging from fusion power to an electric propulsion system- are given. A brief description of the IEC test facility, available at the Institut für Raumfahrtsysteme, is then presented. Further details on the state of the art for inertial electrostatic confinement technology are given in Appendix A. The first research step is aimed at the development of a numerical tool for the one-dimensional simulation of the core plasma in a glow-discharge IEC device. The adopted physical theory and the mathematical procedure underlying the computational algorithm for the plasma simulation are detailed in Appendix B. On the other hand, Chapter 3, after recapitulating the most relevant features of the simulation algorithm, describes its implementation in a computational tool. Finally, the simulation of the IEC device investigated in the IRS test facility is presented and the resulting output discussed. In light of the results provided by the one-dimensional simulation for the investigated device, an alternative physical theory for the description of both the ionisation process and the plasma confinement mechanism is presented in Chapter 4. This theory provides an alternative physical framework for the description of plasma behaviour in the core of an IEC device, introducing the concept of spherical double layer. Consequently, a computational algorithm for the simulation of the IEC core plasma, according to the double layer model, is introduced. In Chapter 5, the through characterisation of the three-dimensional topology of the externally applied field. At a first instance, the problem is simplified by assuming an axial symmetry for the gridded electrodes configuration and a semi-analytical solution is presented for the resulting two-dimensional electrostatic field. Subsequently, a numerical scheme for the evaluation of the three-dimensional electrostatic potential is described: the resulting computational algorithm is implemented in a software, which is then employed for the simulation of the device investigated at IRS. The detailed description of the mathematics underlying both the two- and three-dimensional solutions is deferred to Appendix C. The last step is focused on the study of the plasma behaviour in the core of the investigated device according to the spherical double layer model presented in Chapter 4. Finally, Chapter 7 briefly recapitulates the work carried out and the most relevant results attained, before presenting the projected future research on the numerical investigation of the plasma behaviour in an inertial electrostatic confinement system.

Chapter 2

IEC device: theory and state of the art

2.1 IEC Theoretical background

¶ Operating principle

The simplest way to comprehend the architecture and operating principle of an IEC device is to analyse the basic Farnsworth's fusion reactor, as originally presented in a series of patents that American physician Philo Taylor Farnsworth registered between 1966 and 1968 [6, 23]. Farnsworth's fusion reactor -commonly referred to as "fusor"- is a device originally conceived to generate net power via controlled fusion reaction. It consists of two concentric electrodes, which are assigned to produce an electrostatic field, in order to confine the ultra-hot fusion plasma.

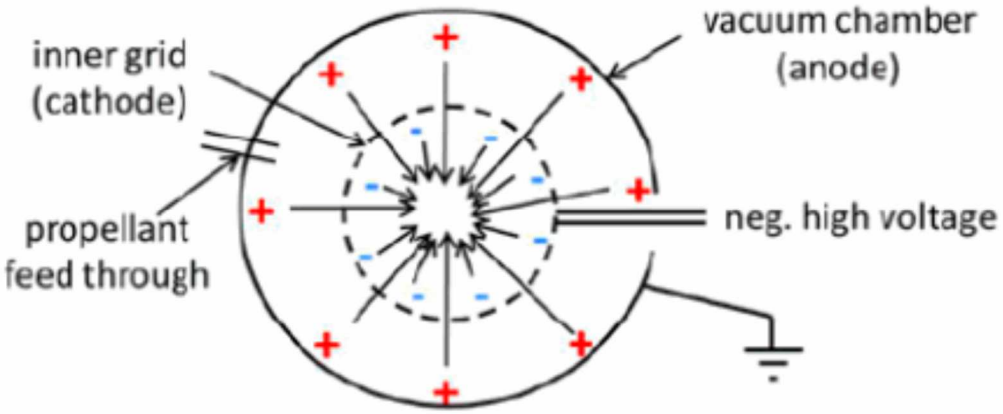

Figure 2.1 Schematic of a spherical Farnsworth's fusor [24]

Electrodes are commonly metal grids formed by pre-fabricated rings welded together so to obtain a proper geometrical shape. Two basic electrode geometry have been most widely employed in the realization of fusors: spherical-symmetric electrodes (Spherical-IEC, S-IEC) and cylindrical-symmetric (Cylindrical-IEC, C-IEC). Either ways, the functioning principle has no dependence on the specific symmetry adopted in electrodes' geometry and different shapes were proposed as well (e.g. in Fig 2.2, an example of helicoidal IEC device is given). As already notice in the introductory chapter, the only important point, as far as electrode geometry is concerned, is that a certain degree of transparency is required for the cathode, in order to have an actual inertial confinement for the ion population[5]. In any case, the most common electrodes have the same convergent shape and differ only by their radius and transparency, where "transparency" is defined as the ratio between the grid open space and its overall surface.

[5] Remember that, according to Earnshaw's theorem [102], a solid electrode in not capable of providing electrostatic confinement of a plasma.

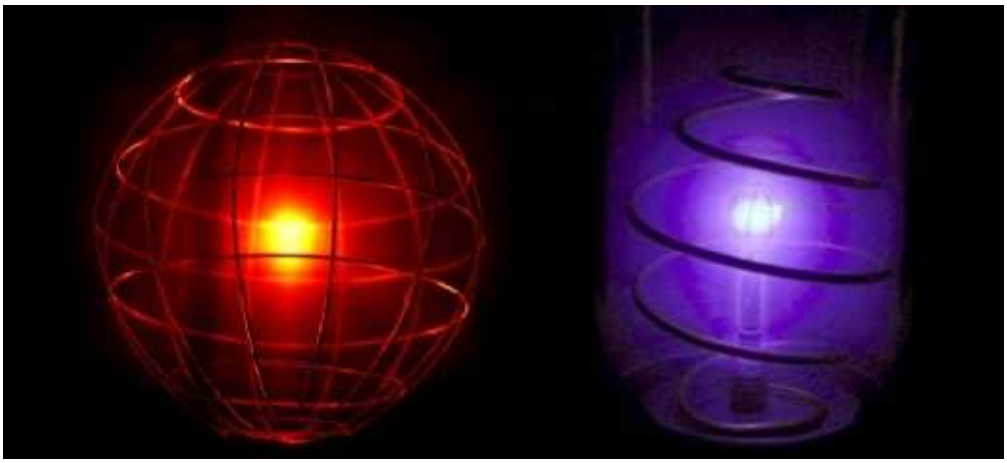

Figure 2.2 Examples of IEC device with different electrode geometries

Throughout its operation, the device is placed in a vacuum chamber equipped with an intake valve, which allows for the introduction and flow regulation of a neutral gas inside the IEC. Depending on the context, this gas may be referred to as "fuel" -for a fusion reactor- or "propellant" -if the device is to be employed as an engine- so that for the purpose of this essay the term "propellant" will serve. The choice of a specific operating propellant is made on the base of the physico-chemical properties of the gas itself [25].

In most practical applications, the interest is focused, besides the mere confinement of the plasma inside the electrostatic field, in providing energy to the ions in order to increase the fusion reaction rate. Hence, the inner electrode is commonly placed to a negative electric potential (from now on this electrode will thus be referred to as "cathode") while the outer has a positive one ("anode") or might be grounded. The resulting electrostatic field inside the device is shown in Fig. 2.3, and a negative potential well is clearly formed in the device itself. The formation of such a potential well is the core concept in the operation of an IEC device, since it is responsible for the simultaneous confinement of the electrons and the energization of the ions.

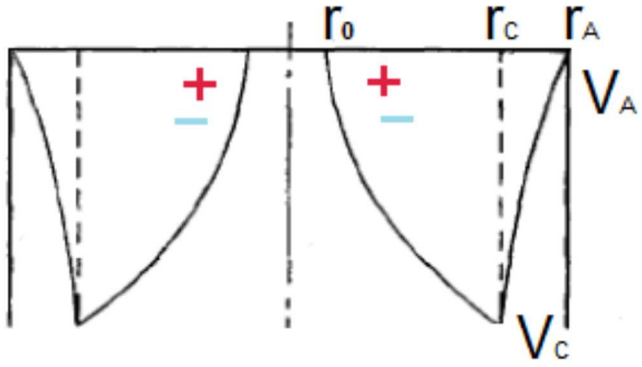

Figure 2.3 Sketch of the electrostatic potential inside the gridded IEC [24]

Consider an ion injected in the IEC, it will be driven by the applied electrostatic potential inside the device itself and will move radially away from the anode, accelerating towards the cathode. Once it reaches the cathode's radial position inside the electrostatic field it can hit the grid and be neutralized or it can pass through the grid's gates and enter the cathode. The latter case is of particular interest since many different scenarios might result:

- Interact with another ion: if the colliding particle have an extremely high energy the inter-nuclei distance can reach the scale of strong nuclear interaction and a fusion reaction may arise.

It should be noted that, if the interest in inertial electrostatic confinement of plasma is aimed at developing an efficient fusion reactor, this is, amongst all the different reactions that the ion could take part into, inside the IEC, the only one that does not represent a loss.

- Interact with an atom or molecule of the background gas, such an interaction must be regarded as an electromagnetic interaction of the ion itself with the electrons in gas particle's outer electron shell. This collision process may have different outcomes whose probability of occurrence, i.e. whose differential cross-section, is strongly dependent on the ion's energy:
  - Scattering, when the incident ion is diverged from its original trajectory,
  - Ionization collision, as previously discussed,
  - Charge-exchange reaction[6], interaction between a fast ion and a slow neutral, which bring to the creation of a slow ion and a fast neutral [24].
- Converge *en route* for the centre of the device being decelerated, according to space-charge limit, by the presence of a "virtual anode" inside the cathode. Hence, the particle moves radially until it reaches a point where its kinetic energy is zero and its motion is reversed, the ions moves then backwards in the inter-electrode area, where it will be again accelerated to the core.
- Pass through the cathode without incurring any scattering process and thus preserving its mechanical energy. On the basis of the energy conservation principle, it can be easily assessed that the ion will then move in the inter-electrode area, until it will reach a potential surface equal to its birth potential and then it will be accelerated backwards, just as pointed out in the previous paragraph.

In case of a relatively low ion current, no potential well inside the cathode is established. Hence, the positive charged particles oscillate through the cathode and within the anode grid envelop. Ions then lose energy the collisions with other ions or neutrals [26]. A representation of such a mechanism is given in Fig. 2.4.a. The output of this phenomenon is a circulating flow of ions in and out of the cathode grid and, hence, the upsurge of the electrostatic potential in correspondence of the device focus, corresponding to the formation of the already-mentioned virtual anode. The genesis of such a virtual anode inside the cathode tends to summon free negative charge-carriers in the plasma toward the centre of the device, originating a core of electrons on a lower scale. Fig. 2.4.b.

Along the lines of the dissertation about the virtual anode and electron core formation it is possible to argue that a multiple shell pattern for the potential profile in the radial direction will ensue: such a voltage configuration inside an IEC device is commonly referred to, in literature, as "multiple wells". It should be noted that the scheme depicted is strongly dependent on the potential difference between the electrodes and therefore on the current provided by the system power source: in case of a relatively low ion current, no potential well inside the cathode is established. In Fig. 2.4.c is represented the multiple wells prediction for the increasing ion current inside the IEC. The inception of multiple wells has been investigated since the very beginning of the study on IEC and was predicted by the steady-state spherical solution of Poisson's equation

$$\nabla^2 \phi = \frac{\rho}{\varepsilon_0} \tag{2.1}$$

Where ϕ, is the electrostatic potential
ε_0, is vacuum permittivity
ρ, is charge density

[6] This kind of reaction should be considered a loss since the low energy ion is most likely to be draw by the cathode, thus colliding with it and neutralizing, while the high energy neutral will collide or cause fusion probably elsewhere in the chamber [8].

Assuming particles with purely radial motion (i.e. with no transverse momentum), so that multiple potential wells are also known, in the literature, as "*poissors*" [9, 17]. In Fig. 2.4.d, different possible poissor patterns are depicted and the fluctuations of charged particles amidst potential peaks or valleys (according to the sign of the charge carried) are included.

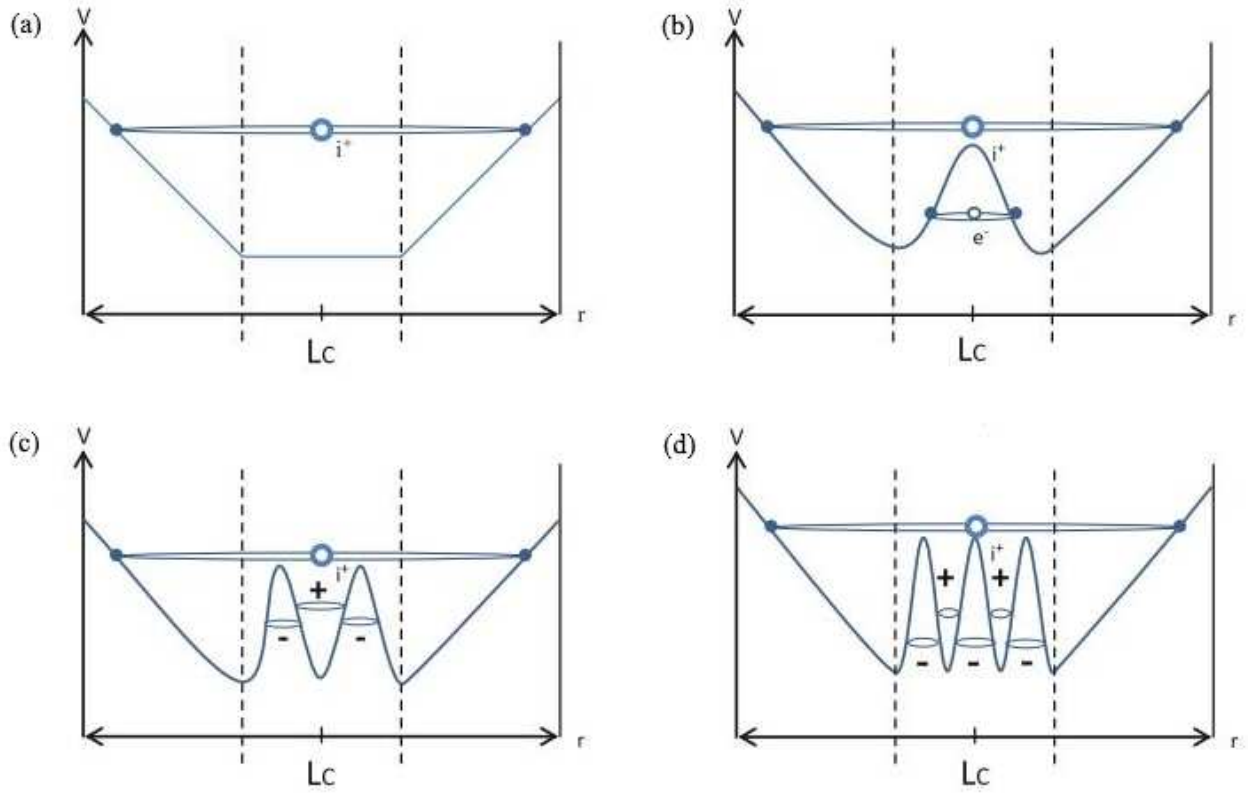

Figure 2.4 (a) Ion confinement inside the IEC cathode, for low ion current: ions travel through space inside the IEC electrodes and oscillate through the cathode grid and the device centre.
(b) Inception of a virtual anode inside the cathode grid: the probability of ions appear at centre of IEC results in the accumulation of space charge potential, which further drive electrons inward to maintain charge equilibrium.
(c) Inception of a double potential well: the accumulation of electrons in the core region is high enough to decrease the space charge in the core of virtual anode and results in two virtual electrodes: an outer virtual anode and an inner virtual cathode.
(d) Inception of a triple potential well [8].

It is worthy of note, nevertheless, that the establishment of a high number of concentric potential wells is most unlikely to appear since the kinetic energy of ions is dissipated due to charge-exchange collision or conversed into internal energy (e.g. rotational energy, due to the upsurge of transverse motion). Moreover, while some experimental verification of the existence of potential wells has been made only on electron-driven electrostatic confinement [15, 27], other beam probe experiments have failed to identify a distinctive electrostatic well structure [13]. Indeed, studies made for ions with finite transverse momentum show the multiple-shell "poissor" structure could not form [17, 27]. Hence, the poissor issue is still somewhat open [28].

As far as fusion energy generation is concerned, it is worthy of mention that fusors suffer from a very low efficiency, in terms of the ratio of fusion output power and system input power. Indeed, due to the reduced dimension of fusional cross-section for ion collisions, in a typical system, the probability that any given ion will be lost to a process other than fusion is approximately 100,000 times higher than that of losing an ion to a fusion reaction. The improvement of charged particle confinement in IEC systems is therefore of paramount interest [29].

¶ Ion sources

Once exposed the physics principle upon which the electrostatic confinement of charged particles relies, it is appropriate to identify the possible sources charge carriers can originate from in an IEC device. Although the original design patented by Farnsworth envisaged the use of ion guns in order to provide the ions to be confined [23], the possibility is given, for an IEC device, to work in discharge mode that is with plasma originating from ionization of the neutral gas introduced in the vacuum chamber. Hence, with respect to the primary ion source for the plasma supply of the device, three different conceptual design of an IEC can be identified [24]:

1. *Glow Discharge* - GD
2. *External Source* - ES
3. *Assisted Glow Discharge* - AGD

As its name suggests, GD design is based on the electric discharge phenomenon occurring in the mass of propellant introduced in the device. As already introduced, glow discharge in a gas is the output of an avalanche multiplication of the electric current driven by the free negative-charge carriers in the gas itself (i.e. *Townsend's avalanche*). In Fig. 2.5 a detailed representation of the voltage-current characteristic of a neutral gas volume, put between planar, solid electrodes, is given: it describes the effect of the potential difference applied on the electrodes, driving the free charge carriers inside the gas.

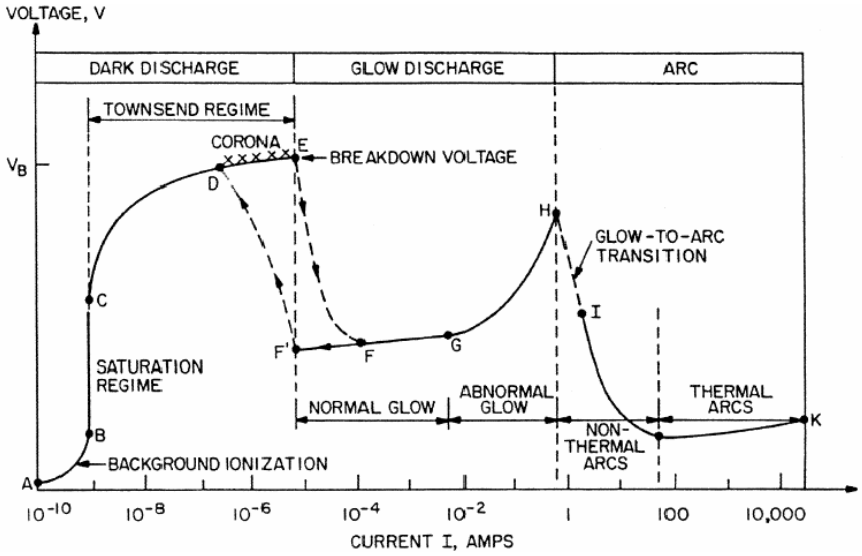

Figure 2.5 Characteristic voltage-current curve of a gas medium involved in the discharge phenomenon. Dependent on the applied voltage, three different regimes can be identified: "*dark*", "*glow*" and "*arc discharge*" [30].

The *saturation regime* identifies the upper limit imposed in the electric current by having all the free electrons (created by the interaction of energetic cosmic rays with neutral particles) accelerated towards the anode: the trigger of the *Townsend discharge* phenomenon overcomes this limit by allowing an exponentially increasing number of free electrons to drive the electric current. Once the breakdown potential is reached, the gas results highly ionized and must be regarded as a *plasma* in its own right. As previously mentioned, this regime is known as "*glow discharge*" because of high rate in photon-emission by excited atoms. In normal glow regime is possible to increase the electric current of several orders of magnitude without affecting the voltage: this is due to the trigger of a mechanism known as *sputtering*, that is the electron-emission by the cathode, owing to the ions accelerated by the electrostatic field and colliding on the electrode itself. When the sputtering involves the entire cathode surface, the plasma enters a transition regime, called "*abnormal glow*", through which a new physical phenomenon arise: the *thermionic emission* [8]. As a result of the high number of energetic ions colliding with the cathode, the electrode itself is heated, until a point is reached, when it spontaneously emits electrons: hence, the electric

current that passes through the plasma is increased by a reduction in the applied voltage, i.e. the plasma shows a negative differential resistance. This final regime is referred to as "*arc discharge*" and it is of capital importance in many practical applications, including space propulsion (e.g. Arcjets, TIHTUS project [31]). While the dependence of the *discharge plasma* characteristics on the applied potential difference should now be plain, it is worth to outline the role played by the background gas pressure on the establishment of the discharge. Indeed, the breakdown voltage for a given gas -i.e. the minimum voltage value under which the discharge is self-sustaining - is related to the gas pressure by an experimental relation, known as "*Paschen curve*". A precise value of pressure (p) can be identified, in whose correspondence the voltage required to spark the discharge is minimum.

In the specific case of an IEC device, whose electrodes have (typically) a spherical or cylindrical geometry and an extremely high transparency, experimental results follow qualitatively the Paschen curve as showed in Fig. 2.6. [24].

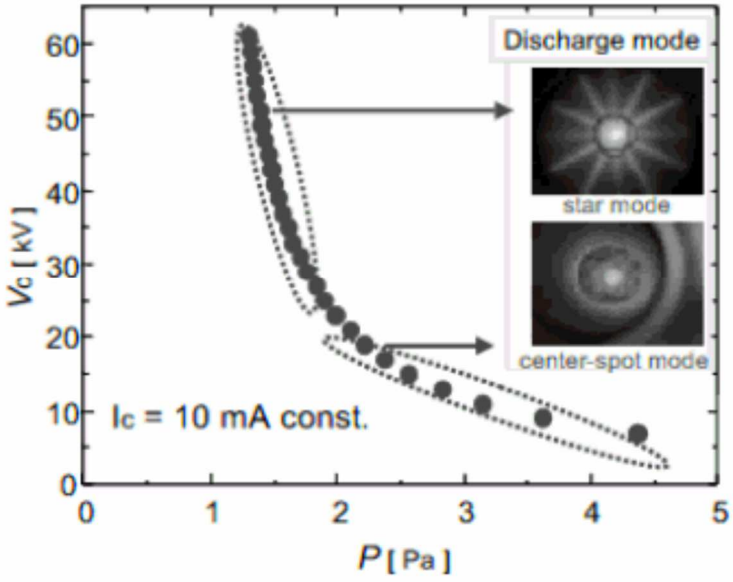

Figure 2.6 Paschen curve experimentally obtained for the discharge plasma in an IEC device. A clear dependence, for the discharge behaviour, on the background neutral gas pressure is observed. In a high pressure and low voltage regime, a glow discharge is obtained at the centre of the IEC device. On the other hand, when operated at low pressure and high voltage, the IEC device shows a steep negative characteristic slope [24].

Nevertheless, from a quantitative point of view, the pressure-voltage characteristics for an IEC are found to be significantly different from those of solid-cathode discharges that operate in the same pressure range since the value of $(p \cdot d)$, is seen to be about three times higher for the solid-cathode discharge than for the transparent cathode. This is primarily because of the high transparency of IEC electrodes [32]. Hence, in GD operated IEC devices, the background gas pressure should be high enough to sustain the gas discharge, which creates ions. On the other hand, however, by doing so the favourite interaction is beam-background kind [33] and consequently a great number of charge-exchange collisions will occur. A decrease in the background pressure will reduce the ion source as well [24].

In an ES design, on the contrary, the use of guns provides for charged particles injection so that ion and electron sources are decoupled. As already mentioned, this was the design originally conceived by Philo T. Farnsworth [6, 23, 34] and subsequently adopted in following researches [35]. This design allows for very low operating pressures, in order to have predominant the beam-beam interactions, thus favouring the fusion rate per unit power [8]. Finally a hybrid design can be conceived, specifically the AGD IEC, which employs a distributed plasma source and a heated filaments, e.g. of Tungsten [24]. In Tab. 2.1 a summarize of the main IEC designs, as far as the charged particles sources are concerned, and

their specifics is given, including a qualitative assessment of the typical "*fusion energy gain*" -defined as the ratio of fusion power produced in a nuclear fusion reactor (P_{fus}) to the power required to maintain the plasma in steady state (P_{in}):

$$Q = \frac{P_{\text{fus}}}{P_{\text{in}}} \tag{2.1}$$

Table 2.1 Different IEC design depending on the employed ion source [24]

IEC design	Ion source	Electron source	Fusion Gain
GD $\lambda_{mfp,i} \gg r_A$[7]	collisional ionization	collisional ionization cathode sputtering	low ($10^{-9} \div 10^{-5}$)
ES $\lambda_{mfp,i} \ll r_A$	ion gun	cathode sputtering thermionic effect	high
AGD $\lambda_{mfp,i} \gg r_A$	collisional ionization ion gun	collisional ionization cathode sputtering thermionic effect	low ($10^{-9} \div 10^{-5}$)

¶ Operating modes

The voltage required for relevant fusion processes to occur in an IEC depends on device's operational conditions such as, for example, the background pressure and the chemical species employed as fuel [26] and, nonetheless, can be identified in a range from 15 up to 20 kV [36]. Below such an order of magnitude for the discharge voltage, the device can be operate in non-fusion mode, which is the relevant functioning regime for the purpose of the present dissertation.

After a stable non-fusion condition is established in a GD-IEC, various operating modes -distinguished by a characterising discharge phenomena- can be induced, given a specific geometry for the gridded electrodes (e.g. the size of grid openings), by adjusting the device's functioning parameters, specifically the propellant feed pressure and the applied voltage. So far, experimental investigations of IEC identified four different operating modes, sketchily portrayed in Fig. 2.7 [37].

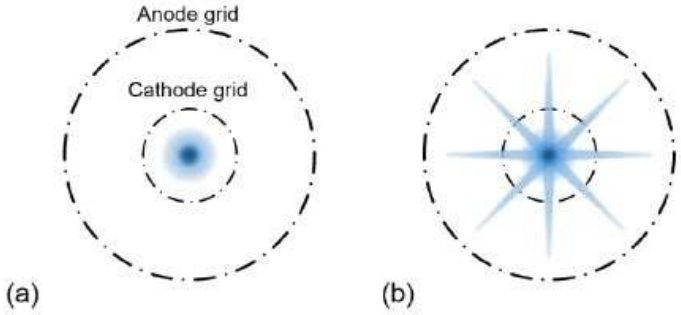

[7] $\lambda_{mfp,i}$ is ions' mean free path and r_A is anode radius.

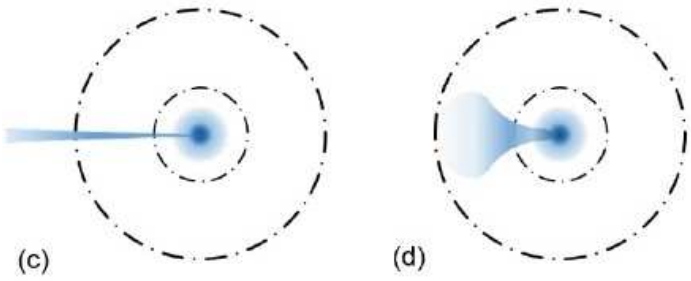

Figure 2.7 Schematic of the four different operating regimes experimentally identified for a gridded IEC device: (a) *Central-spot* mode, (b) *Star* mode, (c) *Tight-jet* mode, (d) *Spray-jet* mode [37].

In *central-spot* mode, a spherical, uniform glow discharge is established in the centre of the inner cathode, with the charged particles flowing almost uniformly through the device [24]. The symmetry exhibited in such a plasma configuration requires the electric field, inside the device, to be extremely symmetrical itself, hence the gridded electrodes should be thoroughly manufactured so to be perfectly spherical. This operational mode is conveniently characterized by determining the cathode's geometric transparency [24] defined, according to [18], as:

$$\eta_g = \frac{Open\ Area}{4\pi \cdot r_c{}^2} \tag{2.2}$$

Where "Open Area" represent the overall openings area and r_c is the cathode's radius.

Star mode is typically achieved for a lower background pressure and a higher applied voltage [24]. This unique discharge phenomenon, "*characterized by beams of light emanated by the centre if the chamber and passing through the grid holes*" [38] (Fig. 2.8) was first observed at the University of Illinois, Urbana-Champaign (UIUC) by George. H. Miley *et al.* [32].

Figure 2.8 Experimental observation of a gridded IEC device, operating in star mode [33].

In star mode, the discharge consists of peculiar current-carrying structures called "micro-channels", following George. H. Miley *et al.*:

> *"These microchannels radiate both outward from the cathode to the anode, and inward where they form a bright spot at the center of the volume circumscribed by the cathode. This implies that the discharge occurs between the anode and the holes in the cathode, i.e. that it seeks the regions of highest transparency."* [32]

Hence, the ion micro-channels are attributed to curvature in equipotential surfaces near the cathode grid, resulting from the use of extended openings sizes in the gridded electrode itself, and the subsequent

deflection of ion trajectories [39, 33]. More specifically the IEC cathode produces concave equipotential lines, which defocus ions as they approach the grid from the outside: once an ion is inside the grid volume, exits the grid [32]. According to the particle dynamics described in Ref. [32], ions are thus accelerated through the centres of the grid openings, resulting in a beam focusing toward the spherical centre. Fig. 2.9 depicts equal potential lines of a cross-sectional surface through the centre of a spherical cathode grid with large openings.

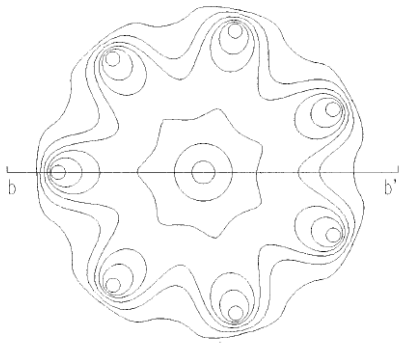

Figure 2.9 Sketch of the equal potential lines of a cross-sectional surface through the centre of a S-IEC [39]

As a result of this mechanism, micro-channelling is a function of the plasma state, cathode potential, and grid openings' size [33]. The resulting focusing effect thus reduces the number of ions colliding on the cathode grid and the "effective" grid transparency is enhanced: the experimental discovery of these micro-channels demonstrated that a perfect spherical grid was not needed for good ion convergence, thus greatly alleviating grid design and construction problems [39]. Furthermore, the ion beams focusing has a peripheral beneficial effect of alleviating electrode sputtering and extending its operational life [39, 36]. George. H. Miley *et al.* conducted a numerical simulation using SIMION, an electric field and ion trajectory program, developed at Idaho National Engineering Laboratory (INEL). Although this software could not account for the electric potential produced by the plasma itself, it enabled researchers to determine the possible trajectories for an ion inside the investigated IEC device. The results provided by such a simulation are perfectly consistent with the theoretical dissertation previously given. In Fig. 2.10, two different trajectories for an ion moving inside an IEC are depicted, depending upon the originating location of the ion at the beginning of the simulation.

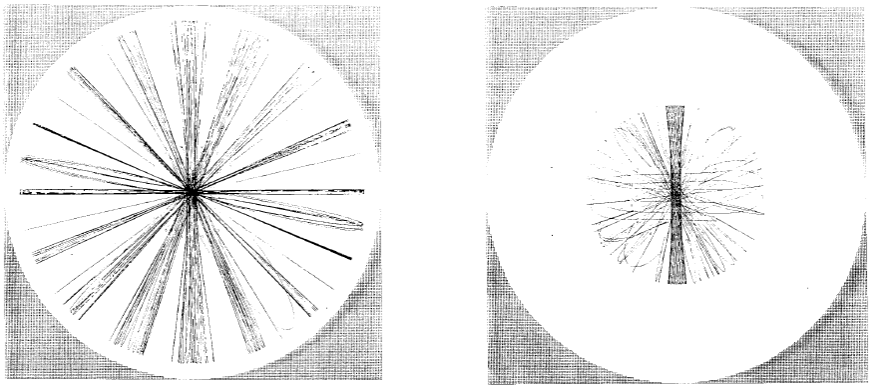

Figure 2.10 SIMION simulation for the ion trajectories in an IEC device [38].

Similar results were obtained by R. Moses who used "Mathematica" to plot ion trajectories in an IEC device [40]. Nonetheless, is should be noted that experimental measurements, confirming the micro-channels to actually represent ion recirculation paths, are still missing to date.

Finally yet importantly, *Jet* mode is unquestionably the most appealing operating condition for practical applications of IEC technology, other than fusion power: as the name implies, this operational mode is distinguished by a stream of energetic particles driven out of the device. As a rule, the jet extraction is attained at higher pressures and lower cathode voltage values than those, which characterize the star mode operations [24]; furthermore, its occurrence is encouraged if a complete symmetry of the grid is not given, but one grid opening is larger than the others [25]. First and foremost, it is critical to distinguish between the *tight-jet* and *spray-jet* modes, as they are characterised by a rather diverse plasma behaviour.

Further experimental measurements, recently conducted at IRS via electrostatic probing, were able to disclose the exact nature of the collimated particle beam observed in a tight-jet operating IEC device. As a matter of fact, according to the data reported in Ref. [41], the observed tight jet is a high-energy electron beam with scattering of secondary ions and electrons. Furthermore, these experimental observations clearly showed a strong dependence of the electron energy on both the propellant background pressure and the applied electrode voltage. The estimated efficiency of the power transmission through the highly collimated electron beam is above 55% [42]. Fig. 2.11 clearly shows that the microchannel structures, in the core plasma inside an IEC device, persist well into jet mode; this phenomenon was experimentally proved by Ryan R. Meyer [33].

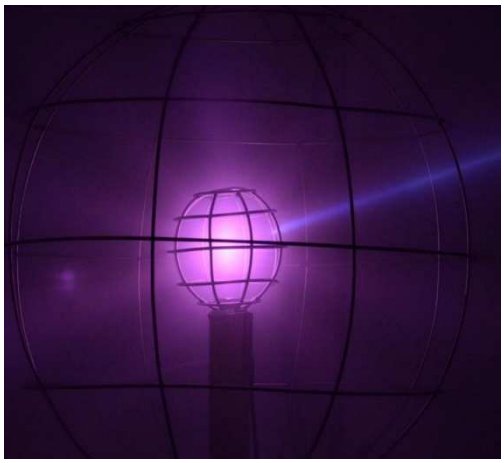

Figure 2.11 Experimental observation of the IRS-IEC device operating on a Helium discharge in tight-jet mode [25].

As far as the spray-jet mode is concerned, on the other hand, although a thorough experimental characterisation of the plasma jet is not available to date, preliminary measurements suggest that, in such a regime, the plume is constituted of both electron and ions [42]. The different nature of the plume escaping confinement in the tight-jet and spray-jet operations might well explain the rather diverse behaviour of the plume itself. Indeed, Fig. 2.11 clearly shows that, on the contrary of the highly collimated electron beam observed in tight-jet regime, the plasma plume constituting the spray jet (as hinted by the name) is rapidly diffused as soon as it get ahead of the cathode grid. This behaviour can be understood by considering the radial profile of the externally applied electrostatic field, given in Fig. 2.3. Once the ions escape confinement, in correspondence of the cathode grid gate, they are accelerated outwards, by the local electrostatic field, in the inter-electrode area. Nevertheless, as the electrostatic potential increases in proximity on the anode grid, the electromagnetic interaction tends to drag the ions and accelerates them backwards. Hence, soon after escaping the cathode grid, the ion plume fans out as the charged particles are driven along the diverging lines of the externally applied electrostatic field and reverse their motion. It is common understanding that, for thrust generation purpose, the acceleration of a relevant number of ions is mandatory: hence, the spray-jet mode appears to be the only operational regime of interest in the use of IEC technology for the development of an advanced plasma thruster. Nonetheless, the plume divergence is a suboptimal behaviour for a plasma thruster and needs to be restrained in order to effectively convert the particles' acceleration in thrust generation, limiting the divergence losses.

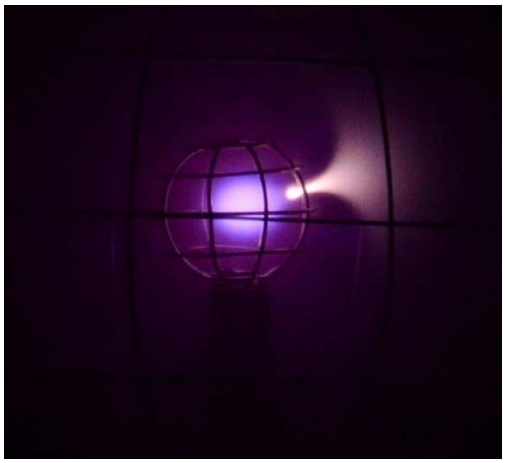

Figure 2.12 Experimental observation of the IRS-IEC device operating on an Argon discharge, in spray-jet mode [25].

A wealth of experimental measurement, conducted in the IRS test facility via electrostatic probing of the plasma plume, extensively characterised the operational regime for tight- and spray-jet mode: in these experiments different electrode configurations and propellant were tested [25, 36, 37]. The transition tight-to-spray jet was observed for a background pressure ranging from $5 \cdot 10^{-3}$ [mbar] to $6.5 \cdot 10^{-3}$ [mbar], this phenomenon was coupled with an abrupt increase in both the measured current in the plasma jet and the discharge voltage: this fact hints an increment in plasma conductivity with the change in discharge mode [25]. Moreover, the tight jet was not observed for higher background pressure values -tested in the experimental campaign- in the range $4 \cdot 10^{-2} \div 2 \cdot 10^{-1}$ [mbar]. Furthermore, the comparison between the measurements conducted on different propellants -namely Nitrogen, Argon and Helium- showed an overall similar discharge behaviour in both the tight- and spray-jet regimes. Nevertheless, only Helium showed a very distinct tight jet reaching out of the electrode grids while Argon presented the more diffusing tight jet. As far as the transition tight-to-spray jet is concerned, it occurs at lower power for Argon than for Nitrogen while, on the contrary, it was not observed in the Helium discharge, for the tested levels: transition might affect the Helium discharge at higher powers [25]. In Fig. 2.13, tight jet and spray jet modes -in case of a Nitrogen discharge- are contrasted: it is clear how, in the second case, the jet diffuses well before reaching out to the anode grid.

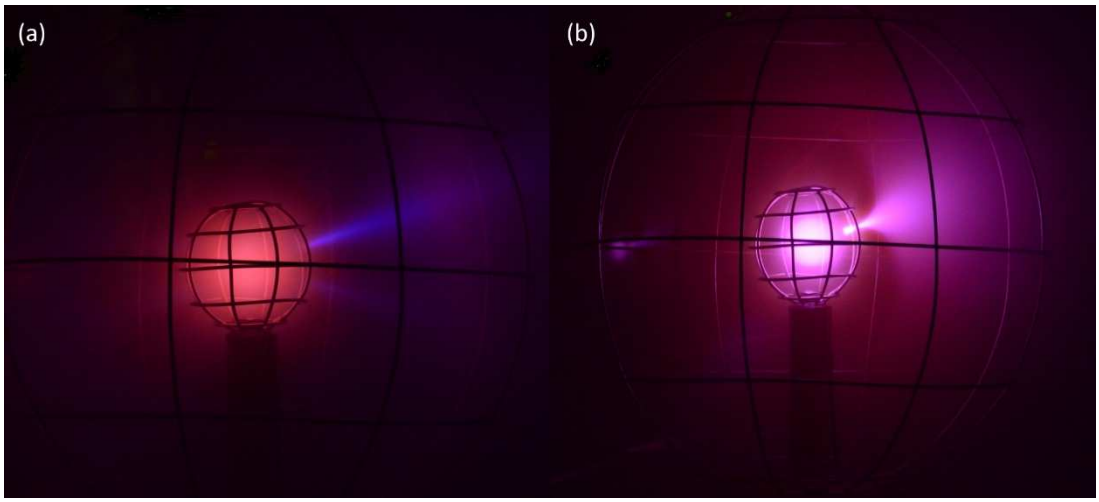

Figure 2.13 Experimental observation of the jet extraction in a gridded IEC device (Helium discharge): (a) Tight-jet, (b) Spray-jet [25].

Although the jet formation mechanism is still under discussion, it is possible to conclude, from experimental observations, that (as all other discharge configurations previously discussed) it strongly depends on the applied voltage, current, grids geometry, background pressure, and on the propellant

used [43]. In Ref. [36], a theory is exposed to explain the jet extraction mechanism: this relies on the consensus that jet extraction is an electron-triggered phenomenon [44]. Given an asymmetry in the electric potential distribution inside the IEC (e.g. due to a major opening in the gridded electrodes), in case a relevant number of electrons manage to escape the electrostatic confinement a local negative electric potential build up forcing the ion to follow out of the device thus originating the plasma jet. A numerical simulation of this model was performed in [44], combining a Particle-In-Cell (PIC) code for the resolution of Maxwell equations, a Direct simulation Monte Carlo (DSMC) solver for chemical processes and a Monte Carlo based Fokker Planck solver for the resolution of the Coulomb collision induced relaxation of electron and ion velocity distribution functions. Even if the electron acceleration was recovered by the kinetic simulations, the complete jet extraction including ions (which should provide the main thrust) was not observed: the results of this numerical study are thus inconclusive for the clear description of the jet extraction mechanism. An alternative description of the jet extraction is found in Ref. [42], setting in the theoretical framework of the spherical double layer model for IEC. According to this pioneering description of plasma behaviour in the investigated device, the jet extraction is triggered by the momentum imbalance for the charge-carrier populations driven by a low-scale electrostatic field, ensuing in correspondence of a localised non-neutral plasma region embedded in the core plasma. Due to the importance of this theory to the research that represented the object of the present dissertation, an entire chapter is devoted to the description of the spherical double layer model. The description of the jet extraction according to this theory is thus delayed to Chapter 4, Section 3, ¶ IEC-SDL model: plasma confinement, ionisation and jet extraction mechanisms.

2.2 IEC technology applications

¶ Thermonuclear fusion

As already stated, the concept of inertial electrostatic confinement of a plasma was originally conceived in the attempt to design a device capable of achieving the breakeven condition: a cornerstone in future power plant development. Despite the initial enthusiasm following Hirsch's work [9], which appeared to promise a ready breakthrough in fusion technology, IEC never achieved the breakeven condition and has soon be disregarded in favour of concurrent confinement techniques, such as Inertial confinement fusion (ICF) and magnetic confinement (i.e. Tokamak). Nonetheless, research on IEC fusion prosecuted and number of conceptual improvement was developed: an extensive description of these concepts can be found in Ref. [8]. Amongst all, it is worth mentioning R.W. Bussard's hybrid IEC magnetic device (also known as "Polywell"), which received strong funding from U.S. Navy and DARPA. Moreover, some private funding have been raised in the attempt to achieve the controlled fusion of an advanced thermonuclear fuel such as Proton-Boron, whose peculiarities makes it extremely appealing for commercial fusion power production. Nevertheless, none of these concepts has received enough funding to achieve breakeven condition [8]. Section 2, in Appendix A of the present thesis, is devoted to the description of the most promising IEC concepts, representing the present state of the art for IEC technology.

¶ Space reactors

On the envisioned future deep space exploration, in both robotic and -hopefully- manned missions, the focus is on the power source feeding both the on-board electronic systems and the electric propulsion system. On-board thermonuclear fusion reactors, which would be able to provide, at the same time, a huge power output -with a very high power to weight ratio- and an extremely dense and hot fusing plasma that might be directly accelerated by the electric thruster, seem to embody the perfect solution to this issue. In this respect, even if IEC never bordered in the breakeven condition (as presented in the previous section of the present chapter), it still provides an extensive database for a possible prompt scaling to the higher Q values required for a fusion thruster [45]. In 2003, R.L. Burton *et al.* proposed a concept design

for an advance 10 crew, manned space ship for deep space exploration. The designed "IEC Fusion Ship II" (an upgrade of a previous design called "IEC Fusion Ship I") is a 300 [m] long space ship, capable of performing fast interplanetary transfer missions. Its propulsion system is composed of two twin assemblies comprising five deuterium–helium-3 S-IEC reactors employed as the power supply for the ion thrusters [46]. The propulsion system -employing Argon as propellant- would a specific impulse of 35000 [s], with an estimated efficiency of 90% [47]. The estimated overall thrust is 4369 [N], making possible the transfer journey from Earth to Jupiter in 210 days and the return one in 152 days [46].

¶ Neutron source

Alongside the effort in achieving a profitable thermonuclear fusion reactor, a number of lower-scale applications for IEC have been proposed over the years, such as the use of an IEC device as a neutron source [48]. The first attempt of developing an IEC that would serve as a neutron source dates back to the late 1990s, to the work of G.H. Miley [8]. Neutron source devices, based on inertial electrostatic confinement of a fusing plasma, have a wide range of practical application that makes them appealing from both a research and an industrial perspective. Such applications include neutron activation analysis, tuneable x-ray source, radioisotope production, oil well logging and non-destructive evaluation [48]. Moreover, additional possible applications can be speculated, for higher Q output, such as fusion material testing, tritium production, subcritical reactors, boron neutron capture therapy (BNCT), nuclear and chemical/biological waste management, etc. (see Fig 2.14).

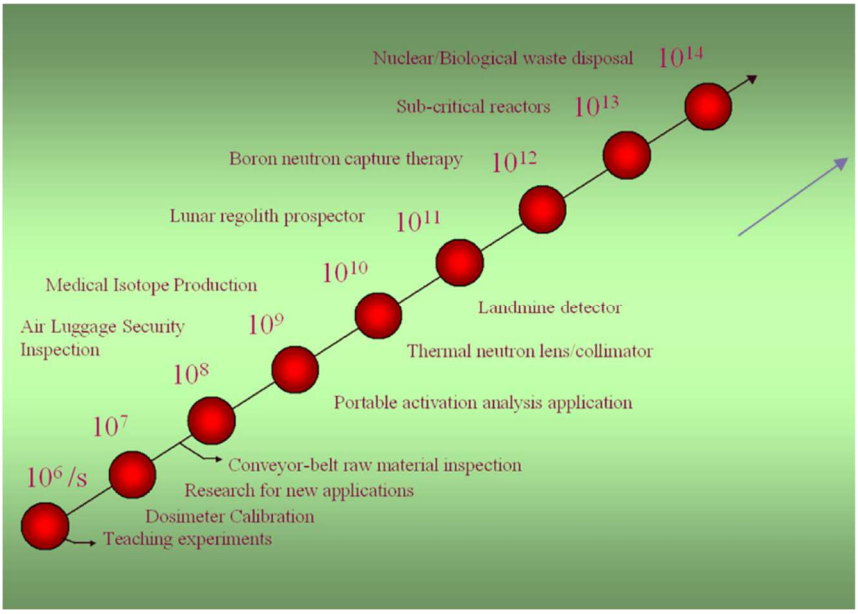

Figure 2.14 Possible applications of an IEC device dependent on the fusion rate. This picture shows an increase in the number of feasible applications for an increasing fusion reaction rate, from $10^{6}[s^{-1}]$ up to $10^{14}[s^{-1}]$ [48]

¶ Space propulsion

The most fascinating application of IEC technology, besides fusion research, is undoubtedly space exploration. In particular, the development of an IEC-based EP system has been originally proposed in Ref. and is the motivation of the research work here presented.

Such an application is based on the discovery of the jet mode (depicted in the first section of the present chapter) in which, provided a non-perfect symmetry condition for the plasma confinement inside the device, an intense plasma jet can be extracted [7]. Although the mechanism at the base of jet extraction in an IEC device is still not verified to date, recent developments in the description of plasma behaviour in the core of the investigated device (see Ref. [42]) promise to effectively portray the physics underlying

the plasma acceleration. The definition of a physical model able to describe the plasma jet extraction, consistently with the plasma confinement model, is vital to the accurate assessment of the propulsion performance of an IEC thruster and to develop significant technology improvements. In particular, the spray-jet mode is the operating regime of interest, in respect of the development of an IEC thruster.

As already mentioned, the most relevant obstacle hindering the effective thrust generation, in an IEC device, is the severe divergence of the ion plume extracted from the core plasma confined inside the cathode grid. Therefore, an efficient design is required in order to focus the extracted plasma jet out of the device. In Ref. [42], one possible solution is identified in the introduction of a magnetic nozzle in correspondence of the cathode grid gate, as depicted in Fig. 2.15: the nozzle is expected to collimate the extracted plasma, thus providing an effective thrust generation. Nonetheless, further investigations -both experimental and numerical- are required to assess the actual interaction of the magnetic field and the externally applied electrostatic field.

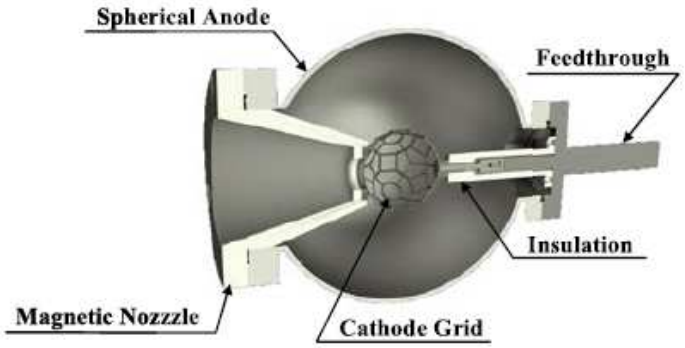

Figure 2.15 Schematic of a S-IEC thruster with a magnetic nozzle design for the plasma jet focusing [42].

An appealing feature of the IEC thruster design is that it would allow a remarkable control over the plasma jet, as both the carried charge and the beam transverse dimension are concerned. Thanks to this outstanding amount of control over the jet, responsible for the thrust generation, and to the great simplicity of the great architectural simplicity of the IEC device -depicted in Section 1 of the present chapter-, the IEC jet thruster appears a promising combination of a lightweight, inexpensive, reliable device and an efficient, high-impulse propulsion system.

The valuable features presented by the concept design of an IEC-based EP system are particularly remarkable when compared to other electrostatic thruster (see Tab. 1.1), namely gridded ion engines (GIEs) and Hall Effect thrusters (HETs). Indeed, an S-IEC device, in its application as an electrostatic space thruster, can be thought of, to some extent, as the transformation of the planar geometry of a conventional ion thruster into a spherically symmetrical one. Hence, it is natural to compare the propulsion performance of the two architecture. The main difference between an IEC device and an ion thruster lies in the plasma confinement principle. In fact, while the ion confinement in a spherical geometry is achieved "inertially", (see Section 1, ¶ Operating modes), in the latter electrostatic confinement is impossible due to Earnshaw's theorem. A magnetic field, perpendicular to the inner electrostatic field, is thus provided here to achieve the plasma confinement and increase the ion path, so to obtain the desired ionisation degree. Furthermore, in a GIE a set of voltage-biased grids is employed to accelerates the ions in the plume, while the IEC thruster concept involves an enlarged grid opening to trigger the jet extraction. Either way, the local distortion of the electrostatic field, in the plasma sheath in correspondence of the grid gates, seems to play a critical role in triggering the ion extraction from both the devices.

Despite the remarkable analogies between the two configurations, an S-IEC device offers a number of advantages [45], with respect of the planar ion thruster, that make it look a superior design:

- Its confining mechanism should guarantee a lower erosion on the cathode. The high transparency of S-IEC grid offers a double benefit as, on the one hand, it greatly enhances the expected operational life for the thruster and, on the other hand, mitigating the demanding requirements for the grid manufacturing.
- Some experimental observations seems to hint the possibility to extract a quasi-neutral jet. Indeed, according to preliminary measurement conducted at IRS, the plasma plume escaping the core of the investigated IEC device -in spray-jet mode- consists of both ions and electrons [41]. This behaviour provides an inherent neutralisation mechanism for the ion beam, avoiding the necessity of a neutralising device and the related system complications.
- The expected high-density plasma jet, which would be extracted from the IEC core, would requires a smaller net opening, with reference to large area grid structure employed in a conventional GIE, thus reducing the propellant gas leakage and increasing the propellant utilisation efficiency.
- The extreme simplicity of its layout drastically reduces the structural weight.

As far as the efficiency is concerned, an S-IEC device can be assumed to have a comparable value to a gridded ion engine. Hence, while conventional GIE and the proposed S-IEC thruster concept seem to have a competing efficiency, the operational advantages offered by the latter promise to make it a superior design [45].

On the back of the striking benefit offered by IEC as a space propulsion system, much research effort have been paid in the US, Japan and Europe, resulting in a number of upgrade of the basic IEC design and new hybrid propulsion concept. Recently, in the light of an innovative model proposed for both the plasma confinement and jet extraction mechanism in a IEC device -depicted in details, in Chapter 4 of the present essay- Y.A. Chan and G. Herdrich proposed two pioneering application of the IEC jet thruster [42].

The first presented application is a combination of the IEC technology with a canonical Hall Effect thruster (HET), thus referred to as "IEC-HET". The discharge plasma in Hall thrusters is produced by means of electron impact ionisation, employing a hollow cathode to provide the required electron population. Despite it being a well-developed technology, hollow cathodes present the flaw of producing a thermalised electron population with a wide velocity distribution, this increase the difficulty in the proper topography definition, design and realisation of the magnetic field necessary to confine the plasma inside the device. Moreover, the kinetic energy of bulk electrons is not efficiently transferred in the ionisation, since only about one third of the total kinetic energy is actually conveyed in this process. In this respect, the use of a collimated, non-thermalized electron beam -provided by an IEC electron source- would improve the ionisation process in a Hall thruster. Indeed, the non-Maxwellian electron beam has lower thermal velocity but collimated drift direction; hence, it simplify the design of field topography for electron guidance and control. In addition, the demanded intensity for the magnetic field is lower as well due to high directional velocity of the electron population. Furthermore, it is possible to decouple the ionisation process from the plasma plume acceleration. In the proposed design for IEC-HET (see Fig. 2.16), the non-Maxwellian, high-energy electron population is extracted from an S-IEC and expanded in a diverging magnetic nozzle. Subsequently, a magnetic field, engendered by cusp coils, redirect the collimated electron beam reducing the axial component of the velocity and increasing the tangential one: a proper design of the magnetic field allows for an efficient kinetic energy transfer in the collisional ionisation process, yielding an high-energy, toroidal plasma volume. It is worth noticing that such a plasma is theoretically quasi-neutral, thus the requirement of a neutralisation circuit downward is uncertain.

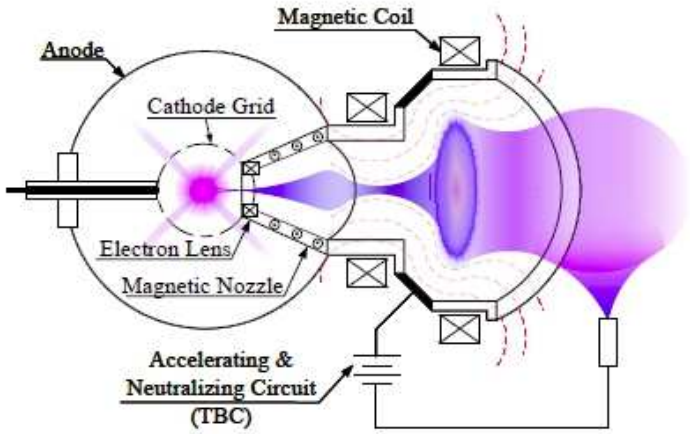

Figure 2.16 Schematics of the IEC-HET concept design [42]

The second proposed design concerns the possibility from the propulsion system, to collect the residual atmosphere, for low Earth orbit (LEO) applications, and employ it as the propellant for an electric thruster. This concept is commonly known as "Atmosphere-breathing electric propulsion" (ABEP) and is aimed to the development of self-sustained, low-orbit spacecrafts. The success of this conceptualisation hinges on the effective design of the atmosphere in-take and on the development of a highly efficient overall system, as both the in-take and the electric thruster are concerned. The main concern here is the extremely rarefied atmosphere collectable at on a LEO, challenging the intake designer: while most of the in-take concepts rely on the passive collection of the inflow, in order to improve the collection efficiency, an active collection mechanism is required. IEC can effectively provide such a mechanism, by introducing a magnetic trap, the electrode beam extracted from the cathode grid can be driven in a circulating motion, so to form an electron cloud (see Fig. 2.17). Neutrals, collected from the external rarefied atmosphere, entering the electron trap can undergo impact ionisation and, subsequently, be driven towards the cathode grid. A locally higher density plasma, as well as a virtual anode, thus yields: basing on DSMC-PIC simulations, the differential pressure resulting at the in-take extremity can reach $0.45\,[\mathrm{Pa}]$, on a $120\,[\mathrm{km}]$ orbit in Earth atmosphere; such a pressure range is, furthermore, suitable for IEC operation. The employment of IEC technology in ABEP provides both an active collection mechanism and an efficient electric propulsion system: hence, the IEC-ABEP promise to be an efficient, compact, lightweight design. Compared to concurrent ABEP concept, IEC-ABEP offers a larger a larger collection area, with an admissible loss in the kinetic energy for the inflowing particles, and the valuable benefit of providing, in the same device, the active collection and propulsive mechanism.

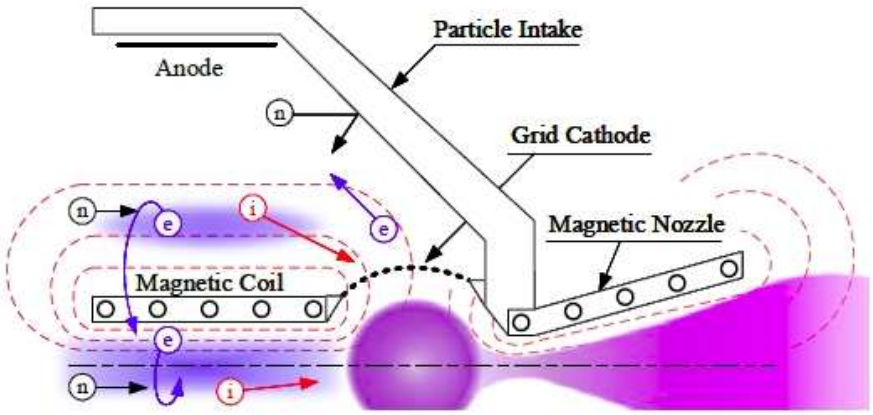

Figure 2.17 Schematics of an IEC thruster for atmosphere-breathing electric propulsion (ABEP) [42].

All in all, IEC jet thruster has the unique ability to cover a wide range of operational power promise to permit a number of application as space propulsion in space including lower orbit operations and deep space explorations as well [42].

¶ Fusion rockets

While the above-described design employs IEC technology only as a power source, providing high energetic alpha particles that are subsequently used in a direct converter, to produce electric power fed to the actual thruster (ultra-high I_{sp} ion thrusters, in the case above), alternative design have been proposed for the direct acceleration of the hot fusing plasma. In light of the long-standing experience in confinement of fusing plasmas in IEC devices, gained through early fusion research back in the 1960s and enhanced in the design and development of IEC neutron sources in more recent times, electrically driven IEC jet thruster could represent a good starting point for the development of proton-boron IEC fusion thrusters. According to Miley *et al.*, indeed, presently IEC neutron sources uses ~ 80 [keV] deuterium ion beams while operation with circulating ions at the required 150 [keV] energy for p-^{11}B fusion reaction has already been carried out at the University of Illinois and several other laboratories working in IECs [45]. The main issues hindering the achievement of an effective proton-boron IEC fusion reactor are the poor ion confinement time and severe ion losses: although several conceptual design have been proposed to overcome these obstacles, much more research effort is still needed to address the relevant technical issues. Nonetheless, electrically driven IEC jet thrusters could be theoretically upgraded to fusion jet thrusters without changing their design [42].

2.3 IEC at Institut für Raumfahrtsysteme (IRS)

Finally, it is appropriate for the reader to have a brief insight into the IEC test facility available at the Institut für Raumfahrtsysteme (IRS) in Stuttgart, which was employed throughout the experimental study reported the following chapters of the present thesis.

The development of an IEC device for the space propulsion at IRS began with a project to understand the jet extraction, in order to evaluate the applicability as a space propulsion device in 2011 [43]. In Fig. 2.18, a schematic representation of the IEC test facility at IRS is given.

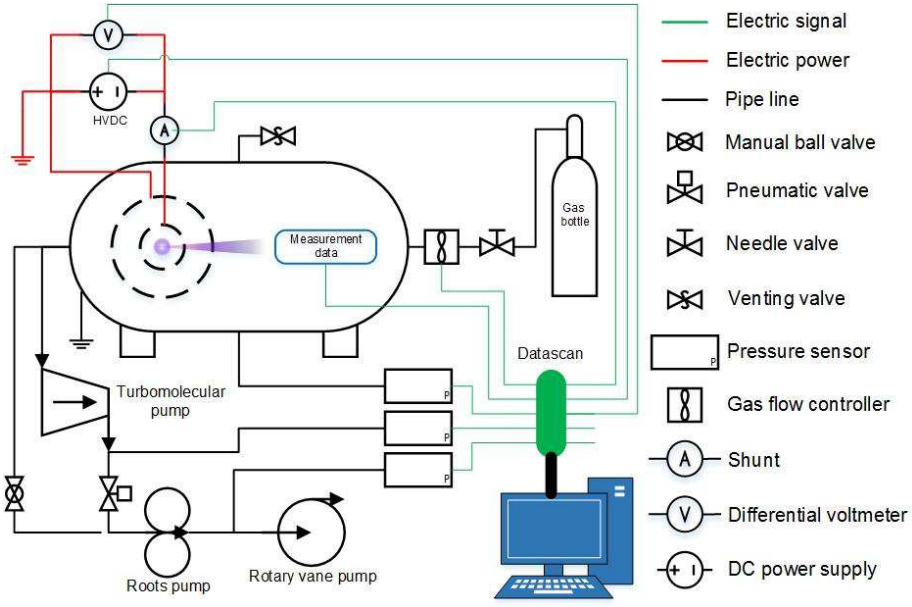

Figure 2.18 Schematic of the IEC test facility at IRS, in Stuttgart [43]

The employed test rig is made of the following subsystems:

1. IEC device (which will be following described in details)
2. Vacuum chamber and attached apparatus
3. Electrical equipment
4. Data acquisition subsystem
5. Propellant tanks

The vacuum system is composed by a cylindrical chamber -of 1 [m] diameter and 2.75 [m] length- along with a fully automatic three-step pumping system, so that this setup is capable of providing an ultimate vacuum condition equal to $1.8 \cdot 10^{-4}$ [mbar]. The system is then equipped with three pressure gauges (PG) -two of them are Pfeiffer™ TPR 280 and one PKR251- in order to monitor the chamber pressure as well as the pressure drop between the pumps. The propellant is stocked in pressurized tanks and can be injected into the vacuum chamber through a valve governed by the flow controller (FC), Tylan® FC2901 4S, which allows the user to adjust the background pressure inside the tested device.

The electrical setup includes a high voltage power supply (HVPS), a different voltage probe (DVP), and a shunt. The power supply is FUG HCN 350M-3500 (-3.5 [kV], 100 [mA]), max. power 350 [W]) which serves the thruster as the power unit. Since the power supply gives only a rough display of voltage, the electric potential drop between the two grids is measured by the voltage probe, TESTEC TT-SI 9110, which provides a measurement range up to 7 [kV]. The current is monitored from two positions: the power supply, which provides the information for the electron current outflow, and a shunt, which is installed at the anode to monitor the backflow current to the power supply.

All data are collected by a MSI Datascan™ 7320 operated by a LabVIEW™ data acquisition software (DAQ) that allows for multi-channels synchronized measurements [37, 25].

As far as the IEC device is concerned, it is made of two concentric gridded electrodes, characterised by a spherical geometry (S-IEC): though different configurations (which will be detailed later in the present paragraph) have been developed and studied, all the employed grids consist of one millimetre diameter wires made from stainless steel. Three different grid setups were used for the discharge and scaling experiments (see Table 2.2). Since scaling of spherical electrodes does not permit changing the electrode surface and the electrode gap independently, ratios are introduced in order to allow a better comparison.

Table 2.2 Grid configurations tested at IRS test facility

		K1	K2a	K2b	Ka3
Anode Diameter	[cm]	30	15	30	15
Cathode Diameter	[cm]	10	5	10	5
Electrode Gap	[cm]	10	5	10	5
Ratio Electrode Surfaces (A_A/A_C)	[−]	9	9	9	9

The first configuration (K1) is composed of an anode of 30 [cm] in diameter and a cathode of 10 [cm] (in Fig. 2.19) and is hang up with nylon wires in the chamber.

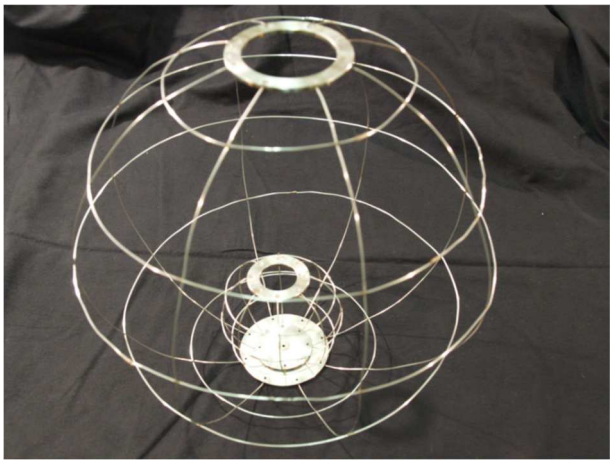

Figure 2.19 C1 configuration [25]

A second configuration K2a is composed of a 15 [cm] anode and a 5 [cm] cathode. The anode of K2a can also be combined with a 3.5 [cm] cathode which is K2b (Fig. 2.20). In this case, the grids are placed on PEEK holders. Grid setups K2a and b were designed in order to facilitate the manufacturing and therefore to increase the symmetry of the grids by reducing the size of the setup. Moreover, K2a was chosen to have the respective diameters in order to scale down the K1 setup by a factor of two and to keep the ratio of electrode gaps and electrode surfaces (anode/cathode). With a cathode of 3.5 [cm] the electrode gap in K2b can be varied, changing the ratio of electrode gaps and electrode surfaces. The number of longitude and latitude wires was maintained for all three configurations (5 latitude / 8 longitude). In that way the size of grid openings was reduced with K2a and K2b [25].

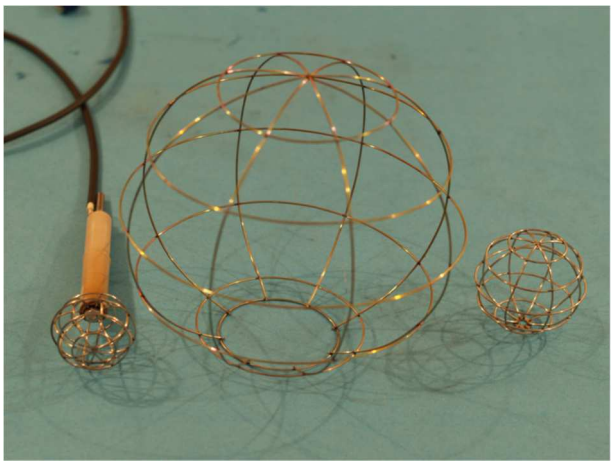

Figure 2.20 K2 configuration, including both K2a and K2b cathode grids [25]

Finally, a further grid configuration was introduced to assess the effect of willingly introducing an asymmetry in the applied electrostatic field topology on the formation of the plasma jet. Since several experimental observations seems to hint that the presence of an asymmetry, in the plasma confinement configuration, plays a critical role in triggering the jet extraction mechanism [37], an enlarged grid opening is introduced in the K3a grid layout. Experimental tests conducted on the K3a-IEC device proved that a proper design of the electrodes' geometry, and this of the topology for the resulting electrostatic field, provides control over the direction of the jet extraction. In the following, reference will be made to this electrode configuration in each and every simulation of the investigated IEC device.

In conclusion, an electrostatic probe measuring system allows for the characterisation of the plasma plume leaking from the core of the investigated device. The experimental setup employs a Faraday probe, an electrostatic probe characterised by a shield surrounding the collector: hence, Faraday probes allow for isolating the current coming from the side of the probe and calibrating the incoming current from the front [41]. The probe adopted in the IRS-IEC measuring system is composed of a 2 [cm] diameter

collector -made of high purity Tungsten-, a stainless-steel case and a Boron Nitride insulator, and is installed on a two-dimensional moving platform. This experimental setup is specially design for the characterisation of the plume generated by the asymmetric IRS-IEC device (i.e. the K3a grid configuration), operating in tight-jet mode. The moving platform allows for the alignment of the probe with the collimated electron beam at a distance of 30 [cm] downstream the IEC extraction port. In Fig. 2.21, a sketch of the experimental setup, with the investigated IEC device and the Faraday probe, is given.

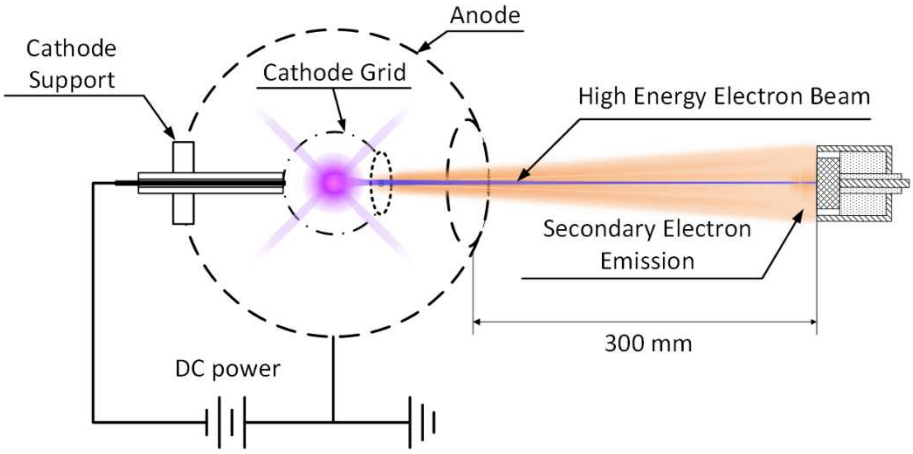

Figure 2.21 Arrangement of the IRS-IEC and Faraday probe for the experimental characterization of the tight jet [41].

Chapter 3
IEC 1D plasma simulation

3.1 Mathematical formulation

¶ Mathematical definition for the simulation model

The previous chapter of the present thesis depicted the typical architecture of an IEC device, along with the most relevant plasma phenomena observed in correspondence of different operating conditions. For the purpose of space propulsion applications of IEC technology, a thoroughly characterisation of the discharge plasma ensuing in an IEC device and the clear assessment of the operating conditions for the jet mode regimes is one of the main objective of the current research. In particular, as mentioned in the previous chapter, an unambiguous theoretical framework for the plasma extraction, occurring when an asymmetry in the plasma confinement is given, is missing to date. This greatly hinders any conceivable attempt to enhance the propulsive performance of an IEC jet thruster. Therefore, a reliable plasma model clearly plays a key role in fostering the comprehension of plasma dynamics inside the device and, subsequently, controlling the plasma extraction for propulsive applications.

In this respect, the first objective of the work here presented is the development of a numerical scheme for the simulation of the discharge plasma produced inside a spherical gridded IEC device. The developed numerical tool is based on the most widely adopted simulation approach, which exploits the geometrical symmetry in IEC devices to reduce the dimensionality of the two-fluid equations for describing the plasma (see Appendix B, Section 1, ¶ Two-Fluid plasma model). The resulting plasma model is the simplest mathematical representation of an IEC device. The first research work presenting such a simulation of the confined plasma in an IEC device is due to Soviet physicist O. A. Lavrent'ev[8]: hence, in the following, this numerical approach will be referred to as "*Lavrent'ev's method*" [9, 15].

As shown in the previous chapter, the steady-state operation of an IEC device can be described by means of Poisson's equation (Eq. 2.1). This is derived, in classical dissertation of electromagnetism, from Maxwell's equations for the electro-magnetic field:

$$\begin{cases} \nabla \cdot \vec{E} = \dfrac{\rho}{\varepsilon_0} & \text{(Gauss's law)} \\ \nabla \cdot \vec{B} = 0 & \text{(Gauss's law for magnetism)} \\ \nabla \times \vec{E} = -\dfrac{\partial \vec{B}}{\partial t} & \text{(Faraday's law of induction)} \\ \nabla \times \vec{B} = \mu_0 \left(\vec{J} + \varepsilon_0 \dfrac{\partial \vec{E}}{\partial t} \right) & \text{(Ampère} - \text{Maxwell law)} \end{cases} \tag{3.1}$$

Where $\vec{E}$, is the electrostatic vector field

ρ, is the charge space density

$\varepsilon_0 = 8.8541878176 \times 10^{-12}$ [F/m], is the *vacuum permittivity* (*free-space permittivity* or *electric constant*)

$\vec{B}$, is the magnetic vector field

[8] "Lavrent'ev considered the case of symmetric ion and electron injection in plane and spherical geometry. Employing arbitrary distribution functions, he solved Poisson's equation" [9].

$\mu_0 = 4\pi \times 10^{-7}$ [N/A^2], is the *vacuum permeability* (*free-space permeability* or *magnetic constant*)

$\vec{J}$, is the current density vector.

For the purpose of IEC operation, the following assumptions can be introduced, in order to simplify the mathematical model:

I. Steady-state conditions

$$\frac{\partial(\cdot)}{\partial t} = 0 \tag{3.2}$$

II. No external magnetic field is applied and the magnetic induction effect –due to the motion of charge particles- is negligible with respect to the external electric field

$$\vec{B} = \vec{0} \tag{3.3}$$

Under such assumptions, the electro-magnetic field is reduced to the simple electrostatic field $\vec{E}$, described by equation Eq. 3.4.

$$\begin{cases} \nabla \cdot \vec{E} = \dfrac{\rho}{\varepsilon_0} & \text{(Gauss's law)} \\ \nabla \times \vec{E} = \vec{0} & \text{(Faraday's law of induction)} \end{cases} \tag{3.4}$$

Hence, since the steady-state electric filed is irrotational, a scalar function V –named electrostatic *potential*- can be defined, such that

$$\vec{E} = -\nabla V \tag{3.5}$$

Thus, Maxwell equations for the electrostatic field can be recast as a second order elliptic partial differential equation (PDE) –which, from a mathematical point of view, corresponds to the Poisson's equation:

$$\nabla^2 V = \frac{\rho}{\varepsilon_0} \tag{3.6}$$

Lavrent'ev's method consists, then, in the numerical resolution of Poisson's equation, once the source term is defined in terms of the spatial distribution of the number densities for the charge-carriers, as a function of the electrostatic potential. The detailed development of the mathematical formulation, derived from physical considerations about the dynamics of a charged particle in the (assumed) symmetrical electrostatic field, is delayed to Appendix B. For the purpose of the present chapter, it will suffice to outline the basic set of equations employed for the one-dimensional plasma simulation of an IEC device.

The core equation employed in the numerical simulation is Poisson's equation for the electrostatic potential. Given the typical symmetry for the device's geometry, being it as S-IEC or a C-IEC, it is reasonable to choose a spherical or cylindrical coordinate system instead of a Cartesian one. Laplace operator can thus be recast in such a reference frame and greatly simplified by assuming the solution to be perfectly symmetrical. This assumption allows for eliminating the dependency of the electrostatic potential on any variable, except for the radial location, and greatly alter the nature of the mathematical problem: the elliptic PDE in Eq. 3.6 is here recast as the second-order ordinary differential equation in Eq. 3.7.

$$\frac{1}{r^2}\frac{\mathrm{d}}{\mathrm{d}r}\left(r^2\frac{\mathrm{d}V}{\mathrm{d}r}\right) = \frac{\rho}{\varepsilon_0} \tag{3.7}$$

Let the number density for the charge-carrier species be defined as the number of particles contained in a unit volume. The charge density given by each of the species can then be expressed as:

$$\rho_s = n_s\, q_s \tag{3.8}$$

Where q_s is the particle charge for the "s" population[9].

Moreover, since double-ionization reaction is much less probable than single-electron ionization, it is assumed that the former is negligible: hence, ion charge will be equal, in terms of absolute value, electron charge

$$n_i q_i = n_e |q_e| \qquad (\text{quasi} - \text{neutrality assumption}) \tag{3.9}$$

With $q_e = -1.60217662 \times 10^{-19}\ [C]$, electron (elementary) charge.

The source term in Poisson equation is thus expressed as the balance of the space-charge densities related to both ion and electron populations, in the form:

$$\frac{1}{r^2}\frac{\mathrm{d}}{\mathrm{d}r}\left(r^2\frac{\mathrm{d}V}{\mathrm{d}r}\right) = \frac{\rho}{\varepsilon_0} = |q_e|\frac{n_i - n_e}{\varepsilon_0} \tag{3.10}$$

In order to simplify the notation is custom, in literature, to normalise Eq. 3.10 with respect to the reference quantities in Tab. 3.1.

Table 3.1 Reference values for the normalisation of the physical quantities in Lavrent'ev's model.

Physical quantity	Unit of measurement (SI)	Reference value
Radial position (r)	[m]	Cathode radius r_c
Electrostatic potential (V)	[V]	Cathode voltage V_c
Electric charge (q)	[C]	Electron charge q_e
Number density (n)	$[\mathrm{m}^{-3}]$	Cathode number density n_c
Mechanical energy (W_s)	[V]	Cathode voltage V_c
Ion angular momentum (L_i)	$[\mathrm{Kg}\cdot\mathrm{m}^2\cdot\mathrm{s}^{-1}]$	$\sqrt{2m_i r_c^2(-q_i V_c)}$
Electron angular momentum (L_e)	$[\mathrm{Kg}\cdot\mathrm{m}^2\cdot\mathrm{s}^{-1}]$	$\sqrt{2m_e r_c^2(eV_c)}$

The final form for the normalised Poisson's equation –that will serve as a mathematical model for the IEC operation- is therefore given in Eq. 3.11:

$$\frac{1}{\rho^2}\frac{\mathrm{d}}{\mathrm{d}\rho}\left(\rho^2\frac{\mathrm{d}\phi}{\mathrm{d}\rho}\right) = \frac{n_i - n_e}{n_c} \tag{3.11}$$

Where ρ, is the normalised radial location

[9] In the following dissertation, the subscripts "i" and "e" will refer to ion and electron populations respectively.

ϕ, is the normalised electrostatic potential.

As a matter of principle, both ion and electron densities inside the device not only are unknown quantities but they do actually depend on the local electrostatic potential. Lavrent'ev's method requires thus the assumption, for each charge-carrier population, of the probability distribution function (PDF) over the phase space and the subsequent assessment of the respective number densities as the zeroth moment of these distribution functions. Following the dissertation on Lavrent'ev's method in Ref. [15], the dynamics of the charged particles inside the device can be described in terms of two constants of motion, namely their translational energy and the angular momentum. Eq. 3.12 defines the normalised constant of motion, for a particle in the "s" species, with reference to the values provided in Tab. 3.1:

$$\begin{aligned} \varepsilon_{\mathrm{s}} &\triangleq \frac{E_{\mathrm{s}}}{V_{\mathrm{c}}} && \textit{normalized transational energy} \\ \lambda_{s} &\triangleq \sqrt{\frac{L_{\mathrm{s}}^2}{2m_{\mathrm{s}}r_{\mathrm{c}}^2\left|q_{\mathrm{s}}V_{\mathrm{c}}\right|}} && \textit{normalized angular momentum} \end{aligned} \tag{3.12}$$

Hence, the PDF for a generic charged species is determined as a function of the following normalised quantities: its radial location, the electrostatic field, its translational energy and its angular momentum, as in Eq. 3.13.

$$f = f(\rho, \phi, \varepsilon, \lambda) \tag{3.13}$$

The number density of each charge-carrier species in the plasma is thus assessed as the integral of the assumed distribution function over the kinetic phase space[10]:

$$n = \int\int f(\rho, \phi, \varepsilon, \lambda)\, d\lambda\, d\varepsilon \tag{3.14}$$

Eq. 3.14 directly links the number density for the charge-carrier species to the unknown electrostatic field and the respective constants of motion. It is then clear that the simulation's accuracy greatly depends on the soundness of the assumed distribution functions: these should properly reflect the physical behaviour of the investigated plasma, modelling the actual dynamics of the constituting particles. The motion of charged particles in the confined plasma can be related to the electric current carried through the plasma itself, by means of Eq. 3.15 and 3.16 expressing the electric charge and mechanical energy conservation, respectively:

$$I_{\mathrm{s}} = 4\pi r^2 \rho_{\mathrm{s}} v_{\mathrm{s}} \tag{3.15}$$

$$\begin{cases} \dfrac{1}{2} m_i v_i^2 = |q_i V(r)| \\ \dfrac{1}{2} m_e v_e^2 = |e(V(r) - V_{\mathrm{c}})| \end{cases} \tag{3.16}$$

Following the line of dissertation presented in the work from C. Dobson and I. Hrbud, it is possible to introduce such a dependency in the source term of Poisson's equation, by defining a new physical variable, the *mono-energetic perveance*. In his seminal work on IEC [9], Robert L. Hirsch first introduced such a physical quantity as the proportionality constant in Child-Langmuir law for a space-charge limited current:

$$K_{\mathrm{s}} = \frac{I_{\mathrm{s}}}{|V_{\mathrm{c}}|^{\frac{3}{2}}} \sqrt{\frac{m_{\mathrm{s}}}{|2q_{\mathrm{s}}|}} \tag{3.17}$$

[10] This concept is more detailed in Appendix B, Section 1, ¶ Two-Fluid plasma model.

The introduction of the perveance for each charge-carrier species, allows for a great simplification in the definition of the mathematical model for the plasma simulation. For a deeper insight of the physics underlying the introduction of perveance in Lavrent'ev's model the reader is urged to Appendix B, Section 2, ¶ Mathematical definition of Lavrent'ev's method. For the scope of the present chapter, Eq. 3.18 will suffice to the definition of the final set of equations employed in the numerical simulation:

$$n_{\mathrm{s}}(\rho) = n_{\mathrm{c}} \frac{K_{\mathrm{s}}}{C_{\mathrm{s}}} \int \int f_{\mathrm{s}}(\rho, \phi, \varepsilon_{\mathrm{s}}, \lambda_{\mathrm{s}})\, d\lambda_{\mathrm{s}}\, d\varepsilon_{\mathrm{s}} \tag{3.18}$$

Where C_{s}, is the normalisation factor for the distribution function, defined in Eq. 3.19.

$$C_{\mathrm{s}} = \sqrt{\frac{m_{\mathrm{s}}}{2|q_{\mathrm{s}} V_{\mathrm{c}}|}} \int \int f_{\mathrm{s}}(1,1,\varepsilon_{\mathrm{s}}, \lambda_{\mathrm{s}}) \cdot v_{\mathrm{r,s}}(1,1,\varepsilon_{\mathrm{s}}, \lambda_{\mathrm{s}})\, d\lambda_{\mathrm{s}}\, d\varepsilon_{\mathrm{s}} \tag{3.19}$$

The simulation algorithm is finally complemented by the knowledge of the ion and electron currents flowing through the discharge plasma inside the device, I_i and I_e respectively. As already pointed out in the previous chapter, the electric current is measured, in the experimental apparatus available in the IRS test facility, at two different locations. The power supply itself monitors the outflowing electric current while the backflow to the power supply is gauged by a shunt, installed at the anode grid. These measures provide an estimate of the circuit current at the power supply I_{PS}, as shown in the schematic of the IEC electrical circuit, in Fig. 3.1.

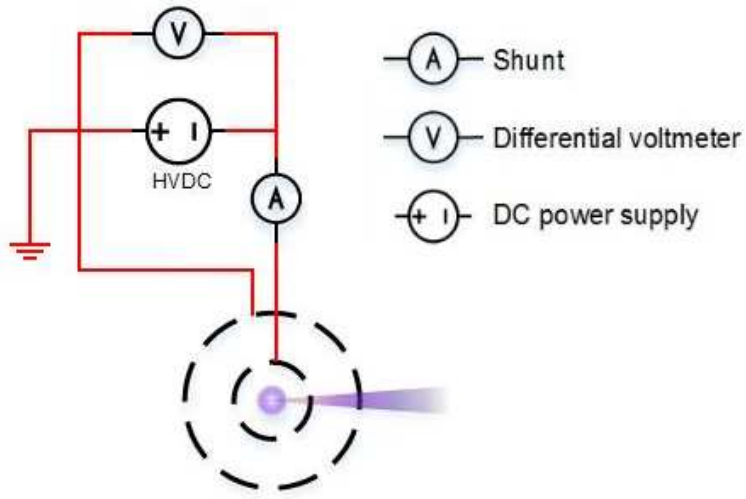

Figure 3.1 Schematic of the electrical circuit for the IEC device in the IRS test facility.

The effective grid openness hence links the ion current to the electric current collected at the cathode grid, denoted as I_{IC}, as in Eq. 3.20:

$$I_i = \frac{2\gamma_e}{1-{\gamma_e}^2} I_{\mathrm{IC}} \tag{3.20}$$

Where γ_e, is the effective grid openness, defined as a function of the geometric cathode grid openness, depending on the electrode configuration.

Under the assumption of negligible secondary photoelectric emission, the electric current collected at the cathode grid can be assumed to coincide with the current measured at the power supply. Thus,

$$I_i \cong \frac{2\gamma_e}{1-{\gamma_e}^2} I_{\mathrm{PS}} \tag{3.21}$$

As far as the electron current inside the device is concerned, it can be thought of as the electron space-charge current into the anode: such a current flows in one direction only and, although I_{PS} has other contributions, the net result is:

$$I_e = I_{\mathrm{PS}} \tag{3.22}$$

Therefore, once the IEC device geometry is known, along with the operating conditions, i.e. the applied voltage and current, the mathematical method for the one-dimensional plasma simulation is at last defined by the following set of equations:

$$\begin{cases} \dfrac{1}{\rho^2}\dfrac{\mathrm{d}}{\mathrm{d}\rho}\left(\rho^2\dfrac{\mathrm{d}\phi}{\mathrm{d}\rho}\right) = \dfrac{n_i - n_e}{n_{\mathrm{c}}} \\ n_{\mathrm{s}}(\rho) = n_{\mathrm{c}}\dfrac{K_{\mathrm{s}}}{C_{\mathrm{s}}}\int\int f_{\mathrm{s}}(\rho,\phi,\varepsilon_{\mathrm{s}},\lambda_{\mathrm{s}})\, d\lambda_{\mathrm{s}}\, d\varepsilon_{\mathrm{s}} \\ K_{\mathrm{s}} = \dfrac{I_{\mathrm{s}}}{|V_{\mathrm{c}}|^{\frac{3}{2}}}\sqrt{\dfrac{m_{\mathrm{s}}}{|2q_{\mathrm{s}}|}} \\ C_{\mathrm{s}} = \sqrt{\dfrac{m_{\mathrm{s}}}{2|q_{\mathrm{s}}V_{\mathrm{c}}|}}\int\int f_{\mathrm{s}}(1{,}1,\varepsilon_{\mathrm{s}},\lambda_{\mathrm{s}})\cdot v_{\mathrm{r,s}}(1{,}1,\varepsilon_{\mathrm{s}},\lambda_{\mathrm{s}})\, d\lambda_{\mathrm{s}}\, d\varepsilon_{\mathrm{s}} \\ I_i = \dfrac{2\gamma_e}{1-{\gamma_e}^2} I_{\mathrm{PS}}\,, \qquad I_e = I_{\mathrm{PS}} \end{cases} \tag{3.23}$$

Hence, Lavrent'ev's method allows for the assessment of the radial distribution for the electrostatic potential and the charged particle number densities in the confined plasma, by assuming the general form for the particle distribution function and numerically integrating the resulting Poisson's equation.

¶ Particle distribution functions

While the numerical integration of Poisson's equation is rather straightforward -once the particles' number densities has been assessed to determine the source term-, the definition of a suitable distribution function for each of the charged particle population needs to be further tackled.

In order for a particular function to represent a sensible PDF, for a particle population, it must be a solution of the kinetic plasma equation that, under the assumption of negligible Coulomb scattering processes, takes the form of Vlasov's equation:

$$\frac{\partial f}{\partial t} + \vec{v}\cdot\nabla f + \frac{q}{m}\left(\vec{E} + \vec{v}\times\vec{B}\right)\cdot\frac{\partial f}{\partial \vec{v}} = 0 \tag{3.24}$$

As pointed out by M. Ohnishi *et al.* [49] and H. Matsuura *et al.* [50], an IEC device is a weak collisional system, where the collision frequency and fusion-reaction rate are small compared with the transit frequency in the potential well. The motion of a charged particle in such a system can be represented by two constants of motion, namely the total kinetic energy E and the angular momentum L. Hence, introducing the normalisation of the physical model with respect to the reference values provided in Tab. 3.1, the PDF takes the form given in Eq. 3.13. Each species of charged particles in the IEC core plasma is thus described by its distribution function over the translational energy and angular momentum, while ρ and ϕ can be considered as parameters.

In literature, many different distribution functions have been employed in Lavrent'ev's method for the simulation of an IEC device. R.L. Hirsch reports [9] that Lavrent'ev himself solved Poisson's equation for "various distribution functions of interest, i.e. parabolic, Gaussian, and Maxwellian". Dolan *et al.* [15] developed two distinct models, using Dirac's delta distribution over total mechanical energy, known as *mono-energetic* model, and Heaviside's step function to simulate a rectangular profile for the particle distribution over energy and angular momentum. M. Ohnishi *et al.* [49] took into account the difference

in the collisional frequency for the ions and electrons: ions were assumed to be mono-energetic; while the thermalisation of the electron population, due to the collisional processes, was modelled by assuming an exponential form. In agreement with such a thermalised model, H. Matsuura *et al.* assumed that "the weak Coulomb collision may slowly relax the distributions towards a Maxwellian process" [50]. Finally, C. Dobson and I. Hrbud [14] compared the number density and electrostatic potential profiles for a number of different distribution functions, namely mono-energetic, rectangular, parabolic and thermal.

For the purpose of the present essay, three distribution functions will be presented and implemented in the mathematical model, as described in the previous section:

- Mono-energetic, i.e. the particles are assumed to have null angular momentum and a Dirac's delta distribution over the total mechanical energy;
- Rectangular, i.e. the particles are assumed to have a Heaviside's step distribution over both the total mechanical energy and angular momentum;
- Thermal, i.e. the particles are assumed to have an exponential form for the distribution function, accounting for the thermalising effect of Coulomb interactions between particles in a collisional plasma.

In the following, the considered distribution functions will be detailed in their physical meaning and the resulting mathematical formulation will be presented. The detailed mathematical development of the final set of equation for each and every distribution function deferred to Appendix B, Section 2, ¶ Probability distribution functions.

Mono-energetic distribution function

The "mono-energetic" distribution function represents the simplest mathematical form for the solution of Eq. 3.24 and can be considered to describe the discharge plasma in an IEC device, under the following simplifying assumptions:

1. The particles have pure radial motion, i.e. their angular momentum is neglected:
$$v_{t,s} = 0 \quad \forall s = i, e \tag{3.25}$$
The mechanical invariants for the charged particles' motion then result:
$$\begin{cases} L_s = m_s r v_{t,s} = 0 \\ E_s = \frac{1}{2} m_s v_{r,s}^2 + q_s V(r) \end{cases} \tag{3.26}$$
Eq. 3.27 yields from the custom normalisation of the constants of motion:
$$\begin{cases} \lambda_s = 0 \\ v_{r,s} = \sqrt{\left| 2 q_s \frac{V_c}{m_s} \right|} \sqrt{|\phi(\rho) - \varepsilon_s|} \end{cases} \tag{3.27}$$
2. The particles in the same population have all the same mechanical energy, i.e. the marginal energy distribution function has the form of Dirac's delta function:
$$f_s(\varepsilon_s) = \delta(\varepsilon_s) \quad \forall s = i, e \tag{3.28}$$
Where Dirac's delta function is the distribution that is null for any real value except zero, where it is infinite (see Fig. 3.2), and whose integral over the entire real line equals one.
$$\delta(x) = \begin{cases} \infty & x = 0 \\ 0 & x \neq 0 \end{cases} \tag{3.29}$$

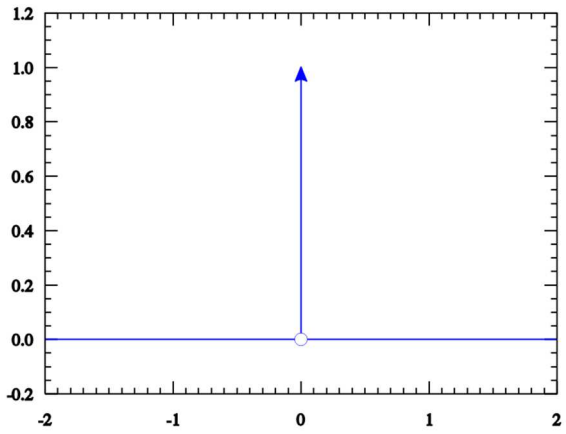

Figure 3.2 Dirac's delta function

Therefore, the particle distribution over the phase space -formulated in terms of translational energy and angular momentum- results

$$f_{\mathrm{M,s}}(\rho, \phi, \varepsilon_{\mathrm{s}}, \lambda_{\mathrm{s}}) = \frac{\delta(\varepsilon_{\mathrm{s}})}{\rho^2 \sqrt{|\phi(\rho) - \varepsilon_{\mathrm{s}}|}} \tag{3.30}$$

Due to the defining property of Dirac delta function of having unitary integral over the real field and the assumptions for mono-energetic plasma model in Eq. 3.27 and 3.28, the normalisation factors for the resulting distribution functions are easily assessed, as:

$$\begin{cases} C_i = \sqrt{\dfrac{m_i}{2|q_i V_{\mathrm{c}}|}} \displaystyle\int_0^{\phi} \frac{\delta(\varepsilon_i)}{\sqrt{1-\phi}} \sqrt{\frac{2|q_i V_{\mathrm{c}}|}{m_i}} \sqrt{\phi}\, d\varepsilon_i = 1 \\ C_e = \sqrt{\dfrac{m_e}{2|eV_{\mathrm{c}}|}} \displaystyle\int_{\phi}^{1} \frac{\delta(\varepsilon_e)}{\sqrt{\phi}} \sqrt{\frac{2|eV_{\mathrm{c}}|}{m_e}} \sqrt{\phi - 1}\, d\varepsilon_e = 1 \end{cases} \tag{3.31}$$

Thus, the normalised number densities in the source term of Poisson's equation are obtained at once, by taking the zeroth-order moment of Eq. 3.30:

$$\begin{cases} n_i(\rho, \phi) = \dfrac{K_i}{\rho^2 \sqrt{\phi}} \\ n_e(\rho, \phi) = \dfrac{K_e}{\rho^2 \sqrt{\phi - 1}} \end{cases} \tag{3.32}$$

The mathematical form in Eq. 3.32, express the dependency of the number densities of the charge-carrier species on the radial location and the electrostatic potential inside the IEC device, which is determined by the energy conservation of the charged particles in radial direction, according to Eq. 3.27. In conclusion, Poisson's equation is recast, for the mono-energetic plasma model, as follows:

$$\frac{\mathrm{d}^2\phi}{\mathrm{d}\rho^2} + \frac{1}{2\rho}\frac{\mathrm{d}\phi}{\mathrm{d}\rho} = \frac{1}{\rho^2 n_{\mathrm{c}}}\left(\frac{K_i}{\sqrt{\phi}} - \frac{K_e}{\sqrt{\phi - 1}}\right) \tag{3.33}$$

This second order ordinary differential equation (ODE) can finally be redraft in the form of a first order ODE system, by means of a canonical substitution [26]:

$$\theta = \frac{\mathrm{d}\phi}{\mathrm{d}\rho} \tag{3.34}$$

$$\Downarrow$$

$$\begin{cases} \dfrac{\mathrm{d}\theta}{\mathrm{d}\rho} = -\dfrac{\theta}{2\rho} + \dfrac{1}{\rho^2 n_{\mathrm{c}}}\left(\dfrac{K_i}{\sqrt{\phi}} - \dfrac{K_e}{\sqrt{\phi - 1}}\right) \\ \dfrac{\mathrm{d}\phi}{\mathrm{d}\rho} = \theta \end{cases} \tag{3.35}$$

Once the radial profile for the symmetric electrostatic potential is assessed -by numerically integrating Eq. 3.35 with proper boundary conditions, which will be extensively discussed in the following section- Eq. 3.32 allows for determining the radial profile for both ion and electron number densities. It is remarkable that the functional relations obtained for the number densities are singular at the respective source electrode and at the IEC device's centre. This result has already been disclosed by R.L. Hirsch, in Ref. [9].

As far as the singularity at the device's centre is concerned, it is not integrable and requires a proper mathematical treatment. The procedure is to replace the central, non-integrable singularity with an infinite series of concentric integrable singularities converging to the centre of the device: these singularities assume the physical meaning of virtual electrodes, ensuing from the space-charge separation in those electrostatic shell structures previously discussed as poissors. The electrostatic potential in proximity of a virtual electrode can be assessed, to some degree of approximation, by means of the equation derived by Langmuir and Blodgett [9]:

$$\begin{cases} \phi \approx \left(\dfrac{9}{4}K_i\right)^{\frac{2}{3}}\left(\dfrac{|\rho - \rho_{\mathrm{v.a.}}|}{\rho_{\mathrm{v.a.}}}\right)^{\frac{4}{3}} & for \quad |\rho - \rho_{\mathrm{v.a.}}| \ll \rho_{\mathrm{v.a.}} \\ \phi \approx \left(\dfrac{9}{4}K_e\right)^{\frac{2}{3}}\left(\dfrac{|\rho - \rho_{\mathrm{v.c.}}|}{\rho_{\mathrm{v.c.}}}\right)^{\frac{4}{3}} & for \quad |\rho - \rho_{\mathrm{v.c.}}| \ll \rho_{\mathrm{v.c.}} \end{cases} \tag{3.36}$$

Where $\rho_{\mathrm{v.a.}}$, is the (normalised) radial position of the virtual anode in the core plasma

$\rho_{\mathrm{v.c.}}$, is the (normalised) radial position of the virtual cathode.

The mean particle density, for both the charge-carrier species, can be finally computed inside the shell around the relative virtual electrode, by substituting Eq. 3.36, through Eq. 3.32 [14]. In Fig. 3.3 the radial profile for the ion density, computed by R.L. Hirsch for a mono-energetic plasma model [9], is given. The reported solution clearly shows the simulation of two virtual anode and a virtual cathode inside the physical cathode grid. Moreover C. C. Dobson and I. Hrbud underlined that, in the proximity of virtual electrodes, "there are clearly defined limits, imposed by the space charge, on the magnitude of the currents: given a ratio of electrode radii there is a unique solution for which both currents are space-charge limited" [14].

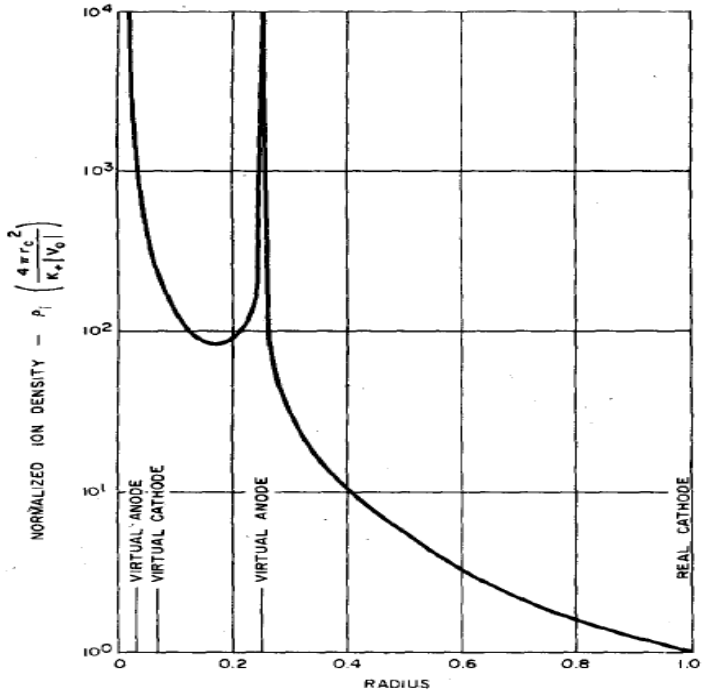

Figure 3.3 Normalised ion density as a function of the radial location inside the cathode grid, as reported in Ref. [9].

Rectangular distribution function

The plasma simulation inside a steady-state operating IEC requires taking into account the tangential component of motion for the charged particles, as in Eq. 3.37.

$$\overrightarrow{v_s} = v_{r,s}\hat{r} + v_{t,s}\hat{t} \tag{3.37}$$

Hence, the resulting constants for the motion of a charged particle, are given in Eq. 3.38:

$$\begin{cases} E_s = \frac{1}{2}m_s v_{r,s}^2 + \frac{1}{2}m_s v_{t,s}^2 + q_s V(r) \\ L_s = m_s r v_{t,s} \end{cases} \tag{3.38}$$

It is of worth noting that -as C.C. Dobson underlined [51]- despite the model being fundamentally one-dimensional (given a spherical symmetry for the device), the introduction of a finite angular momentum brings it, to some extent, on a higher dimension. Indeed, as the transverse motion of the charged particles inside the IEC is now accounted for, the average quantities defining the fluid components of the plasma (see Appendix B, Section 1, ¶ Two-Fluid plasma model), are to be defined by taking the relative moments, over both the translational energy and the angular momentum.

The so-called "rectangular model" is one of the simplest model introducing a finite angular momentum for the charge-carrier species inside the IEC and has been widely employed over the years [14, 15, 49]. Such a model is based on the use of Heaviside step function to express the dependence of the particles' distribution function over translational energy and angular momentum: the unit step function is defined as the derivative of the ramp function:

$$H(x) \doteq \frac{\mathrm{d}}{\mathrm{d}x} max\{x, 0\} \tag{3.39}$$

Thus, it can be expressed in the following conditional form (see Fig. 3.4):

$$H(x) = \begin{cases} 0 & x < 0 \\ 1 & x \geq 0 \end{cases} \tag{3.40}$$

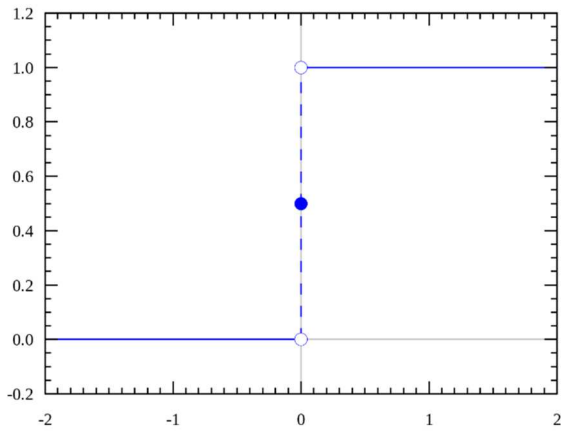

Figure 3.4 Heaviside step function

The distribution function for the charge-carriers populations inside the device is therefore established as the product of unit step functions, so to build a *continuous uniform* (or *rectangular*, hence the model's name) probability density function over both the mechanical energy and angular momentum:

$$f_{\mathrm{H,s}}(\rho,\phi,\varepsilon_{\mathrm{s}},\lambda_{\mathrm{s}}) = \frac{H(\lambda_{max}-\lambda_{\mathrm{s}})H(\varepsilon_{max}-\varepsilon_{\mathrm{s}})H(\varepsilon_{\mathrm{s}}-\varepsilon_{min})}{\rho^2\sqrt{|\phi(\rho)-\varepsilon_{\mathrm{s}}|-\frac{\lambda_{\mathrm{s}}^2}{\rho^2}}} \tag{3.41}$$

Hence, a uniform spread of both the particles' translational energy and angular momentum is assumed [15]. From a physical point of view, the distribution function in Eq. 3.41, for the ion population, represents an even distribution of ion birth sites [14]. Since the effect of Coulomb scattering between charged particles is also neglected in this model, the particles engage an oscillating motion between radial positions at the same potential as described in Chapter 2, Section 1, ¶ Operating principle. Thus, as expressed by C.C. Dobson "*the range of particle energies at a point is constrained only by the local potential, i.e. low energy ions are absent where* $(1-\phi)$ *is large and low energy electrons are absent where* ϕ *is large*" [14].

The normalisation factors for the rectangular distribution function can be determined by recalling Eq. 3.19 and substituting the general form for the particles' radial velocity in a two-dimensional model, and the distribution function in Eq. 3.41:

$$\begin{cases} C_i = \dfrac{1}{\rho}\displaystyle\int_0^{\phi}\sqrt{\varepsilon_i-\phi}\,d\varepsilon_i = \dfrac{2\phi^{\frac{3}{2}}}{3\rho} \\ C_e = \dfrac{1}{\rho}\displaystyle\int_{\phi}^{1}\rho\sqrt{\phi-\varepsilon_e}\,d\varepsilon_e = \dfrac{2(1-\phi)^{\frac{3}{2}}}{3\rho} \end{cases} \tag{3.42}$$

The ion and electron number densities are thus assessed by integrating Eq. 3.41 over both the translational energy and the angular momentum, and subsequently introducing the respective normalisation factor in Eq. 3.42:

$$\begin{cases} n_i(\rho,\phi) = \dfrac{3}{4}\pi\dfrac{K_i}{\sqrt{\phi}} \\ n_e(\rho,\phi) = \dfrac{3}{4}\pi\dfrac{K_e}{\sqrt{1-\phi}} \end{cases} \tag{3.43}$$

It is then possible to write the source term in Eq. 3.11 in terms of these number densities, recasting Poisson's equation as follows:

$$\frac{\mathrm{d}^2\phi}{\mathrm{d}\rho^2}+\frac{1}{2\rho}\frac{\mathrm{d}\phi}{\mathrm{d}\rho}=\frac{\rho^2}{n_\mathrm{c}}\frac{3}{4}\pi\left(\frac{K_i}{\sqrt{\phi}}-\frac{K_e}{\sqrt{1-\phi}}\right) \tag{3.44}$$

Again, this second order ODE can finally be redraft, at once, in the form of a first order ODE system:

$$\begin{cases}\dfrac{\mathrm{d}\theta}{\mathrm{d}\rho}=-\dfrac{\theta}{2\rho}+\dfrac{3}{4}\dfrac{\pi}{n_\mathrm{c}}\left(\dfrac{K_i}{\sqrt{\phi}}-\dfrac{K_e}{\sqrt{1-\phi}}\right)\\ \dfrac{\mathrm{d}\phi}{\mathrm{d}\rho}=\theta\end{cases} \tag{3.45}$$

Indeed, Dolan *et al.* derived the mono-energetic solution by assuming a null angular momentum and an infinitesimally narrow energy spread [15]. It is still worth noticing that the rectangular model is able to predict the particle distribution within IEC in a more realistic way than the mono-energetic model presented in the beginning of the subsection.

Thermal distribution function

Finally, the simulation of the plasma inside the IEC can be obtained by introducing what has been referred to as the "thermal" model [49, 50, 14].

An adequate understanding of such a model requires to dwell on the actual motion of charged particles inside an IEC device. The mathematical model derived in the previous subsection is based on the *a priori* assumption of a solution for Vlasov's equation (Eq. 3.24): this is tantamount to assuming the plasma inside the IEC device by using the two-fluid model, but neglecting the collisional processes. Hence, the motion of an ion inside the IEC is described, to lowest order, by a collision-less orbit model, only dependent on the particle's radial position in the device: any perpendicular component for the particle's motion is merely included through conservation of angular momentum [18]. However, the actual physical behaviour for the charged particles inside an IEC is far more complicated since, as expressed by T. A. Thorson et al., "the local ion flow, electron distribution, and the plasma potential distribution all interact and adjust themselves accordingly to achieve a self-consistent equilibrium" [18]. Thus, a comprehensive description of the dynamic equilibrium for the plasma system requires the introduction of the interaction between charged particles along three-dimensional trajectories (e.g. Fokker-Planck operator).

Although not dwelling so deeply in the above-mentioned physical analysis, the thermal model accounts for the scattering processes inside the IEC, by modelling the resulting slow relaxation of the distributions towards a Maxwellian-Boltzmann distribution [50]. Hence, an exponential term is introduced in the mathematical form for the particle distribution function over energy and angular momentum, as in Eq. 3.46:

$$f_{\mathrm{T,s}}(\rho,\phi,\varepsilon_\mathrm{s},\lambda_\mathrm{s})=\frac{H(\lambda_{max}-\lambda_\mathrm{s})H(\varepsilon_{max}-\varepsilon_\mathrm{s})H(\varepsilon_\mathrm{s}-\varepsilon_{min})\lambda_\mathrm{s}e^{-\left[\frac{|\phi-\varepsilon_\mathrm{s}|}{\varepsilon_{r,\mathrm{s}}}-\frac{{\lambda_\mathrm{s}}^2}{\rho^2}\left(\frac{1}{\varepsilon_{r,\mathrm{s}}}-\frac{1}{\varepsilon_{t,\mathrm{s}}}\right)\right]}}{\rho^2\sqrt{|\phi(\rho)-\varepsilon_\mathrm{s}|-\dfrac{\lambda_\mathrm{s}^2}{\rho^2}}} \tag{3.46}$$

Where the kinetic energy, related to the radial and transverse component of particles' motion, is normalised with respect to the reference energy value in Tab. 3.1:

$$\begin{aligned}\varepsilon_{r,\mathrm{s}}&=\frac{\mathrm{k}\,T_{r,\mathrm{s}}}{|q_\mathrm{s}V_\mathrm{c}|}\\ \varepsilon_{t,\mathrm{s}}&=\frac{\mathrm{k}\,T_{t,\mathrm{s}}}{|q_\mathrm{s}V_\mathrm{c}|}\end{aligned} \tag{3.47}$$

Being $T_{r,\mathrm{s}}$, is the radial temperature of the considered species

$T_{t,s}$, is the transverse temperature of the considered species

$k = 1.38064852 \cdot 10^{-23} \left[\frac{m^2\,kg}{s^2\,K}\right]$, is Boltzmann constant.

In addition, the radial temperature, same as in rectangular model, is assumed to be equal to the transverse one for both the charge-carrier species:

$$T_{r,s} = T_{t,s} \quad \forall s = i, e \tag{3.48}$$

Thus, the exponential term only depends on the particles' kinetic energy and the thermalisation effect in the presumption of weak Coulomb collisions, which are introduced as in Eq. 3.49 [51]:

$$f_{T,s}(\rho, \phi, \varepsilon_s, \lambda_s) = \frac{H(\lambda_{max} - \lambda_s)H(\varepsilon_{max} - \varepsilon_s)H(\varepsilon_s - \varepsilon_{min})\lambda_s e^{-\frac{|\phi - \varepsilon_s|}{\varepsilon_{r,s}}}}{\rho^2 \sqrt{|\phi(\rho) - \varepsilon_s| - \frac{\lambda_s^2}{\rho^2}}} \tag{3.49}$$

Moreover, considering the non-normalised law of conservation for the translational energy of a charged particle (Eq. 3.16), it is clear that the exponential terms is exclusively dependant, under the simplifying assumption in Eq. 3.48, on the particles' kinetic energy:

$$\frac{|\phi - \varepsilon_s|}{\varepsilon_{r,s}} = \frac{E_{kinetic}}{kT} \tag{3.50}$$

$$\Downarrow$$

$$e^{-\frac{|\phi - \varepsilon_s|}{\varepsilon_{r,s}}} = e^{-\frac{E_{kinetic}}{kT}} = e^{-\frac{m \cdot v^2}{2kT}} \tag{3.51}$$

The resulting distribution function, hence, resembles the Maxwell-Boltzmann distribution function, which entails the investigated plasma to be in local thermal equilibrium:

$$f_{\text{Maxwell-Boltzmann}} = 4\pi \left(\frac{m}{2\pi kT}\right)^{\frac{3}{2}} v^2 e^{-\frac{m \cdot v^2}{2kT}} \tag{3.52}$$

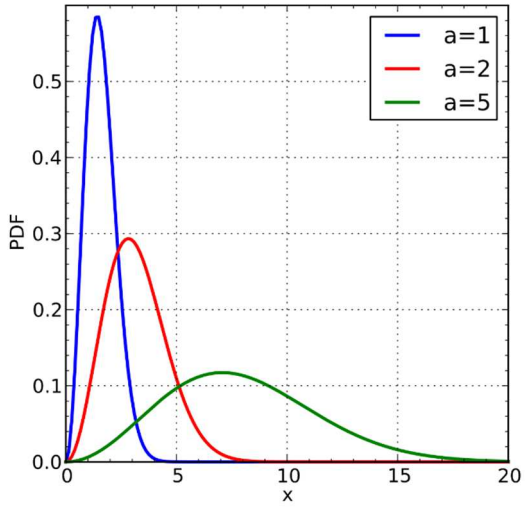

Figure 3.5 Maxwell-Boltzmann distribution function

It is easily seen, from Eq. 3.47 and 3.49, that the assessment of the thermodynamic temperature for the particle species (i.e. the ion and electron populations) in the investigated plasma is required to completely define the thermal model. An additional simplifying assumption is thus introduced in the

following: the (radial and transverse) temperature for each charge-carrier species is set to determine, at a given ρ and ϕ, a mean kinetic energy that is equal to that of the rectangular distribution [14]:

$$\overline{U}_{\mathrm{T,s}} = \overline{U}_{\mathrm{H,s}} \quad \forall \mathrm{s} = i, e \tag{3.53}$$

The mean kinetic energy of any particle population can be assessed as the expectation value for the respective probability density function:

$$\overline{U}_{\mathrm{s}}(\rho, \phi) = \int\int |\phi - \varepsilon_{\mathrm{s}}| \cdot f_{\mathrm{s}}(\rho, \phi, \varepsilon_{\mathrm{s}}, \lambda_{\mathrm{s}})\, d\lambda_{\mathrm{s}}\, d\varepsilon_{\mathrm{s}} \tag{3.54}$$

Being $|\phi - \varepsilon_{\mathrm{s}}|$, the normalized kinetic energy for a particle in the "s" species.

Solving the resulting integral equation, at a specific radial position and for a given electrostatic potential, allows for the determination of the normalised kinetic energy related to the particle radial motion and, subsequently, the local thermodynamic temperature for each charge-carrier population inside the IEC. Once the radial temperatures for both the ion and electron population are known, the respective particle distribution functions, in Eq. 3.49, are completely defined.

Consequently, it is possible to assess the normalisation factors for the thermal distribution function according to Eq. 3.55:

$$\begin{cases} C_i = \dfrac{\varepsilon_{r,\mathrm{i}}}{2}\left[\varepsilon_{r,\mathrm{i}} - e^{-\frac{1}{\varepsilon_{r,\mathrm{i}}}}\left(\varepsilon_{r,\mathrm{i}} + 1\right)\right] \\ C_e = \dfrac{\varepsilon_{r,\mathrm{e}}}{2}\left[\varepsilon_{r,\mathrm{e}} - e^{-\frac{1}{\varepsilon_{r,\mathrm{e}}}}\left(\varepsilon_{r,\mathrm{e}} + 1\right)\right] \end{cases} \tag{3.55}$$

Therefore, the normalised number densities in the source term of Poisson's equation are obtained as follows:

$$\begin{cases} n_i = n_{\mathrm{c}} K_i \dfrac{2\sqrt{\varepsilon_{r,\mathrm{i}}}\left[\dfrac{\sqrt{\pi}}{2}\ erf\left(\sqrt{\dfrac{\phi}{\varepsilon_{r,\mathrm{i}}}}\right) - e^{-\frac{\phi}{\varepsilon_{r,\mathrm{i}}}}\sqrt{\dfrac{\phi}{\varepsilon_{r,\mathrm{i}}}}\right]}{\left[\varepsilon_{r,\mathrm{i}} - e^{-\frac{1}{\varepsilon_{r,\mathrm{i}}}}\left(\varepsilon_{r,\mathrm{i}} + 1\right)\right]} \\ n_e = n_{\mathrm{c}} K_e \dfrac{2\sqrt{\varepsilon_{r,\mathrm{e}}}\left[\dfrac{\sqrt{\pi}}{2}\ erf\left(\sqrt{\dfrac{1-\phi}{\varepsilon_{r,\mathrm{e}}}}\right) - e^{-\frac{1-\phi}{\varepsilon_{r,\mathrm{e}}}}\sqrt{\dfrac{1-\phi}{\varepsilon_{r,\mathrm{e}}}}\right]}{\left[\varepsilon_{r,\mathrm{e}} - e^{-\frac{1}{\varepsilon_{r,\mathrm{e}}}}\left(\varepsilon_{r,\mathrm{e}} + 1\right)\right]} \end{cases} \tag{3.56}$$

Poisson's equation is thus recast, in the context of the thermal plasma model, as in Eq. 3.57:

$$\frac{\mathrm{d}^2\phi}{\mathrm{d}\rho^2} + \frac{1}{2\rho}\frac{\mathrm{d}\phi}{\mathrm{d}\rho} = \left\{ K_i \frac{2\sqrt{\varepsilon_{r,\mathrm{i}}}\left[\frac{\sqrt{\pi}}{2}\ erf\left(\sqrt{\frac{\phi}{\varepsilon_{r,\mathrm{i}}}}\right) - e^{-\frac{\phi}{\varepsilon_{r,\mathrm{i}}}}\sqrt{\frac{\phi}{\varepsilon_{r,\mathrm{i}}}}\right]}{\left[\varepsilon_{r,\mathrm{i}} - e^{-\frac{1}{\varepsilon_{r,\mathrm{i}}}}\left(\varepsilon_{r,\mathrm{i}} + 1\right)\right]} - K_e \frac{2\sqrt{\varepsilon_{r,\mathrm{e}}}\left[\frac{\sqrt{\pi}}{2}\ erf\left(\sqrt{\frac{1-\phi}{\varepsilon_{r,\mathrm{e}}}}\right) - e^{-\frac{1-\phi}{\varepsilon_{r,\mathrm{e}}}}\sqrt{\frac{1-\phi}{\varepsilon_{r,\mathrm{e}}}}\right]}{\left[\varepsilon_{r,\mathrm{e}} - e^{-\frac{1}{\varepsilon_{r,\mathrm{e}}}}\left(\varepsilon_{r,\mathrm{e}} + 1\right)\right]} \right\} \tag{3.57}$$

In conclusion, the differential problem is written as a first order ODE system:

$$\begin{cases} \dfrac{\mathrm{d}\theta}{\mathrm{d}\rho} = -\dfrac{\theta}{2\rho} + \left\{ K_i \dfrac{2\sqrt{\varepsilon_{r,\mathrm{i}}}\left[\dfrac{\sqrt{\pi}}{2}\ erf\left(\sqrt{\dfrac{\phi}{\varepsilon_{r,\mathrm{i}}}}\right) - e^{-\frac{\phi}{\varepsilon_{r,\mathrm{i}}}}\sqrt{\dfrac{\phi}{\varepsilon_{r,\mathrm{i}}}}\right]}{\left[\varepsilon_{r,\mathrm{i}} - e^{-\frac{1}{\varepsilon_{r,\mathrm{i}}}}\left(\varepsilon_{r,i} + 1\right)\right]} - K_e \dfrac{2\sqrt{\varepsilon_{r,\mathrm{e}}}\left[\dfrac{\sqrt{\pi}}{2}\ erf\left(\sqrt{\dfrac{1-\phi}{\varepsilon_{r,\mathrm{e}}}}\right) - e^{-\frac{1-\phi}{\varepsilon_{r,\mathrm{e}}}}\sqrt{\dfrac{1-\phi}{\varepsilon_{r,\mathrm{e}}}}\right]}{\left[\varepsilon_{r,\mathrm{e}} - e^{-\frac{1}{\varepsilon_{r,\mathrm{e}}}}\left(\varepsilon_{r,\mathrm{e}} + 1\right)\right]} \right\} \\ \dfrac{\mathrm{d}\phi}{\mathrm{d}\rho} = \theta \end{cases} \tag{3.58}$$

3.2 Computational algorithm

Before going into details on the computational implementation, it might be of use recapitulating the mathematical model and the conceived computational algorithm, which will be employed for the one-dimensional simulation of the IEC device.

As outlined in the previous section (see Eq. 3.11 and 3.14), Lavrent'ev's method consists in forming a pair of functions $n_i(\rho,\phi)$ and $n_e(\rho,\phi)$ -where ρ and ϕ are independent variables- by specifying constraints on the distribution over the kinetic phase space, for each charge-carrier species. This fundamentally provides a relation between ϕ and motion of particles inside the IEC, which is bounded to the translational energy and the angular momentum (Eq. 3.12). Since both the operating power-supply current and cathode voltage are known quantities, is then possible to determine the mono-energetic perveances as well as the normalisation factors for the relative PDFs. Thus, Eq. 3.59 is the resulting formulation for Poisson's equation:

$$\frac{\mathrm{d}^2\phi}{\mathrm{d}\rho^2}+\frac{1}{2\rho}\frac{\mathrm{d}\phi}{\mathrm{d}\rho}=\left[\frac{K_i}{C_i}\int\int f_i(\rho,\phi,\varepsilon_i,\lambda_i)\,\mathrm{d}\lambda_i\,\mathrm{d}\varepsilon_i-\frac{K_e}{C_e}\int\int f_e(\rho,\phi,\varepsilon_e,\lambda_e)\,\mathrm{d}\lambda_e\,\mathrm{d}\varepsilon_e\right] \tag{3.59}$$

All in all, the steady-state one-dimensional simulation of an IEC device is reduced to the resolution of a second-order boundary value problem, by numerically integrating Eq. 3.59 with proper boundary conditions[11] (BCs). The choice of the suitable BCs to impose for the resolution of Poisson's equation is linked to the definition of the integration domain itself.

According to Ref. [26], the one-dimensional path from the anode grid towards the IEC centre –i.e. the radial domain for the electrostatic potential profile function $\phi(\rho)$- is divided, for simulation purposes, in two or more sections with different BCs, conditional to the number of virtual electrodes (see Chapter 2, Section 1, ¶ Operating principle). In Fig. 3.7, a schematic depiction of the IEC cross-section is given, along with the representation of the different regions the inner volume is divided into:

- *Rim area*, is the section that extends between the IEC gridded electrodes;
- *Inner Area*, constrained between the cathode and the centre of the IEC, if no virtual electrodes occur in the device; otherwise the inner area spread from the cathode grid toward the first virtual electrode, which is an anode characterized by null electrostatic potential;
- *Sub Area*, if virtual electrodes are simulated inside the cathode, which actually depends on the form chosen for the particles distribution function over translational energy [15], [27], the inner area is divided into two or more regions.

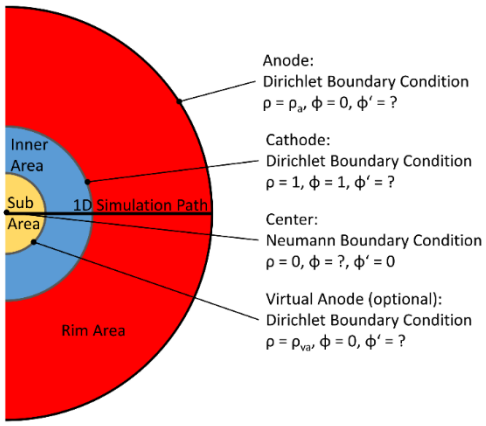

Figure 3.6 IEC radial integration domain [26].

[11] From this point on, in the text, the boundary condition will be denoted as "b.c." for clarity purpose.

As far as the boundary conditions over the different integration domains are concerned, a Dirichlet BC is constituted at both the anode and the cathode, resulting in the following Cauchy problem:

$$\begin{cases} \dfrac{\mathrm{d}^2\phi}{\mathrm{d}\rho^2} + \dfrac{1}{2\rho}\dfrac{\mathrm{d}\phi}{\mathrm{d}\rho} = \left(\dfrac{K_i}{C_i}\displaystyle\int\int f_i \,\mathrm{d}\lambda_i \,\mathrm{d}\varepsilon_i - \dfrac{K_e}{C_e}\int\int f_e \,\mathrm{d}\lambda_e \,\mathrm{d}\varepsilon_e\right) \quad \rho \in [1, \rho_a] \\ \phi|_{\rho=0} = 1 \qquad (Dirichlet\ b.c.\ at\ the\ cathode) \\ \phi|_{\rho=\rho_a} = \phi_a \qquad (Dirichlet\ b.c.\ at\ the\ anode) \end{cases} \tag{3.60}$$

Analogously, the electrostatic potential profile in the inner area is determined by integrating Eq. 3.59 between the cathode grid and alternatively the first virtual anode or the device's centre: the BC at the cathode is the same as it is for the rim area and at the virtual anode. A similar Dirichlet BC should thus be imposed:

$$\phi|_{\rho=\rho_{virtual\ anode}} = 0 \tag{3.61}$$

In the IEC centre, on the other hand, Neumann BC applies. Hence, if no virtual anode is established inside the device, the electrostatic field inside the cathode is described a mixed BC differential problem, as in Eq. 3.62:

$$\begin{cases} \dfrac{\mathrm{d}^2\phi}{\mathrm{d}\rho^2} + \dfrac{1}{2\rho}\dfrac{\mathrm{d}\phi}{\mathrm{d}\rho} = \left(\dfrac{K_i}{C_i}\displaystyle\int\int f_i \,\mathrm{d}\lambda_i \,\mathrm{d}\varepsilon_i - \dfrac{K_e}{C_e}\int\int f_e \,\mathrm{d}\lambda_e \,\mathrm{d}\varepsilon_e\right) \quad \rho \in [0,1] \\ \left.\dfrac{d\phi}{dx}\right|_{\rho=0} = 0 \qquad (Neumann\ b.c.\ in\ the\ centre) \\ \phi|_{\rho=0} = 1 \qquad (Dirichlet\ b.c.\ at\ the\ cathode) \end{cases} \tag{3.62}$$

On the other hand, if virtual electrodes are simulated inside the cathode grid, one or more sub-regions are identified: the boundary values of the virtual electrode, on the border between two neighbouring sub-areas, depends on its electrical load at the edges of the adjoining subsection.

In the end, a computational algorithm can be outlined, as depicted in the flowchart in Fig. 3.7: its software implementation allows for the development of the final simulation tool, employed for the investigation of the core plasma in the IRS-IEC device [52].

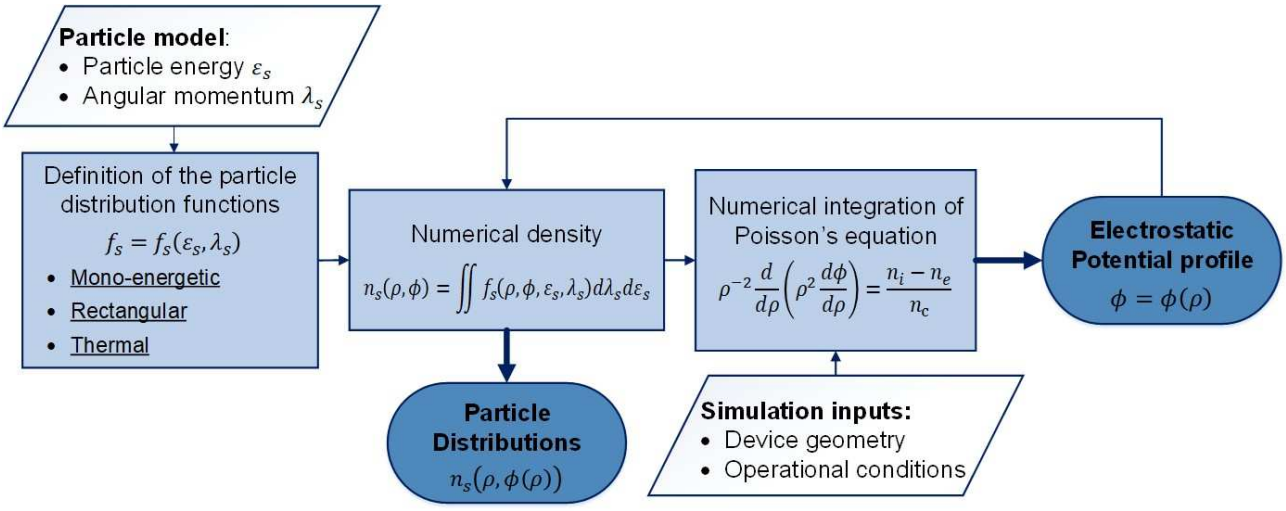

Figure 3.7 Flowchart representing the computational algorithm for the one-dimensional simulation of the investigated IEC device.

The resulting computational tool allows for the numerical evaluation of the electrostatic field and the simulation of the number density for charge-carrier population inside the investigated IEC device:

1. The general form for the particle distribution functions is *a priori* assumed as $f_s(\rho, \phi, \varepsilon_s, \lambda_s)$. This fundamentally introduces the physical assumptions over the motion of the charged particles inside the device.
2. The integration of the assumed distribution functions over translational energy and angular momentum (Eq. 3.18), along with the calculation of the relative normalisation factors (Eq. 3.19), allows for defining of the source term in Poisson's equation. Hence, the mathematical problem is assigned in the form of a first-order ODE system:

$$\begin{cases} \dfrac{\mathrm{d}\theta}{\mathrm{d}\rho} = -\dfrac{\theta}{2\rho} + \dfrac{n_i - n_e}{n_c} \\ \dfrac{\mathrm{d}\phi}{\mathrm{d}\rho} = \theta \end{cases} \tag{3.69}$$

3. The IEC volume is divided into different integration domains (see Fig. 3.6) and a specific Cauchy problem is assigned for each subdomain.
4. The input value for the calculation are provided:
   - Electrodes voltage, typically the anode is assumed to be grounded ($V_a = 0$) so that only cathode voltage (V_c) is required,
   - Power-supply current I_{PS},
   - IEC geometry: since in a one-dimensional simulation electrodes are assumed to be continuous surfaces, the grids radii (r_a, r_c) are the only quantity required for the computation.
5. Each Cauchy problem is solved for values assigned to the mono-energetic perveance (K_s): the electrostatic potential profile along the radial direction, inside the IEC, yields.
6. The resulting density profile for both ion and electron population is attained through Eq. 3.18.

The above-outlined computational algorithm is then employed for the numerical simulation of the discharge plasma inside the S-IEC device available at the IRS test facility: three different plasma models, presented in the previous section of the present chapter, were employed for the simulation.

3.3 Software implementation

The research work described in the following is a prosecution of that done by Mr. Daniel Galla, in the context of his Bachelor's thesis [26]. The above-depicted simulation algorithm has been implemented in a Matlab script to perform the needed calculations and subsequently provide an effective visualisation of all the meaningful results.

As far as the numerical integration for the differential problems given in Eq. 3.60 and 3.62 is concerned, a different computational approach has been chosen for the distinct plasma models. The main issue uprising, in pursue of numerical integration of the resulting Poisson equation, is that the ODE problem does not take the common form of an "initial value" differential problem. Indeed, the boundary conditions in the Cauchy problem of Eq. 3.60 and the mixed-boundary conditions in Eq. 3.62 are not assigned at the same point of the computational domain. Hence, the custom numerical methods for ordinary differential equations (e.g. Euler's method, Heun's method, *etc.*) cannot be employed for the desired resolution of the one-dimensional Poisson equation, as they use the assigned initial values to forward propagate the solution. Therefore, alternative approaches have been proposed to the numerical resolution of two-point boundary-value problems; broadly speaking, the developed methods can be divided into two different classes: shooting methods and relaxation schemes [53].

The shooting method can be then thought of as following the trajectory of a shot from a gun, the initial boundary point, to the target, the final boundary point (see Fig. 3.8a): hence the name. Any trial

solutions satisfy the differential equations, but the boundary value problem is only satisfied by that trajectory that match the assigned value at the final boundary [53]. In a relaxation scheme, on the other hand, the differential equations are replaced by finite-difference equations on a mesh of points that covers the integration domain. A trial solution consists of values for the dependent variables at each mesh point, not satisfying the desired finite-difference equations, nor necessarily even satisfying the required boundary conditions [53]. The iteration, also referred to as "relaxation", consists of adjusting all the values on the mesh so as to bring them into successively closer agreement with the finite-difference equations and, simultaneously, with the boundary conditions (see Figure 3.8b).

A shooting scheme is thus employed for the integration of Poisson equation for the mono-energetic model, making use of a fourth-order Runge-Kutta method. The computation of both the rectangular and thermal plasma solutions, on the other hand, is performed by taking advantage of the Matlab built-in routine `bvp4c`, which is based on a relaxation scheme, namely the three-stage Lobatto IIIA formula. Further details on the software implementation of Lavrent'ev's method for the numerical simulation of the IRS-IEC device can be found in Ref. [52].

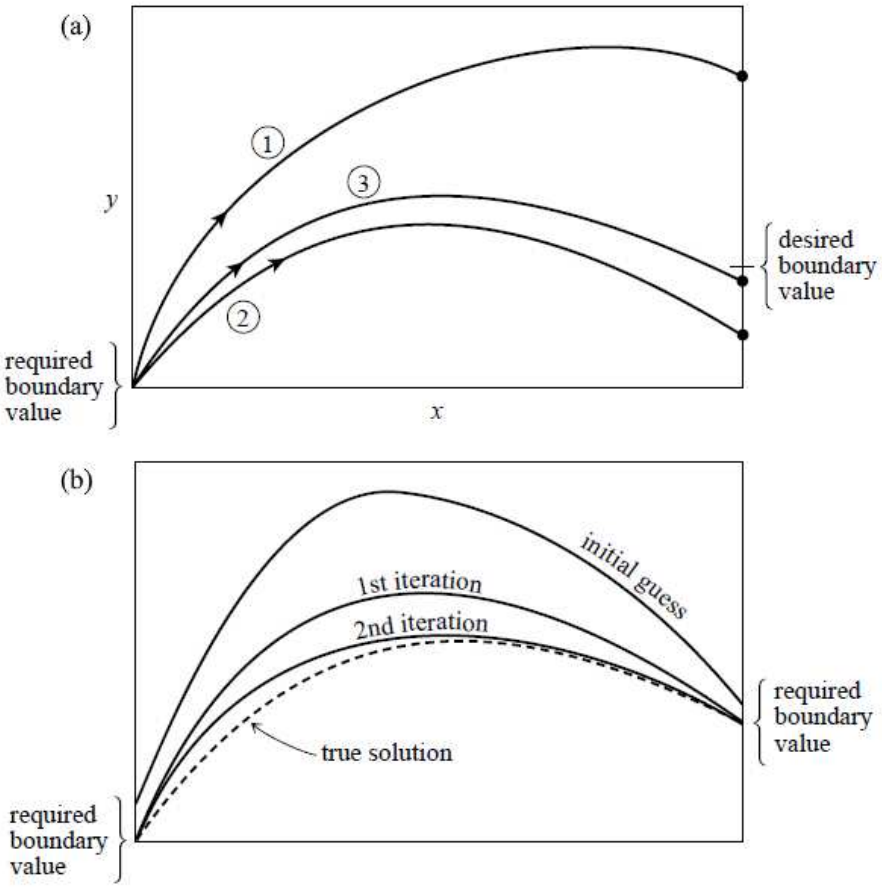

Figure 3.8 Shooting scheme for a two-point boundary-value problem [52].

3.4 Simulation Results

The resolution of Poisson's equation allows for the assessment of the one-dimensional plasma behaviour in the IEC, by describing it in terms of the number density for each particle species. Moreover, the simulation assesses the one-dimensional electric field, resulting from the Debye shielding of the externally applied electric field on the device's electrodes. Hence, the simulation output provided by the numerical Poisson solver regards the following physical quantities:

- Electrostatic potential, V
- Charged particle densities, (n_i, n_e).

Since the particle models are based on the spherical symmetry, these quantities result then to be only varying along the device radial direction. Thus, the simulation output will consist of radial profiles, i.e. the plasma inside the IEC will be described by the variation of the electrostatic potential and charged particle densities along the device's radius.

First of all, it is possible to compare such a computational output with a similar simulation, from C.C. Dobson and I. Hrbud, whose input values are reported in Table 3.2.

Table 3.2 Input values for the simulation reported in Ref. [14].

Cathode radius	r_c	[mm]	150
Anode radius	r_a	[mm]	300
Cathode voltage	V_c	[kV]	-1
Anode voltage	V_a	[kV]	0
Power supply current	I_{PS}	[mA]	50

The simulation carried out in Ref. [14] refers to a an IEC device characterised by a different geometry (compare data in Tab. 3.4 with the IRS-IEC characteristics in Tab 2.2 and 3.3), operating on a different power-supply current. Nonetheless, it is significant how the simulation results for the IRS-IEC device essentially match those reported by the authors (see Fig. 3.9), in terms of the overlapping of the electrostatic potential and density profiles. Indeed, the potential profiles, in Fig 3.9, shows that the thermal profile qualitatively resembles that provided by the rectangular model but it is characterised by lower values, especially in the core region inside the cathode grid. Indeed, the gap between the value of the electrostatic potential -in the bulk plasma at the device centre- in the rectangular and thermal model, as is broadly comparable to that observed in the results provided by the IRS-IEC simulation (see Fig. 3.10). Hence, despite the fact that the numerical results reported in Ref. [14] do not represent a valid quantitative benchmark, the consistency of the simulation output with that of Dobson and Hrbud, provides a standard for the reliability of the developed simulation tool, at least in a qualitative sense.

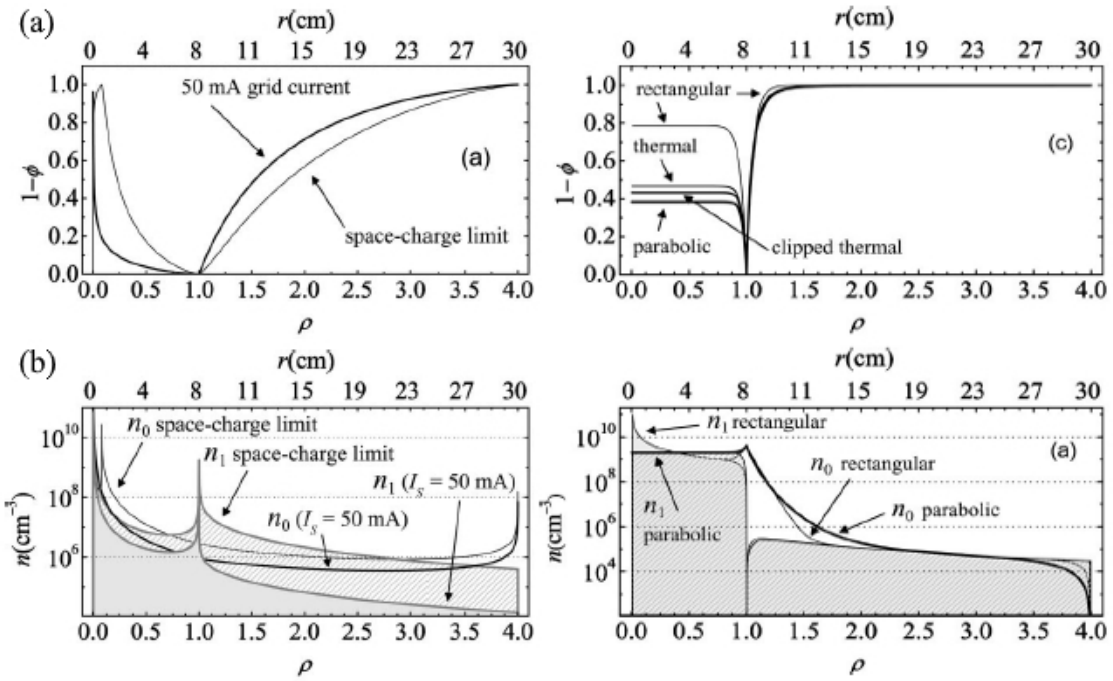

Figure 3.9 Results of the plasma simulation performed by C.C. Dobson and I. Hrbud [14].
(a) Radial profile for the electrostatic potential: $\phi(\rho)$
(b) Radial profile for the ion and electron number densities. $n_i(\rho)$, $n_e(\rho)$.

As far as the simulation of the IEC device investigated in the IRS test facility is concerned, the input quantities are the main parameters characterising the device itself -in its geometry and experimental operating conditions-. Tab. 3.3 reports their respective values, assigned for the simulation under discussion: in particular, reference is made to the K3a grid configuration presented in the previous chapter (see Chapter 2, Section 3).

Table 3.3 Simulation input values

Cathode radius	r_c	[mm]	25
Anode radius	r_a	[mm]	75
Cathode voltage	V_c	[kV]	-1
Anode voltage	V_a	[kV]	0
Power supply current	I_{PS}	[mA]	15

In Fig. 3.10, the radial profile for the electrostatic potential inside the IEC device is depicted for the three different plasma models. The first remarkable outcome is the consistency of the electrostatic potential in the mono-energetic model with the results found in the related literature [15, 9]. On the other hand, the potential profile determined according to the thermal model presents a similar trend as in the rectangular model. Both the simulation models envisage the presence of a virtual anode inside the cathode grid, as the potential tends to increase moving from the cathode itself to the device centre, but the thermal model is characterised a lower value, for the electrostatic potential, over the entire radial extension of the device. A plateau is clearly observed inside the cathode grid, which is an indication of the quasi-neutrality of the simulated plasma.

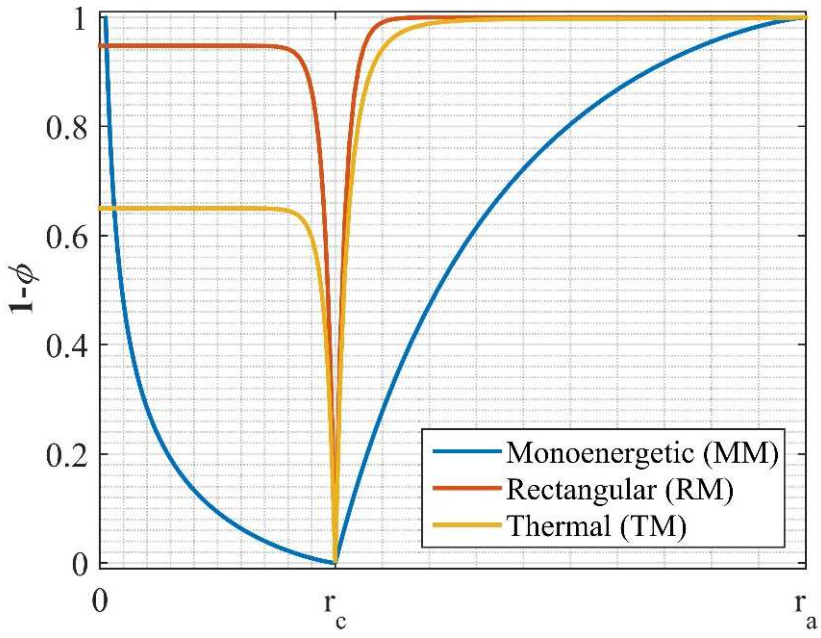

Figure 3.10 Electrostatic radial profile for mono-energetic, rectangular and thermal plasma models.

In Fig. 3.11, the density profiles for both the charge-carriers specie and for the different plasma models, are presented: solid lines in the left-hand side graph are referred to the ion population while the dash-dotted lines in the right-hand side graph represent the electron density profiles. The same qualitative accordance of the rectangular and thermal models underlined for the electrostatic potential profiles is found in the radial distribution of the charged particles inside the device. As a matter of fact, the mono-energetic model is the only model that predicts the inception of multiple, concentric potential wells, in

accordance with the "poissor" theoretical model (see Chapter 2, Section 1, ¶ Operating principle). Both the rectangular and the thermal model, on the other hand, envisage the achievement of the quasi-neutrality in the plasma volume inside the cathode grid: the ion and particle number densities indeed do coincide, so that no non-neutral plasma structure is observed inside the cathode grid, other than the virtual anode. In addition, it is possible to observe that the magnitude of the simulated plasma density at the device's centre is far lower in the thermal model than in the mono-energetic and rectangular models.

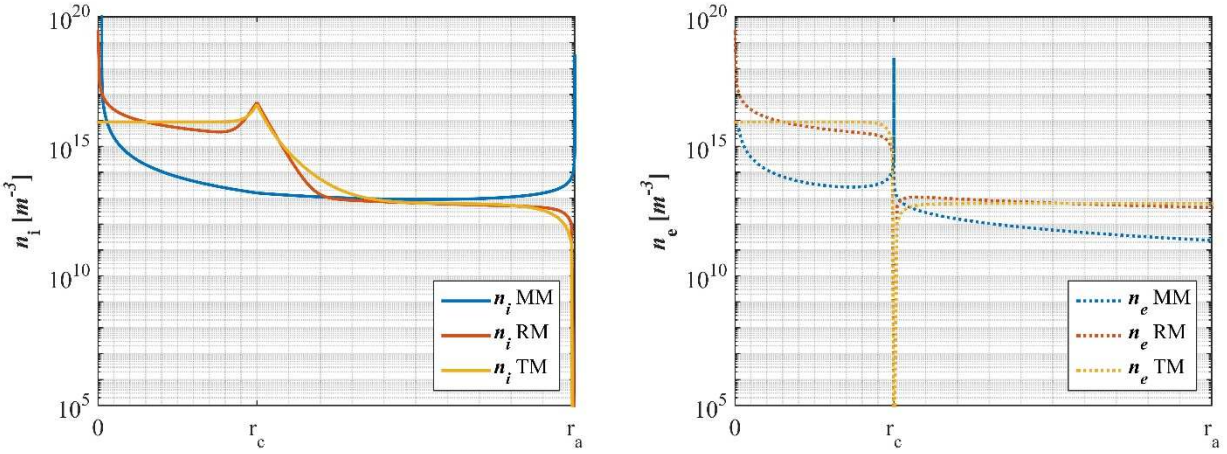

Figure 3.11 Radial profile of ion (n_i) and electron (n_e) densities for mono-energetic (MM), rectangular (RM) and thermal plasma (TM) models.

From the previous discussion about the one-dimensional plasma simulation, is clear that the thermal model employs the most reasonable assumptions, as it not only considers a spread of the particles' distributions over the phase-space, but also accounts for the thermalisation of those distributions due to particles' collisions. Nonetheless, this model still simplify some non-negligible issues: the inherent one-dimensionality and the attempt to relax the particles distributions toward a Maxwellian distribution. First of all, the adopted point (or axial) symmetry for the mathematical model evidently entails the one-dimensionality of the relevant plasma behaviour: this assumption greatly simplifies the computational complexity of the resulting Poisson equation, but results in the waiving of an accurate description for the existence of gridded electrodes. In fact, the actual three-dimensional layout of the employed electrodes seems to play a significant role in many plasma phenomena observed in IEC devices (e.g. micro-channel formation [38]) and might be critical to the physical processes underlying the plasma jet extraction. A more detailed discussion of the three-dimensional electric field topography is presented in Chapter 5 of the present essay. Moreover, the thermal model does not simulated collisional process but rather accounts *ex post* for their ending results. A more accurate plasma model should be able to depict all the spectrum of different collisional processes (including the electron-impact ionisation of the background), introducing a suitable collisional operator as a source term in the kinetic plasma equation.

In conclusion, the most remarkable result inferable from the one-dimensional simulation of the studied IEC device is that no more than one virtual electrode is expected to exist. Indeed, in a GD-IEC architecture the collisional processes play a significant role, as they are responsible for the plasma generation. Hence, the mono-energetic model has little capability of effectively depicting the plasma behaviour in an IEC device such as that investigated at IRS and, more generally, designed for space propulsion applications. Such an observation leads logically to questioning the "poissors" model: since the actual effects of particles' motion in the device entail serious instability issues for the multiple potential-shell structures, plasma confinement due to poissors' inception is extremely unlikely. This conclusion drove to the research of an alternative confinement mechanism and, ultimately, led to the definition of the spherical double layer model that will thoroughly described in the following chapter.

Chapter 4
Spherical double layer model

4.1 Motivation for the IEC-SDL model

Recently, a pioneering physical model has been proposed, at the IRS in Stuttgart, which promises to describe both the ionisation process in a GD-IEC device, the plasma confinement in the core region of the device itself, and the plasma jet extraction mechanism, in a thorough, self-consistent physical framework.

The proposal of an alternative theory, capable of describing all the main plasma features observed in IEC jet thrusters, was justified by the lack of experimental observations [19] for a number of concentric electrostatic shell-structures in the core plasma, expected according to the canonical poissor model (see Chapter 2, Section 2, ¶ Operating principle). By the same token, the jet extraction mechanism is still, to some extent, an obscure phenomenon that struggles to find its place in the traditional physical framework, for GD-IEC of plasma. General agreement was achieved, about the jet extraction been initiated by a prime leakage of electrons out of the confined core plasma, thereby triggering the ions to escape the confinement, so that a quasi-neutral plasma beam yields. Nonetheless, none of the several models proposed to explain the jet extraction mechanism is adequately verified by measurements [54]. The electrostatic field engendered by the voltage-biased gridded electrodes in an S-IEC device has a complex three-dimensional topography. Indeed, even if high quality manufactured electrodes are employed, so that a perfect spherical symmetry in the global geometry can be assumed, their gridded structure[12] determines a local distortion of the electrostatic equipotential surface, provoking the filed lines to reach onto the device centre at the grid openings.

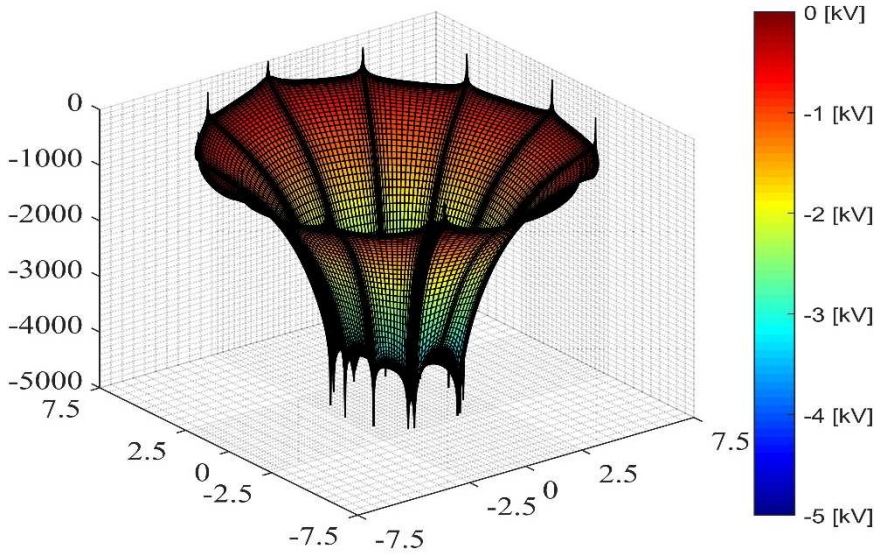

Figure 4.1 Potential map of equatorial cross-section of an IEC thruster.

Furthermore, on the heels of the experimental discovery that, by enlarging one of the IEC grid openings by 50-100%, an intense quasi-neutral ion jet is extracted at the larger grid opening [7], asymmetric S-IEC

[12] It is worth remarking that the use of a highly transparent structure for the electrodes is key feature in an IEC device. As a matter of fact, the electrode transparency is the primary trait upon which the inertial electrostatic confinement operation is based: due to Earnshaw's theorem [102], a solid electrode is not capable of providing a self-sufficient electrostatic confinement of plasmas.

devices have been developed for space propulsion purposes. Actually, the local asymmetry introduced by the enlarged hole, produces a non-negligible distortion of the electrostatic field, yielding the equipotential surface to extend deeper into the inner grid volume, with respect to the smaller, "standard" grid openings [45]. Inside the core plasma in a GD-IEC device, electrons are both confined by the high negative voltage applied to the cathode grid and by the virtual anode, arising at the centre, due to the ions' recirculating through the inner grid. This confining mechanism, for the electron population, can although be overcome if the electrostatic field is distorted by introducing an enlarged grid opening, enough for the field lines to reach the trapped electrons, where the negative potential is less intense [54]. If the electrons have a sufficiently high thermal velocity, they might be able to overcome the wrenched electrostatic potential barrier at the main cathode hole and, subsequently, to be accelerated by the curved potential surface and focused in a non-Maxwellian electron beam, in the fashion of a collimating lens. While the above-depicted phenomenon has been numerically validated in a Direct Monte Carlo Simulation-Particle in Cell (DSMC-PIC) code [44], no explanation is provided in literature about the ion beam formation: several experimental observations [54, 44, 45, 7] have showed that the outflowing plasma jet is composed of both electrons and ions, resulting close to charge-neutrality. An educated guess here concerns that the escaping electrons attract the ions, thus triggering the ion jet formation. Once the ion flow is initiated, the ions would, in turn, attract the electrons along with them in a positive feedback: a quasi-neutral plasma flow emanates then from the IEC core plasma. Nonetheless, this explanation conflicts with the recirculating ions being much heavier and more energetic than the leaking electrode [54]. Hence, electrostatic interaction alone seems insufficient to the triggering of the ion beam extraction.

Since 2011, the IEC research performed at IRS has been focused on the assessment of the applicability of IEC technology for electric space propulsion. The research campaign was structured in three distinct phases, dealing with deepening the comprehension of the confinement principle, understanding the jet extraction mechanism and, finally, designing a propulsion laboratory model [44]. Particular effort was paid to the characterisation of the jet formation and, in 2012, a numerical simulation was performed, in collaboration with ESA, in the attempt to underpin and, possibly, to improve the theoretical model [25]. These efforts paid off a short while ago, resulting in a cutting-edge GD-IEC model based on the description of the core plasma in terms of the well-known double layer theory [19].

4.2 Double layer theory

¶ Double layer background

A double layer (DL) is an electrostatic structure often observed to ensue in a number of different physical contexts. This concept covers a wide range in plasma scaling, from non-fusion laboratory plasmas, such as those engendered in Q-machines and dusty plasma experiments [55, 56, 57], to a variety of space plasmas [56, 20]. Many mathematical models have been developed to describe the physical behaviour of a variety of DLs, and employed in the analytical description of several physical phenomena: e.g., DLs have been theorised to play a critical role in diverse astrophysical events such as terrestrial aurorae, solar flares and the deceleration of the accreting matter in binary X-ray pulsars [20].

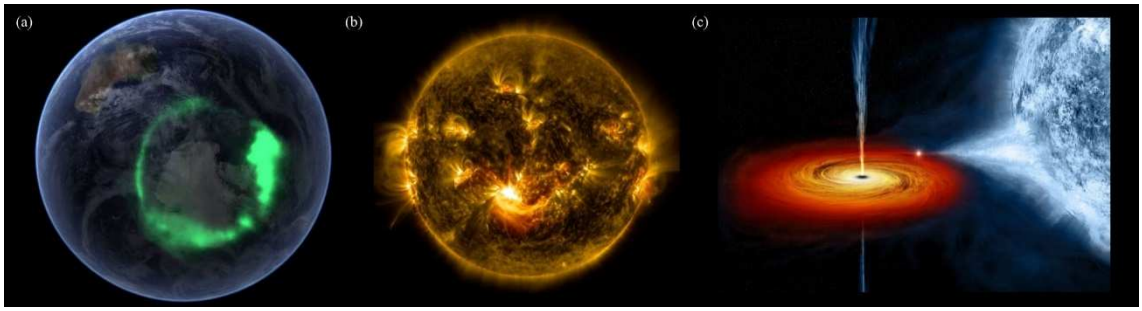

Figure 4.2 Examples of astrophysical plasmas whose behaviour have been depicted in terms of double layer: (a) terrestrial aurorae [58], (b) solar flares [59], (c) binary X-ray pulsars [60]

According to G. Hairapetian and R.L. Stenzel, from University of California at Los Angeles, potential double layers can be defined as in the following:

"localized electrostatic potential structures created by two equal but opposite space-charge layers, which are capable of sustaining high potential drops in collisionless plasmas" [61].

Hence, double layers present themselves as transitional sheets, whose thickness -dependant on the local plasma parameters- is typically much smaller than the dimension of the plasma region embedding it. Broadly speaking, a low collisional plasma sustains a significant electric field only at its boundaries, where it undergoes an abrupt change from the long-distance condition to the boundary electrostatic potential, through a thin volume commonly referred to as "sheath". This is due to a basic property of the plasma medium that is its ability to shield out electric potentials applied to it, in a behaviour called "Debye shielding". Consider a steady state, collisionless, uniform plasma and imagine slowly[13] inserting in it a test charge: the particle will exert an electrostatic force on both ion and electron population, attracting the one and repelling the other, depending on the sign of the test particle. This slight displacement results in a small but finite potential in the plasma, which partly cancels the test charge field for an observer located away from the test particle itself. More specifically, if the distance is of an order of magnitude greater than the Debye length, the test charge is completely screened by the surrounding shielding cloud [62]. If a voltage-biased electrode is inserted into a plasma, the same behaviour is observed: the charged-particle populations in the plasma are electrostatically driven to screen the electrode field. Hence, a screening region -characterised by non-neutrality- extends in the plasma, from the electrode wall, for a length in the order of the Debye length: this is called the sheath.

In the sheath, the plasma potential decreases[14] monotonically to match the boundary condition at the electrode wall (see Fig. 4.3.a), thus producing an electrostatic field that exerts the same and opposite electrostatic force on ions and electrons. Due to their greatly differing masses, electrons experience a much greater accelerations than ions; this results in a larger ion density, so that the region is often referenced to as "ion sheath" or "single layer".

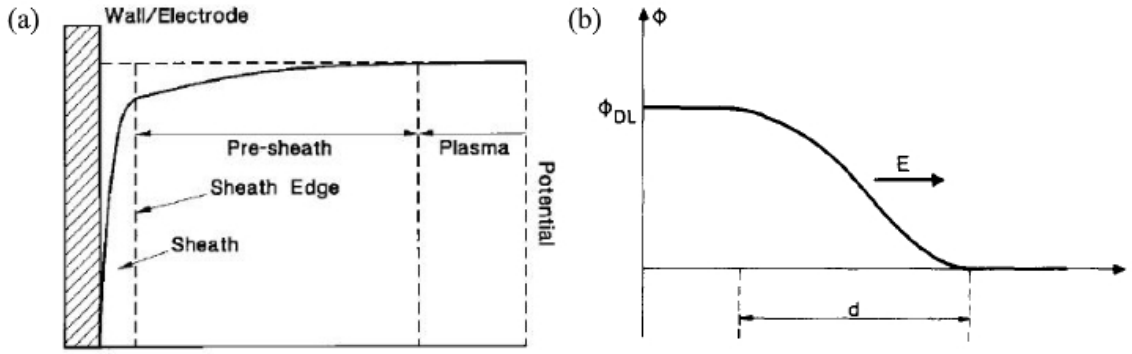

Figure 4.3 Sketch of the electrostatic potential trend in:
(a) Debye sheath, in correspondence of a negatively-biased electrode wall: three distinct plasma regions can be identified (moving rightwards): the plasma sheath, a pre-sheath region, where ions are accelerated to the Bohm velocity $\sqrt{kT/m}$ [56], and the bulk plasma under the far-off conditions
(b) Monotonic Double-layer

[13] It is worth to underline that the assumption, for the considered perturbation to be slow, is critical to the extent that it allows to neglect inertial effects, inductive electric fields and temperature gradient effects [62].

[14] For a negatively biased electrode.

Despite being distinct plasma structures, double layers show striking similarities to the above-described plasma sheath. Indeed, in Ref. [63] the following definition can be retrieved:

> *"A double layer consists of a positive-plus-negative Debye sheath, connecting two quasineutral regions of a small Debye-length (λ_D) plasma".*

Furthermore, in the same work, the metamorphosis of an electrode sheath into a detached boundary DL is predicted. If a sufficiently high voltage is applied to the considered solid wall, the plasma breakdown happens at a distance from it and the boundary layer -coupling the electrode plasma conditions to the far-off bulk plasma ones- is detached from the wall. The boundary layer (i.e. the DL structure) is thus composed of two contiguous sheets of positive (ion sheath) and negative charges (electron sheath), hence its nomenclature. Therefore, ionisation processes dominate the DL physics [56] and the resulting electrostatic structure presents a highly non-linear behaviour [20, 61]. Three main characteristics can be identified, defining a plasma boundary layer as an electric double layer [56, 20]:

- The DL, as a whole, has no net charge, and the surrounding plasma exhibits no significant electric field and is charge neutral.
- No charge neutrality is locally given. On the contrary, two distinct thin region of opposite net charge, due to the dominance of a charged particle population over the other, are identified.
- Consequently, a large electrostatic potential drop (ϕ_{DL}), associated with a relevant electric field, is engendered between the two opposite-charged layers (see Fig. 4.3.b).

To some extent, thus, the behaviour of a DL resembles that of a laminar shock wave in fluid dynamics. A basic feature of a DL is the electrostatic interaction of its inner electric field with the charged particles in the plasma environment embedding it. In case of a monotonic double layer, the charged particle traversing the double layer are unidirectionally accelerated by the net potential difference, and decelerated when moving in the opposite direction. Considering the case of a charged particle moving against the DL electric field, this is decelerated by the net potential difference as its kinetic energy is isentropically[15] converted into electrostatic potential energy. If the DL potential is greater than the particle's kinetic temperature[16], the latter will not be able to surpass the double layer, but will penetrate it to a certain degree before stopping and reverting its motion; otherwise the particle will cross the DL, decelerating in the process anyway. On the other hand, if the test particle moves according to the orientation of the DL field lines, it will be continuously accelerated across the plasma boundary layer. It has bene theorized that, in the most common case, a DL is determined by four different particles' populations: [56, 20, 64]:

1 *Free* (or *passing*) ions, population of high energy ions that overcome the net potential difference as they move from the low to the high potential side of the double layer, such particles decelerate in the crossing.

2 *Trapped* or (*reflected*) ions, population of low energy ions incapable of passing across the layer and trapped in the low potential side, thus furthering the positively charged layer of the DL.

3 *Free* (or *passing*) electrons, population of high energy electrons, which overcome the net potential difference as they move from the high to the low potential side of the double layer, decelerating in the crossing.

4 *Trapped* or (*reflected*) electrons, population of low energy electrons arrested in the crossing and trapped in the high potential side, these particles foster the negatively charged layer of the DL.

[15] The process here described can be assumed to be isentropic as long as scattering processing and electromagnetic induction effects are negligible.

[16] The temperature (T) for a charged particle population, measured in , can be expressed in thanks to the following scale transformation: $T[\mathrm{eV}] = \mathrm{k/e} \cdot T[\mathrm{K}] \approx 8{,}61673324(78) \cdot 10^{-5}\, T[\mathrm{K}]$. Sometimes, the nomenclature "equivalent thermal potential" is found in literature to specify the temperature when expressed in electron volt.

In many cases, the presence of charged particles moving across the DL according with the electric field lines results in the flow of accelerated ions and electrons, from the high and low potential side respectively, yielding two energetic particle beams [56]. It is worth noticing here that a double layer cannot be supported by only one Boltzmann distributed and one non-thermalised fluid species, but at least two thermalised particles' populations are required to foster the double layer structure [56, 20]. In Fig. 4.4, a thorough schematic of the most common scenario for the charge-carriers interaction with the DL net potential difference is provided.

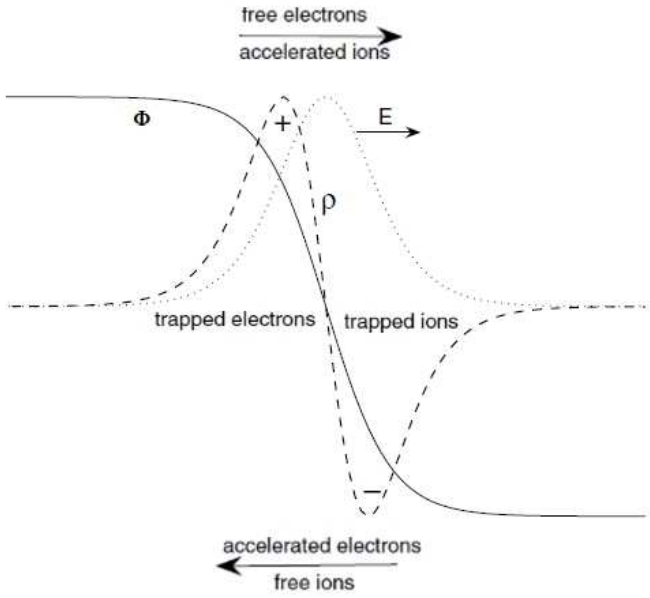

Figure 4.4 Schematic of potential for a double layer between two plasma sources or in an expanding plasma. In the figure a sketch for the DL potential (solid line), electric field (dotted line) and charge density (dashed line) is provided, along with the representation of the free and trapped charge-carrier populations [56].

Many different classifications are found in literature for double layers, grouping the numerous experimentally observed DLs on the basis of a number of physical parameters (e.g. the comparison of the DL net potential difference with the electron rest energy provides a distinction in non-relativistic, quasi-relativistic and relativistic DLs). For the purpose of the present essay, the two most broad and commonly employed categorisations are to be presented: *strong/weak* double layers and *current-driving/current-free* double layers. The former refers to the comparison between the DL potential and the equivalent thermal potential for the charged particles in the plasma ($\mathrm{k}T/\mathrm{e}$). More specifically, in Ref. [56] the DL potential is compared to the kinetic temperature of the free electrons on the low potential side of the double layer $\left(T_{e_f}\right)$:

- *Strong* double layer, if the electrostatic potential is at an order of magnitude higher than the trapped electrons' equivalent thermal potential, i.e. $\left(e\phi_{\mathrm{DL}}/\mathrm{k}T_{e_f} > 10\right)$.
- *Weak* double layer, if the electrostatic potential is at comparable to the trapped electrons' equivalent thermal potential, i.e. $\left(e\phi_{\mathrm{DL}}/\mathrm{k}T_{e_f} < 1\right)$.

The latter, on the contrary, is based on the presence or absence of a net electric current flowing through the double layer:

- *Current-driving* double layer, if the charge-carrier fluxes across the DL are not balanced net electric current (I) results (e.g. in most cases the free ions term is negligible [56]). In this case the double layer acts like an electric load, dissipating energy at the rate $(I \cdot \phi_{\mathrm{DL}})$: nonetheless, this energy is not degraded -due to Joule effect- like in an ohmic resistance, but it is instead converted in the kinetic energy of the accelerated particle populations. In this respect, the current-driving double layer can

be regarded as an "inertial" resistance, powered by an external electric source, in order to maintain the DL electrostatic field [20].

- *Current-free* double layer (CFDL), seldom observed in laboratory plasmas -most frequently in proximity of strong magnetic field gradients [61, 63]. This kind of DL occurs at the boundary surface between two plasma regions characterised by different physical properties (e.g. electron temperature, density).

¶ Existence criteria and Langmuir double layer

In the light of the exposition given in the previous subsection, it is well understood that the structure of a DL is self-consistently determined by the interaction of the charged particle with the electric field produced by their net charge distributions themselves [20]. Henceforth, several DL models have been analysed and experimentally observed in literature, depending on the number of distinct particle populations involved in the setting of the DL plasma structure.

A steady state one-dimensional double layer can be described in terms of the Vlasov-Poisson equations (see Appendix B, Section 1, for more details), complemented by the global charge neutrality condition and the local zero electric field and net charge conditions at the DL boundaries [56, 20].

$$\begin{cases} \dfrac{\mathrm{D}f_{i,e}}{\mathrm{D}t} \equiv \dfrac{\partial f_{i,e}}{\partial t} + v\dfrac{\partial f_{i,e}}{\partial x} + \dfrac{q_{i,e}E}{m_{i,e}}\dfrac{\partial f_{i,e}}{\partial v} = 0 \\ \varepsilon_0 \dfrac{\mathrm{d}^2\phi}{\mathrm{d}x^2} = -[q_i n_i(\phi) + q_e n_e(\phi)] \end{cases} \tag{4.1}$$

Where $f_{i,e}$ are the PDFs, for the electrons' and ions' populations, over the phase space;

d, is the thickness of the double layer.

Poisson equation can be integrated once to give the following:

$$\frac{1}{2}\varepsilon_0 \left(\frac{\mathrm{d}\phi}{\mathrm{d}x}\right)^2 + V(\phi) = \Pi \tag{4.2}$$

Where Π, is the integration constant;

$V(\phi)$, is the Sagdeev or "classical" potential. To within the additive constant depending on the choice of Π, this quantity equals the total particle pressure -i.e. the sum of kinetic and thermal pressure- given by the second moment of the particles' distribution functions [20].

Therefore, Eq. 4.2 can be recast in terms of the charged particles' distribution functions and the double layer net potential difference, so to express the stress balance[17] in the DL plasma:

$$-\frac{1}{2}\varepsilon_0 E^2 + \sum_{i,e} \int_{-\infty}^{+\infty} m_{i,e} v^2 f_{i,e}(x,v)\mathrm{d}v = -\Pi \tag{4.3}$$

A second integration of Poisson equation allows to retrieve the one-dimensional, spatial layout of the double layer. Note, however, that a numerical integration is typically needed to assess the relationship linking the DL potential and the electric current driven through the double layer [20], i.e. the charge flow resulting from the free and accelerated, ions' and electrons' populations.

The DL solution can be achieved by means of direct integration of Poisson equation, once assigned the distribution functions for the charge-carrier populations, if Sagdeev potential satisfies the following existence conditions, referred to as "Langmuir generalised criteria":

[17] Since, for the purpose of the present essay, the magnetic field is neglected, only the electric field part of the Maxwell stress tensor is considered in Eq. 4.3.

1. Zero electric field at the DL boundaries, this condition can be recast in terms of Sagdeev potential, using of Eq. 4.2, as

$$V(\phi|_{x=0}) = V(\phi|_{x=\mathrm{d}}) = 0 \tag{4.4}$$

2. Charge neutrality for the plasma at the DL boundaries, using Eq. 4.3 and Eq. 4.4, this condition is expressed as in Eq, 4.5[18]

$$V'(\phi|_{x=0}) = V'(\phi|_{x=\mathrm{d}}) = 0 \tag{4.5}$$

3. In order to exclude imaginary values for the electric field intensity, Eq. 4.2 determines an additional condition, to be satisfied everywhere in the DL:

$$V(\phi) < \Pi \tag{4.6}$$

   If the Sagdeev potential is at least twice differentiable at the DL boundaries, this requirement can be recast in the form of "generalised Bohm criterion":

$$\begin{aligned} V''(\phi|_{x=0}) &< 0 \\ V''(\phi|_{x=\mathrm{d}}) &< 0 \end{aligned} \tag{4.7}$$

The generalised Bohm criterion thus requires the potential to have true maximum values at the DL boundaries. A potential minimum often appears on the low potential side of strong double layers, such a minimum is only possible in a dynamic state, or possibly because of the three-dimensional structure of the DLs [20].

Strong DLs have special relevance for the purpose of this thesis, and particular attention will be paid to a specific model, originally conceived by Nobel awarded physician and chemist Irving Langmuir, called "Langmuir double layer". In 1929, Langmuir proposed the first double sheath model for the plasma spawned between an electron emitting cathode and an ion-emitting anode [56], basing on the following assumptions:

- Only two charged particles populations are taken into account: the accelerated electrons, flowing from the cathode to the anode, and the accelerated ions, flowing in the opposite direction. These particles are assumed to be mono-energetic, with zero incident velocity at the DL boundaries [56, 20].
- The electrostatic potential is much greater than the equivalent thermal potential for the charged particles emitted by the electrodes (Eq. 4.8), i.e. the following analysis holds for strong double layers.
- The plasma is assumed to be non-magnetised and non-collisional, and, in addition, the ionisation effects are neglected.

The structure of the Langmuir's "double sheath" is then determined by the dynamics of the accelerated particles in the assigned electrostatic field: this is a basic model for the behaviour of any strong DL. Indeed, if the electrostatic potential is higher than the kinetic temperatures for the charge-carriers, a portion of the inflowing particles will hardly penetrate the double layer, whose internal structure will hence be dictated by the net charge and by the dynamics of the free particles.

Introducing the generalised Langmuir criteria, Langmuir deduced the following condition for the current ratio, i.e. the ratio of the electron current density (j_e) over the ion current density (j_i), under the implicit assumption of non-relativistic DL[19]:

[18] Note that, in addition, this condition ensures that the double layer as a whole has no net charge [20].

[19] Relativistic effects are introduced for astrophysical applications and the solution for a relativistic Langmuir DL can be retrieved in Ref. [20].

$$\frac{j_e}{j_i} = \sqrt{\frac{m_i}{m_e}} \tag{4.8}$$

Hence, due to the great difference between the ions' and electrons' masses, electron current dominates the double layer [20]; alternatively, Eq. 4.8 expresses the fact that the electron current density, drawn across the DL, is limited by the ion current density, flowing in the opposite direction [56]. Furthermore, several laboratory experiments have proved that the Langmuir condition in Eq. 4.8 determines the equilibrium location of a strong double layer [21, 22].

An important focus in the double layer research has been the stability Langmuir DL: experimental observations showed that if the charge-carrier fluxes across the DL (i.e. the ion- and electron-carried current densities) do not satisfy Eq. 4.8 in the laboratory reference frame, the DL moves accordingly. B. Song *et al.* tackled this behaviour, adopting a theoretical approach, in Ref. [21]: they developed a mathematical criterion for the macroscopic stability of a strong double layer. Such a criterion was derived in a one-dimensional perturbative theory, under the assumptions that the DL stability depends on the net potential difference rather than on the detailed DL structure and, consequently, any change in the shape of the DL -related to the introduced perturbation- is negligible. A modified Langmuir condition was determined considering the continuity equation and the momentum balance in the double layer reference frame: Eq. 4.9 describes the equilibrium condition for a strong DL moving with velocity u_{DL} with respect to the lab frame.

$$j_i - n_{i,H} u_{\mathrm{DL}} = \sqrt{\frac{m_e}{m_i}} j_e \tag{4.9}$$

Where $n_{i,H}$, is the ion density on the high potential side of the double layer.

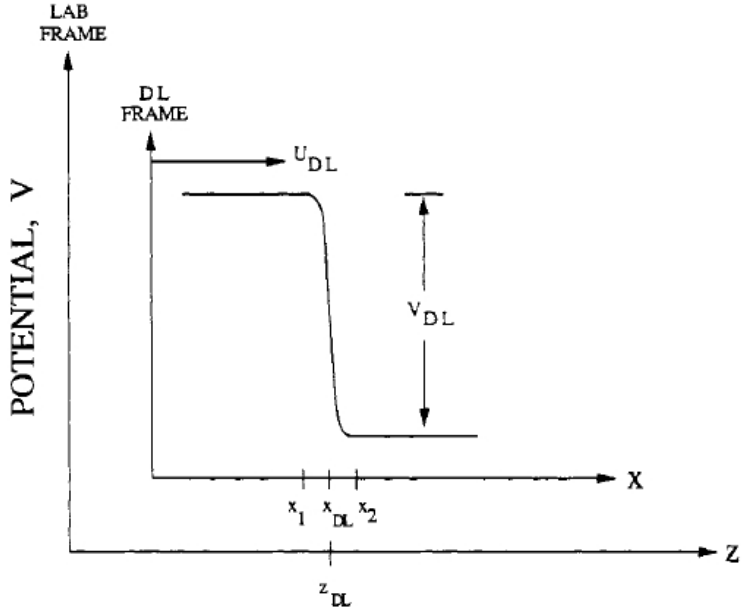

Figure 4.5 Schematic of the double layer in the laboratory and DL reference frame

In Eq. 4.10 the resulting stability criterion is given:

$$\frac{\mathrm{d}}{\mathrm{d}x}\left(j_i - \sqrt{\frac{m_e}{m_i}} j_e \right)\Bigg|_{x_{\mathrm{DL},0}} < 0 \tag{4.10}$$

Where $x_{\mathrm{DL},0}$, is the equilibrium location for the DL.

The analytic model proposed by Song *et al.* was proved to correctly predict the DL stable equilibrium location observed in a number of laboratory experiments, including strong DLs in a weakly magnetised plasma and in a non-uniform magnetic field [21]. Thereafter, on the basis of these confirmations, Song *et al.* developed a specific experiment, aimed at the validation of the strong DL stability criterion, for an ionisation-produced spherical double layer, with zero magnetic field.

¶ Spherical double layer

In literature, several observations of a quasi-spherical, luminous structure in a discharge plasma have been reported. These objects, referred to as "fireballs" or "anode spots" are most likely to be observed in correspondence of a disc anode when a threshold value is exceeded, for the applied voltage bias. In Ref. [22], Song *et al.* reported of previous observations of a fireball emerging in correspondence of a $40 \div 50[V]$ biased disc anode, in an Ar, Kr or Xe discharge plasma, and they analysed the anode spot in terms of a spherical double layer (SDL).

The dynamic of an "exploding" fireball, i.e. the time-evolution of the double layer from plasma conditions similar to those of an unstable anode sheath to those of a stable DL structure -detached from the anode wall- was investigated by means of the stability criterion for a Langmuir DL in Eq. 4.10. A further advanced analysis of this process was recently conducted by B. Scheiner in Ref. [65]: the neutral background gas ionisation in the anode sheath and the consequent ensuing of a potential well, with secondary electron trapping, are identified as the key processes determining the fireball explosion. Considering the Debye shielding for a positively biased electrode and the relative electron sheath, if the applied voltage is high enough, electrons are accelerated through the sheath and gain kinetic energy sufficient to the impact ionisation of neutral species. Locally, this phenomenon enhances the ionisation process -already taking place across the whole discharge plasma- inside the anode sheath. As a result, a positive space charge layer is formed at the anode and a negative charge space layer, due to the secondary electrons produced in the ionisation reaction, takes shape, adjacent to the bulk plasma: an anode double layer yields, called "anode glow" (see Fig 4.7.a). If the local ionisation collisions inside the anode sheath happen at such a rate that they compensate for and prevail on the ion losses through the DL surface, a local maximum is found in the DL potential profile, i.e. a potential well ensues at the anode surface. This acts like an electron trap, attracting the low energy electrons born in the ionisation process, and the electron density in the negative sheath increases to the point that a quasi-neutral plasma region is formed between the anode glow and the bulk plasma.

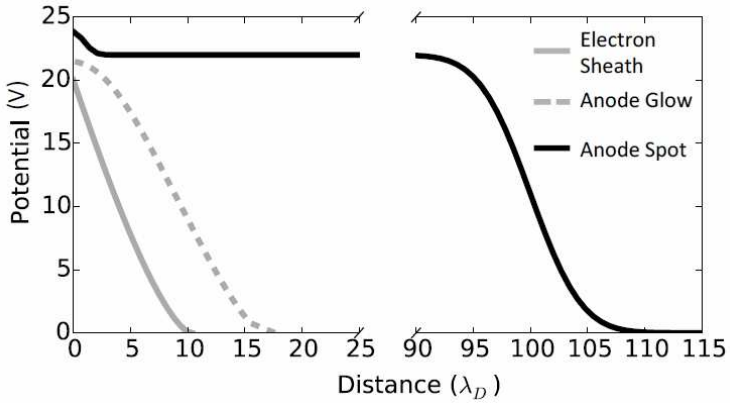

Figure 4.6 Potential profiles for three exemplary sheath-like structures that are possible in the vicinity of a positively biased electrode: an electron sheath (grey solid line), an anode glow (grey dashed line), and an anode spot (black solid line) [65].

The quasi-neutrality condition entails the Langmuir generalised criteria to be satisfied in that the following conditions (Eq. 4.4 and 4.5) at the anode DL high-potential side boundary hold:

$$E \approx 0$$
$$n_e \approx n_i \tag{4.11}$$

The evolution of the double layer is then predicted according to the modified Langmuir condition (Eq. 4.9), depending on the charge-carrier fluxes entering the DL. An electron pre-sheath (i.e. a plasma region where the sheath boundary conditions are linked to those of the bulk plasma) joins the low-potential side of the anode DL to the bulk, and electrons are accelerated through such a region up to their thermal speed $v_{\mathrm{T},e} = \sqrt{T_e/m_e}$. Hence, the electron-carried current density -flowing from the negative sheath toward the positive one- results:

$$j_e = \mathrm{e}\, n_{e,\mathrm{B}} \sqrt{\frac{T_{e,\mathrm{B}}}{m_e}} \tag{4.12}$$

Where $n_{e,\mathrm{B}}$, is the electron number density in the bulk plasma;

$T_{e,\mathrm{B}}$, is the electron temperature in the bulk plasma.

As far as ions are concerned, they enter the high-potential side of the double layer -adjacent to the electrode- at their sound speed, according to Bohm criterion, and the relative current density is:

$$j_i = |\mathrm{e}|\, n_{i,\mathrm{H}} \sqrt{\frac{T_{i,H}}{m_i}} \tag{4.13}$$

Where $n_{i,\mathrm{H}}$, is the ion number density in the bulk plasma;

$T_{i,\mathrm{H}}$, is the ion temperature in the bulk plasma.

The potential unbalance of the two particle fluxes determines the motion of the DL with a velocity u_{DL}, dictated by Eq. 4.9, until the position of stable equilibrium is reached. If the ion flux, fostered by the collisional ionisation processes, prevails, the double layer will detach from the anode surface, becoming an interfacing structure between the high potential, quasi-neutral, luminous plasma (i.e. the fireball) from the dark bulk plasma, in Fig. 4.7.b.

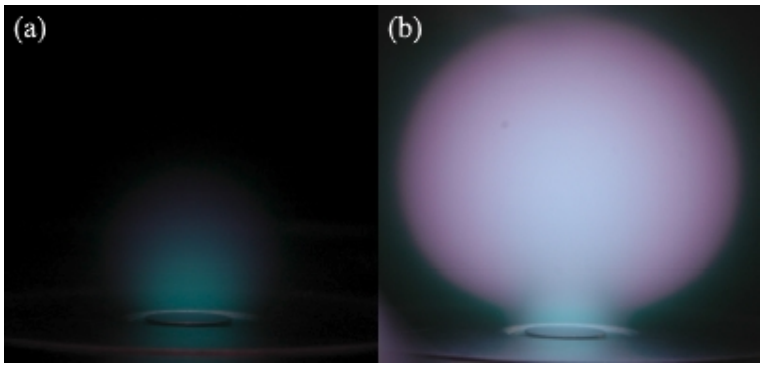

Figure 4.7 Experimental observation of two different sheath structures within a discharge plasma, in correspondence of a disc anode: (a) Anode glow, (b) Anode spot [65].

Hence, the transition process between an anode glow and an anode spot does not require any instability, laying at the basis of the spot onset mechanism, contrary to what previous works had theorised [65].

If a spherical anode of radius r_0 is given, for an increasing value of the applied voltage drop between the electrodes, the early electron sheath will evolve in the sheath-like structures depicted in the previous paragraphs (whose electrostatic potential profile is given in Fig. 4.6). The locally enhanced ionisation processes within the anode sheath will determine the ensuing of the anode double layer observed in the anode glow; a further increase in the applied voltage leads to the rapid formation of the anode spot [65], according to the equilibrium equation, Eq 4.9, provided in Ref. [21]. A strong, spherical double layer -

modelled according to Langmuir condition- is thus established in the discharge plasma, provided that $r_{DL} \gg r_0$: assuming the double layer to be traversed by a net electric current (i.e. a current-driving DL), an external power supply is required to maintain the anode voltage ϕ_0. From a circuital point of view, the spherical DL can be represented as a resistor R, connecting the low potential side of the DL to that of the power supply [22]. The resistor introduces both the inertial resistance of the double layer structure and an additional resistance contribution, due to the possible dirt at the interface of the bulk plasma and the vacuum vessel wall: the two resistance components are assumed to be in series. Using Ohm's law, the voltage drop across the spherical double layer can be expressed as a linear function of the electric current I, flowing from the anode, as in Eq. 4.14.

$$\phi_{DL} = \phi_0 - IR \tag{4.14}$$

Assuming the SDL thickness to be small, compared to the DL radius, the same Langmuir condition determined for a planar double layer can be assumed[20] to hold here:

$$\Psi_i(r_{DL}) = \sqrt{\frac{m_e}{m_i}}\, \Psi_e(r_{DL}) \tag{4.15}$$

Introducing the background neutral gas number density N and cross-section for electron ionisation impact -as a function of the DL net potential difference, responsible for electron acceleration in the double sheath structure, $\sigma(\phi_{DL})$-, the ions production rate from the enhanced ionisation volume, within the DL, is related to the incoming electron flux, as:

$$\mathrm{P}_{i,\mathrm{yield}} \doteq \frac{\mathrm{d}n_i}{\mathrm{d}t} = 4\pi\, r_{DL}^3\, N\, \sigma(\phi_{DL})\, \Psi_e(r_{DL}) \tag{4.16}$$

Assuming a perfect spherical symmetry for the anode spot, ions are lost through the spherical surface to the bulk plasma, at the rate

$$\mathrm{P}_{i,\mathrm{loss}} = 4\pi\, r_{DL}^2\, \Psi_i(r_{DL}) \tag{4.17}$$

Balancing these rate for the SDL equilibrium condition, the following relation linking the ion and electron fluxes is found:

$$\Psi_i(r_{DL}) = N\, r_{DL}\, \sigma(\phi_{DL})\, \Psi_e(r_{DL}) \tag{4.18}$$

The Langmuir condition in Eq. 4.15 is then recast as

$$N\, r_{DL}\, \sigma(\phi_{DL}) \sqrt{\frac{m_e}{m_i}} = 1 \tag{4.19}$$

The electron current collected at the anode is the sum of the integral of the inflowing electron-carried current density, over the SDL surface, and an auxiliary electron flux, due to secondary electrons produced in the ionisation processes through the anode spot thickness. Since $N\sigma r_{DL} \ll 1$, the auxiliary current term is negligible with respect to the main electron flux through the DL:

$$I = 4\pi\, r_{DL}^2\, \mathrm{e}\, \Psi_e(r_{DL}) + 4\pi\, r_{DL}^3\, N\, \sigma(\phi_{DL})\, \mathrm{e}\, \Psi_e(r_{DL}) \approx 4\pi\, r_{DL}^2\, \mathrm{e}\, \Psi_e(r_{DL}) \tag{4.20}$$

Experimental observations showed that, over a large range of neutral gas pressure, the electron density is proportional to the neutral density itself [22] hence voltage drop across the spherical double layer is recast as in Eq. 4.21.

$$\phi_{DL} = \phi_0 - R \cdot (\beta N r_{DL}^2) \tag{4.21}$$

[20] Note that, for clarity purpose, Eq. 4.9 is here recast in terms of particle fluxes rather than electric density current, nonetheless Eq. 4.9 and 4.13 are perfectly equivalent, to within a gauge factor equal to the elementary charge e: $j_{i,e} = |\mathrm{e}|\, \Psi_{i,e}$.

Where β, is a proportionality constant[21].

Finally, the anode spot solutions -i.e. the spherical double layer radius r_{DL} and the relating electrostatic potential drop ϕ_{DL}- can be assessed by solving the transcendental, algebraic system in Eq. 4.22

$$\begin{cases} N\, r_{\mathrm{DL}}\, \sigma(\phi_{\mathrm{DL}}) \sqrt{\dfrac{m_e}{m_i}} = 1 \\ \phi_{\mathrm{DL}} = \phi_0 - R \cdot (\beta N r_{\mathrm{DL}}^2) \end{cases} \tag{4.22}$$

Moreover, Song *et al.* proved, in their theoretical analysis, that DL stability is promoted by a large circuital resistance, high background pressure and a rapid variation of the ionisation cross-section with the energy of the accelerated electron population [22].

4.3 Spherical double layer model for IEC

¶ IEC-SDL model: plasma confinement, ionisation and jet extraction mechanisms

The existence of a deep potential well, i.e. (as in Fig. 2.4.b), in the core plasma engendered in a glow discharge IEC device has been confirmed in a number of experimental observations [8, 39, 18], as well as in the one-dimensional plasma simulation presented in the previous chapter, whichever the assumed particle distribution functions were. Nevertheless, as far as the inception of multiple potential wells -in the form of the poissor structures depicted in Chapter 2, Section 1, ¶ Operating principle- is concerned, plasma simulations based on Lavrent'ev's method yield a flat plasma profile, in correspondence of the IEC device centre, for both the rectangular and thermal distribution function simulations. Hence, in case of a GD-IEC device, where the mono-energetic pdf for the charge-carrier population seems to fall, the formation of a virtual cathode is not observed. This justifies some criticism on the possible extension of the canonical potential-well theory -conceived in the context of the original external source design for the Farnsworth-Hirsch fusor [23, 34]-, to the confinement mechanism for the glow discharge plasma, in the core region of an IEC jet thruster.

Recently, Y.A. Chan and G. Herdrich, from the Institut für Raumfahrtsysteme in Stuttgart, proposed an alternative model aimed at the thorough explanation of all the main physical phenomena observed in the core plasma of a GD-IEC device, including plasma confinement, ionisation processes and jet extraction in an asymmetric grid configuration [19]. Such a model relies on the double layer theory detailed in the previous section of the present chapter: more specifically, the luminous core plasma observed in the centre region of an IEC jet thruster is interpreted as a spherical double layer. Hence, the same nomenclature as in Ref. [19] is adopted in this thesis, and the proposed model is referred to as "IEC-SDL model".

The ensuing of a virtual anode in the glow discharge plasma, in the centre region of the IEC device, indicates the existence of a non-neutral region inside the cathode grid. Indeed, the virtual anode represents a positive space charge region, which attracts and accelerates the electrons population in a centre pointing electron wind. A voltage threshold may be identified, analogous to that observed in the formation of an anode spot in proximity of a solid anode [21, 65], over which the electrostatic potential accelerating the electron inflow exceeds the ionising potential for the background neutral gas. Hence, a further electron impact ionisation process, simultaneous to the Townshend avalanche fostering the discharge, ensues locally in the sheath-like ion structure at the IEC centre. In this respect, remarkable is the resemblance of the potential profile inside the IEC cathode, given in Fig. 4.8, and the anode sheath potential depicted in Fig. 4.6 (grey solid line). The virtual anode is thus a sheath-like function where the

[21] In the order of $10^{-14}[\mathrm{A \cdot cm}]$, for typical experimental parameters [22].

secondary ionisation process creates ions with approximately the same thermal velocity as the background gas [19].

$$v_i \approx \sqrt{\frac{2\,\mathrm{k}\,T_n}{m_i}} \tag{4.23}$$

Where T_n, is the background neutral gas' temperature.

The negatively charged particles in the electron wind, on the contrary, have a high drifting velocity due to the virtual anode acceleration:

$$v_e \approx \sqrt{\frac{2\,\mathrm{e}\,\phi_{\mathrm{DL}}}{m_e}} \tag{4.24}$$

The build-up of a negative space charge layer, enveloping the virtual anode, determines the formation of a spherical double layer in the core plasma of the IEC device. When the global quasi-neutrality condition is reached over the double layer structure, the momentum balance[22], for the charge-carriers populations fostering the SDL, determines is evolution, according to Eq. 4.9. If the outward ion flux overcomes the inward electron wind, the IEC double layer will expand in a dynamic analogous to that of an exploding fireball, described in Ref. [20] and [56].

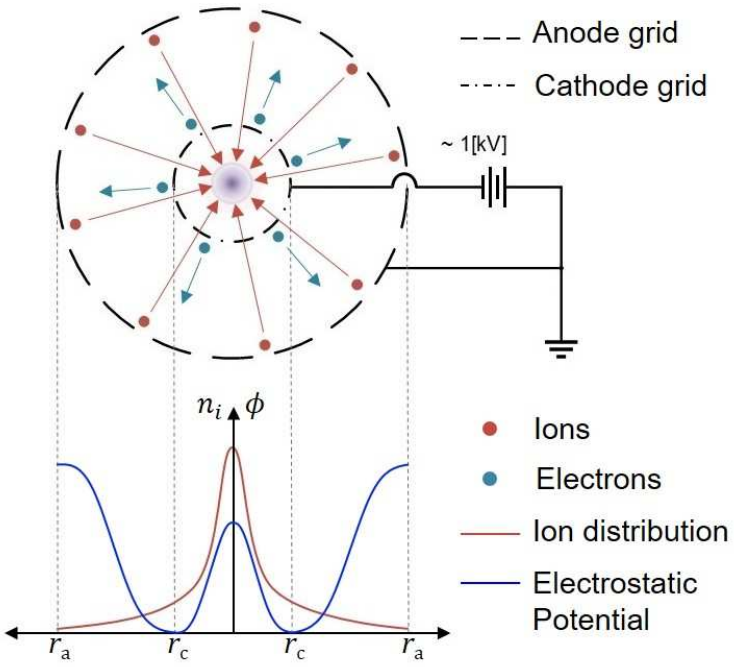

Figure 4.8 Schematic of a GD-IEC device along with particle and potential profiles.

Since ions and electrons are required to have high kinetic energy to penetrate the spherical double layer, which is unlikely in case of non-drifting particles, the SDL provides a confinement mechanism for the core plasma in the centre of the IEC device. Moreover, the ionising mechanism entailed in the double layer formation provides a high degree of ionisation of the background neutral gas and is supported by experimental observations. In fact, experimental field research reports of a spontaneous current jump from power supply as soon as the plasma jet extraction initiates: this abrupt change in the plasma conductivity suggests that the main current flow is localised in the core plasma, inside the cathode, rather

[22] Remember that, according to [20], eq. 4.2 expresses the stress balance in the DL plasma. Langmuir condition (in Eq. 4.8), thus, represents the momentum balance for a strong double layer, where the total particle pressure of a species (i.e. ions or electrons) is dominated by the dynamical pressure of the accelerated particle beam.

than in the inter-electrodes volume [19]. In light of this observation, it may be inferred that, in a jet-mode operating IEC device, the ionising collisions in the intra-cathode region outnumber those happening in the inter-electrodes one: this is in accordance with the enhanced ionisation predicted by the SDL model. According to Y.A. Chan and G. Herdrich:

> "*The spherical double layer model offers a more the SDL model offers a more reasonable assessment of an IEC configuration by solving momentum conservation equation and ionization of plasma. The results show a much better and reasonable correspondence with the experimental data and observations than the potential and density histories from the Poisson's solver.* […] *These indications provide very strong evidence for the existence of an SDL in the IEC numerically, affirmed by the currently available and relevant experiments. The SDL offers both efficient ionization and confinement of plasma*" [19].

On top of that, the IEC-SDL model promises to provide a self-consistent description of the jet extraction mechanism in the asymmetric IEC grid configuration, in terms of ionisation processes and charged particles momentum balance.

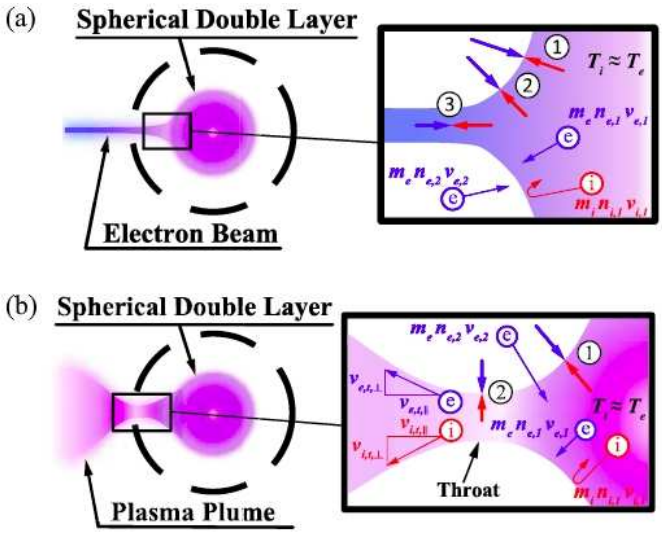

Figure 4.9 Schematic of the plasma extraction mechanism, as depicted in the SDL-IEC model [19]. The plasma jet initiation is determined by the imbalance of the ion and electron flows, in correspondence of the enlarged grid hole (due to electric field distortion). Firstly, a collimated, highly non-Maxwellian electron beam ensues (a); subsequently ions escape the DL confinement and a quasi-neutral plasma jet yields (b).

In Fig. 4.10 a sketch of the spherical double layer inside the IEC device is presented, along with the electron jet emerging from the enlarged grid hole, in tight-jet operating regime (see Chapter 2, Section 1, ¶ Operating principle).

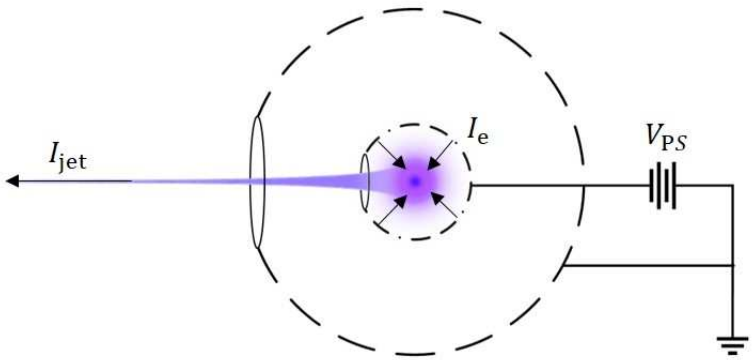

Figure 4.10 Schematic of the spherical double layer inside the cathode grid of an IEC thruster, operating in tight-jet mode.

¶ IEC-SDL simulation

As remarked in the previous section, the double layer position can be determined, under the assumption of the spherical double layer -in the core plasma of an IEC device- being locally analogous to a Langmuir double layer, by means of Eq. 4.22. To this end, B. Song *et al.* defined an auxiliary function as in Eq. 4.25, whose zeros coincide with the roots of Eq. 4.19 [22].

$$F(r) = 1 - N\, r_{\mathrm{DL}}\, \sigma(\phi_{\mathrm{DL}}) \sqrt{\frac{m_e}{m_i}} \tag{4.25}$$

Such a function equals unity in correspondence of the device centre ($r = 0$) and for radius values greater than the limit value r^*, defined as the value of the radius for which Eq. 4.26 is satisfied:

$$\phi - R \cdot \left(\beta N r^{*2}\right) = \phi_{\mathrm{ion}} \tag{4.26}$$

Where ϕ_{ion}, is the ionisation potential of the background neutral gas.

Equivalently, the limit value r^*can be thought as the radius value, which entails a null ionisation cross section, as in:

$$\sigma(\phi)|_{r=r^*} = 0 \tag{4.27}$$

As can be observed in Fig. 4.11, if the function F has any real zero, it has two of them, hence two distinct solutions can be computed for the spherical double layer: B. Song *et al.* claim that only the larger root of Eq. 4.19 satisfies the stability criterion for a strong double layer, given as in Eq. 4.28 [21].

$$\frac{\mathrm{d}}{\mathrm{d}r}\left(\Psi_i - \sqrt{\frac{m_e}{m_i}}\,\Psi_e\right)\Bigg|_{r_{\mathrm{DL}}} < 0 \tag{4.28}$$

Hence, the non-linear system in Eq. 4.22 allows for the assessment of the main characteristics of a spherical double layer, once the anode voltage ϕ_0 and the equivalent circuital resistance R are known.

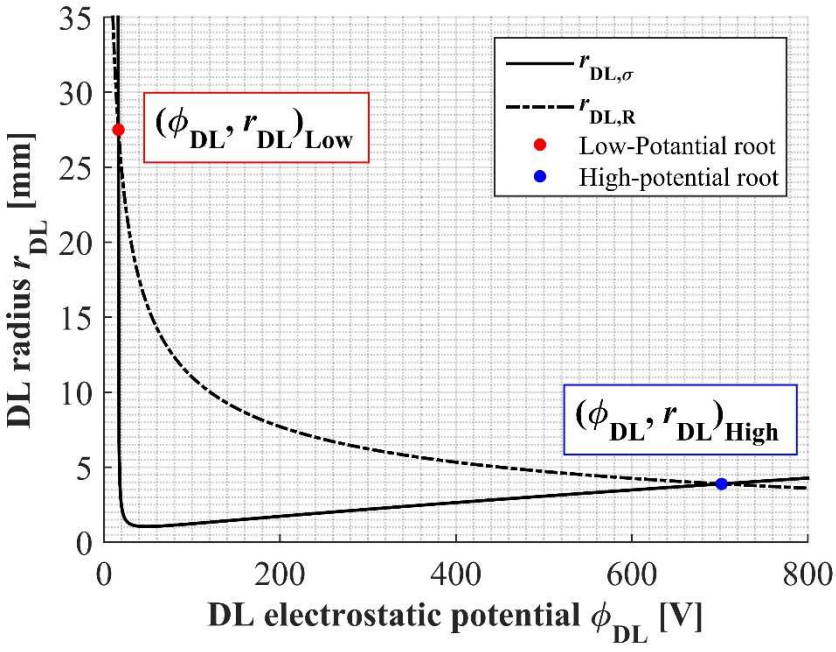

Figure 4.11 Solution of the circuital model for the SDL simulated in an IEC device operating on a 0.5 [Pa] background pressure, for an applied electrode voltage of 1 [kV] and an extracted jet current of 30 [mA]. The solid line represents the computed solution for the charge

continuity equation while the dash-dotted one is referred to Ohm's law. Two distinct solution are clearly identified: the red point marks the low-potential SDL solution while the high-potential solution is marked by the blue point.

In the attempt of extending this circuital model to the case of the spherical double layer, which has been theorised to ensue in the glow discharge plasma inside an IEC device, the following assumptions are made:

- First of all, the detailed DL geometry must be negligible in the global definition of the non-neutral structure; this assumption entails the DL thickness to be much smaller than the radius [22]:
$$t_{\mathrm{DL}} \ll r_{\mathrm{DL}} \tag{4.29}$$
- Secondly, the spherical double layer is supposed to be an overall neutral structure so that, to a first approximation, the electric current carried by the extracted jet -which, in tight-jet mode, is experimentally observed to be a negative current, i.e. an electron-carried electric current- equals the incoming electron flux on the SDL surface:
$$I_{\mathrm{e}} \approx I_{\mathrm{jet}} \tag{4.30}$$

Furthermore, the equivalent electrostatic resistance is recast in terms of the electron current flowing across the double layer surface, denoted as I_{jet} in the present work (adopting the notation found in Ref. [19]), according to Ohm's law, in the following form:

$$R = \frac{(\phi_0 - \phi_{\mathrm{DL}})}{I_{\mathrm{jet}}} \tag{4.31}$$

Hence, the SDL solution can be obtained solving Eq. 4.22 for assigned values of the anode voltage and the electron current across the double layer surface.

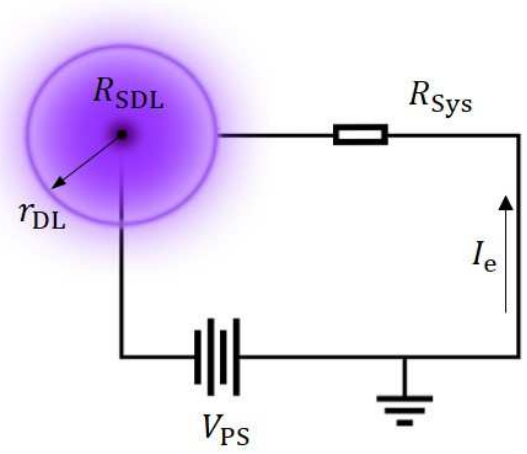

Figure 4.12 Schematic of the electric circuit for the IEC-SDL: the circuital resistance is due to the contribution of the spherical double layer R_{SDL} and the device electric system R_{Sys}.

Critical to the assessment of the double layer properties, according to the described model, is the knowledge of the ionisation cross section for the propellant gas, employed in the IEC device, as a function of the double layer electrostatic potential. As already mentioned, the most commonly employed propellant -introduced inside the device to generate the discharge plasma- are noble gases such as Argon, Krypton and Xenon. While many data are available in literature about the electron-impact ionisation process, particular reference is made here to the work of M.A. Lennon *et al.* who provided accurate data for the ionisation cross-section of atoms and ions concerning species, in the periodic table, from Fluorine to Nickel. In their published paper, convenient expressions are proposed for the recommended cross-sections and rate coefficients: in particular, the mathematical form given in Eq. 4.32 is proposed for the

computation of the investigated cross-section, depending on the species' ionisation potential and the incident electron energy.

$$\sigma(E) = \frac{1}{\phi_{\text{ion}} E}\left[A \ln\left(\frac{E}{\phi_{\text{ion}}}\right) + \sum_{i=1}^{N} B_i \left(1 - \frac{\phi_{\text{ion}}}{E}\right)\right] \tag{4.32}$$

Where E, is the incident electron energy,

B_i, are computed by means of a least-square fitting procedure, given in Ref. [66],

A, is a Bethe coefficient[23], which determines the high-energy behaviour of the cross section.

The computational method described above was then employed for the simulation of the spherical double layer in the core plasma at the centre of an IEC device. Assuming an Argon discharge to ensue inside the device, the ionisation cross section was computed as function of the double layer's electrostatic potential, according to Eq. 4.32.

In Fig. 4.13 and 4.14, the spherical double layer solutions, calculated by solving Eq. 4.22 for an assumed Argon background pressure of 0.5 [Pa], are presented. Fig. 4.14 provides a visual output of the DL electrostatic potential computed for the assumed values of the electron current and electron-accelerating potential. More specifically, two different plots are presented for the IEC-SDL solution attained in correspondence of the distinct solutions of Eq. 4.19: the left-hand side figure represents the high-potential solution, while the right-hand side one is referred to the low-potential solution. It is remarkable that the two solutions show a very different behaviour, indeed the high-potential solution tends to increase for both increasing electron current and applied voltage. The low potential values, on the other hand, decreases for higher currents and electron-accelerating voltages.

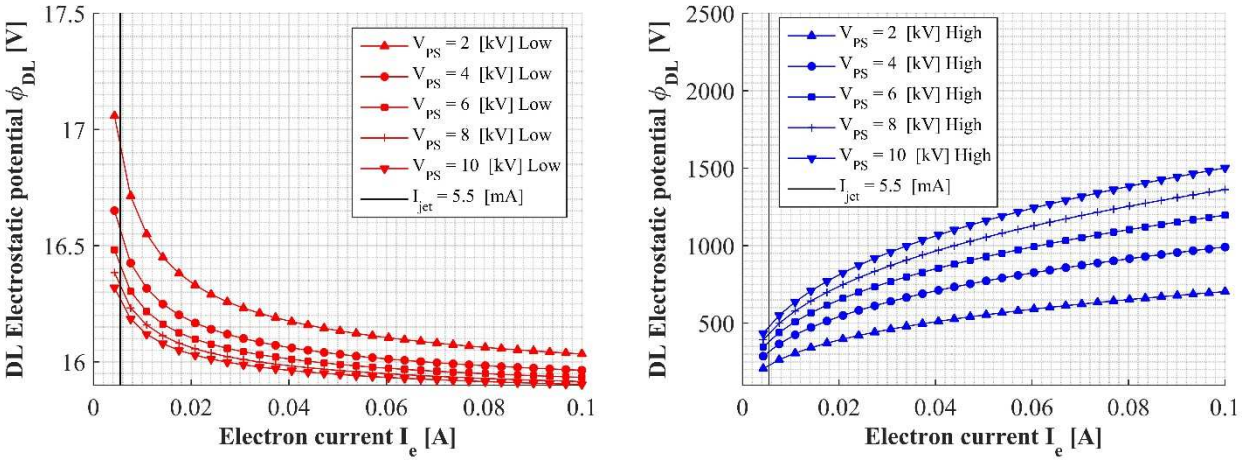

Figure 4.13 Computed solutions of the double layer electrostatic potential for the IEC-SDL ϕ_{DL}, depending on the net current I crossing the IEC-SDL and the applied voltage V_{PS}, with a neutral background gas pressure of 0.5 [Pa]. The solid vertical line refers to a jet current of 5.5 [mA] and represents the experimental observation of the SDL inside the IRS-IEC device given in Ref. [19].

In Fig. 4.14, the corresponding values for the radius of the spherical double layer are plotted against the assumed electric current across the DL surface, for different values of the electrostatic potential

[23] Bethe coefficient is calculated by fitting Eq. 4.34 to the high-energy Born approximation and its value is provided in Ref. [66] as well.

$$\sigma(E) = \frac{1}{\phi_{\text{ion}} E}[A \ln(E) + B] \tag{4.33}$$

accelerating the electrons on the low-potential side of the double layer itself. It is worth noticing that, for both the possible solutions of Eq. 4.19, greater values of the SDL radius are obtained for increasing electron current, while smaller radii correspond to higher voltages. In addition, it is possible to observe that the low-potential solution entails the greater radius for the simulated double layer: hence, it represents the only stable solution according to [22]. Other considerations, concerning the comparison of the two possible solutions calculated for the IEC-SDL, require a deeper analysis of the plasma physics for a Langmuir double layer and are presented in the next section.

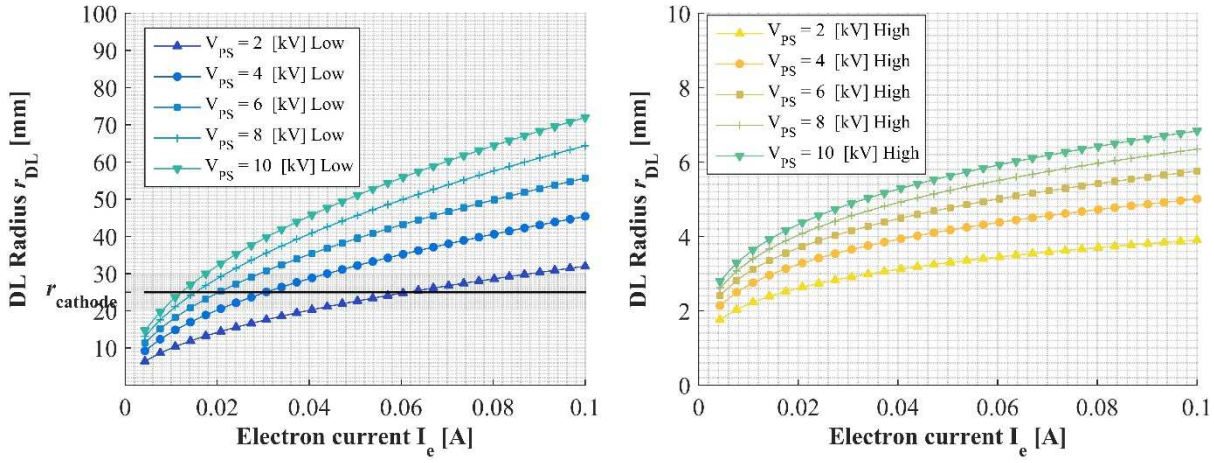

Figure 4.14 Computed solution of the double layer radius for the IEC-SDL r_{DL}, depending on the electron current I_e on the surface of the IEC-SDL and the electron-accelerating voltage V_{PS}, with a neutral background gas pressure of 0.5 [Pa].

¶ Detailed structure of Langmuir double layer

The circuital model developed to assess the main properties of the spherical double layer depicts such an electrostatic structure in terms of a thin shell embedded in a uniform plasma. A critical assumption for this description is thus that of the thickness of the non-neutral plasma region being much smaller than the mean radius of the spherical structure: hence, the electrostatic shell can be locally related to the case of the double layer produced in the plasma between two planar, parallel electrodes [21]. Hence, it is necessary to develop a physical model to assess the thickness of the double layer in the IEC core plasma: such an attainment is necessary to properly define the limitations of the above-presented IEC-SDL model. In this respect, it is worth stressing out the fact that the double layer model for the discharge plasma in the core of an IEC device -as presented in Ref. [19]- does not imply, itself, any specific theory for the description of the double layer structure.

For the scope of the work here reported, the theory of double sheaths, developed by I. Langmuir in the first decades of the twentieth century, was chosen to depict the fundamentals of the investigated spherical double layer. A brief description of the electrostatic structure depicted in Langmuir's theoretical work -referred to as "Langmuir double layer"-, and its arrangement in the general framework of double layer theory, was previously presented in the present chapter. Nonetheless, it is well timed to delve a little deeper into the physical theory of Langmuir double sheath, so as to assess its detailed internal structure and how this reflects on the bulk plasma confined inside the spherical double layer.

In 1911 and 1913 respectively, Clement D. Child and Irving Langmuir independently attained an exact solution for the problem of describing the space-charge limited electric current flowing between two electrodes. They considered the case of two infinitely extended, conductive plates, placed at a finite voltage difference and assumed that a perfect vacuum volume between them. When the potential drop between the electrodes is high enough, the cathode spontaneously emits electrons due to the field emission effect, which are accelerated by the uniform electric field towards the anode, where they neutralise: an electron-carried current yields between the electrodes. The spontaneous emission of

electrode from the surface of the cathode entails the build-up of an electron population between the plates, whose number density increases with the emission rate, up to a point where a negative potential results in the electron fluid volume. The resulting electrostatic field counters the externally applied voltage between the electrodes and, finally, a dynamic balance is reached: the space-charge density in the electron fluid volume limits the particle emission at the cathode surface. The above-depicted phenomenon is nowadays known as space-charge limited current and was described by I. Langmuir, who attained the mathematical relation in Eq. 4.34, describing the dependence of the space-charge limited current (per unit area) on the three-halves power of the applied electrode voltage [67].

$$j_{\mathrm{SCL}} = \frac{1}{9\pi}\varepsilon_0\sqrt{\frac{2\mathrm{e}}{m_e}}\frac{\Delta V^{\frac{3}{2}}}{d^2} \tag{4.34}$$

Where j_{SCL}, is the space-charge limited current flowing between the electrodes

ΔV, is the electrostatic potential applied on the electrodes

d, is the distance between the electrodes.

In addition, Langmuir further developed its dissertation, analysing the effect of the introduction of a certain amount of positively charged particles in the inter-electrode volume: the partial neutralisation of the electron space-charge allows for an increase in the emission rate at the cathode surface.

More than a decade after this publication, Langmuir found an experimental application, for his theoretical dissertation, to the case of the ionised Caesium gas in contact with a hot cathode. Indeed, it was observed that if even a small amount of gas is present between the electrodes and the applied potential is sufficient for the electron-impact ionisation reaction to happen at a relevant rate, a glow discharge plasma yields. In the plasma, the presence of ions neutralises the negative space-charge on distances greater than Debye length: the current is then only limited by the electron emission rate, which is, in turn, dependant on either the applied potential -in the field emission regime, for low cathode temperatures-, or the cathode temperature -in thermionic emission regime- [68]. In conclusion, Langmuir's dissertation on the physical properties of low pressure discharges lead to a rather extensive characterisation of the plasma phenomena observed in gas discharge tubes. In this context, fundamental concepts, such as plasma sheath and double layer, found their first formalisation [69]. In the following, the lines of reasoning that lead to the formalisation of Langmuir's double sheath are presented with respect to the glow discharge phenomena in a gas-filled tube, like the one shown in Fig. 4.15.

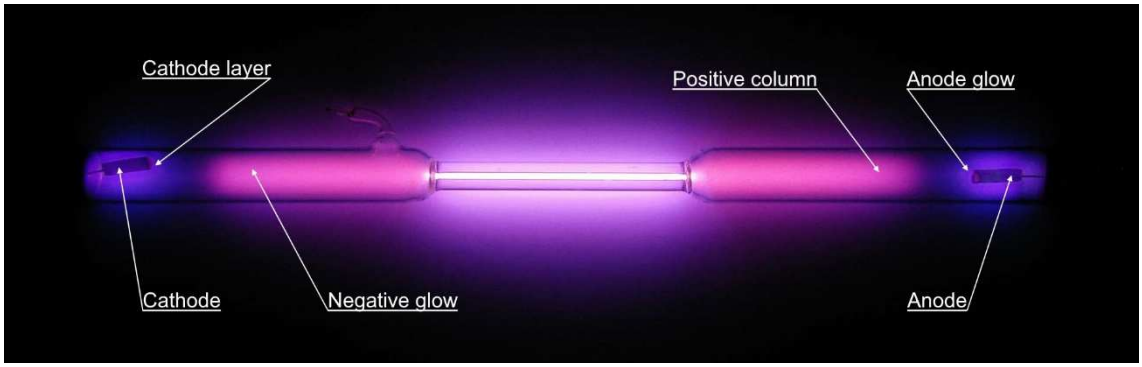

Figure 4.15 Glow discharge structure in an Argon gas-filled tube.

First and foremost, Langmuir devised a mathematical model for the description of the electron emission from an infinitely extended, plane cathode when a given amount of ions are provided: both the case were considered of introduction of ions with negligible and non-negligible velocity. Assuming the ions to be introduced in the system with zero velocity and uniformly distributed over a plane between the electrodes, the partial neutralisation of the negative space-charge determines an increase in the cathode-emitted electron current. From the continuity equation for the electric charge, it is possible to

express the current density for the emitted electrode and the provided, neutralising ions, in terms of their space-charge density and velocity, as in Eq. 4.35:

$$\begin{aligned} j_e &= \rho_e \cdot v_e \\ j_i &= \rho_i \cdot v_i \end{aligned} \tag{4.35}$$

Assuming only singly charged ions and neglecting possible scattering processes, the particles' motion between the electrodes is driven by the conservation of total mechanical energy, given in Eq. 4.36.

$$\begin{aligned} \frac{1}{2} m_e v_e^2 &= V_{\mathrm{C}} \cdot \mathrm{e} \\ \frac{1}{2} m_i v_i^2 &= (V_B - V_{\mathrm{C}}) \cdot \mathrm{e} \end{aligned} \tag{4.36}$$

Where V_{C}, is the cathode voltage

V_B, is the voltage in correspondence of the ion insertion plane.

Recalling Poisson's equation, extensively employed for the plasma modelling in Chapter 3, this describes the electrostatic field between the electrodes, depending on both the cathode-emitted current and the neutralising ion current:

$$\frac{\mathrm{d}^2 V}{\mathrm{d}x^2} = 4\pi \, (\rho_e - \rho_i) \tag{4.37}$$

It is advisable, at this point, to normalise the problem, introducing the gauge transformation, for the electrostatic potential and the (one-dimensional) space, in Eq. 4.38.

$$\begin{aligned} \phi &\doteq \frac{V}{V_{\mathrm{A}}} \\ \lambda &\doteq \frac{x}{t_{\mathrm{DL}}} \end{aligned} \tag{4.38}$$

Where V_{A}, is the anode voltage.

In addition, Eq. 4.37 allows for eliminating the particles' velocities in Eq. 4.35. It is then useful to introduce the following non-dimensional parameter:

$$\alpha = \left(\frac{j_i}{j_e}\right) \sqrt{\frac{m_i}{m_e}} \tag{4.39}$$

Finally, the normalised Poisson's equation can be equipped with a Neumann B.C. at the cathode, expressing the space-charge limitation on the electron current. Hence, Eq. 4.37 can be recast as the boundary value problem in Eq. 4.40.

$$\begin{cases} \dfrac{\mathrm{d}^2 \phi}{\mathrm{d}\lambda^2} = \dfrac{4}{9} \dfrac{j_e}{i_{\mathrm{SCL}}} \left[\phi^{-\frac{1}{2}} - \alpha (\phi_{\mathrm{B}} - \phi)^{-\frac{1}{2}} \right] \\ \left. \dfrac{\mathrm{d}\phi}{\mathrm{d}\lambda} \right|_{\lambda=0} = 0 \end{cases} \tag{4.40}$$

Integrating once the resulting ODE, the mathematical form for the electric field between the plane electrodes, yields:

$$\frac{\mathrm{d}\phi}{\mathrm{d}\lambda} = \frac{4}{3} \sqrt{\frac{j_e}{j_{\mathrm{SCL}}}} \left\{ \phi^{\frac{1}{2}} + \alpha \left[(\phi_{\mathrm{B}} - \phi)^{\frac{1}{2}} - \phi_{\mathrm{B}}^{\frac{1}{2}} \right] \right\}^{\frac{1}{2}} \tag{4.41}$$

The resulting model thus accounts for the introduction of ions at a generic plane between the electrodes; the direct emission of neutralising ions from the anode surface is then encompassed as the limit case when the ion-insertion plane coincides with the anode, i.e. for $\phi_B = 1$:

$$\frac{d\phi}{d\lambda} = \frac{4}{3}\sqrt{\frac{j_e}{j_{SCL}}}\left\{\phi^{\frac{1}{2}} + \alpha\left[(1-\phi)^{\frac{1}{2}} - 1\right]\right\}^{\frac{1}{2}} \tag{4.42}$$

It is remarkable that, according to Eq. 4.42, the electric field at the surface of the emitting anode is proportional to the squared root of the difference between the unit and the value of α:

$$\left.\frac{d\phi}{d\lambda}\right|_{\lambda=1} = \frac{4}{3}\sqrt{\frac{j_e}{j_{SCL}}(1-\alpha)} \tag{4.43}$$

Therefore, when the ratio of the ion current over the electron current is equal to the squared root of the ratio between the electron mass and the ion mass ($\alpha = 1$), the electric field at the anode surface is zero and the ion current results to be space-charge limited, just as the electron current. This condition is analogous to the one presented in Eq.4.8 and referred to as "Langmuir condition for a double layer".

In conclusion, is possible to assess the one-dimensional distribution for the electrostatic potential between the electrodes, numerically integrating Eq. 4.42 for a given value of the electron current from the anode and the current ratio parameter α:

$$\int_0^1 \left\{\phi^{\frac{1}{2}} + \alpha\left[(1-\phi)^{\frac{1}{2}} - 1\right]\right\}^{-\frac{1}{2}} d\phi = \frac{4}{3}\sqrt{\frac{j_e}{j_{SCL}}}\lambda \tag{4.44}$$

The thickness of a double layer can thus be assessed, according to Langmuir's theory, by an analogy between the local double layer structure and the above-presented solution for the space-charge limited current flowing between two unbounded, plane electrodes. Following such a line of reasoning, the spatial extension of the region of non-neutrality in the discharge plasma is computed as the distance of two parallel plane electrodes, upon which a voltage drop is assigned, equal to the double layer potential ϕ_{DL}. Hence, the thickness of the resulting double layer is computed in terms of the potential difference and both electron and ion currents, according to Eq. 4.45 [20]:

$$(j_e + j_i)t_{DL}^2 = \left(1 + \sqrt{\frac{m_e}{m_i}}\right)\frac{4}{9}C_0\varepsilon_0\sqrt{\frac{2e}{m_e}}{\phi_{DL}}^{\frac{3}{2}} \tag{4.45}$$

Where $C_0 \approx 1.86518$, according to M.A. Raadu who computed it in terms of elliptic integrals [70].

It is customary to refer to the net electric current flowing across the double layer, resulting from the contribution of the electron and ion emission from the electrodes:

$$j \equiv (j_e + j_i) \tag{4.46}$$

Hence, the following equation yields:

$$t_{DL} = \left[\left(1 + \sqrt{\frac{m_e}{m_i}}\right)\frac{4}{9}C_0\varepsilon_0\sqrt{\frac{2e}{m_e}}\frac{{\phi_{DL}}^{\frac{3}{2}}}{j}\right]^{\frac{1}{2}} \tag{4.47}$$

Once a double layer solution has been determined for a non-neutral structure embedded in a uniform discharge plasma, according to Langmuir's model Eq. 4.47 provides the thickness of the double layer. Thus, substituting Eq. 4.47 into Eq. 4.48, the validation condition for the spherical double layer solution can be recast as a limit value for the double layer potential, as a function of the electric current driven

across it. Fig. 4.37 provides a representation of such a validation criterion in the form of increasingly constraining limit curves.

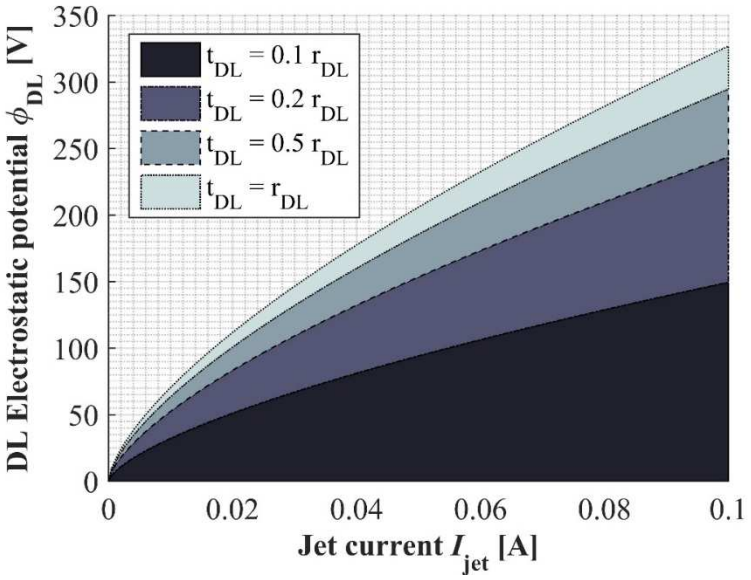

Figure 4.16 Limit curves for the double layer solution.

The comparison of these limit curves and the computed electrostatic potential for the spherical double layer model (see Fig. 4.17) justifies the thorough rejection of the "high potential" solution presented in Fig. 4.13. Hence, the high potential solution computed according to the above- presented SDL model for the IEC device, needs to be ruled out due to the violation of the condition given in Eq. 4.29. Moreover, this conclusion is in agreement with a further discussion on the stability of a spherical double layer. Indeed, B. Song *et al.* demonstrated that only one root of Eq. 4.19, expressing the momentum balance across the DL surface, represents a stable double layer solution: such a root corresponds to the lowest value for the double layer potential [21].

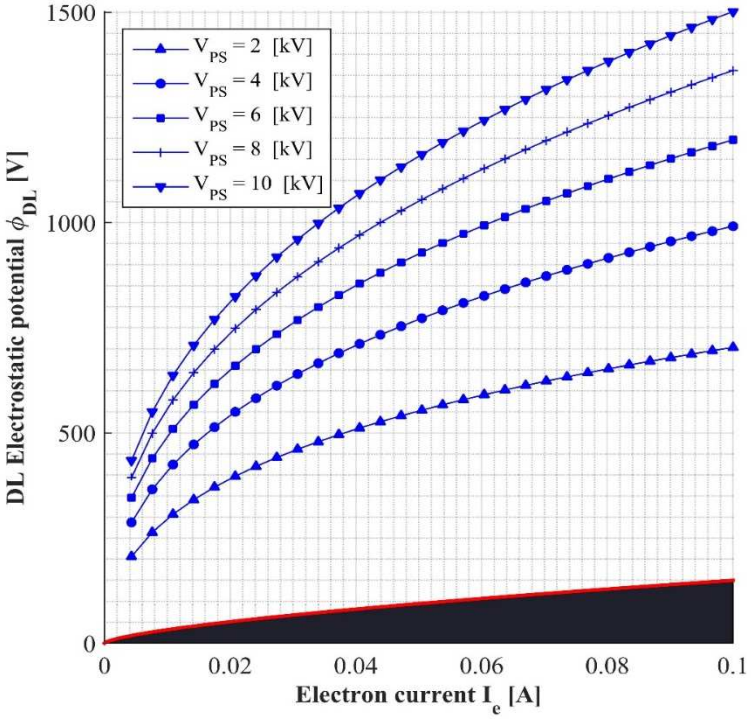

Figure 4.17 Comparison of the limit curves and the high potential solutions for the spherical double layer model. The computed DL solution refers to a background neutral pressure of 0.5

[Pa]. The red curve represents the limit condition for the double layer solution (i.e. the hatched area), when the thickness of the non-neutral region equals the radius of the spherical structure.

Therefore, the plasma simulation of the IEC device at the IRS, according to the spherical double layer model, will refer to the above-presented low-potential solution. In addition, it is remarkable that the value of the DL potential, computed by means of the described circuital analysis, is in perfect agreement with the experimental observations of an anode glow reported by I. Langmuir in Ref. [69]. In fact, Langmuir observed that, if the background neutral gas pressure is high enough, when the positive anode drop is increased up to ionisation potential an enhanced ionisation effect is observed, manifest in the ensuing of a globular light-emitting plasma structure: the anode glow (see Chapter 4, Section 2, ¶ Spherical double layer). Hence, Langmuir first described the formation of a double layer, in the proximity of the anode surface, in terms of the development of a "second plasma". According to its observations, the resulting double sheath was characterised by a potential drop in the order of the background gas ionisation potential. It is thus possible to observe that the computed low-potential solution, represented in Fig. 4.18, excellently matches Langmuir's observations: in fact, the expected double layer potential is in the order of 16 [V], just above the Argon first ionisation energy [66], namely 15.8 [eV].

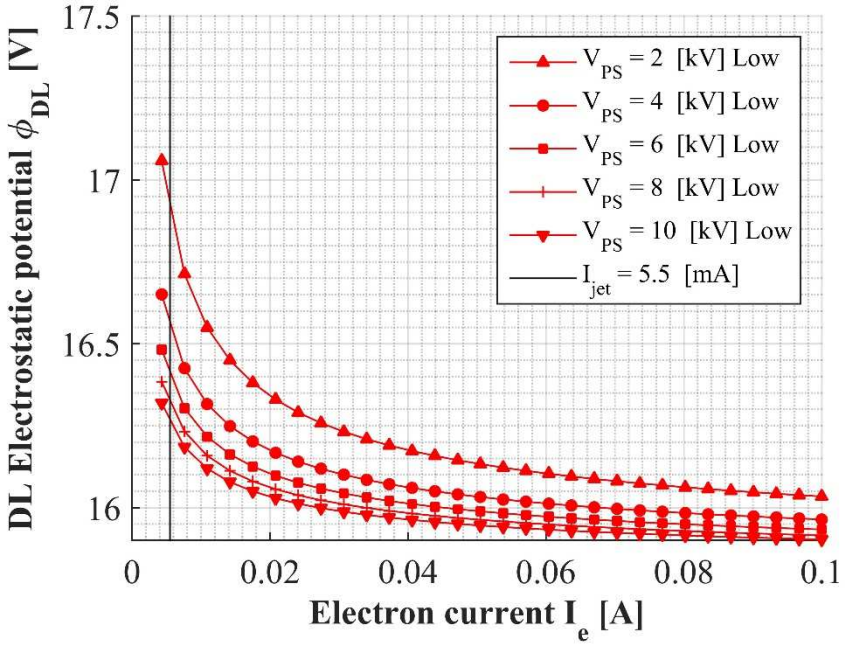

Figure 4.18 Low potential solutions for the spherical double layer model, computed for a background neutral pressure of 0.5 [Pa]. The solid vertical line refers to a jet current of 5.5 [mA] and represents the experimental observation of the SDL inside the IRS-IEC device given in Ref. [19].

Chapter 5
Free-space electrostatic potential

5.1 Free-space electrostatic potential and Laplace equation

As depicted in the second chapter of the present essay, an inertial confinement device is characterised by a rather simple design, made up of two concentric electrodes (being they spherical, cylindrical or of any other kind of geometry), upon which a voltage drop is applied by means of an external power supply. While, in Chapter 3, the detailed electrodes' geometry was neglected in favour of a one-dimensional description of the plasma physics inside the device, the electrode geometry has indeed a key role in determining the topography of the engendered electrostatic field and, thus, it greatly affects the physical behaviour of the electrostatically confined discharge plasma.

In Ref. [44] the locally asymmetric configuration of the electrodes is identified as a triggering factor for the electrons, in the electrostatically confined plasma, to form a jet (as observed in Fig. 2.13a) by introducing local gradients in the electrostatic potential. This concept might be reinforced by the recent observation -both theoretical and experimental- of the presence of electrostatic structures, such as a spherical double layer, ensuing in the core plasma of an IEC device. These structures, besides being responsible for the actual confinement an enhanced ionisation of the core plasma, are closely coupled to the detailed three-dimensional topography of the externally generated electrostatic field. In fact, while most of the experimental observations of spherical double layer have been realised in correspondence of electrostatically biased disk anodes [21, 65] or small almost-spherical electrodes [22], R.L. Stenzel and J.M. Urrutia, from UCLA, reported the observation of a fireball enclosed in a grid-like structure [57]. This proves that the electric field produced by the gridded electrodes, in a typical S-IEC configuration, is capable of naturally driving the inertially confined plasma to the arrangement of local structures where the quasi-neutrality assumption breaks, as described in Chapter 4, Section 2.

Moreover, an important entailment of such a phenomenon is that, on the scale of the double layer's thickness, the charge-carriers electromagnetically interact with each other, thus showing a collective behaviour allowing for the introduction of the concept of surface tension for a spherical double layer. According to Hora H. *et al.,* surface tension of condensed matter arises from the cohesive forces between the particles constituting the matter itself [71]: in a uniform gaseous plasma, the residual cohesive force is much smaller than the kinetic pressure. From this point of view, a uniform plasma behaves like a neutral gas due to the Debye shielding, which confines the electrostatic interaction to the scale of Debye length; this results in an extremely small value for the intrinsic surface tension. On the other hand, if a confinement mechanism -capable of constraining a finite volume of plasma- is provided, a region of non-homogeneity may arise, where the quasi-neutrality assumption is locally violated: a local gradient for the electrostatic field (i.e. an electrostatic field) ensue, determining an electrostatic interaction much greater than the residual cohesive field of a uniform plasma. This provides a theoretical frame to define the surface tension for an electrostatic structure -embedded in a uniform plasma- as the ratio between the corresponding electrostatic energy in the region of non-uniformity and the surface area, at the boundary of the structure itself [71]. Hence, the cited work seems to suggest the possibility of computing the surface tension for the theorised SDL in the core plasma of an IEC device. The local deformation of the electrostatic field, due to the asymmetric electrode configuration, acts on the spherical double layer, stretching it in correspondence of the enlarged grid opening: the above described surface tension might explain how the double layer is deformed in a non-symmetric electric field topography. When the local gradient induced by the asymmetry of the external electrostatic potential reaches a critical value, it might overcome the double layer surface tension, resulting in an outward acceleration of the confined plasma.

Thus, in this scenario, the plasma jet extraction is theoretically depicted as analogous to the well-known phenomenon of Taylor cone formation and electro-spray [72].

The key role played by the detailed geometrical structure of electrodes and the corresponding topography of the induced electrostatic field in determining the plasma dynamics for an IEC device, is therefore manifest. Hence, the present chapter is aimed at providing a detailed mathematical description of the electromagnetic field engendered within the gridded electrodes: since, for the scope of this analysis, the actual presence of a glow discharge plasma -inside the IEC device- is neglected, the investigated electrostatic potential will be referred to as "free-space" potential[24].

This physical issue will be tackled in the context of classical electromagnetism: Maxwell equations will thus represent the physical framework of the mathematical description of the free-space potential in an IEC device. It is well understood that, under the following assumptions:

- steady-state condition;
- negligibility of magnetic induction effects, due to the motion of charged particles inside the IEC device;
- absence of any external magnetic field;

The characterisation of an electromagnetic phenomenon is reduced to the depiction of an electrostatic effect. Hence, an IEC device operating under such conditions can be modelled by employing only Maxwell equation for the electrostatic field:

$$\begin{cases} \nabla \cdot \vec{E} = \dfrac{\rho}{\varepsilon_0} & \text{(Gauss's law)} \\ \nabla \times \vec{E} = \vec{0} & \text{(Faraday's law of induction)} \end{cases} \tag{5.1}$$

Where $\vec{E}$, is the electrostatic vector field,
ρ, is the charge space density,
$\varepsilon_0 = 8.8541878176 \times 10^{-12}$ [F/m], is the *vacuum permittivity* (*free-space permittivity* or *electric constant*).

As underlined in the previous paragraph, the purpose of the present work is the assessment of the topography of the free-space electrostatic potential: the IEC device is, thus, thought of as operating in an empty vacuum chamber and no free charge distribution is considered. Hence, the charge space density within the electrodes needs to be considered equal to zero:

$$\rho = 0 \tag{5.2}$$

$$\Downarrow$$

$$\nabla \cdot \vec{E} = 0 \tag{5.3}$$

Gauss's law expresses, then, the fact that, under the absence of free charges inside the IEC device, the electrostatic field is a solenoidal (or "incompressible") vector field. Moreover, according to Faraday's law, under the above-stated hypotheses of absence of an external magnetic field and negligibility of the magnetic induction effects, the electric field is non-rotational as well. The irrotationality of the electrostatic field allows for the introduction of the well-known electrostatic potential, i.e. a scalar field $\phi : \mathbb{R}^n \to \mathbb{R}$, so that:

$$\vec{E} = -\nabla\phi \tag{5.4}$$

[24] The expression "free-space" was chosen in order to intuitively conceive the idea that the searched potential solution represents the actual electrostatic potential in absence of a neutral gaseous medium fostering the discharge plasma, i.e. in perfect vacuum condition.

Hence, Maxwell equations for the electrostatic field can be recast in the form of Laplace equation, i.e. the homogeneous, second order, elliptic PDE:

$$\nabla^2\phi = 0 \tag{5.5}$$

It is worth noting that Laplace equation is closely related to Poisson equation, being its associated homogeneous equation. As reported in the whole basic literature on the topic of inertial electrostatic confinement [9, 32], Poisson equation represents the prime mathematical tool allowing for the physical portrayal of the electrostatic plasma structures within a steady-state IEC device: previous work has been indeed focused on the resolution of the one-dimensional Poisson equation [26, 52]. Therefore, the capability of attaining a detailed description of the three-dimensional structure for the electrostatic field within the device is closely related to the possibility of solving Laplace equation with the assigned boundary conditions. More specifically, Dirichlet boundary conditions need to be established in correspondence of the IEC electrodes.

For the sake of simplicity, let a spherical design (i.e. an S-IEC device) be taken into account. If the problem domain D is thought to be the spherical space included within the outside spherical electrode (i.e. the anode), the domain boundary -on witch the boundary conditions are assigned- can be thought of as a set of curves, corresponding to the electrode grids G_k, defined in Eq. 5.6:

$$\partial D_{\text{b.c}} = \bigcup_{k}^{K} G_k \tag{5.6}$$

The corresponding Dirichlet problem for the Laplace equation has, subsequently, the form provided in Eq. 5.7:

$$\begin{cases} \nabla^2\phi = 0 & on\ D \equiv S^3 \\ \phi = \bar{\phi} & on\ \partial D_{\text{b.c}} \end{cases} \tag{5.7}$$

Where $\bar{\phi}$, is the assigned boundary value,

K, the total number of grid wires.

In correspondence of each point in an electrode wire, the electrostatic potential must match the voltage value assigned to the relative electrode by the external power source, hence on the bounded frontier of the three-dimensional sphere the following Dirichlet condition needs to be met, in order for the function $\phi(\vec{x})$ to represent the correct electrostatic potential:

$$\begin{cases} \phi = \phi_{anode} & on\ \ \partial D_{\text{b.c}}^{(a)} \\ \phi = \phi_{cathode} & on\ \partial D_{\text{b.c}}^{(c)} \end{cases} \tag{5.8}$$

Where the different boundaries are defined as:

$$\partial D_{\text{b.c}}^{(a)} = \bigcup_{l}^{L} G_l \tag{5.9}$$

$$\partial D_{\text{b.c}}^{(c)} = \bigcup_{m}^{M} G_m \tag{5.10}$$

Being L and M, the total number of anode and cathode grid wires, respectively.

In conclusion, the resulting mathematical model, portraying the electrostatic potential within a spherical IEC device, is:

$$\begin{cases} \nabla^2\phi = 0 & on\ D \\ \phi = \phi_{anode} & on\ \partial D_{\mathrm{b.c}}^{(a)} \\ \phi = \phi_{cathode} & on\ \partial D_{\mathrm{b.c}}^{(c)} \end{cases} \tag{5.11}$$

Many different approaches have been proposed, in literature, for the resolution of Laplace equation on complicated geometrical domains or for peculiar boundary conditions, as in the present case. In this respect, it is worth mentioning the research work performed on this topic at the Space Lab of the Massachusetts Institute of Technology in the 2000s. In his doctoral thesis, Dr. Thomas J. McGuire illustrated several different numerical methods employed for the resolution of the free space electrostatic potential in an S-IEC, both in two and three dimensions, including finite difference method and finite element method (FEM) [28]. In parallel, an analogous work was carried on by Dr. Carl Dietrich, who solved Eq. 5.11 by introducing a spherical harmonics expansion for the three-dimensional electrostatic potential [29].

5.2 Two-dimensional solution

¶ Analytic solution for 2D Laplace equation

In Appendix C, Section 2, ¶ Analyticity of harmonic functions, the intimate relation between Laplace equation and analytical functions on the complex field is detailed. For the scope of the present chapter, it suffices to recall that -due to the coincidence of the complex field $\mathbb{C}$ and the two-dimensional Euclidian space $\mathbb{R}^2$- the two-dimensional Lagrange equation can be transposed on Argand-Gauss plane and its solution found as the real part of a complex-valued harmonic function.

Given the rotational symmetry of Laplace operator ∇^2 (see Appendix C, Section 2, ¶ Harmonic function properties), the solution of Eq. 5.5 is intrinsically radial. Hence, adopting a polar reference frame (r, θ) seems the most sensible choice:

$$\begin{aligned} x &= r\cos\theta \\ y &= r\ \sin\theta \end{aligned} \tag{5.12}$$

Laplace equation is thus recast as:

$$\frac{1}{r}\frac{\partial}{\partial r}\left(r\frac{\partial\phi}{\partial r}\right) + \frac{1}{r^2}\frac{\partial^2\phi}{\partial\theta^2} = 0 \tag{5.13}$$

Recall Euler's equation for the complex number $z \in \mathbb{C}$,

$$r\ e^{i\theta} = r\ (\cos\theta + i\ \sin\theta) \tag{5.14}$$

It is then possible to transpose Eq. 5.13 on the complex field and to adopt the following general formula for the solution of such equation:

$$\phi = \Re\left\{A + B\ln z + \sum_m [\gamma_m(\alpha_m - i\beta_m)z^m + \delta_m(a_m + ib_m)z^{-m}]\right\} \tag{5.15}$$

Once the two-dimensional electrostatic potential has been assessed as solution of Eq. 5.15, the electrostatic field can subsequently be obtained by differentiating the scalar field ϕ with respect to the complex variable z:

$$\frac{\mathrm{d}\phi}{\mathrm{d}z} = -E_x + iE_y \tag{5.16}$$

In Ref. [28], McGuire provided the two-dimensional solution to Dirichlet problem for Laplace equation given in Eq. 5.15, for the case of a multigrid IEC device (see Appendix A, Section 2, ¶ Multi-

grid device), characterised by a number N of concentric electrode couples, this solution is written accordingly in the following form:

$$\phi(z) = \sum_{i=1}^{N} k_i \left[\ln(z^{n_i} + {r_i}^{n_i}) - \ln\left(z^{n_i} + \left(\frac{{r_\mathrm{a}}^2}{r_i} \right)^{n_i} \right) \right] \tag{5.17}$$

Where i, identifies each electrode grid,

r_i, is the radius of each cathode grid,

n_i, is the number of evenly spaced wires in each grid,

k_i, is the constant introducing the boundary value over each grid

r_a, is the radius of the anode grid.

In the potential solution given in Eq. 5.17, the contribution of each set of grids -in the investigated multigrid configuration- is introduced as a set of source terms, assigned at the location of the grid wires, and a set of reflection terms establishing a circular boundary condition at the anode. The required electrostatic potential is thus obtained as the superimposition of the single contributions, due to the several gridded electrodes considered. Finally, the desired boundary conditions (i.e. the externally assigned voltage over each electrode grid) are introduced by adopting an adequate value for the charge constant k_i of each set of grids. Nonetheless, it is remarkable that while a different value needs to be assessed for each charge constant, these are not independent quantities since each of them is dependent on the contributions of the remaining grids to the potential field: hence, it is possible to assign a square system of consistent equations for the evaluation of the charge constants k_i.

For the scope of the present thesis, only one couple of concentric electrodes needs to be considered, hence the required potential solution is obtained in the simplified form:

$$\phi(z) = k \left[\ln(z^n + {r_\mathrm{c}}^n) - \ln\left(z^n + \left(\frac{{r_\mathrm{a}}^2}{r_\mathrm{c}} \right)^n \right) \right] \tag{5.18}$$

Where r_c, is the cathode's radius,

r_a, is the anode's radius.

The constant factor k allows for the adjustment of the charge distribution at the cathode grid, in order to match the respectively assigned boundary conditions. Hence, this approach does not allow for a direct assignment of the applied voltage on the electrode grids, but rather requires to iteratively change the charge distribution constant in order to obtain the desired boundary potential. Moreover, it is worth noticing that the provided solution holds for a symmetric electrode configuration, i.e. for gridded electrodes where none enlarged opening is provided. Indeed, the mathematical form provided in Ref. [28] relies on the following property of complex number to model localised potential sources at equally spaced angular locations: a complex number may be taken to the power of another complex number and complex exponentiation satisfies Eq. 5.19.

$$(a + i\,b)^{(c+i\,d)} = (a^2 + b^2)^{(c+i\,d)/2} e^{i(c+i\,d)\,arg(a+i\,b)} \tag{5.19}$$

Hence, the complex function $f : \mathbb{C} \to \mathbb{C}$

$$f(z) = z^n - k \tag{5.20}$$

Where $k \in \mathbb{C}$ and $n \in \mathbb{N}$,

Is multi-valued on the complex plane, where it has exact roots equally spaced -in an azimuthal sense- on a circumference as shown in the two examples reported in Fig. 5.1

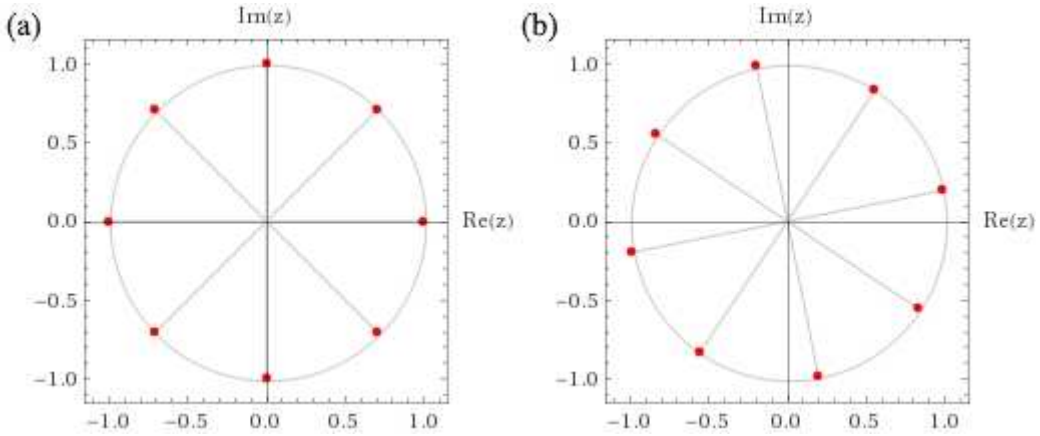

Figure 5.1 Roots of function $f(z) = z^n - k$ on the complex plane
(a) $n = 8, k = 1$
(b) $n = 8, k = i$

Therefore, a set of charges -introduced as electrostatic potential sources- is imposed in correspondence of the electrode wire locations, i.e. equally space over the circumference, corresponding to the grid radius.

Nonetheless, it is possible to find the solution for non-equally spaced electrode grids, by further manipulating the general solution form given in Eq. 5.17. This task requires the assignment of pointwise sources in correspondence of each grid wire, whose location $(x, y)_j$ -with $j = 1, \dots, G$- is given according to:

$$z_j = x_j + iy_j = r_g \, e^{i\theta_j} \quad \forall j = 1, \dots, G \tag{5.21}$$

Where M, is the total number of conductive wires in each electrode grid.

Hence, the electrostatic potential for an asymmetric IEC device can be assessed by means of a mathematical formulation, developed along the same line of reasoning that lead to Eq. 5.18, where the single contribution of each conductive wire is introduced at its relative location, according to Eq. 5.21. The required electrostatic potential is, thus, computed as in Eq. 5.22.

$$\phi(z) = k \sum_{j=1}^{G} \left[\ln\left(z + r_g \, e^{i\theta_j}\right) - \ln\left(z + \frac{{r_a}^2 e^{i2\theta_j}}{r_g}\right) \right] \tag{5.22}$$

In conclusion, the use of Eq. 5.18 and 5.22 allows the assessment of the two-dimensional electrostatic field inside an IEC device, given a symmetric or asymmetric configuration, respectively. This model is quite powerful and provides useful field data for assessing both the dynamics of individual ions and modelling the beam envelope, for the discharge plasma inside the device [28]. It is important to underline that the two-dimensional representation of the electrostatic field is most suitable for a cylindrical design, whose potential is correctly represented by the given solution, as long as the device's finite longitudinal extent is negligible. Nevertheless, the given solution can be adopted, to a first approximation, for spherical devices: some remarkable result for the simulation of the S-IEC device, available in the test facility at IRS (see Chapter 2, Section 4), will be presented in the next subsection.

¶ 2D simulation results

Finally, it is worth to report an example of the free-space electrostatic potential simulation for the spherical IEC device, tested at the Institut für Raumfahrtsysteme test facility in Vaihingen, Stuttgart. A detailed description of the main geometrical features of this device was provided in Chapter 2, so for the scope of the present section, the referring to Table 5.1 will suffice.

Table 5.1 Simulation input values

Cathode radius	r_c	[mm]	25
Anode radius	r_a	[mm]	75
Cathode voltage	V_c	[kV]	-1
Anode voltage	V_a	[kV]	0

In the following, two distinct simulations will be presented, referring to different gridded electrode configurations:

- Symmetric configuration, the electrode wires are assumed to be equally spaced in an azimuthal sense;
- Asymmetric configuration, the electrode wires are equally spaced except for an enlarged opening between two of them.

For each one of these simulations, suitable visual outputs are provided, illustrating the most relevant features of the investigated free-space electrostatic field inside the IEC device.

Symmetric configuration

In the simulated symmetric configuration, the angular gap between two adjacent wires is simply given by a turn (i.e. 360°), divided by the number of grid wires: in the present case, each grid is made of eight longitudinal grid wires (see Fig. 5.2) so that the resulting spacing is 45°.

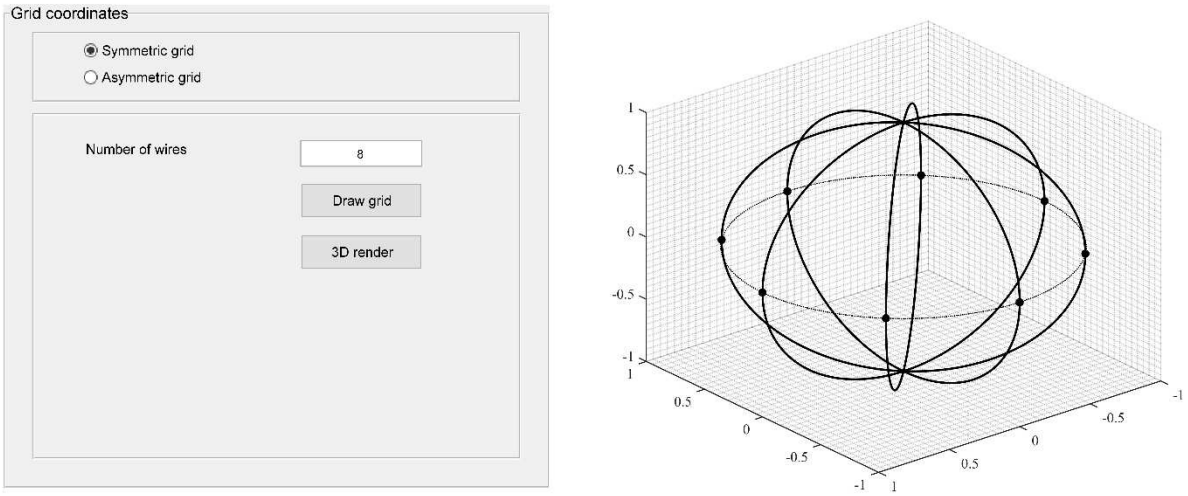

Figure 5.2 3D visualisation of the symmetric configuration for an electrode grid, in the Matlab simulation script. Note that the grid dimensions are not to scale

Given the electrode voltage values (Tab. 5.1), assigned to each electrode grid by means of the external power supply, it is possible to use Eq. 5.18 to compute the electrostatic potential on a discrete mesh grid over the plane volume enclosed inside the anode grid. As already remarked, it is not possible to directly assign the boundary condition to the obtained solution of Laplace equation. In order to overcome this issue, an iterative procedure is adopted: a first guess value is assigned for the charge constant k and the electrostatic potential is computed accordingly, the potential value in correspondence of the grid wires is then confronted with the required value in Tab. 5.1. By adjusting the k-value, so to adequately match the assigned boundary conditions, the required electrostatic potential is finally obtained, via numerical computation. The above presented algorithm was implemented in a Matlab script and several visual output were produced, able to provide an intuitive comprehension of the most relevant characteristics of the investigated physical quantities.

In Fig. 5.3, a tree-dimensional surface representation of the electrostatic potential inside the IEC device is presented, along with a contour line visualisation: it is possible to notice the high degree of

symmetry in the obtained solution, reflecting the symmetrical configuration assumed for the gridded electrodes. Moreover, this result can be compared to the one given in Ref. [29], and reported in Fig. 4.1 of the present thesis, C. Dietrich employed a spherical harmonic expansion to assess the three-dimensional electrostatic potential in a multigrid IEC device; nonetheless, that result is qualitatively comparable to the one reported in the present chapter.

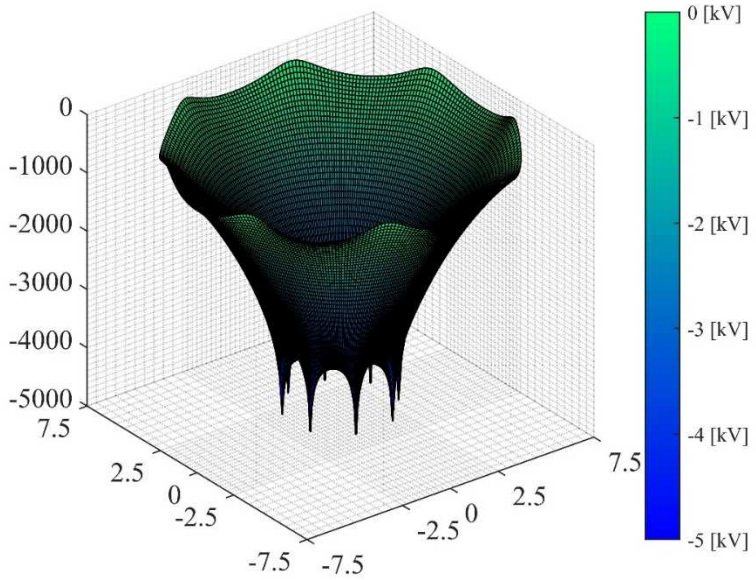

Figure 5.3 Surface representation of the two-dimensional, free-space electrostatic potential distribution inside a symmetric IEC device.

The contour line plot shown in Fig. 5.3 is better appreciated in Fig. 5.4, where it is accompanied by a visual representation of the electrostatic field lines by means of arrows: these lines, point along the positive flux direction of the electric field and their dimension is related to the local strength of the field itself. The detail shown in Fig. 5.4 clearly illustrates how the field intensity is greater in proximity of the grid wires: this reflects the common understanding that the electrostatic field is stronger in correspondence of steeper variations of the electrostatic potential. Moreover, according to the definition in Eq. 5.4, the electric field is the vector obtained as gradient of the scalar potential field. Hence, the electric field flux lines are orthogonal to the contour lines for the electrostatic potential: this reflects in the orientation of the field arrows in Fig. 5.4, which tend to cross the contour lines at right angles.

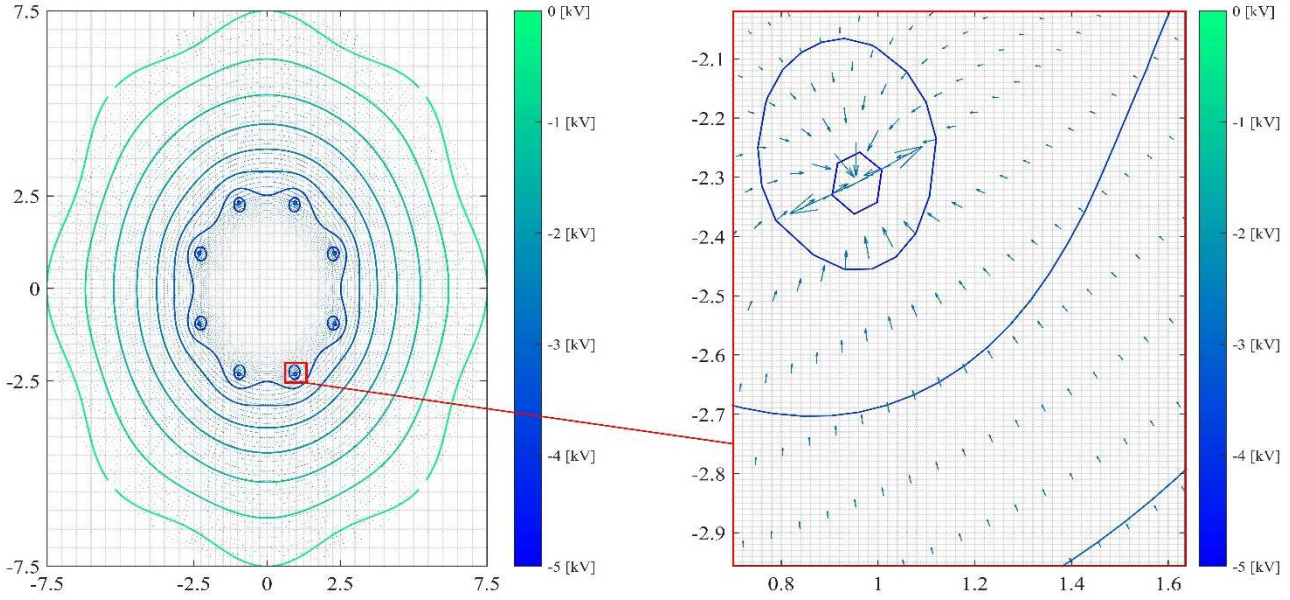

Figure 5.4 Contour line plot of the electrostatic potential inside the symmetric IEC device together with an arrow

visualisation of the electrostatic field. The righ-hand side picture is the detail of the figure enclosed in the red box.

Asymmetric configuration

The asymmetric grid configuration is modelled introducing greater angular gap between two of the grid wires: again, the common spacing is 45°, except for the fact an enlarged opening is introduced by increasing one gap and reducing the two adjacent, as shown in the three-dimensional rendering in Fig. 5.5. In the following example, the simulated device is characterised by eight wires and an enhanced angular gap of 75°.

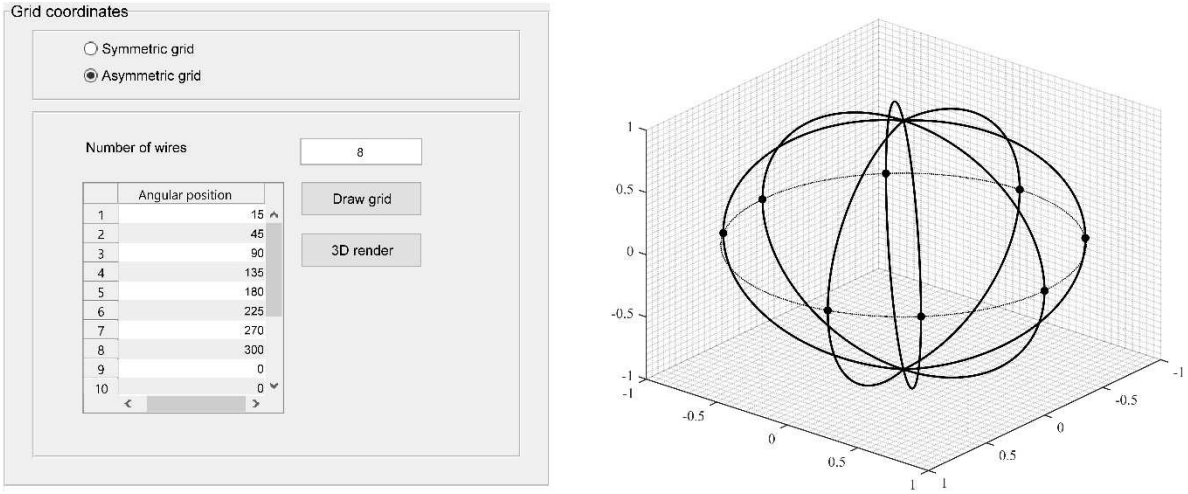

Figure 5.5 3D visualisation of the asymmetric configuration for an electrode grid, in the Matlab simulation script. Note that the grid dimensions are not to scale

In Fig. 5.6, a tree-dimensional surface representation analogous to that presented in Fig. 5.3 is given: it is possible to notice that in the present case the symmetry of the previous simulation is broken in correspondence of the enlarged grid hole. There, the potential surface is strained and the correspondent electrostatic field is twisted. This behaviour is better understood by looking at the contour lines plotted in Fig. 5.7.

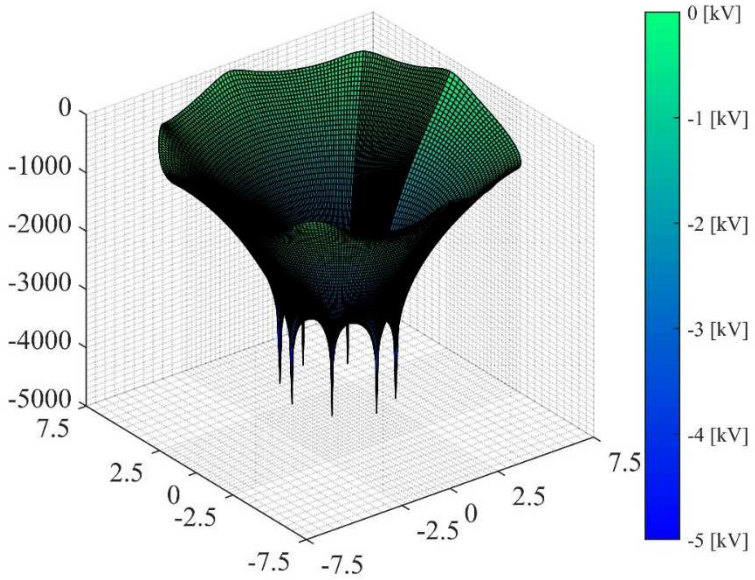

Figure 5.6 Surface representation of the two-dimensional, free-space electrostatic potential distribution inside an asymmetric IEC device.

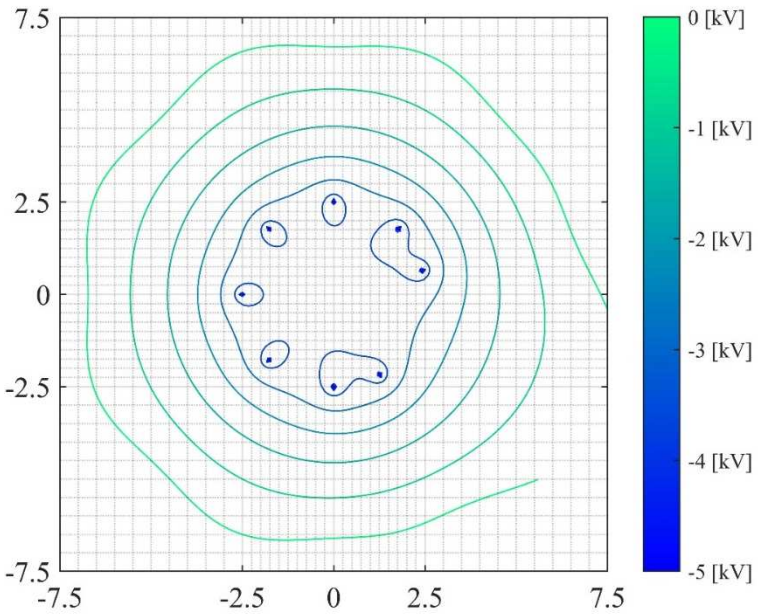

Figure 5.7 Contour line plot of the electrostatic potential inside the IEC device, for an asymmetric grid configuration.

This local distortion of the electrostatic field, in correspondence of the enlarged grid opening, intuitively proves the electron escape mechanism mentioned at the beginning of the present chapter. Since in correspondence of the enlarged spacing between the grid wires the electrostatic potential is reduced -in terms of its absolute value-, a potential gradient ensues. Hence, the topography of the electrostatic field produced by the gridded electrodes is locally distorted and the repulsive electrostatic interaction, confining the electrons, is thus reduced. Once the discharge plasma is generated inside the device, this behaviour, in conjunction with gas dynamics and plasma dynamics effects (neglected in the present discussion), might determine the electron beam extraction.

5.3 Three-dimensional solution

¶ Numerical solution for 3D Laplace equation

The previous subsection was focused on the resolution of Laplace equation for the free-space electrostatic potential engendered inside an IEC device: as already mentioned, the two-dimensional solution, determined by means of complex analysis, is most suitable for the simulation of C-IEC devices. While, to a first approximation, the reported results might be assumed to apply to an S-IEC, the actual spherical electrode configuration entails a significant difference in the free-space potential topography, which should not be neglected if an accurate investigation is required. Thus, the boundary condition problem given in Eq. 5.11 should be solved over a three-dimensional space, so to properly take into account the actual geometry of the simulated device.

To this purpose, the IEC device available at the *IRS* test facility is considered: in particular, reference is made to the C2a grid configuration, introduced in Chapter 2, Section 4 of the present essay.

Table 5.2 K3a grid parameters

		Anode	Cathode
Grid diameter Φ	[mm]	150	50
Opening diameter ϕ	[mm]	73	23
Hole-center displacement d	[mm]	65	23
Hole angular width β	[°]	58.64	53.14

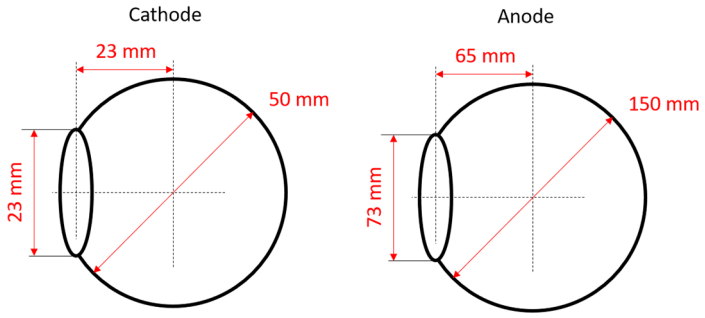

Figure 5.8 Technical drawing for the cathode and anode grid of the IEC device at IRS test facility

The first step for the simulation of the three-dimensional free-space potential is the definition of an adequate reference frame over $\mathbb{R}^3$: given the spherical symmetry of the electrode configuration at hand, the most sensible choice is the spherical coordinate system in Eq. 5.23.

$$\begin{cases} r = \sqrt{x^2 + y^2 + z^2} \\ \theta = \cos^{-1}\dfrac{z}{\sqrt{x^2 + y^2 + z^2}} = \cos^{-1}\dfrac{z}{r} \\ \varphi = \tan^{-1}\dfrac{y}{x} \end{cases} \tag{5.23}$$

Where r, is the radial position, $r \in [0, +\infty[$

θ, is commonly referred to as "inclination", "polar angle" or "latitude", $\theta \in [0, \pi]$

φ, is the "azimuth", "azimuthal angle" or "longitude", $\varphi \in [0, 2\pi]$

Such a reference frame has been defined by adopting the convention most commonly employed in physics[25] (Fig. 5.9a). However, since the most intuitive representation of an IEC device demands the enlarged hole to be aligned with the y-axis of the Cartesian reference frame in Fig. 5.9 -so to have a horizontal plasma beam in jet-mode operating condition- a different representation might be useful in the earlier stages of the grid geometry definition. Indeed, mathematicians often refer to the θ angle as azimuth while φ is defined as the inclination angle (see Fig. 5.9b) By adopting such a convention, the IEC spherical grids result to have eight azimuthal wires and six latitudinal wires.

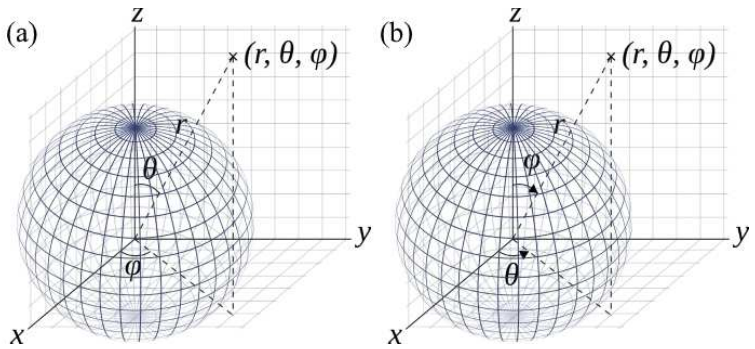

[25] As specified by ISO standard 80000-2:2009.

Figure 5.9 Spherical coordinate system: (a) ISO convention, (b) Alternative convention

Hence, the ring wire representing the enlarged opening is simply represented by an additional latitudinal wire whose inclination φ can be easily determined, by means of simple trigonometrical relations, once the grid diameter and the space gap between the opening and the device's centre are known (Tab. 5.2):

$$\varphi = 180° - \frac{1}{2}\tan^{-1}\left(\frac{\phi}{2d}\right) = 180° - \frac{1}{2}\beta \tag{5.24}$$

Finally, the most intuitive representation of the S-IEC geometry can be retrieved by means of a 90° rotation of the grids about the x-axis, so as to have a final configuration with the y-axis passing through the opening centre-point.

The present section aims at illustrating an alternative numerical model for the resolution of Laplace equation, for the electrostatic potential in an IEC device -however complex the electrodes geometry might be-, basing on the concept of fundamental solution for a PDE. Appendix C of the present thesis is devoted to the detailed description of the mathematical frame of Laplace equation and its basic properties and Section 3, in particular, provides a proper insight of the mathematical theory of fundamental solutions. Therefore, in the following, only a brief introduction of the topic is given, along with the basic definitions, the reader is referred to the above-mentioned appendix for a more rigorous dissertation.

According to [73], given a partial differential equation, with smooth coefficients (i.e. functions of class C^∞), in the form:

$$Lf(\vec{x}) = 0 \quad \vec{x} \in \mathbb{R}^n \tag{5.25}$$

where $L(f)$, is the differential operator defining the partial differential equation, the fundamental solution can be defined as the solution of the PDE interpreted in the sense of the theory of generalised functions, i.e. the function $F(\vec{x},\vec{y})$ that satisfies, for $\vec{y}$ fixed in $\mathbb{R}^n$, Eq. 5.26:

$$LF(\vec{x},\vec{y}) = \delta(\vec{x}-\vec{y}) \quad \vec{x} \neq \vec{y} \tag{5.26}$$

Where $\delta(\vec{x}-\vec{y})$, is Dirac's delta-function.

A fundamental solution satisfying the given definition can be determined for any partial differential equation with constant coefficients, and for an arbitrary elliptic differential operator. In particular, for Laplace operator the following definition of the fundamental solution holds [74]:

$$\Phi(\vec{x}) = \begin{cases} -\frac{1}{2\pi}\log|x-x'| & (n=2) \\ \frac{1}{n(n-2)V\left(\mathcal{B}(x,x')\right)}\frac{1}{|x-x'|^{n-2}} & (n \geq 3) \end{cases} \qquad \vec{x} \in \mathbb{R}^n, \vec{x} \neq \vec{0} \tag{5.27}$$

Where $\alpha(n)$ denotes the volume of the unit ball in $\mathbb{R}^n$, in particular in the three-dimensional Euclidian space $\alpha = 4\pi/3$.

The concept of fundamental solution is the reformulation, in the modern language of distribution theory, of the precedent idea of Green function, which normally further addresses boundary conditions [74]. Indeed, given a boundary value problem for a linear differential equation, its Green function can be defined as the fundamental solution for such a differential equation, satisfying homogeneous boundary conditions. Hence, the Green function can be thought of as the kernel of the integral operator, inverse to the differential operator, generated by the given differential equation along with the homogenous boundary conditions [73]. Despite it formally being an abuse of notation, the expression "Green function" will be adopted, throughout the following text, referring to the fundamental solution of Laplace operator, neglecting the fact that the boundary conditions in Eq. 5.11 are non-homogenous.

In particular, considering Laplace equation for the electrostatic potential, induced by a point-charge located at $\vec{r'}$ in the spherical reference system defined by Eq. 5.23, referring to the form given in Eq. 5.27 for the fundamental solution of the three-dimensional Laplace operator, the electrostatic potential at a generic $\vec{r}$ location in the spherical domain D results:

$$\phi = \frac{1}{\left\|\vec{r} - \vec{r'}\right\|}\frac{q}{4\pi} \quad \vec{r} \in D, \vec{r} \neq \vec{r'} \tag{5.28}$$

The Green function can thus be thought of as the effect of a point-charge q at a given location $\vec{r'}$ in the three-dimensional space, over a different generic location $\vec{r}$: as it is well known, the stationary charge will induce an electrostatic field over the surrounding space, whose potential function has the form given in Eq. 5.28.

The use of Green function allows, then, the recasting of the original differential Lagrange problem in Eq. 5.11 in an algebraic form by choosing the functional space over which the solution is to be assessed. The electrostatic potential described by such an equation is then a function in the form given in Eq. 5.28: the only unknown is the charge constant q that has to be determined for each point in the electrode wires.

¶ 3D solver algorithm

The numerical resolution for the differential problem of assessing the three-dimensional layout for the electrostatic potential engendered in an IEC device, when operating in perfect vacuum, is based on two different approximations.

First of all, the tree-dimensional volume inside the device needs to be discretised by introducing a structured grid; this can be defined as a regular tessellation of the tree-dimensional Euclidian space by means of cuboids. The curvilinear grid is then suitably defined by assigning a proper discrete step for the coordinate variables:

- Δr, radial spacing
- $\Delta\theta$, latitudinal spacing
- $\Delta\varphi$, longitudinal spacing

Each vertex in the resulting spherical grid can thus be addressed by introducing the integer indexes (i, j, k), the vertexes will then have coordinates: $(i \cdot \Delta r, j \cdot \Delta\theta, k \cdot \Delta\varphi)$. It is worth noting that the discrete steps employed in the grid definition are not required to be constant over the entire volume that needs to be discretised: this allows for the definition of adaptive grids, i.e. grids whose spacing is tighter where the potential gradient is most steep.

The employment of adaptive grids has a dual beneficial effect, allowing a more accurate numerical solution where the solution is expected to be most varying and, at the same time, saving computational resources by avoiding the repetition of the calculation where the solution is almost constant. Once the computational grid has been defined, it is critical to give a pointwise definition of the device's electrodes. While one might think of defining the discrete grid in such a manner that the electrodes are naturally included in it -having two of the discrete radial locations coinciding with the gridded electrodes radii- this would result in a singular calculation of the Green function at that very location. In fact, it is easily checked in Eq. 5.28 that if a point in the computational grid, i.e. the discrete grid where the electrostatic potential is to be valued, does coincide with whichever point in the electrode grids, the vector difference in Green function's denominator is identically zero and the solution is locally singular. Hence, a great attention needs to be paid when defining both the computational and the electrode grids.

Secondly, due to the cancellation issue just mentioned, the pointwise charge distribution cannot be assessed at the exact electrode location: since the computation is performed by assuming the applied

voltage value at the gridded electrodes, the charge distribution valued at the same location would be identically null. The solution consists, then, in assuming the charge distribution to be just a small distance away from the actual electrode grids' location and, once it has been computed, to assign such a distribution to the exact electrode's location. This can be visualized by defining a couple of electrodes, which in the following will be referred to as "shadow electrodes", located close to the real ones: while the boundary condition is correctly imposed on the physical electrodes, the charged distribution is assumed on the shadow electrodes. The approximation, intrinsic to the proposed computational model, hence lies in the collapsing of the shadow electrodes on the physical ones when the assessed charged distribution is employed for the computation of the electrostatic potential inside the device. The choice of the proper value to be assigned to the gap between the physical and shadow electrodes is thus a trade-off between the mathematical model's accuracy and the numerical solution's resolution. Indeed, while a negligible value for the gap would imply a small approximation, well within the actual conductive wire dimension, this may result in a largely distorted numerical solution when implemented and solved in a computer software.

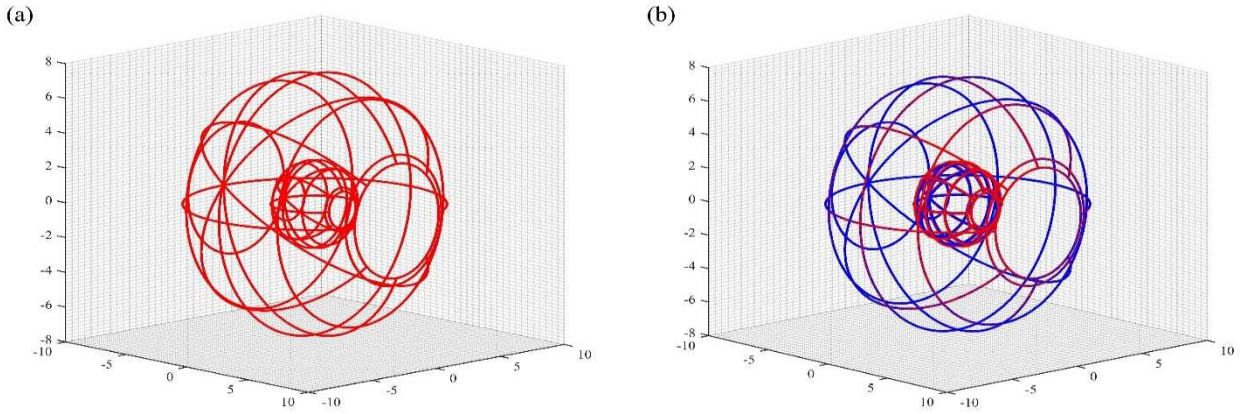

Figure 5.10 Three-dimensional rendering of the gridded electrodes for the *IRS*-IEC device, as described by the Matlab simulation script:
(a) Voxel imaging of the IEC electrodes;
(b) Three-dimensional representation of the device electrodes (red lines) and the shadow electrodes (blue lines) employed for the electrostatic potential computation.

As pointed out by Professor Ray Sedwick, from University of Maryland, such a numerical model for the resolution of Laplace equation on a complex-bordered domain is conceptually straightforward, despite being numerically intensive [75].

Once the mathematical model has been disclosed, the following computational algorithm can be outlined, which allows for the computation of the three-dimensional electrostatic potential in an IEC device, whichever the electrode's geometry:

7. The input values for the calculation are provided
   - Electrodes' voltage: typically, the anode is assumed to be grounded ($V_a = 0$) so that only cathode voltage (V_c) is required
   - IEC geometry: the number of input parameters required to assess the device geometry depends on the complexity of the geometry itself. For a quite simple symmetric S-IEC only the number of parallel and longitudinal wires in the gridded electrodes is required. On the contrary, if a much more accurate depiction of the tree-dimensional electrostatic potential is desired, each and every electrode's wire needs to be defined in the spherical reference frame given in Eq. 5.23.
8. The spacing for the gridded electrodes' definition is provided as an input value, along with the distance of the shadow electrodes. The electrode grids are thus defined pointwise and each discrete

location on the electrodes can be saved as vector data, e.g. a three-field structure vector can be employed to save the three spherical coordinates of each point.

9. The spacing for the computation grid are then provided as input values: a structured grid is thus defined for the IEC inner volume. By assuming a non-constant spacing, an adaptive computational grid can be obtained. Again, a vector variable can be employed to save the grid vertexes coordinates.
10. If the electrode grid locations and their respective shadow electrode locations have been saved in two different vectors of N elements each (e.g. the vector variables $\{r_{electrode}\}$ and $\{r_{shadow}\}$), Green function can be computed between two generic location in the physical and shadow electrodes and its computed value saved in a $N \times N$ elements' matrix $[A]$

$$A_{ij} = \frac{1}{4\pi} \frac{1}{\left\| \vec{r}_{electrode,i} - \vec{r}_{shadow,j} \right\|} \; for \; 1 \leq i,j \leq N \tag{5.29}$$

11. The charge distribution can thus be assessed over the shadow electrode's locations, by solving the following linear algebraic equation, in matrix form:

$$[A]\{q\} = \{V\} \tag{5.30}$$

Where $\{q\}$, is the N-elements vector for the computed charge values

$\{V\}$, is the N-elements vector for the boundary conditions, i.e. the electrostatic potential at the electrode locations.

12. Once the charge distribution $\{q\}$ has been determined over the shadow electrode locations, its values are assigned to the respective physical electrode locations and the Green function is computed again between each point in the electrode grid and the computation grid, the resulting values are saved in a new matrix $[A']$

$$A'_{ij} = \frac{1}{4\pi} \frac{1}{\left\| \vec{r}_{grid,i} - \vec{r}_{electrode,j} \right\|} \; for \; \begin{matrix} 1 \leq i \leq M \\ 1 \leq j \leq N \end{matrix} \tag{5.31}$$

13. Finally, the electrostatic potential can be attained for every discrete location in the computation grid by the following:

$$\{\phi\} = [A']\{q\} \tag{5.32}$$

For details about the software implementation of this algorithm the reader is referred to [43], for the purpose of the present essay, it will suffice to present some relevant output provided by the simulation of the IEC device (Tab. 5.2).

¶ 3D simulation results

In conclusion, it is appropriate to disclose the output provided by this simulation tool: hence, an example is provided, regarding the simulation of the IEC device available in the IRS test facility. The numerical simulation of the resulting electrostatic potential's layout has been carried out by means of the computing tool, assuming the simulation input values found in Tab. 5.1.

First of all, it is possible to compare the electrostatic potential in correspondence of the equatorial plane (see object "b" in Fig. 5.13) of the simulated IEC device -as computed by means of the simulation tool described above- with the two-dimensional solution provided by complex analysis. A visual representation of such potential is given in the form of a three-dimensional surface, analogous to the results shown in Fig. 5.3 and Fig. 5.6. The comparison of the different results provided by the two simulation tools allows, on one hand, to validate the three-dimensional algorithm depicted in the previous subsection and, on the other, to appreciate the higher accuracy of the results provided by the three-dimensional analysis. Moreover, the Green function approach to the numerical resolution of Eq. 5.11 shows a higher capability to assess the electrostatic field's topography, taking into account the detailed

geometry of the device's electrodes and, at the same time, has a greater adaptability to different electrode configurations (such as cylindrical, helicoidal, *etc.*).

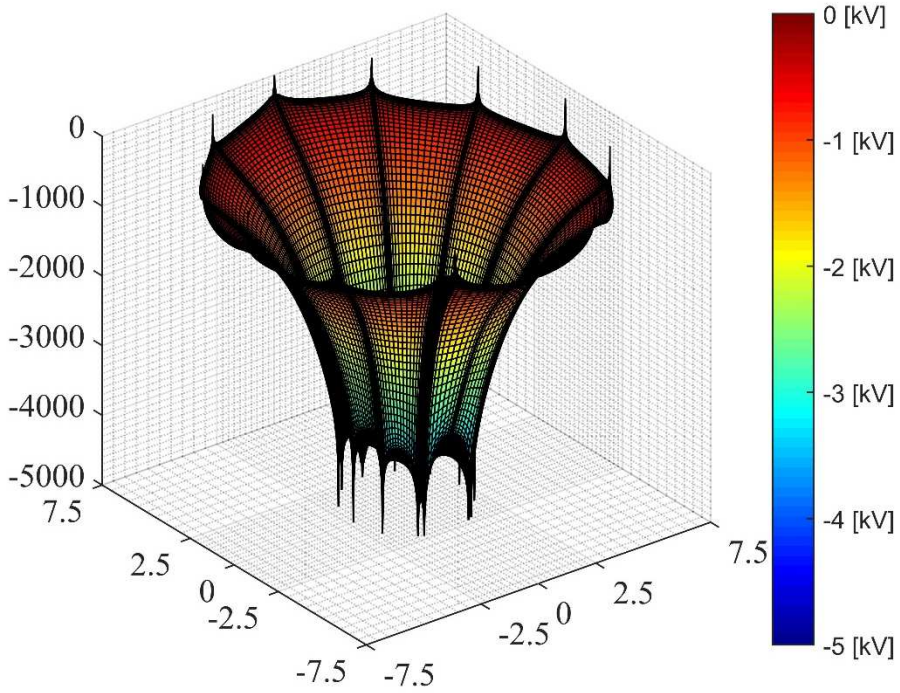

Figure 5.11 Surface representation of the three-dimensional, free-space electrostatic potential distribution inside the IRS-IEC device.

In Fig. 5.13, 5.14 and 5.15, many different visual outputs are provided, representing the simulation tool's ability to detail the geometric outline of the electrostatic potential distribution, i.e. the topography of the electrostatic field. More specifically, the reported figures all refer to the potential distribution on two different sectional planes:

(a) Meridian plane identified by an azimuthal angle of 22.5°

(b) Meridian plane identified by a null azimuth
Due to the most commonly employed visualization of an S-IEC -having the longitudinal axis, i.e. the one passing through both the IEC and opening centres, horizontally aligned- it is intuitive to refer to such a plane as "equatorial plane".

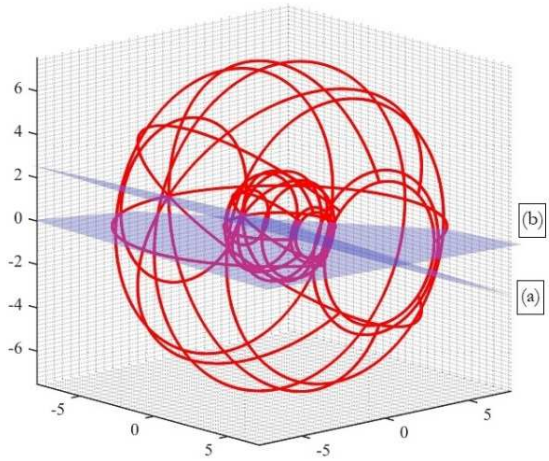

Figure 5.12 3D IEC rendering and sectional planes: (a) 22.5° inclined on the equator line, (b) equatorial

The main difference in the two resulting distribution concerns the fact that, while in case (a) the sectional plane intersect each and every latitudinal plane at different punctual locations, the equatorial section plane only intersects one latitudinal meridian plane, namely the one having a zero azimuthal coordinate. Hence, it is possible to observe, both in the surface representation and in the three-dimensional contour plot (Fig. 5.13 and 5.14 respectively), that the boundary conditions, i.e. the voltage value applied to the electrodes, are met point-wise at the local intersection between the inclined sectional plane and the electrode wires. The electrostatic potential distribution on the equatorial plane, on the other hand, shows a continuous tendency in correspondence of the electrodes' location.

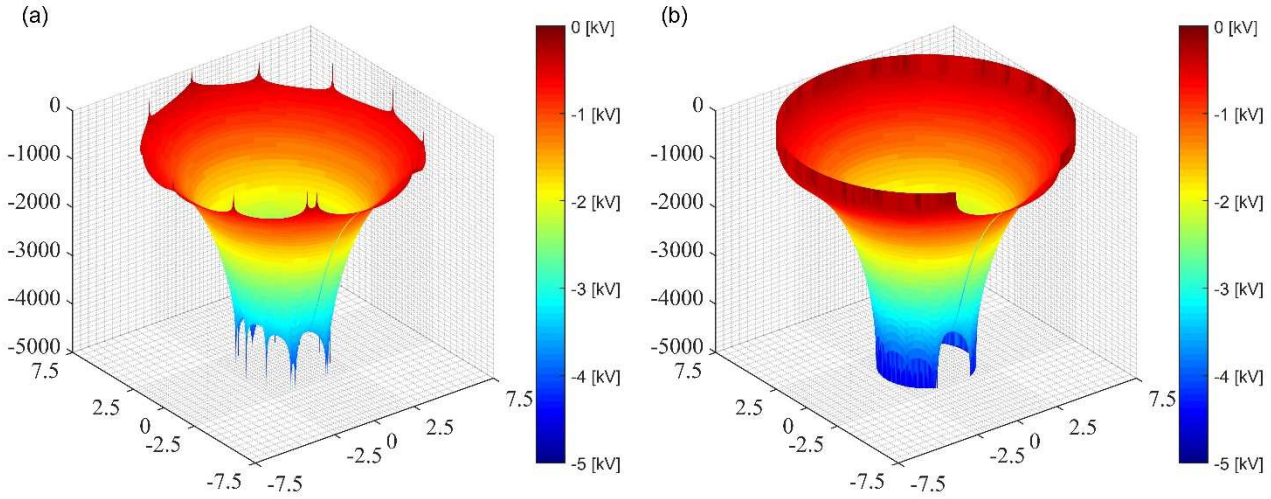

Figure 5.13 3D surface representation of the free-space electrostatic potential distribution on the two defferent sectional planes: (a) 22.5° inclined on the equator line, (b) equatorial

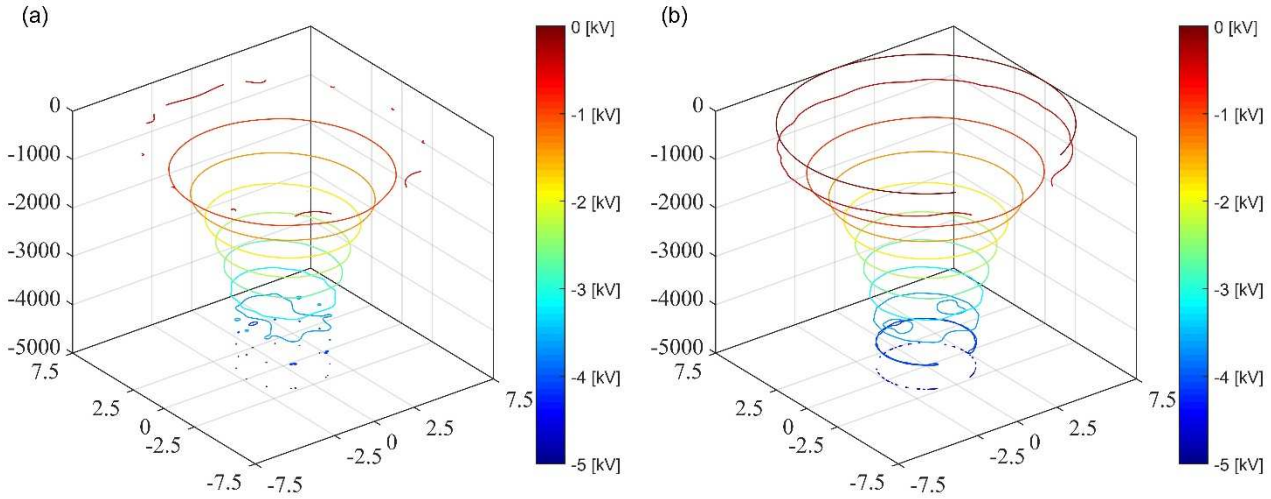

Figure 5.14 3D contour plot of the free-space electrostatic potential distribution on the two defferent sectional planes: (a) 22.5° inclined on the equator line, (b) equatorial

Another detail worth stressing out is that, in correspondence of the enlarged grid openings, the electrostatic field is locally deformed so that a perfect axial symmetry (with respect to the Cartesian z-axis) is not given and the potential surface in Fig. 5.14 is distorted both on the equatorial and the inclined sectional plane. This behaviour is particularly evident on the contour plot presented in Fig. 5.15, where it is possible to observe the local warp in the equipotential lines, especially inside the cathode grid.

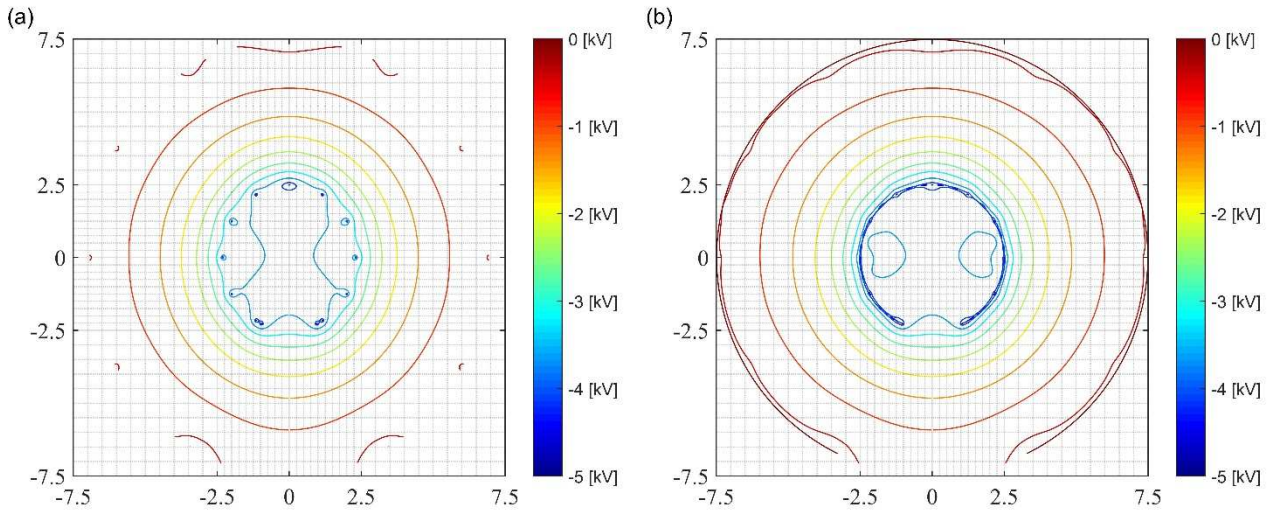

Figure 5.15 2D contour plot of the free-space electrostatic potential distribution on the two defferent sectional planes: (a) 22.5° inclined on the equator line, (b) equatorial

The electrostatic potential distribution, in correspondence of the inclined sectional plane (a) in Fig. 5.12 can be further detailed by representing its radial profile, i.e. the electrostatic potential along the radial direction, from the S-IEC device centre up to the anode grid radius. In Fig. 5.16, such a representation is provided, for the radial potential trend along three different directions on the Cartesian *x-y* plane:

a. The S-IEC longitudinal axis, i.e. the radial direction passing through both the device's centre and the enlarged grid's opening. No intersection is thus given between such an axis and the electrode's wires.

b. A half-line originating from the device's centre and passing through a regular grid hole. As in the case above, this line does not intercept any grid wire.

c. A half-line originating from the device's centre and intercepting a latitudinal wire both at the cathode's and anode's radial location.

Fig. 5.16 also provides a normalised plot, which allows for the comparison of the electrostatic potential trends along the above-mentioned radial directions. Here, the electrostatic potential is normalised with respect to the cathode's voltage and the difference between the resulting value and the unity is plotted against the radial location.

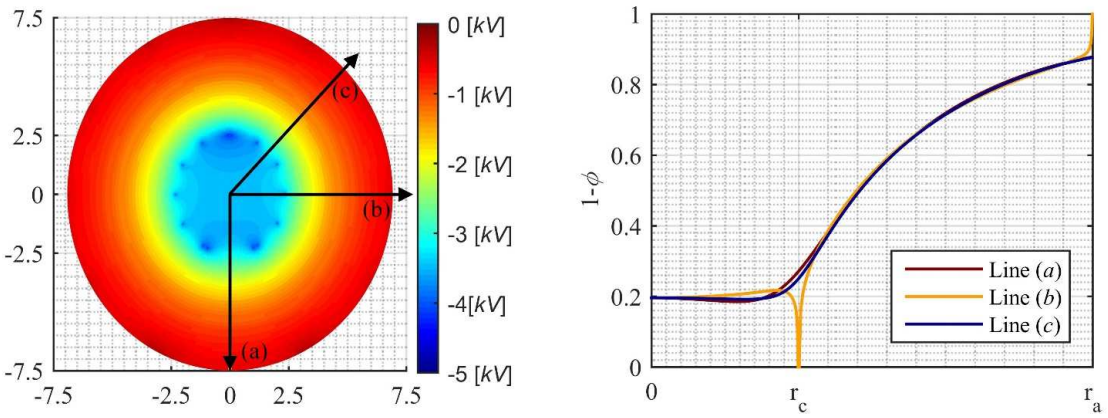

Figure 5.16 Comparison in the radial profile for the electrostatic potential along three different direction in the device's equatorial plane

It is worth noting that the potential trends along the (b) and (c) directions match almost perfectly in the vast majority of the radial span. A wildly different behaviour is only shown in proximity of the

electrode grids where the (b)-axis passes through a regular grid hole, thus showing a continuous trend at the electrode location, while the (c)-axis intercepts the grid wires and has an abrupt change in order to adapt to the local boundary condition. As far as the electrostatic potential along the radial axis is concerned, on the other hand, its tendency qualitatively resembles the (b) case; however, it assumes different values due to the local distortion of the electrostatic field determined by the local grid discontinuity represented by the enlarged opening.

The most relevant advantage of the presented three-dimensional free-space solver is the extreme versatility as it can adapt to the description of any electrode configuration. The results presented in this dissertation are referred to the spherical device investigated at IRS, but a proper definition of the electrode geometry would allow for the simulation of different IEC devices characterised by different geometries (e.g. gridded C-IEC, helicoidal electrode IEC, *etc.*). In addition, its being theoretically straightforward represents a computational advantage as the numerical solver shows little, if none, convergence issues; the only relevant issue is the possible numerical cancellation error and ill-conditioned computational matrix when the point-wise charges are located too closely to the boundary of Laplace equation. On the other hand, as already stressed out, this approach entails a considerably high computational cost that might hinder its coupling with other simulation tools. In this respect the further development of an auxiliary routine, devoted to the definition of an adaptive grid, is recommended: this solution would provide a two-fold benefit as it could greatly reduce the computational time and determine the most suitable charge distribution on the grid wires, avoiding by default those configuration that would result in an ill-conditioned problem.

In the literature, a semi-analytical model can be found, developed by Dr. C. Dietrich, employing a truncated spherical harmonic expansion of the three-dimensional electrostatic potential. With respect to such a model, however, the numerical approach adopted here has the remarkable advantage of being far more straightforward, from a theoretical point of view [75]. In addition, the semi-analytical model has some limitations due to the need of truncating the series expansion, for computational purpose, and the assumption of a uniform charge distribution along the conductive wires of the electrode grids. The Green's function approach, on the contrary, determines the point-wise charge distribution in the grid wires in accordance with the given boundary condition, i.e. the applied electrode voltage. As far as alternative numerical schemes, such as finite difference and finite element methods, no benchmark data is available for the comparison. However, it is sensible to assume that the use of FEM would probably present the advantage of a better grid definition, thus reducing the computational effort, along with proven possibility coupling with further numerical simulation tools, such as a Particle-In-Cell solver. Nevertheless, the development of an independent numerical algorithm allowed for saving both money and time, as there was no need of acquiring a proprietary software for the electromagnetic FEM simulation nor the typical long time and solid experience required by the definition of a proper, reliable grid.

Chapter 6
Plasma solution in the SDL model for IEC

6.1 Plasma solution in Langmuir DL model for the IRS-IEC

¶ Plasma solution in the outer double layer region $r \geq r_{DL}$

The double sheath model depicted in the fourth chapter of the present dissertation allows for the mathematical description of the local structure of the spherical double layer that is theorised to ensue in the core plasma inside the cathode grid of an IEC device. As this description allowed for the rejection of a family of solutions for the Langmuir spherical DL, the next step is to characterise the embedding discharge plasma in correspondence of the only admissible set of double layer solutions.

The following characterisation of the discharge plasma, produced and confined in an IEC device, refers to the two-fluid plasma description, focusing on the volume embedded inside the cathode grid. On the back of experimental observations and numerical simulations, confirming the presence of a virtual anode inside the cathode grid, the solution in the inter-electrodes region is expected to be less relevant in the assessment of plasma properties according to the double layer model for an IEC device. In order to achieve a preliminary characterisation of the plasma surrounding the double layer structure in the core of the device, it is convenient to define two distinct regions in the investigated discharge itself:

- Outer double layer region
  In the context of the present chapter, the "outer region" identifies the portion of the volume, inside the cathode grid, surrounding the simulated spherical double layer.
- Inner double layer region
  On the contrary, the expression "inner region" will be used, in the following, referring to the space enveloped by the spherical double layer.

In Fig. 6.1 the schematic of the ion and electron fluxes on the high and low potential side of the spherical double layer is given.

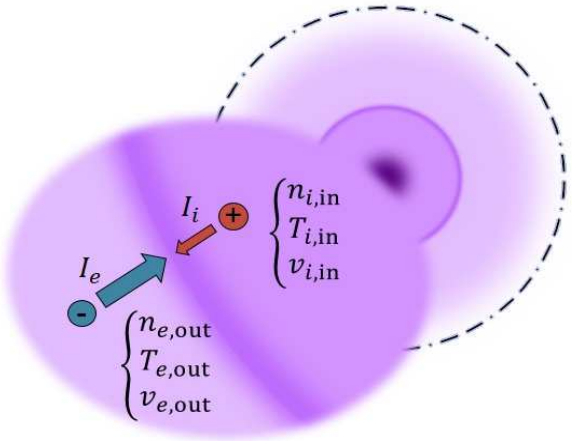

Figure 6.1 Schematic of the plasma properties analysis in the inner and outer double layer regions.

As far as the plasma in the outer region is concerned, only the electron population will be accounted for, since the total mechanical energy of the electrons can be directly linked to the topology of the electrostatic field inside the cathode grid, according to Eq. 6.1. In this respect, it is important to stress out that a significant simplification was made here, as the free-space potential -as computed according to

the three-dimensional numerical algorithm presented in Chapter 5, Section 3- was assumed to represent the electrostatic potential in the inner region plasma (see Fig. 6.2). Such an assumption clearly entails neglecting the shielding effect of the plasma on the electrostatic field produced by the gridded electrodes: hence, it introduces a certain degree of error in the subsequent assessment of the physical properties for the electron population. Nevertheless, on the basis of experimental observation, it is possible to claim that the plasma density is at its maximum inside the spherical DL and should rapidly decrease in the outer region, so that the shielding effect on the externally applied electrostatic field is expected to be small there. Hence, this assumption should not undermine the validity of the following results, at least for a preliminary evaluation of the plasma properties in the investigated region.

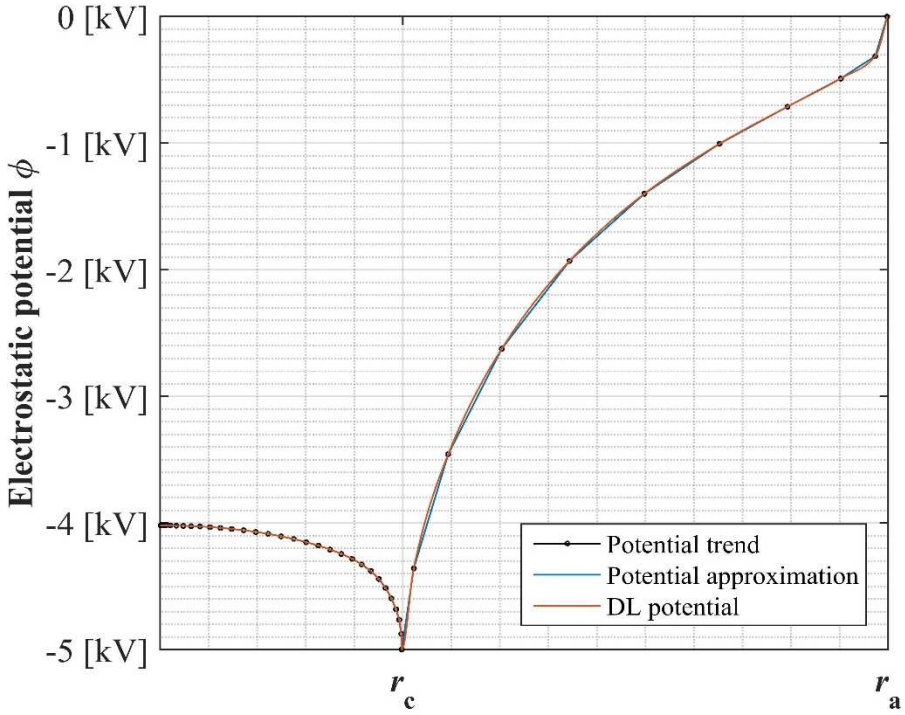

Figure 6.2 Free-space potential.

The electrons are driven by the electromagnetic interaction along the lines of the electrostatic field, toward the centre of the IEC device and thus form an accelerated flow, which can be depicted as an electron "wind", streaming into the spherical double layer. Once the value of the free-space electrostatic potential on the low-potential side of the simulated double layer is known -thanks to the free-space solver presented in the previous chapter-, the kinetic temperature of the electron population in the outer, negatively space-charged sheath in the spherical double layer, as a measure of the particles' kinetic energy. In fact, as the collisional processes are assumed to be negligible in the plasma surrounding the DL, the total mechanical energy of the charged particles in it must be conserved as in Eq. 6.1.

$$E_e(\vec{x}) = \frac{1}{2} m_e v_e^2(\vec{x}) + \mathrm{e}\, V(\vec{x}) \tag{6.1}$$

Introducing then Boltzmann constant, it is possible to define the kinetic temperature of the electron population as the thermodynamic temperature that the particles would have if collisional processes happened at such a rate as to completely convert the mechanical energy in thermal energy. Eq. 6.2 thus provides the kinetic temperature of the electron wind pursing the double layer on its low-potential side.

$$T_{e,\mathrm{out}} = \frac{\mathrm{e}\left||V_\mathrm{C}| - |V_\mathrm{FS}|\right|}{\mathrm{k}} \tag{6.2}$$

It is clear that the electron fluid component in the investigated plasma does not represent a thoroughly thermalised plasma but it is rather a highly accelerated particle flow, whose isentropic velocity can be determined, by substituting Eq. 6.2 into Eq. 6.1, as:

$$v_{e,\mathrm{out}} = \sqrt{\frac{2\mathrm{k}T_{e,\mathrm{out}}}{m_e}} = \sqrt{\frac{2\mathrm{e}\left||V_\mathrm{C}| - |V_\mathrm{FS}|\right|}{m_e}} \tag{6.3}$$

The assessment of the velocity of the electrons, accelerated along the electrostatic field lines inside the cathode grid towards the device centre, allows to compute the respective particle density on the outer surface of the spherical double layer. If the electron current across the DL surface is known, the circuital model for the SDL provides the radius of the double layer itself, is thus possible to solve Eq. 6.4 for the electron number density.

$$n_{e,\mathrm{out}} = \frac{j_e}{\mathrm{e}v_{e,\mathrm{out}}} = \frac{I_e}{4\pi r_\mathrm{DL}^2 \mathrm{e}v_{e,\mathrm{out}}} \tag{6.4}$$

The electron kinetic pressure can subsequently be defined by introducing the ideal gas law (Eq. 6.5), it should be noted that this concept is purely artificial as it follows the same line of reasoning presented in the definition of the kinetic temperature for the electron population.

$$p_{e,\mathrm{out}} = n_{e,\mathrm{out}}\,\mathrm{k}T_{e,\mathrm{out}} \tag{6.5}$$

Substituting Eq. 6.5 into Eq. 6.4 the electron wind pressure yields,

$$p_{e,\mathrm{out}} = n_{e,\mathrm{out}}\,\mathrm{e}\left||V_\mathrm{C}| - |V_\mathrm{FS}|\right| \tag{6.6}$$

In conclusion, Eq. 6.7 allows for assessing the Debye length for the electron population on the boundary of the negatively space-charged sheath of the spherical double layer. Such a length represents a measure of the shielding distance in an ideal, thermalised particle population [3]; i.e. the radius of the maximum spherical volume, around a test charged particle, that could be emptied due to statistical fluctuations in the Brownian motion of the surrounding particles in an ideal, uniform plasma in perfect thermal equilibrium.

$$\lambda_{\mathrm{D}e,\mathrm{out}} = \sqrt{\frac{\varepsilon_0 \mathrm{k}T_{e,\mathrm{out}}}{n_{e,\mathrm{out}}\mathrm{e}^2}} \tag{6.7}$$

It is worth stressing that the definition of thermodynamic quantities for the electron population incurring into the double layer is somewhat arbitrary, since the described population is far from thermodynamic equilibrium. Nonetheless, the extension of these concepts to the present description of the electron wind provides a useful mean for the quantitative characterisation of its kinetic energy, by the same token of the definition of the total temperature and pressure in gas dynamics. Moreover, such a description is formally uniform to the following assessment of the plasma properties in the inner double layer region, where such concepts assume much more significance, due to the assumption of a thermalised plasma.

¶ Plasma solution in the inner double region $r < r_\mathrm{DL}$

The inner region of the discharge plasma confined inside the cathode grid of an IEC device identifies, in the present context, the plasma volume enveloped by the inner surface of the double layer. The plasma thus represents here the bulk plasma on the high potential side of the spherical double layer and its characterising parameters can be assessed by referring to the following assumptions:

1. Quasi-neutrality
   According to the previously given definition of a double layer, the plasma in the inner region is assumed as a uniform medium, hence it is quasi-neutral. This assumption is in agreement, at least

from a qualitative point of view, with the one-dimensional density distribution assessed by means of Lavrent'ev's method, in the case of thermal distribution functions for the charged particles in the discharge plasma (see Chapter 3, Section 4). In Fig. 3.9 indeed, is possible to appreciate a plateau in the radial profile for the electrostatic potential, for the plasma inside the cathode grid: this behaviour corresponds to a uniform, quasi-neutral plasma in the core region of the simulated IEC device. Such a physical behaviour can be described, in mathematical terms, by assuming the local equivalence of the expectation value of the distribution function for the ion and electron population in the inner plasma. In other terms, on a scale greater than Debye length, the mean number density values for the ion and electron populations are the same:

$$n_i \equiv n_e \tag{6.8}$$

2. Thermalisation

As the spherical double layer represents the main confinement mechanism in the core plasma of an IEC device (see Chapter 4, Section 1, ¶ IEC-SDL model: plasma confinement, ionisation and jet extraction mechanisms), it is sensible to assume that the confined particles in the bulk plasma will undergo a relevant number of collisions. The ultimate outcome of the collisional processes is the thermalisation of the plasma confined in the inner region, i.e. the achievement of a thermal equilibrium for the fluid component of the investigated plasma. Thus, the ion population is assumed to be at room temperature:

$$T_i \cong T_{\mathrm{n}} \tag{6.9}$$

In the context of the kinetic model, this assumption corresponds to choosing the Maxwell-Boltzmann distribution as the PDF, over the kinetic phase space, for the ion and population, as in Eq. 6.10.

$$f_i(v_i) = 4\pi \sqrt{\left(\frac{m_{\mathrm{s}}}{2\pi \mathrm{k} T_i}\right)^3}\, v_i^2\, e^{-\frac{m_{\mathrm{s}} v_i^2}{2\mathrm{k} T_i}} \tag{6.10}$$

In the following, the most relevant plasma parameters are to be assessed, in the framework of the two-fluid plasma model, on the basis of the above-presented physical assumptions. All the quantities involved in the analysis of the plasma confined in the inner region will be denoted by the subscript "in".

Ion population

In the assessment of the physical quantities, characterising the ion and electron populations in the inner region plasma is convenient to consider the ion population first.

Eq. 6.9 gives the knowledge of the thermodynamic temperature for the ion population. In addition, since such a population is in thermal equilibrium, the collisional processes dominate the ions' motion in the investigated plasma and the mean velocity for the ion population is the thermal speed. As it is well known, the thermal velocity for a particle population in a gaseous medium can be directly determined from its Maxwell-Boltzmann distribution. In this respect, many distinct statistical definitions can be given, but the preferred definition (e.g. the most probable speed or the mean of the magnitude of the particles' velocity) in the present paper is the room mean square of the three-dimensional velocity, as given by Eq. 6.11.

$$v_{i,\mathrm{in}} = \sqrt{\frac{3\mathrm{k} T_{i,\mathrm{in}}}{m_i}} \tag{6.11}$$

Once the mean velocity of the ion population in the bulk plasma confined in the core of the spherical double layer structure is known, it is possible to assess the respective number density. According to the two-fluid plasma model, the number density and the mean velocity of a particle population are respectively the zeroth and first-order moment of the corresponding distribution function (see Appendix

B, Section 1, ¶ Two-Fluid plasma model). Nevertheless, the obvious method to determine the ion density is provided by Eq. 6.12, which links both the particles' number density and mean velocity to the electric current flux (per unit area), carried by the charged particles themselves.

$$\overrightarrow{J_s} = n_s \, q_s \langle \overrightarrow{v_s} \rangle \tag{6.12}$$

Hence, if the electron current across the double layer surface is assumed *a priori* for the computation of the DL solution (see Chapter 4, Section 3, ¶ IEC-SDL simulation), Langmuir condition for the double layer (Eq. 4.8) provides the value for the ion-carried component of the net electric current and the ion number densities is given as in Eq. 6.13.

$$n_{i,\mathrm{in}} = \frac{j_i}{\mathrm{e} v_{i,\mathrm{in}}} = \frac{I_i}{4\pi r_{\mathrm{DL}}^2 \mathrm{e} v_{i,\mathrm{in}}} = \frac{I_e \sqrt{m_e / m_i}}{4\pi r_{\mathrm{DL}}^2 \mathrm{e} v_{i,\mathrm{in}}} \tag{6.13}$$

Finally, substituting Eq. 6.11 into Eq. 6.13 yields the final equation for the computation of the ion density in the bulk plasma in the double layer inner region:

$$n_{i,in} = \frac{I_e}{4\pi r_{\mathrm{DL}}^2 \mathrm{e}} \sqrt{\frac{m_e}{3 \, \mathrm{k} \, T_{i,\mathrm{in}}}} \tag{6.14}$$

The knowledge of the first two velocity moments of the ion distribution function (as in Eq. 6.14 and 6.11) allows for the thorough characterisation of the ion population as a fluid component of the plasma. As detailed in the second appendix of the present essay, the physical properties of a fluid component in the two-fluid plasma model emerge as statistical moments of the assumed particle distribution function. In the present case, the thermalisation assumption in Eq. 6.9 entails that the ion population in the bulk plasma is depicted in terms of common thermodynamic quantities. Therefore, the state equation for the ion population in the investigated plasma is the classical ideal gas law:

$$p_{i,\mathrm{in}} \mathcal{V} = \mathrm{R} \, T_{i,\mathrm{in}} \tag{6.15}$$

Where $\mathcal{V}$, is the gas volume in the inner region of the spherical double layer

$\mathrm{R} = 8.3145 \; [\mathrm{J} \cdot \mathrm{mol}^{-1} \cdot \mathrm{K}^{-1}]$, is the universal gas constant.

Eq. 6.15 combines the states variable of the thermalised ion population and, introducing Boltzmann constant, allows for the computation of the ion thermodynamic pressure, as:

$$p_{i,\mathrm{in}} = n_{i,\mathrm{in}} \, \mathrm{k} \, T_{i,\mathrm{in}} \tag{6.16}$$

In conclusion, it is possible to determine the Debye length for the ion population in the bulk plasma inside the double layer, as in Eq. 6.17.

$$\lambda_{\mathrm{D}_{i,\mathrm{in}}} = \sqrt{\frac{\varepsilon_0 \, \mathrm{k} \, T_{i,\mathrm{in}}}{n_{i,\mathrm{in}} \, \mathrm{e}^2}} \tag{6.17}$$

Electron population

The thermodynamic description of the electron population in the investigated plasma follows from the same assumption in Eq. 6.8. In the present case, though, the electron current in the bulk plasma is unknown, thus it cannot be assumed as a background *datum* in the analysis of the physical properties of electron population. On the other hand, the assumed quasi-neutrality for the bulk plasma, according to the definition of a double layer as a non-neutral structure embedded in a uniform plasma volume, allows for the trivial determination of the electron number density as:

$$n_{e,\mathrm{in}} = n_{i,\mathrm{in}} \tag{6.18}$$

The thermodynamic pressure for the electron fluid component in the bulk plasma can subsequently be assessed by writing an energy balance equation, across the surface of the spherical double layer. The main assumption in the following analysis is that the momentum of the incoming electrons, accelerated by the electrostatic potential gradient in the plasma region, outside the double layer, provides both the enhanced background ionisation and the plasma confinement [19]. Therefore, the pressure balance for the fluid plasma components across the DL surface can be determined as the difference between the kinetic energy of the incoming electrons and the energy (per unit volume) spent on the ionisation process inside the DL inner volume.

$$\left[\left(p_{i,\mathrm{in}} + p_{e,\mathrm{in}}\right) - \left(p_{\mathrm{n}} + p_{e,\mathrm{out}}\right)\right] = n_{e,\mathrm{out}} \cdot \left(\frac{1}{2} m_e \, v_{e,\mathrm{out}}^2\right) - n_{i,\mathrm{in}} \, E_{\mathrm{ionisation}} \tag{6.19}$$

Hence, the thermodynamic pressure for the electron population in the DL inner region is assessed according to Eq. 6.20.

$$p_{e,\mathrm{in}} = n_{e,\mathrm{out}} \, \mathrm{e} \left| |V_{\mathrm{cathode}}| - |V_{\mathrm{FS}}| \right| - n_{i,\mathrm{in}} \, E_{\mathrm{ionisation}} + \left(p_{\mathrm{n}} + p_{e,\mathrm{out}}\right) - p_{i,\mathrm{in}} \tag{6.20}$$

The ideal gas law (in Eq. 6.16) can then be employed to assess the electron thermodynamic temperature, as follows:

$$T_{e,\mathrm{in}} = \frac{p_{e,\mathrm{in}}}{n_{e,\mathrm{in}} \, \mathrm{k}} \tag{6.21}$$

Since the thermalisation assumption holds for both the fluid component of the bulk plasma inside the double layer volume, the mean velocity for the electron population is assessed as the particle population's thermal velocity, analogously to the result in Eq. 6.22:

$$v_{e,\mathrm{in}} = \sqrt{\frac{3 \, \mathrm{k} \, T_{e,\mathrm{in}}}{m_e}} \tag{6.22}$$

The electron Debye length is hence determined as in Eq. 6.23.

$$\lambda_{\mathrm{D}_{e,\mathrm{in}}} = \sqrt{\frac{\varepsilon_0 \, \mathrm{k} \, T_{e,in}}{n_{e,in} \mathrm{e}^2}} \tag{6.23}$$

Finally, it is possible to assess Debye length for the discharge plasma confined in the inner region of the spherical double layer, combining the Debye length for the fluid components, given in Eq. 6.17 and 6.23, according to Eq. 6.24.

$$\lambda_{\mathrm{D,in}} = \sqrt{\frac{1}{\lambda_{\mathrm{D}i,\mathrm{in}}^2} + \frac{1}{\lambda_{\mathrm{D}e,\mathrm{in}}^2}} = \sqrt{\frac{\varepsilon_0 \, \mathrm{k}}{\mathrm{e}^2 \left(\frac{n_{i,\mathrm{in}}}{T_{i,\mathrm{in}}} + \frac{n_{e,\mathrm{in}}}{T_{e,\mathrm{in}}}\right)}} \tag{6.24}$$

¶ Plasma simulation for the IRS-IEC device: results and discussion

The above-presented plasma study was employed to assess the fluid parameters of the charge-carrier population in the discharge plasma in the core region of the simulated IEC device. In particular, the IEC-SDL model presented in the fourth section of Chapter 4 provided a database of solutions -in terms of double layer potential and radius- for the double layer generated in the IEC device at the IRS test facility, in correspondence of different operational conditions. In Tab. 6.1 the different operational parameters are reported, along with the variation ranges and steps adopted in the simulation.

Table 6.1 Range of variation for the simulation parameters.

	Background pressure p_n	Electron current I_e	Electron-accelerating voltage V_{PS}
	[Pa]	[mA]	[kV]
Range	0.3 ÷ 0.8	1.1 ÷ 100	0.2 ÷ 10
Step	0.1	0.3	0.2

Moreover, the experimental observation of core plasma in the IRS-IEC device given in Ref. [19] provides an estimate of the radius of the spherical double layer: in the following, this datum will be employed for the comparison with the numerical simulation of the SDL radius in the investigated device. In Tab. 6.2, the operating conditions for the IRS-IEC device and the estimated SDL radius in the experimental observation are reported.

Table 6.2 Operating conditions for the IRS-IEC device, in the experiment reported in Ref. [19].

Background pressure [Pa]	Applied voltage [kV]	Jet current [mA]	Estimated SDL radius [mm]
0.5	5	5.5	7.9

As already pointed out in Chapter 4, Section 3, the high-potential solution provided by the circuital model does not represent a reasonable description for the spherical double layer, since the corresponding thickness of the non-neutral plasma region would be greater than the radius of the electrostatic structure itself. Hence, solely the low potential solution for the spherical double layer was taken into account in the following plasma analysis.

In Fig. 6.3, the corresponding values for the radius of the simulated spherical double layer are reported along with the experimental observation of the fireball in the core of the IRS-IEC device, for the operating conditions given in Tab. 6.2.

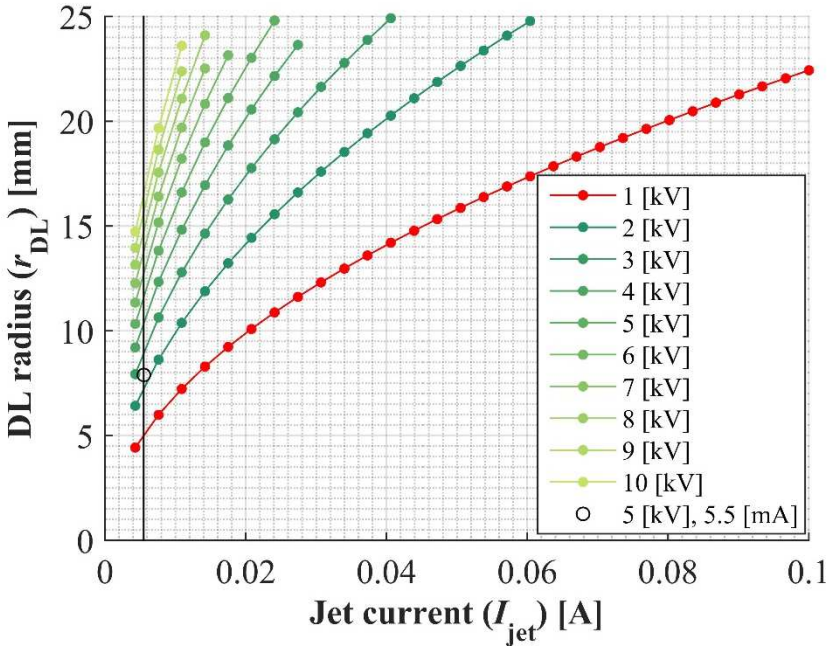

Figure 6.3 Radius of the spherical double layer. The marked lines represent the numerical simulation while the dot marks the experimental observation reported in Ref. [19].

It is possible to observe that, for an applied voltage of 5 [kV] on the device's electrodes, the resulting electron-accelerating voltage in the low-potential side of the SDL is 1 [kV] (corresponding to the line marked in red in the reported graph). The comparison between the value provided by the simulation tool and that experimentally observed shows that the SDL simulation underestimates the radius. Nonetheless, the error is within 3 [mm] and can be justified, at least to some extent, considering that the circuital model developed for the simulation of the IEC-SDL only considers singly charged ions.

The double graph reported in Fig 6.4 allows for the direct comparison of the DL radius, assessed as the low potential root of Eq. 4.22, with the thickness of the double layer itself, computed by means of Eq. 4.47, in accordance with the Langmuir's theory of double sheaths. It is possible to observe that the thickness of the investigated plasma structure is much lower than the respective radius, over a relevant portion of the variation range for the simulation parameters. In particular, the best behaviour for the simulated SDL is observed in correspondence of lower values for the electron-accelerating voltage, due to the smaller thickness of the double layer, and for higher values of the extracted jet current, entailing a greater radius of the fireball. Thus, the low potential solution for the spherical double layer is consistent with the basic assumption of the IEC-SDL model.

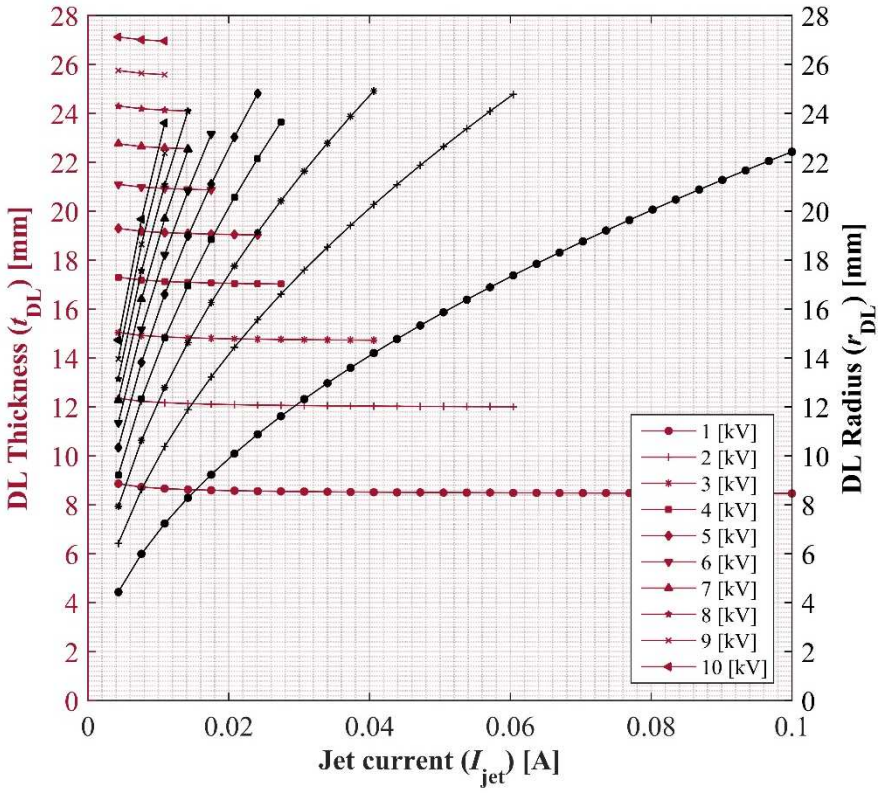

Figure 6.4 Thickness and radius of the simulated spherical double layer: the left-hand scale is referred to the DL thickness while the right-hand scale refers to its radius. This double plot allows for a direct comparison of the two geometrical quantities: it is clearly observed that for low voltages and high jet currents the SDL solution is well within the limits of validity of the IEC-SDL model. The reported results refer to an IEC device operating in correspondence of a background pressure of 0.5 [Pa].

Once the soundness of the spherical double layer solution -computed according to Langmuir condition for the current ratio on the double layer surface- is validated, the most relevant plasma properties can be assessed both in the outer and inner regions, according to the above-presented two-fluid description. *En passant,* it is worth noticing that, in the following, the simulation outputs reported in the presented pictures are referred to the case of a background pressure of 0.5 [Pa], which is assumed to represent the most reasonable operating condition for the IEC device investigated at IRS.

Outer region

The assessment of the physical properties of the plasma surrounding the simulated spherical double layer is focused on the electron population. As already described, the externally applied electrostatic field drives the negatively charged particles toward the centre of the IEC device, electrostatically accelerating them away from the cathode grid. To a first assumption, the whole electron population, in the outer DL region, is assumed to constitute a mono-energetic beam, radially focused against the external surface of the spherical double layer.

Due to the assumption of mono-energetic distribution for the accelerated electrons, their total mechanical energy is a constant of motion: in the electrostatic acceleration of the negatively charged particles against the double layer surface, their potential energy is converted in kinetic energy, according to Eq. 6.1. As already mentioned, the kinetic energy of the resulting electron wind can be assessed in terms of the relating kinetic temperature, as given in Eq. 6.2. In Fig. 6.5, the evaluation of such a quantity in correspondence of the different experimental conditions, given in Tab. 6.1, is reported. It is possible to observe that the computed electron temperature is almost independent on the extracted jet current (actually, a slight dependence exists, but cannot be noticed to the scale of the figure). On the other hand, it is strongly dependent on the applied electrode voltage and its trend is quite straightforward: for an increasing applied voltage the electron-accelerating potential -reported as the parameter in the following graph- increases as well, thus the higher kinetic temperature for the incoming electron wind on the outer surface of the spherical double layer.

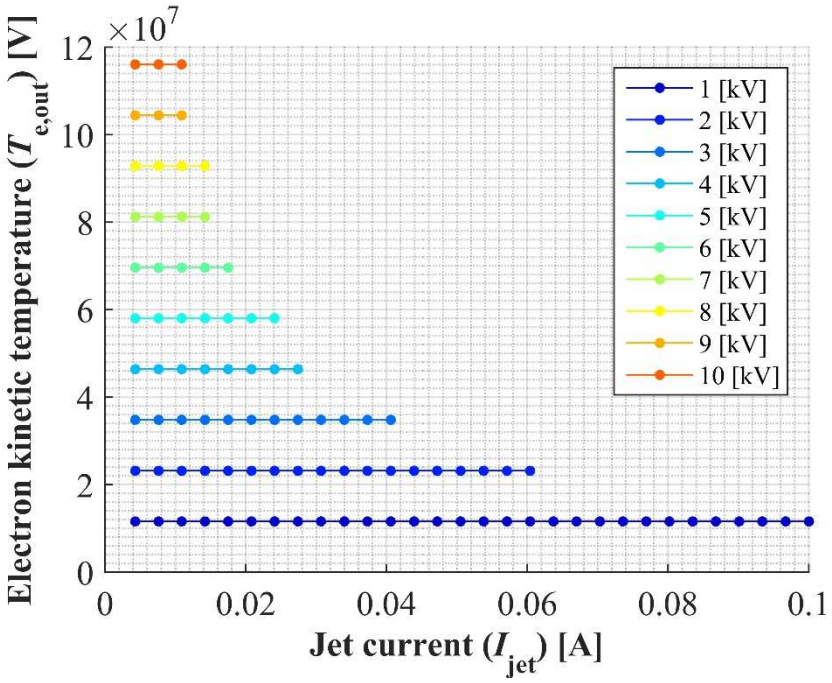

Figure 6.5 Kinetic temperature of the electron population in the outer region. The reported results refer to an IEC device operating in correspondence of a background pressure of 0.5 [Pa].

This trend is reflected in the number density of the electron population on the outer surface of the simulated spherical double layer, as observed in Fig. 6.6. The higher density for the incoming electron wind is simulated in correspondence of the lowest accelerating potential (i.e. 1 [kV]), corresponding to an applied electrode voltage of 5 [kV]. This behaviour is understood in the light of Eq. 6.4 where, for a known value of the electron current across the surface of the double layer, the electron density is inversely proportional to the electron velocity, i.e. to the squared root of the particles' kinetic energy. Hence, the higher electrostatic potential drop, accelerating the electrons in the outer region, the lower the density of the resulting electron wind.

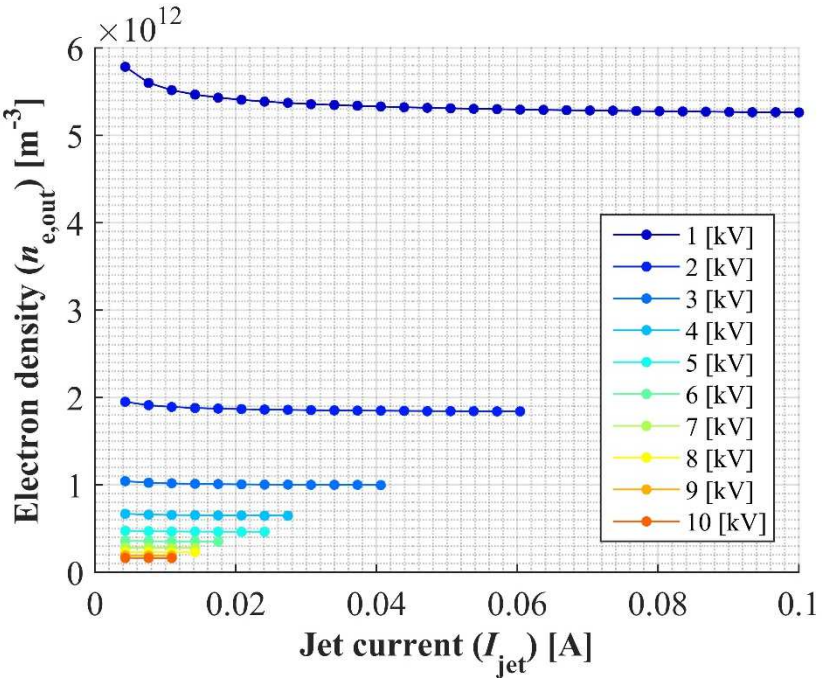

Figure 6.6 Electron number density in the outer region. The reported results refer to an IEC device operating in correspondence of a background pressure of 0.5 [Pa].

Inner region

As far as the bulk plasma inside the surface of the spherical double layer is concerned, as already described, it is considered a uniform, thermalised plasma: hence, the mean number densities for the ion and electron populations in the investigated plasma coincide. Therefore, in the following, reference is made to the "plasma density", referring indistinctly to the ion and electron populations. In Fig. 6.7, such a plasma density is plotted, for the different operating conditions, against the corresponding values of the radius for the simulated spherical double layer. This visual representation allows to notice the consistency of the presented plasma density output with the theoretical description provided by Eq. 6.13: indeed, the density trend reflects the dependency of the number density on the inverse of the squared radius of the double layer. Hence, the density of the bulk plasma in the inner region is higher for lower applied electrode voltages and weakly decreases with the jet current.

The computed Debye length for the uniform, thermalised plasma inside the simulated spherical double layer -reported in Fig. 6.8- is consistent with the density output, as it reflects its variation with the electrode potential and jet current. Indeed, to a lower density in the investigated plasma corresponds a reduced Debye shielding effect of the charged particles in the plasma: such a behaviour is observed in the increase of the Debye length for both greater values of the electron-accelerating potential and jet-carried electron current.

In conclusion, it is possible to observe that the values obtained for the particle density inside the spherical double layer are rather modest. This fact is particularly evident if the plasma density is compared to the values predicted by the one-dimensional simulation presented in the third chapter of the present thesis. In Fig. 3.10, the number density of both the ion and electron populations are presented in case of an applied voltage of 1 [kV]: it is easily seen that, even the most rarefied plasma (corresponding to the thermal model) presents a particle density one order of magnitude greater than that predicted by the IEC-SDL model. This discrepancy can be justified, to some extent, considering that the thermal model does not take into account any energy loss: as a matter of fact, the particles' mechanical energy is assumed to be converted, in the collisional processes, in thermal energy. In the present plasma simulation, on the other hand, a significant fraction of the incoming electron energy is assumed to be spent in the electron-

impact ionisation reaction, taking place in the positively space-charged sheath of the spherical double layer, according to Eq. 6.19.

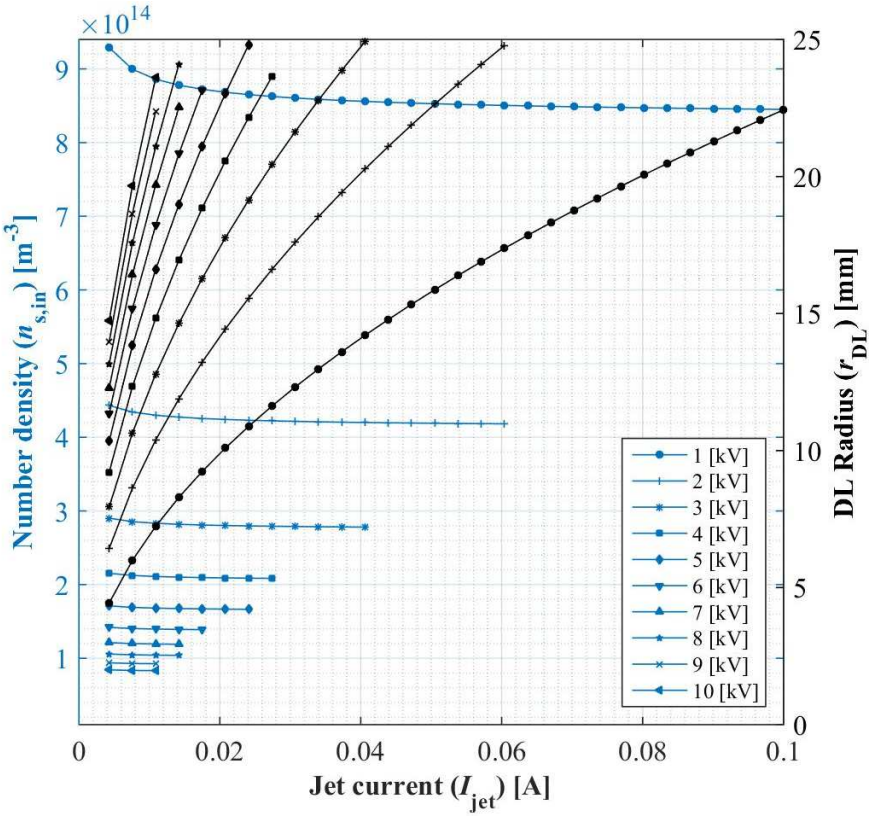

Figure 6.7 Radius of the spherical double layer and plasma density in the inner region: the left-hand scale is referred to the particle density inside the SDL while the right-hand scale refers to its radius. The reported results refer to an IEC device operating in correspondence of a background pressure of 0.5 [Pa].

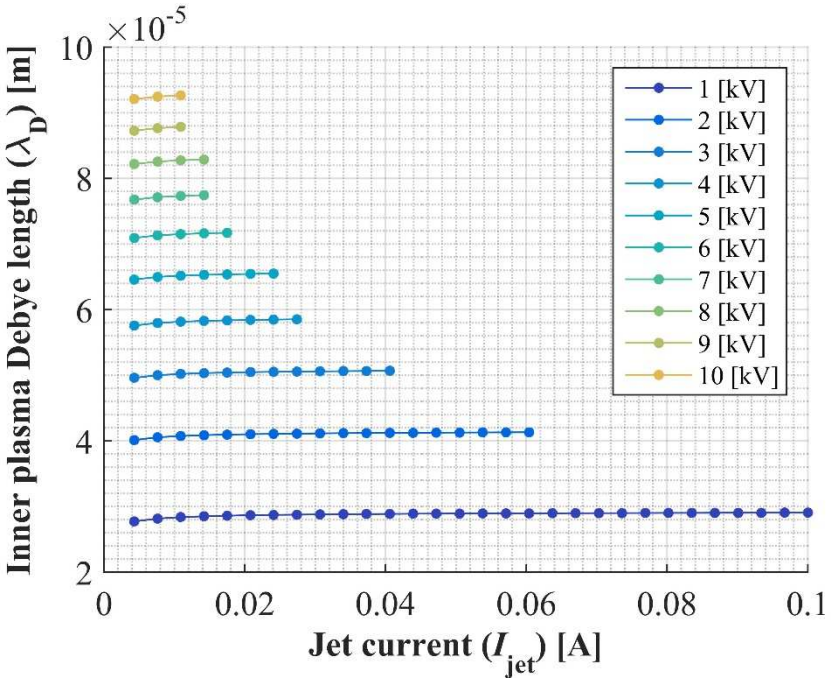

Figure 6.8 Debye length for the simulated bulk plasma inside the surface of the spherical double

layer. The reported results refer to an IEC device operating in correspondence of a background pressure of 0.5 [Pa].

6.2 Alternative double layer model

¶ Relaxation of Langmuir condition

The assumption of the Langmuir condition for the spherical double layer, which is theorised to ensue in the core plasma inside the IEC device providing an intrinsic mechanism for the enhanced background gas ionisation and plasma confinement, allowed the assessment of many relevant physical properties for the investigated plasma. Nonetheless, this assumption seems to represent a strong limitation on the plasma density in the inner double layer region, according to Eq. 6.13. As a matter of fact, for a given double layer solution -i.e. for a given radius of the spherical structure-, the density is limited by the incoming electron current. Thus, the results provided by the SDL model and presented in the previous section of the present chapter, despite being quite promising as a preliminary study, present a too little accordance with the expected density values.

For this reason, the next step in the investigation of the plasma properties in the proposed DL model for the IEC device was the relaxation of Langmuir condition for the spherical double layer. It is worthwhile, before going into the details, to clarify the concept implied here by the term "relaxation" of Langmuir condition. The following dissertation shall refer to the same basic assumption that lead to the definition of the SDL model presented in Chapter 4, Section 3; namely, the exact three-dimensional geometry of the double layer is assumed to play a negligible role in the definition of the equilibrium position for the double layer [19, 21]. In this respect, the local geometry of the non-neutral plasma region is assimilated to the case of planar, parallel electrodes and Langmuir's theory of the double sheath is extended to the present issue. The crucial concern raised here is the violation of the simple relation determined by Langmuir, quantifying the ratio between the ion and electron fluxes -in the case of space-charge limited current in both the positive and negative sheath constituting the double layer- as the squared root of the ratio between the electron and the ion mass. If the electron current flowing through the DL is a known quantity, as in the circuital model developed in Ref. [19], such a violation is equivalent to assuming the ion current to be varied independently of the electron one itself. In order to do so, the circuital model for the IEC was modified so as to account for the relaxation of Langmuir condition by introducing the inverse of the non-dimensional parameter in Eq. 4.39:

$$f \doteq \left|\frac{j_e}{j_i}\right| \sqrt{\frac{m_e}{m_i}} \tag{6.25}$$

Hence, in the context of the present dissertation, f is referred to as the "relaxation parameter" in that it quantifies the assumed violation of the Langmuir condition for the assumed spherical double layer. Assuming a value for the relaxation parameter other than one, thus, entails setting the Langmuir condition aside, postulating a different ratio between the particle fluxes fostering the spherical double layer in the IEC core plasma. The *a priori* assumption of such a relationship between the electron current, driven by the applied filed topology on the low potential side of the SDL, and the positive current, due to the thermal motion of the ions in the quasi-neutral plasma confined inside the electrostatic structure, is critical to the assessment of the SDL solution. Therefore, the value assigned to the relaxation parameter determines, to some extent, the physics underlying the plasma confinement and ionisation processes inside the IEC device. In particular, it is possible to study the spherical double layer structure and the confined plasma in correspondence of values of the relaxation parameter in two different ranges:

- $f < 1$
  Amounts to postulating an enhanced ion current on the high potential side of the double layer: hence, the conservation of linear momentum at the SDL surface dictates a higher ion flux, with respect to that of a Langmuir DL, to balance the incoming electron wind. As will be later discussed, such an occurrence is beyond the limit of Langmuir's theory of double sheaths. Nonetheless, experimental observations proved the existence of double layer characterised by a value of f well below the unit. Indeed, the well-documented existence of current-free double layers [61, 63] requires the ion density to compensate for the reduced particle motility, with respect to the much faster electrons, so that the particle fluxes on the DL surface equals each other:

$$\begin{gathered} I_i = I_e \\ \Downarrow \\ f = \sqrt{\frac{m_e}{m_i}} \end{gathered} \tag{6.26}$$

  Thus, the existence of current-free double layers violates Langmuir condition, presenting values of the relaxation parameter much smaller than one[26].

- $f > 1$
  This condition entails a reduced ion current on the high potential side of the double layer: the higher electron motility and kinetic energy on the low potential side of the electrostatic structure determine a momentum equilibrium where the ion flux from inside the double layer is much lower than the incoming electron wind.

Fig 6.9 provides a visual representation of the physical meaning assumed by the relaxation parameter in the charged particles dynamics on the surface of the spherical double layer.

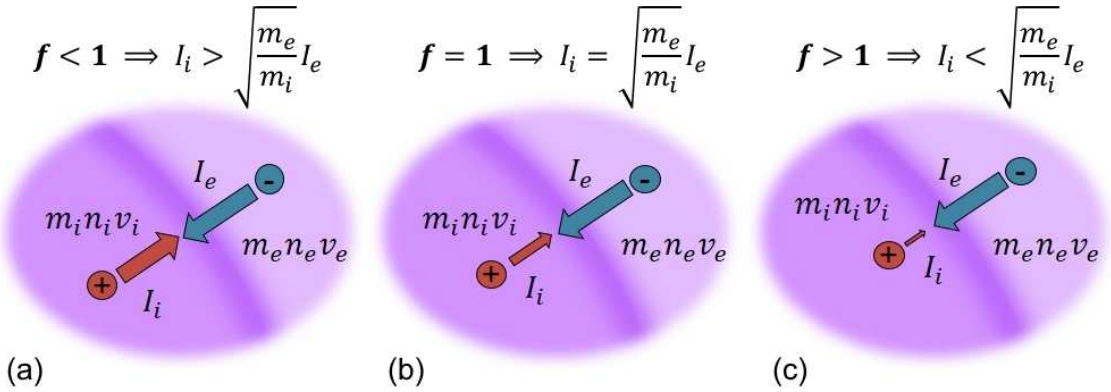

Figure 6.9 Schematic of the particle fluxes balance across the double layer surface for different values of the relaxation parameter:
(a) Enhanced ion flux, for $f < 1$
(b) Langmuir double layer, for $f = 1$
(c) Reduced ion flux, for $f > 1$.

From a computational point of view, the introduction of the relaxation parameter is a rather convenient artifice that allows for the straightforward adjustment of the circuital model presented in the fourth chapter of the present thesis. It is thus possible to simulate the spherical double layer structure at the centre of the IEC device, in correspondence of a set of different values for the relaxation factor, by solving the following set of non-linear equations:

[26] E.g. in case of a current-free DL in a Hydrogen plasma the value of f is about $2.3337 \cdot 10^{-2}$ [64].

$$\begin{cases} N\, r_{\mathrm{DL}}\, \sigma(\phi_{\mathrm{DL}}) \sqrt{\dfrac{m_e}{m_i}} \dfrac{1}{f} = 1 \\ \phi_{\mathrm{DL}} = \phi_0 - R \cdot (\beta N r_{\mathrm{DL}}^2) \end{cases} \tag{6.27}$$

By comparing this equation with Eq. 4.22, it is evident that Eq. 6.27 represents a trivial modification of the equilibrium equation for the spherical DL, as developed by Song *et al.* in Ref. [22]. Therefore, implementing the violation of Langmuir condition for the SDL model only required a slight modification of the pre-existing computational model. The numerical resolution of Eq. 4.22, by means of a dedicated Matlab® script, allowed for the definition of different database of solutions for the simulated double layer -i.e. the SDL radius and electrostatic potential-, each one corresponding to a distinct value for the relaxation parameter. In Tab. 6.3, the ranges for the main parameters varied in the assessment of the plasma properties in the core discharge of the IRS-IEC device are reported.

Table 6.3 Range of variation for the simulation parameters.

	Electron-accelerating voltage V_{PS}	**Electron current** I_{e}	**Relaxation parameter** f	
	[kV]	[mA]	[−]	
Range	$0.2 \div 10$	$1.1 \div 100$	$0.1 \div 1$	$1 \div 10$
Step	0.2	0.3	0.1	1

As far as the thickness of the spherical shell representing the non-neutral structure embedded in the core plasma inside the cathode grid is concerned, it can be estimated by direct interaction of the Langmuir equation for the electrostatic potential across the double sheath (Eq. 4.44). Following the reasoning of M.A. Raadu [70], it is useful to separately evaluate the left-hand side of Eq. 4.44 and assign the value of the corresponding integral to the following function:

$$\mathrm{C}_1(f) = \left\{ \frac{3}{4} \int_0^1 \left\{ \phi^{\frac{1}{2}} + \frac{1}{f} \left[(1-\phi)^{\frac{1}{2}} - 1 \right] \right\}^{-\frac{1}{2}} \mathrm{d}\phi \right\}^2 \tag{6.28}$$

It is notable that this term plays, in the evaluation of the double layer thickness, the exact same role as the constant term C_0 in Eq. 4.45. According to Langmuir's model for the double sheath, as presented in the previous section, the electron current carried across the double layer is a function of the double layer potential, in the following form:

$$j_e t_{\mathrm{DL}}^2 = \mathrm{C}_1(f) \frac{4}{9} \varepsilon_0 \sqrt{\frac{2\mathrm{e}}{m_e}} {\phi_{\mathrm{DL}}}^{\frac{3}{2}} \tag{6.29}$$

Substituting the resulting equation in Eq. 6.25 is then possible to refer to the net current crossing the double layer:

$$j t_{\mathrm{DL}}^2 = (j_e + j_i) t_{\mathrm{DL}}^2 = \left(1 + \frac{1}{f} \sqrt{\frac{m_e}{m_i}} \right) \frac{4}{9} \mathrm{C}_1 \varepsilon_0 \sqrt{\frac{2\mathrm{e}}{m_e}} {\phi_{\mathrm{DL}}}^{\frac{3}{2}} \tag{6.30}$$

Hence, the thickness of the spherical double layer can be determined, according to Langmuir's model, as a function of the three simulation parameters indicated in Tab. 6.3:

$$t_{\mathrm{DL}} = \left[\left(1 + \frac{1}{f} \sqrt{\frac{m_e}{m_i}} \right) \frac{4}{9} \mathrm{C}_1 \varepsilon_0 \sqrt{\frac{2\mathrm{e}}{m_e}} \frac{\phi_{\mathrm{DL}}^{\frac{3}{2}}}{j} \right]^{\frac{1}{2}} \tag{6.31}$$

In the following analysis of the SDL structure -in case of the relaxation of Langmuir's condition-, the existence of two distinct roots for the DL equilibrium equation (Eq. 6.26), resulting from the circuital model for the IEC double layer, is expected. Since no data is *a priori* available for both the solutions of Eq. 6.27 and 6.31, it is not possible to exclude the validity of the high-potential root of Eq. 6.27 on the basis of the comparison between the double layer radius and thickness. Thus, contrary to the previous section, in the following both the low- and high-potential solutions of the double layer model will be reported along with the assessment of the corresponding plasma behaviour inside the spherical double layer.

Indeed, once the numerical resolution of the circuital model provided a database of double layer solutions for the different values of the relaxation parameter, the focus is shifted to the evaluation of the main physical properties of the core plasma, with particular attention to the plasma density. Such an analysis is based on the assumption of a quasi-neutral, thermalised plasma inside the double layer shell, thus it will follow the same line of reasoning presented in "¶ Plasma solution in the inner double region $r < r_{\mathrm{DL}}$".

Due to the non-linearity of the equilibrium equation for the spherical double layer (Eq. 6.27) and the mathematical relationship between the ion density in the core plasma and the double layer radius (Eq. 6.14), it is a priori unknown which values of the relaxation parameter would prompt a higher plasma density inside the spherical double layer. Hence, several simulations were conducted for values of the relaxation parameter both above and below the unit, representing the exact Langmuir condition for the double layer. The range of the relaxation parameter, adopted in the numerical simulation of the IEC device, is presented in Tab. 6.3: it is worth remarking that such a range was divided in two distinct regions, corresponding to values below and above the unit. In the following, the results provided by the circuital model for the SDL and the corresponding two-fluid plasma simulation will be presented in two district subsections, referring to values of the relaxation parameter higher ($f > 1$) and lower ($f < 1$) than one respectively.

¶ Plasma simulation for $f > 1$: results and discussion

The first case to be presented in the following is the plasma simulation in the IEC-SDL model assuming a reduced ion flux on the high potential side of the double layer. Indeed, according to the definition of the relaxation parameter, given in Eq. 6.25, when the assigned value is higher than the unit, the ratio between the ion and the electron current across the double layer is lower than the squared root of the electron-to-ion mass ratio. The local structure of the investigated double layer can thus be assessed according to the above-presented Langmuir's theory. More specifically, in correspondence of each value assumed for the relaxation parameter, the thickness of the non-neutral plasma region can be evaluated by means of Eq. 6.28 and 6.31: in Tab. 6.4, the investigated values of the relaxation parameter are presented, along with the corresponding evaluation of the integral function $\mathrm{C}_1(f)$ according to Eq. 6.28.

Table 6.4 Relaxation of Langmuir condition for the double sheath model, $f > 1$ region.

f	1	2	3	4	5	6	7	8	9	10
α	1.000	0.500	0.333	0.250	0.200	0.167	0.143	0.125	0.111	0.100
$\mathbf{C_1}$	1.8652	1.2506	1.1501	1.1073	1.0836	1.0684	1.0579	1.0502	1.0443	1.0397

In Fig. 6.10, the low- and high-potential SDL solutions are presented in the case $f = 2$.

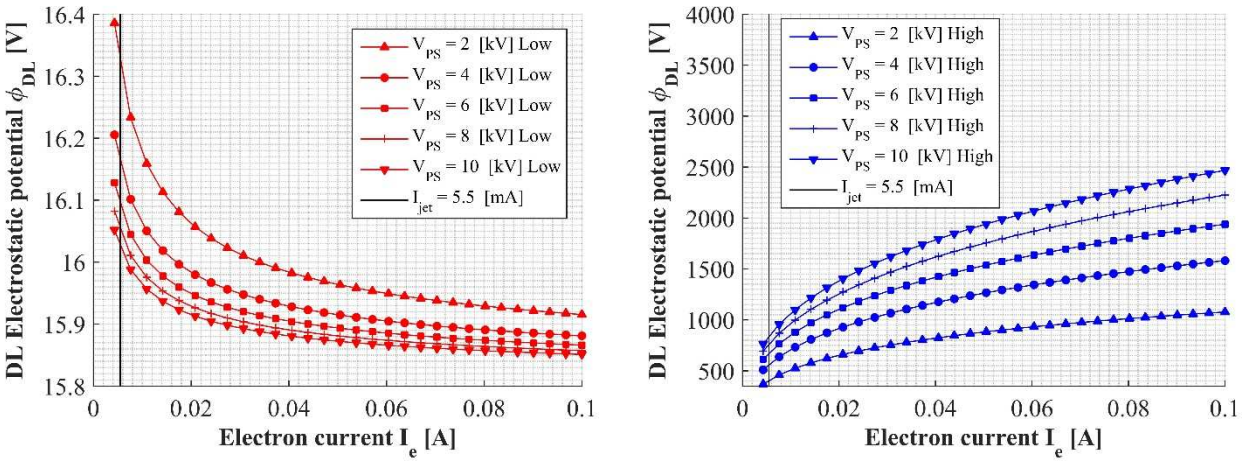

Figure 6.10 Electrostatic potential for the IEC-SDL, in case of a relaxation parameter equal to 2.

Low-potential SDL solution

The first step in the evaluation of the low potential solution for the spherical double layer is the assessment of its thickness and the subsequent comparison with the radius of the electrostatic structure itself. Once Eq. 6.27 is numerically solved to determine the DL radius for each experimental condition considered in the simulation (see Tab. 6.3), it is possible to employ the value for the integral function $C_1(f)$ for the assessment of the DL thickness according to Eq. 6.31. In Fig. 6.11, the direct comparison of the double layer thickness and radius is possible for any specific value adopted for the relaxation parameter. The parametric double plot clearly shows that the main assumption of the spherical double layer being locally akin to a plane, one-dimensional double layer (Eq. 4.29) is satisfied over the vast majority of the tested current range. Hence, the solution provided by the IEC-SDL is preliminarily validated for the case of a reduced ion current on the low potential side of the double layer. In addition, it is possible to appreciate, in Fig. 6.11, that the computed DL radius is almost independent from the ration between the ion and electron current on the surface of the DL itself. Hence, the error between the simulated SDL radius and the experimental observation in Ref. [19] is again within 3 [mm].

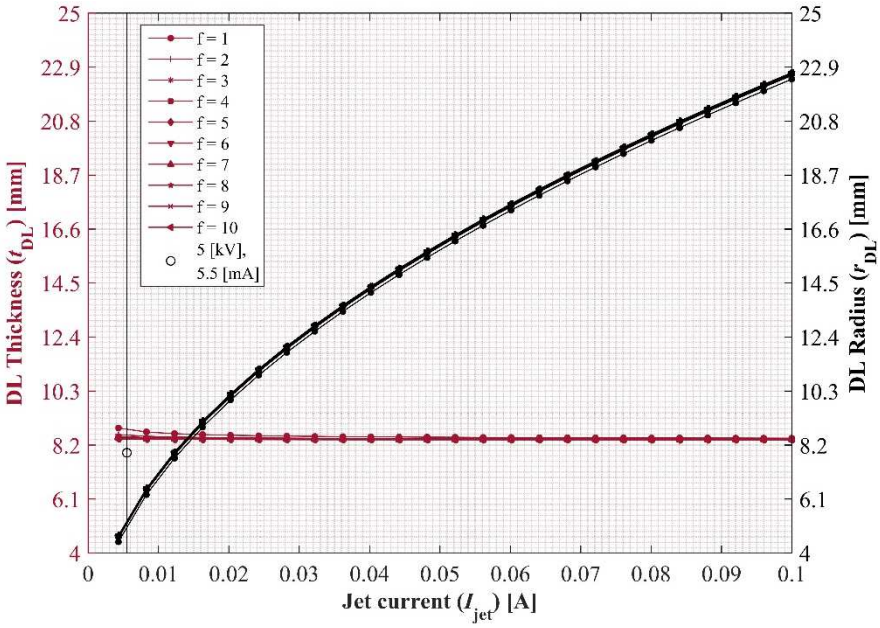

Figure 6.11 Thickness and radius of the simulated spherical double layer: the left-hand scale is referred to the DL thickness while the right-hand scale refers to its radius. This double plot allows for a direct comparison of the two geometrical quantities for any tested value of the relaxation parameter. The reported results refer to an IEC device operating in correspondence of a background pressure of 0.5 [Pa] and an

electrode voltage of 5 [kV].

Once the validity of the low-potential solution provided by the IEC-SDL model -accounting for the violation of Langmuir condition by assuming $f > 1$ - is proven, the research focus shifts on the evaluation of the plasma density inside the simulated fireball. Solving Eq. 6.13 in correspondence of each investigated operating condition for the IEC device, the number density of both the ion and electron populations in the quasi-neutral bulk plasma is computed. The resulting output is reported in the parametric graph given in Fig. 6.12: for a clearer visualisation, the plotted data are only referred to the case of an applied electrode voltage of 5 [kV]. This graph clearly shows that for an increasing value of the relaxation parameter the plasma density in the inner DL region is remarkably reduced and its value is almost independent on the extracted electron current.

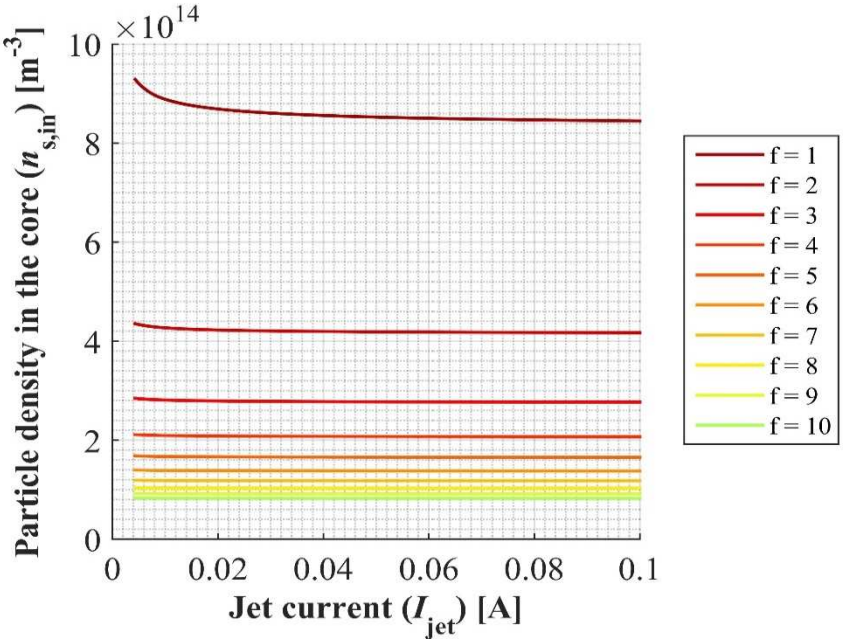

Figure 6.12 Plasma density in the inner region of the low potential SDL, in case of the violation of Langmuir condition, assuming different values for reduced ion flux on the surface of the double layer.

Therefore, the low potential solution for the SDL, computed in correspondence of values of the relaxation parameter greater than one, is reasonable in terms of the comparison between the radius and the thickness of the resulting electrostatic structure. Nonetheless, the resulting plasma behaviour is deteriorating for a greater violation of Langmuir condition, with the plasma rarefaction quickly escalating so that the computed plasma density gets to two orders of magnitude lower than that computed by the thermal model simulation (see Chapter 3, Section 4). Such a behaviour is in open contrast with the idea of the spherical double layer providing the plasma confinement inside the cathode grid.

High-potential SDL solution

As far as the high-potential solution provided by the IEC-SDL model is concerned, the relaxation of Langmuir condition for the double layer unfortunately does not satisfy the basic assumptions of the circuital model. As a matter of fact, following the same line of reasoning presented in Chapter 4, Section 3, ¶ Detailed structure of Langmuir double layer, the high-potential solution needs to be rejected in the light of the comparison between the simulated double layer radius and the corresponding thickness. In Fig. 6.13, these two quantities are both plotted in the same graph: the left-hand side scale is referred to the thickness of the investigated plasma structure; on the contrary, the right-hand side one refers to its radius. The resulting thickness of the spherical double layer is much greater than the corresponding dimension of the spherical structure itself: the physical impossibility represented by such a solution is rather evident. It should be noted that the issue here presented is due to the combination of two different

causes. On one side, the computed thickness of the spherical double layer is rather towering and hardly reasonable given the geometric scale of the IEC device itself. On the other hand, the radius of the spherical double layer, computed when the higher potential drop is assumed across it, is extremely small. The values computed are in fact in the order of the millimetre, while experimental observations showed that the fireball produced inside the cathode grid has a diameter in the order of the centimetre (see Fig. 2.11, 2.12 and 2.13).

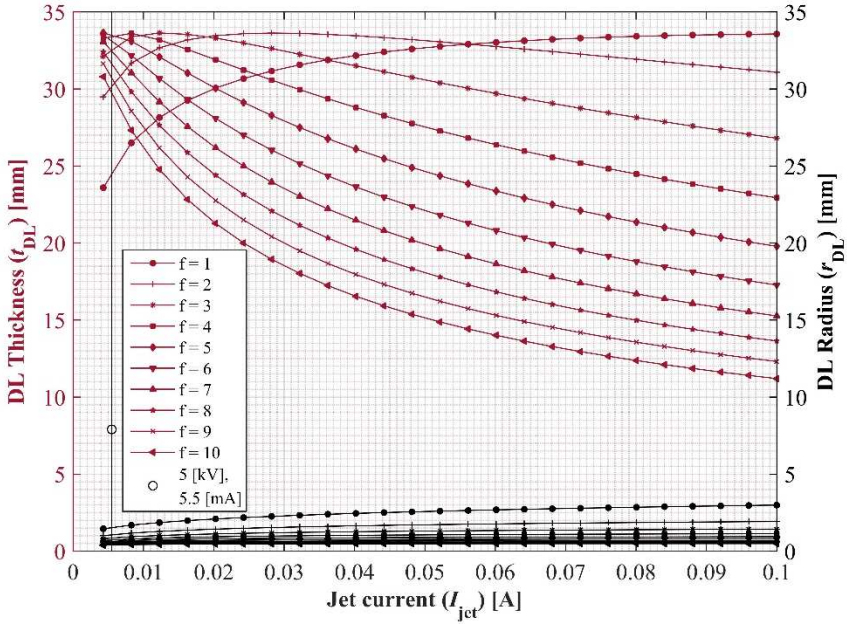

Figure 6.13 Thickness and radius of the simulated spherical double layer: the left-hand scale is referred to the DL thickness while the right-hand scale refers to its radius.

In Fig. 6.14, the computed particle density is reported to underline how the violation of Langmuir condition allows for attaining a remarkably high density, for the confined plasma inside the double layer, in correspondence of the high-potential solution.

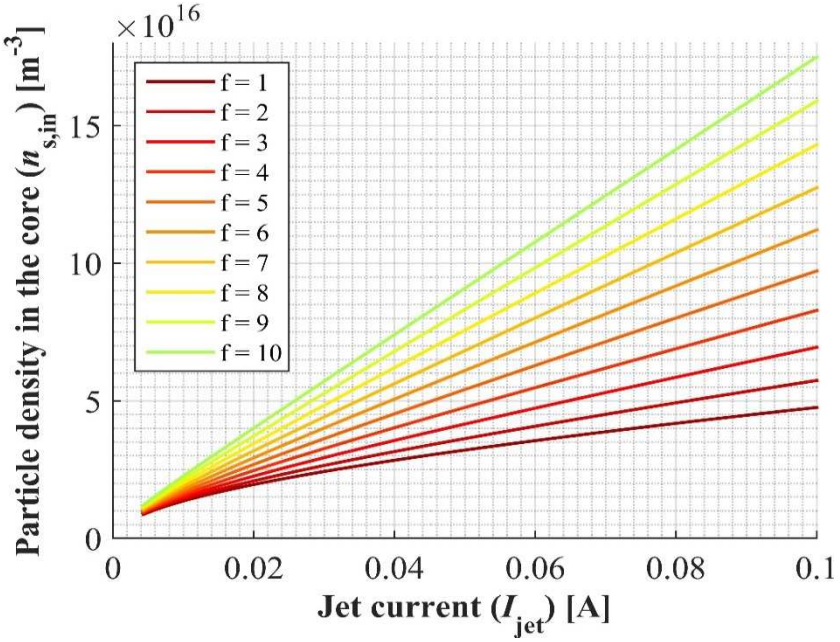

Figure 6.14 Plasma density in the inner region of the high potential SDL, in case of the violation of Langmuir condition, assuming different values for reduced ion flux on the surface of the double layer.

In conclusion, the relaxation of Langmuir condition in the sense of reducing the positive electric current, carried by the ions accelerated by the double layer potential against the incoming electron wind, provides a description that has little agreement with the observed plasma behaviour in the core of the investigated IEC device. In fact, while the low potential solution predicts such a small plasma density inside the spherical double layer that is scarcely compatible with the concept of plasma confinement, the high potential solution depicts a remarkably dense plasma confined in an extremely small fireball. Therefore, neither of the two concurring solutions provide a reliable description of the plasma physics for the glow discharge produced in the investigated IEC device.

¶ Plasma simulation for $f < 1$: results and discussion

Finally, the case of an enhanced ion current flowing from inside the spherical double layer is discussed. Assuming a value lower than the unit, for the relaxation parameter, equates to postulating the ratio between the ion and the electron current across the double layer to be greater than the squared root of the electron-to-ion mass ratio. Such an assumption entails moving from the case of a Langmuir double layer towards a current-free double layer [64]: indeed, the lower limit for the relaxation parameter is given as the value that determines the balance of the ion and electron currents across the double layer, according to Eq. 6.26. In the present case, the investigated IEC device is assumed to operate on an Argon discharge plasma: hence, the lowest admissible value for the relaxation parameter is $f \cong 3.7037 \cdot 10^{-2}$. Nevertheless, for values below $f = 0.1$, no solution was found for the IEC-SDL model. Hence, in the following, the reported simulation results will make reference to the values given in Tab. 6.5.

Table 6.5 Relaxation of Langmuir condition for the double sheath model, $f < 1$ region.

f	1	0.9	0.8	0.7	0.6	0.5	0.4	0.3	0.2	0.1
α	1	1.11	1.25	1.43	1.67	2.00	2.50	3.33	5	10

Fig. 6.15 reports the low- and high-potential SDL solutions, in the case $f = 0.5$.

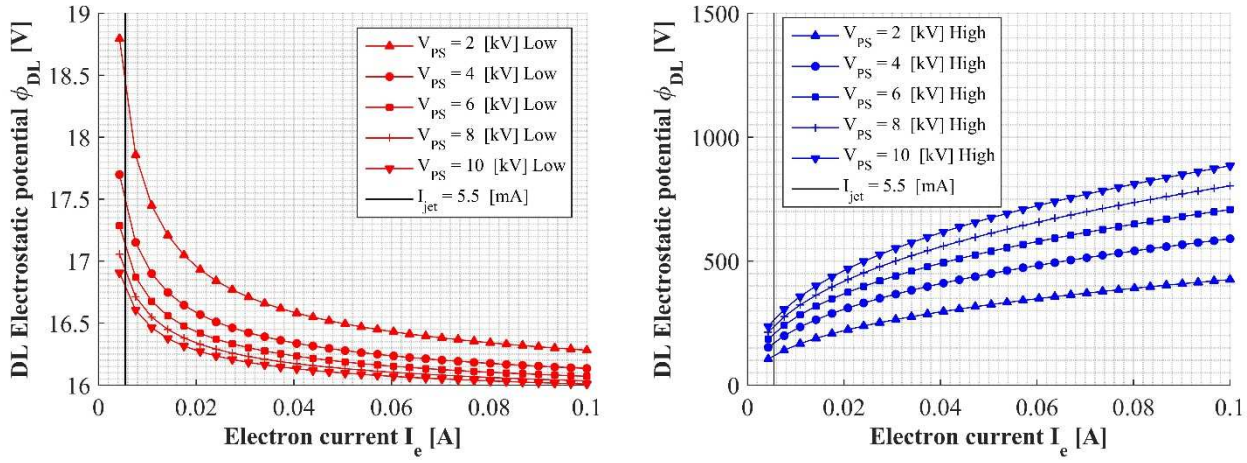

Figure 6.15 Electrostatic potential for the IEC-SDL, in case of a relaxation parameter equal to 0.5.

Low-potential SDL solution

At a first instance, it is worth analysing the radius of the computed spherical double layer for the different values of the relaxation parameter. From the values reported in Fig. 6.16 -for the low-potential SDL simulated in the investigated IEC device, operating on an applied voltage of 5 [kV] and 0.5 [Pa] background pressure- is clear that the violation of Langmuir condition slightly affects the dimensions of the fireball. Indeed, only when the current ratio is raised to about ten times that prescribed by Langmuir

condition, an appreciable reduction in the DL radius is observed. Therefore, as far as the dimensions are concerned, the simulated spherical double layer is consistent with the experimental observations.

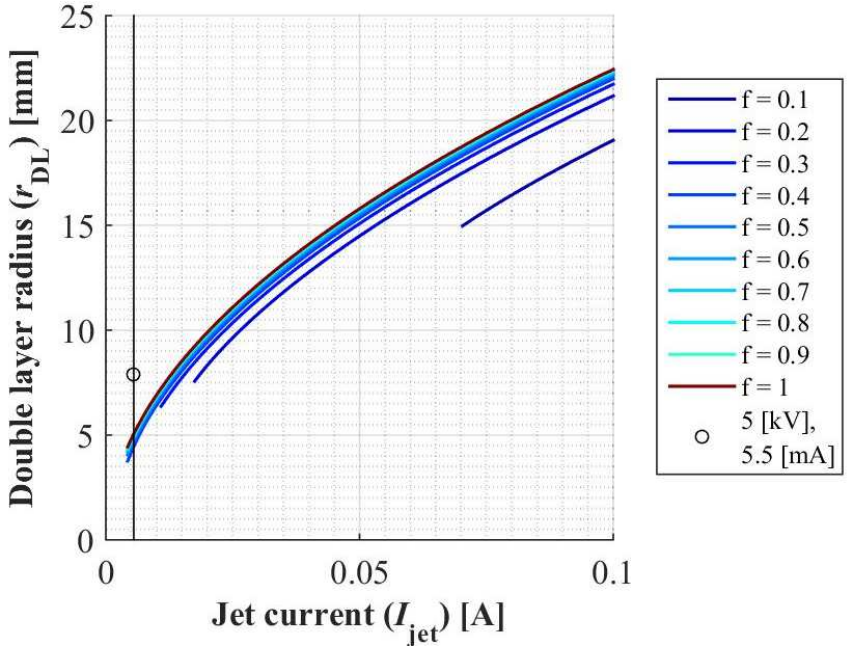

Figure 6.16 Radius of the low potential SDL, in case of the violation of Langmuir condition, assuming different values for enhanced ion flux on the surface of the double layer.

The subsequent evaluation of the plasma density inside the DL surface reveals that the assumption of an enhanced ion flux emerging from the fireball promotes the density of the investigated plasma itself. As a matter of fact, it is possible to observe, in the visual output presented in Fig. 6.17, that if the ion current on the SDL surface is doubled, the corresponding plasma density is about four time greater than that simulated for the Langmuir double layer, under the same operational conditions. In addition, is worth noticing that the extracted jet current has little effect on the variation of the core plasma density, especially for higher values of the relaxation parameter.

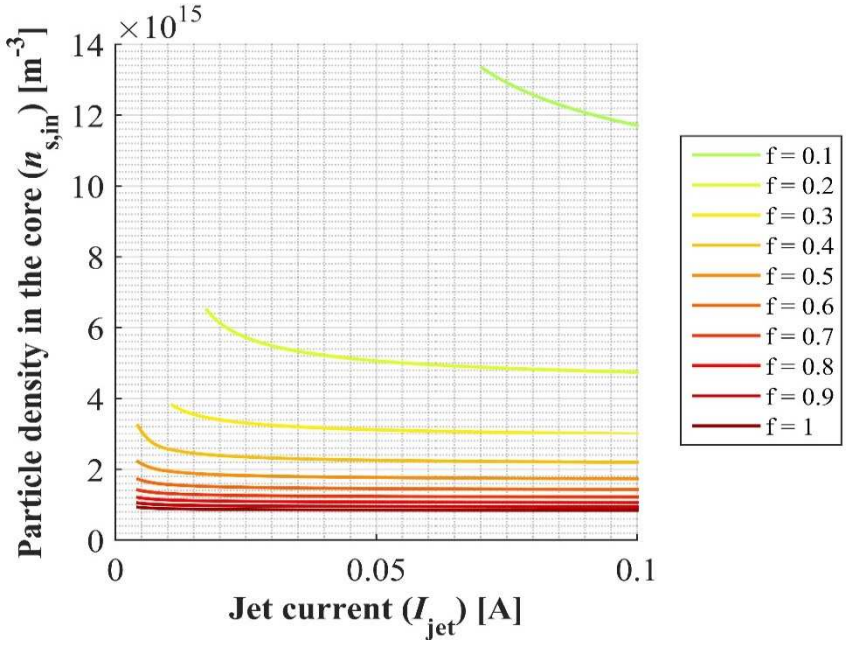

Figure 6.17 Plasma density in the inner region of the low potential SDL, in case of the violation of Langmuir condition, assuming different values for enhanced ion flux on the surface of

the double layer.

All in all, the numerical outputs provided by the preliminary simulation of the low-potential IEC-SDL, relaxing Langmuir condition in the sense of an increased ion current, are in good agreement with both the results provided by the one-dimensional Poissor solver and the experimental observations of the fireball produced in the investigated IEC device operating in tight and spray-jet mode.

High-potential SDL solution

Finally, the high potential solution of the IEC-SDL model is taken under exam, in order to assess the features of the spherical double layer and the physical properties of the confined plasma.

In Fig. 6.18 provides a visual representation of the radius assessed for the high-potential solution of the IEC-SDL model. The comparison of such a result with the one presented in the case of a reduced ion flux on the SDL surface -as in Fig. 6.13- plainly shows a more reasonable dimension of the simulated double layer. In fact, for a decreasing value of the relaxation parameter, the DL radius is significantly increasing. Unfortunately, for the lowest values of the relaxation parameter the circuital model provides no solution in correspondence of the experimental conditions tested in the IRS facility [19]. Nevertheless, extrapolating the trend of the simulation output given in Fig. 6.18, it is possible to observed how, for decreasing values of the relaxation parameter below the unit, the simulated SDL radius increases and tends to move towards the value measured in the experiments.

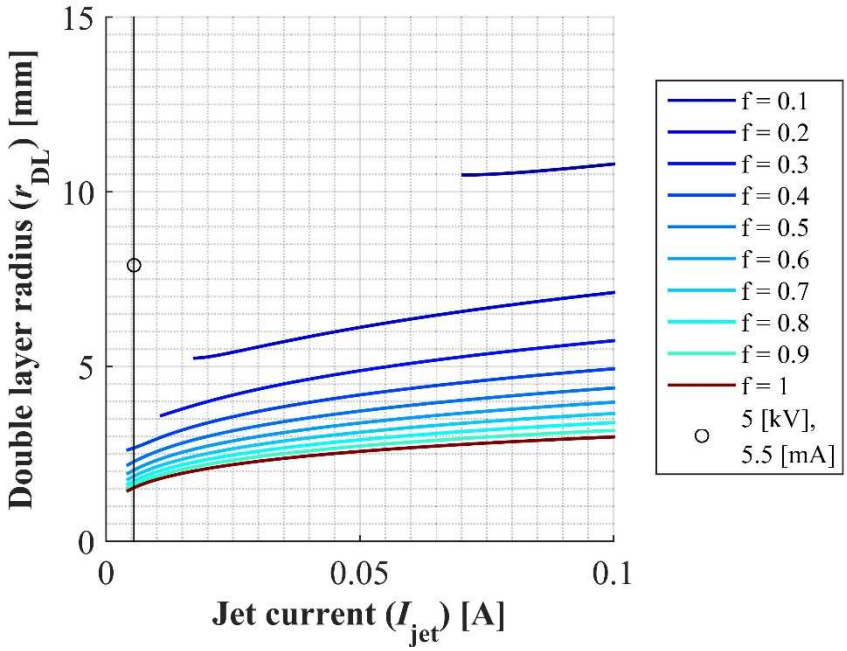

Figure 6.18 Radius of the high potential SDL, in case of the violation of Langmuir condition, assuming different values for enhanced ion flux on the surface of the double layer.

The subsequent analysis of the bulk plasma confined inside the surface of the simulated spherical double layer reveals a rather promising behaviour, as the particle density is remarkably high despite the volume of plasma confined being greater. The particle density, evaluated according to Eq. 6.14 under the different operating conditions and assumed values for the relaxation parameter, is graphically reported in Fig. 6.19. Although the highest values for the plasma density are obtained in correspondence of Langmuir condition, its violation in the sense of an increased ion current does not severely affect the density: in fact, even when the relaxation parameter is reduced to one tenth, the number density for the charged particle in the confined plasma is in the order of 10^{16} [m^{-3}]. This result is in perfectly good agreement with the output provided by the one-dimensional simulation of the IEC device under study, according to the thermal model for the particle distribution function (see Chapter 3, Section 4).

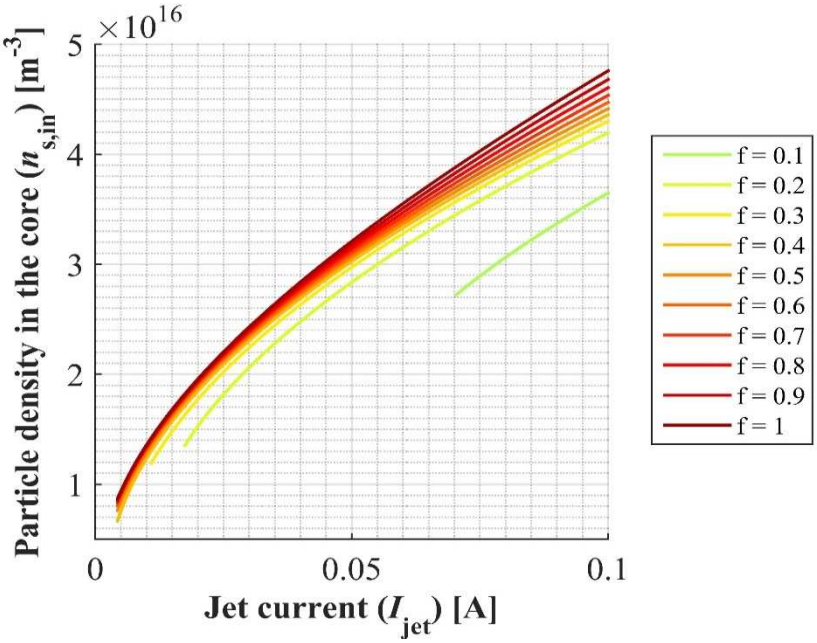

Figure 6.19 Plasma density in the inner region of the high potential SDL, in case of the violation of Langmuir condition, assuming different values for enhanced ion flux on the surface of the double layer.

In conclusion, the violation of Langmuir condition for the analysed SDL, assuming values lower than the unit for the relaxation parameter, allowed for simulating a high-density, thermalised bulk plasma in the core of the IEC device under investigation. Nonetheless, it is still unclear, to date, whether the thickness of the non-neutral shell is small enough, compared to the radius of the electrostatic structure itself, for such a solution to be consistent with the assumptions underlying the circuital model for the spherical double layer (i.e. if Eq. 4.29 is here satisfied).

As already pointed out, the evaluation of the double layer thickness is hindered by the intrinsic limitations of Langmuir's model for the double sheath. Such shortcomings are best understood by looking at Eq. 4.43: it is quite clear that the integrand in this equation assumes, over the integration domain, only real values when the parameter α is smaller than one.

$$\alpha < 1 \Rightarrow \not{f}(\phi) = \frac{1}{\sqrt{\sqrt{\phi} + \alpha\left(\sqrt{1-\phi} - 1\right)}} \in \mathbb{R}, \forall \in]0,1[\tag{6.32}$$

Eq. 6.32 thus entails the impossibility for the relaxation parameter to assume values below the unit, according to Langmuir's double layer model. Indeed, this fact perfectly reflects the physics underlying the double sheath model: the electric current flowing through the cathode (in the description of the plasma observed in a vacuum discharge tube [69]) is space-charge limited until the ionisation of the background gas generates enough ions to counter the negative space-charge. When a stable discharge is established the plasma is self-organised in the previously described discharge structure (see Chapter 4) and the double sheath in proximity of the anode surface is crossed by a net electric current, whose value is limited by the local non-neutrality of the plasma. As a matter of fact, the ions produced by the enhanced ionisation inside the double layer tends to counter the electron space-charge in the negative sheath, increasing the electron carried current. Nonetheless, a limit value exists for the rate of ion emission from the positive sheath, due to the local positive space-charge in it. Hence, the maximum electric current is obtained across the double layer when both the current components are limited by the local non-neutrality in the ion and electron sheaths. Under such conditions, the ion current is limited to a fraction of the electron current, corresponding to the square root of the ratio between the masses of the electron and the ion: this is precisely the Langmuir condition for a double layer, given in Eq. 4.8.

Although this fact might seem rather discouraging, it is critical to underline that the non-applicability of Langmuir model to the simulation of the IEC double layer, for values of the relaxation parameter lower than one, does not invalidate the above-presented simulation outputs. In fact, both the circuital model for the SDL in an IEC device and the subsequent two-fluid plasma modelling in the core region are based on rather general assumptions which do not require the Langmuir model to be enforceable. Moreover, in literature many examples can be found of double layer models, in which $f < 1$: Langmuir condition, hence, does not have general validity, on the contrary of Bohm's criterion[27], which holds for any value of f [64]. Nonetheless, the non-applicability of the double sheath model to the present case leaves the question of the double layer thickness still pending and an alternative DL model is this thus required in order to validate the high-potential solution by comparing the thickness and the radius of the resulting double layer.

[27] Please refer to Chapter 4, Section 2, ¶ Langmuir double layer.

Chapter 7
Conclusions

The master thesis work reported in the present essay was focused on both the theoretical study and the numerical simulation of an inertial electrostatic confinement device, with particular reference to the attainable application of such a technology to an advanced plasma propulsion system, for space applications.

The main issue hindering the development of an effective propulsion system, based on IEC technology, is the current obscurity of some of the plasma phenomena observed in the operation of an IEC device. In particular, the lack of a self-consistent plasma model, capable of depicting the totality of the relevant plasma processes -namely, ionisation, confinement and jet extraction- in an enclosed theoretical background, prevented any reliable prevision of the propulsion performance, an IEC jet thruster might attain. The definition of a physical model for the plasma extraction mechanism, in the specific, is the key component in an effective description of a perspective electric propulsion system relying on IEC technology.

A significant step forward in the comprehension of the plasma physics underlying the operation of a spherical IEC device was recently made at the Institute of Space Systems of Stuttgart University, as Y.A. Chan and G. Herdrich proposed an original theory to model the physical behaviour of the discharge plasma in the core of a spherical device [19]. Until then, the peculiar features of electrostatic confinement in a gridded-electrode configuration had been depicted as resulting from the spontaneous inception of concentric, oppositely charged, electrostatic charges, termed "poissors". It is well known, on the other hand, that such a description of the plasma behaviour inside a glow discharge IEC device has very little accordance with both numerical simulation results and experimental observation: a stable self-organisation of the confined plasma in multiple potential-well structures is extremely unlikely. Such a remarkable issue justified the quest for an alternative physical theory, potentially capable of representing the whole set of the observed plasma phenomena in a thorough, self-consistent picture. The research on IEC technology at IRS thus focused on the development of the alternative double layer model presented in the fourth chapter of the present essay: the behaviour of the core plasma in a spherical IEC device is described in terms of a thin, almost spherical, non-neutral structure, termed "spherical double layer". The specific nature and features of such a double layer determines its electrostatic interaction with the charged particles in the embedding plasma and hence it presents itself as an effective mean for the confinement and enhanced ionisation of the core plasma. Moreover, the envisaged coupling of this electrostatic structure with the actual topology of the electric field, produced by the gridded electrodes, could allow for the long-missing definition of a suitable theoretical model for the jet extraction mechanism.

The work reported in the present dissertation was performed at the IRS, under the supervision of Dr. -Ing. G. Herdrich and M.Sc. Y.A. Chan, and thus formed part of the broader the research effort above depicted. In particular, this master thesis research was mainly aimed at the assessment of the most relevant physical parameters characterising the discharge plasma produced in a spherical IEC device. More specifically, a significant role in the operation of an IEC device is identified as played by the topology of the externally applied electrostatic field, engendered inside the gridded electrodes, and by the spatial distribution of the charged particles inside the device, assessed in terms of the distribution function of each fluid component of the investigated plasma.

The research work in the present thesis was carried out through three main research path, along with the parallel development of the research campaign at IRS:

1. Development of a Poisson solver for the one-dimensional simulation of the device.

2. Development of both a two-dimensional and a three-dimensional Laplace solver for the numerical evaluation of the electrostatic field topology.
3. Assessment of the relevant physical quantities in the confined plasma, described by means of the spherical double layer model, over a range of varying operating conditions.

In the following, the main results achieved are recapitulated and critically discussed. In addition, where sensible, conceivable further developments are delineated in both their objectives and the proposed course of action.

One-dimensional plasma simulation

The reported research focused, at the outset, on the development of a computer tool aimed at the numerical simulation of the discharge plasma confined at the centre if the spherical IEC device available at the IRS test facility. The best numerical approach, for the preliminary assessment of the relevant physical properties of the discharge plasma under investigation, was identified in Lavrent'ev's method, as presented in the third chapter of the present dissertation. The numerical scheme developed by the soviet physicist is indeed the most commonly employed mathematical tool for the numerical evaluation of both the electrostatic potential and the number density distribution for the charge carriers in the core plasma of an IEC device.

This task had already been undertaken -at least to some extent- in 2016, leading on the software implementation of Lavrent'ev's numerical scheme, assuming both mono-energetic and rectangular PDFs for the charged particle populations in the investigated plasma [26]. The work done by C.C. Dobson and I. Hrbud [14] was referred, in the research work conducted by B.Sc. D. Galla at IRS [26], for both the definition of the distribution functions -in the mono-energetic and rectangular models- and the validation of simulation results. Despite the IEC device at IRS having a different geometry with respect to that simulated by C.C. Dobson and I. Hrbud, the simulation output reported in Galla's dissertation -in the form of the electrostatic potential profile- show a significant qualitative agreement with those presented in Ref. [14]. Moving from the endeavour already carried out on the mono-energetic and rectangular simulation models, the present research focused on the definition of a physical model relying on more reasonable assumptions: the thermal modelled depicted in Ref. [14] was thus identified as the best alternative. Such a plasma model accounts for the effects of the collisional processes in the core plasma, neglected in lower level models such as the mono-energetic and the rectangular. Through the particle collisions, the plasma inherently tends to reach the thermodynamic equilibrium; hence, the collisional processes determine the relaxation of the initial particle distribution functions toward a Maxwell-Boltzmann distribution. The thermal model thus accounts for the particle collisions inside the IEC device by considering a Maxwellian-like form for the distribution functions. This model was hence implemented in a computer script and an overall simulation tool was developed in Matlab environment, integrating the mono-energetic, the rectangular and the thermal model in a unified numerical solver.

The consequent simulation of the investigated IEC device, by means of the developed numerical tool, proved that the "poissor" theory is inconsistent with the predicted plasma behaviour in a glow-discharge device. Indeed, as the effect of the charged particles' recirculating motion across the cathode grid is taken into account, along with the collisional processes, the inception of multiple potential-wells is not observed neither in laboratory experiences nor in the numerical plasma simulation. This conclusion drove the research towards the development of an alternative model more capable of effectively depict the physics underlying both the background ionisation and the plasma confinement mechanisms. Such an effort finally led to the definition of the spherical double layer model, discussed below.

Free-space potential solver

In pursuing a novel plasma model for the IEC device, the research moved from the above-discussed one-dimensional simulation toward a different path, focusing on the preliminary assessment of the three-dimensional layout of the externally applied electrostatic field. The aim of this analysis was to describe

the peculiarity of the electrostatic confinement provided by a gridded electrode configuration: as already stressed out, the electrostatic confinement of a plasma is only possible when the employed electrodes are characterised by a high degree of effective transparency with respect to the charged particles' motion, which are thus "inertially" confined. Hence, the peculiar topology of the electrostatic field produced by the gridded electrodes conceivably plays a significant role in the plasma behaviour inside a gridded IEC device. Although the evaluation of the externally applied electrostatic field needs not to account for the presence of the discharge plasma, such a task represent still a difficult endeavour due to the typical complexity of the electrode geometry.

At a first instance, the mathematical problem was reduced to the simpler case of assessing the two-dimensional topology of the free-space field, assuming an axial symmetry for the device. Hence, the numerical resolution of Laplace equation, describing the investigated electrostatic field, was attained by transposing the problem from the plane to the complex field and, subsequently, deriving the solution in the form of a complex power series. The most significant limitation of such a semi-analytical model is due to the two-dimensional nature of the solution provided, resulting in a non-negligible approximation for the case of a spherical device, such as that available at IRS. The research, therefore, further focused on the assessment of the three-dimensional topology of the externally applied electrostatic field. An original approach was adopted, on suggestion of Professor Ray Sedwick from University of Maryland, relying on Green's function for describing the effect of a point-wise charge, acting as a source for the electrostatic field. The resulting numerical solver was then employed in the simulation of the free-space electrostatic field produced in the IEC device available in the IRS laboratories. This simulation provided an accurate assessment of three-dimensional topology for the electrostatic field, along with quantitative assessment of the local distortion of the electrostatic field in correspondence of the enlarged grid hole. The observation of such a distortion provided a clear hint of the role plaid by the local distortion in breaking the plasma confinement in the core of the device, triggering the plasma jet formation. As far as the field topology is concerned, the calculations are in good agreement, from a quantitative point of view, with those provided by the two-dimensional analysis. On the other hand, the comparison between the visual output of the two and three-dimensional simulation of the same device clearly illustrates the higher level of accuracy of the latter, in depicting the desired field topology.

Given the limited scope of the research, as it was conducted in the framework of a master thesis project, the actual employment of the results achieved in the simulation of the three-dimensional topology for the free-space electrostatic field was, in truth, rather limited. Indeed, the subsequent analysis of the discharge plasma in the core of the investigated device, according to the spherical double layer model proposed in Ref. [19], was based the possibility of neglecting the effect of the actual field topology, assuming the global double layer structure to be akin to a sphere. The resulting DL model for the IEC device is obviously one-dimensional, so that the simulated three-dimensional electrostatic is only employed, with a certain degree of approximation, to assess the value of the electrostatic potential on the low-potential surface of the double layer, as depicted in the sixth chapter of the present dissertation. Nonetheless, the developed free-space solver is a valid tool for the preliminary simulation of the electrode-generated electrostatic field, as the field topology itself seems to play a critical role in the most relevant plasma phenomena characterising the discharge plasma produced in a gridded device.

Plasma simulation in the IEC-SDL model

The final step taken in the characterisation in IEC technology for advanced plasma propulsion was the numerical assessment of the plasma properties according to the spherical double layer model presented by Y.A. Chan and G. Herdrich [19]. According to such a theory, the discharge plasma generated inside the gridded electrodes is supposed to arrange itself in an enclosed structure characterised by a local electrostatic field. This structure has the form a thin shell constituted by two adjacent layers of plasma each one dominated by a charged particle population, so that the resulting layers are oppositely charged and an electrostatic potential drop results across the shell thickness. The resulting plasma structure has an approximately spherical shape and, due to the electromagnetic interaction between the charged particle

in the surrounding plasma and its inner electrostatic field, provides the both the plasma confinement and an enhanced electron-impact ionisation.

Assuming the spherical double layer to be an overall neutral plasma volume, a circuital model was developed, providing an estimate of the double layer radius and of the voltage drop across it, in correspondence of different values for the applied electrode voltage and the electric current carried by the extracted jet. This model further requires the *a priori* assumption of the current ratio on the SDL surface, i.e. the ratio between the ion flux on the high potential side of the DL, due to the particles' thermal motion, and the electron flux on the low potential side, driven by the topology of the applied electrostatic field. At a first instance, Langmuir condition was theorised to hold for the investigated double layer, so that the ion-to-electron current ratio equated the squared root of the electron-to-ion mass ratio. The spherical double layer was then simulated over a range of different operating conditions, for a varying electrode voltage, power-supply current and background neutral gas pressure: a solution database for the Langmuir SDL was thus obtained.

The two-fluid modelling of the bulk plasma confined inside the DL surface subsequently allowed for assessing the most relevant plasma features in correspondence of each solution in the database: particular attention was paid to the particles' density in the plasma, since the ensuing of a double layer is expected to result in a highly dense core plasma. Moreover, Langmuir's theory of double sheaths provided a theoretical background for analysing the local DL structure and assessing its thickness. The circuital model for the IEC-SDL provided two distinct solutions, characterised by rather distant values for the electrostatic potential, for each operational condition simulated: the preliminary comparison of the SDL radius and thickness allowed for discarding the high potential solution. Hence, the only low potential solution for the Langmuir spherical double layer was taken into account: the consequent plasma analysis revealed a value for the particle density lower than what reasonably expected.

The subsequent step taken in the numerical assessment of the SDL model for the investigated IEC device was the relaxation of Langmuir condition. A suitable quantity, the relaxation parameter, was introduced to account for the violation of Langmuir condition on the current ratio: this parameter allowed for simulating a different behaviour for the double layer under exam. The analysis of the SDL in case of a reduced ion flux -for increasing values of the relaxation parameter, above the unity- resulted in non-sensible solutions: the low potential solutions entail a lower plasma density while the high potential solution dictates a high density but an extremely small radius for the spherical double layer. On the contrary, promising results were obtained in case of an enhanced ion flux -for decreasing values of the relaxation parameter, below the unity-: higher plasma density values are obtained in case of the low potential solution while the high potential solution presents both a remarkably high plasma density and reasonable values for the SDL radius. Nonetheless, the adopted double sheath model proved itself incapable of assessing the thickness of the double layer structure in case of an enhanced ion flux.

In conclusion, the plasma simulation in the core of the investigated IEC device was only partially successful. In particular, the final plasma modelling was able to pin down the most promising range of double layer solutions, entailing a highly dense plasma confined inside a fireball, whose dimensions are consistent with the experimental observations. Nevertheless, a precise value for the ratio between the electron and ion currents on the SDL surface could not be exactly determined, nor the analysis was able to assess whether the high potential solution for the spherical double layer is more reasonable than the low potential one.

Further research and development

The research work carried out achieved a number of different objectives in the characterisation of the investigated IEC device and the assessment of the plasma behaviour inside it. The most remarkable accomplishment being the important role it played in aiding the development of the spherical double layer model presented in Ref. [19], which promise to represent the novel background in the study of inertial electrostatic confinement. Nonetheless, the narrow scope of the presented research effort limited

the possibility of thoroughly characterise the actual double layer structure in the core plasma inside the cathode grid. It is thus clear that further effort needs to be spent on the IEC-SDL model, in order to attain a clear, reliable plasma model capable of thoroughly describing the physics underlying the whole set of plasma phenomena observed in the operation of an IEC device.

The two-fluid plasma modelling further showed the limitations of the employed Langmuir's double sheath theory, which is incapable of accounting for an enhanced ion flux on the inner surface of the double layer. Hence, the first objective of the future investigation on the IEC-SDL model should be the definition of a proper theory for the description of the spherical double layer, accounting for the peculiarity of the investigated electrostatic structure. In this respect, particular attention should be paid to the detailed description of the geometrical configuration of the DL in a non-symmetric electric field topology.

A preliminary theoretical analysis of the IEC double layer could be carried out by means of a theoretical model, developed from the Bernstein-Greene-Kruskal method [20] or, alternatively, employing "classical potential" (or "Sagdeev potential") method [64]. Both these methods provide a kinetic description of the investigated plasma, thus allow for a suitable definition of the distribution function for the charged particle populations fostering the double layer. Hence, a preliminary analytic description of the spherical double layer should be attainable under the simplifying assumption of neglecting the actual three-dimensional geometry of the SDL.

As the actual topology of the DL seems to play a critical role in the both the plasma confinement and the jet extraction, though, the three-dimensional nature of the plasma dynamics needs to be tackled. Hence, the employment of a Particle-In-Cell simulation is proposed, in light of the simulation carried out by B. Scheiner *et al*, which proved the method to be a valuable tool for the assessment of the generation and dynamics of a spherical double layer [65]. Moreover, PIC method could allow for modelling the electromagnetic interaction of the cathode-emitted electrons with the electrostatic field and relative dynamics. The possibility of simulating the resulting double layer under different field topologies should provide a deeper insight into the influence of the electrostatic field in the overall double layer configuration and the jet extraction mechanism.

In addition, the IEC-SDL model could provide a theoretical framework for the analytical description of the plasma physics underlying the jet extraction mechanism. As already pointed out, many experimental observations showed the existence of a plasma jet escaping from the plasma confinement under suitable operating condition [7]; yet, to this day, a reliable explanation of such a phenomenon is still missing. Given the critical role played by the jet formation in the potential application of inertial electrostatic confinement as an electric propulsion technology for space applications, is vital to devise a theoretical model, self-consistently explaining such a behaviour in the broader context of IEC plasma physics. The IEC-SDL is expected to achieve such a key goal, due to the extension of the well-known concept of surface tension to the plasma volume confined inside the spherical double layer.

Surface tension of condensed matter is due to the cohesive forces, exerted among the constitutive particles, which keep the matter condensed. In general, the cohesive forces in a uniform plasma are negligible due to the Debye shielding and the resulting quasi-neutral behaviour. On the other hand, if a local non-uniformity is provided in the plasma, such as in the case of a double layer, an electrostatic field ensue across the inhomogeneous region (i.e. the DL thickness) and the resulting electromagnetic interaction is much more relevant than the residual cohesive field in a uniform plasma. Therefore, it is possible to define the surface tension of a spherical double layer as the ratio between the electric field energy, inherent to the non-neutral plasma structure, and the DL surface area [71]. The local deformation of the electrostatic field, due to the asymmetric electrode configuration, acts on the spherical double layer stretching it in correspondence of the enlarged grid opening. When the local gradient induced by the asymmetry of the external electrostatic potential reaches a critical value, it might overcome the double layer surface tension, resulting in an outward acceleration of the confined plasma. Thus, in this scenario, the plasma jet extraction is depicted as analogous to the well-known phenomenon of a Taylor cone

formation and electro-spray [72]. The well-established knowledge of the physics underlying this phenomenon and its practical application in the Field Emission Electric Propulsion technology [76] would be the basis of the definition of a surface tension model, for the DL in the core plasma of an IEC device, aimed at the assessment of the extraction mechanism for the plasma jet.

In conclusion, the developed spherical double layer model promise to be the novel background theory for the inertial electrostatic confinement of a plasma, depicting all the relevant plasma phenomena observed to take place in an IEC device -i.e. background ionisation, plasma confinement and jet extraction-, in a thorough, self-consistent theoretical framework.

Appendix A
Technology development and State of the art

A.1 Historical background

According T. Dolan [5], the idea of containing highly energetic plasmas by means of the inertial electrostatic confinement scheme -detailed in Chapter 2 of the present essay- was originally conceived by Ukrainian physicist Oleg. A. Lavrent'ev, in the former Soviet Union, on June 22nd, 1950. On top of that, Lavrent'ev was the first one to ponder, in 1951, the employment of magnetic field to enhance and stabilise the electrostatic confinement, anticipating R.W. Bussard's concept for high-energy power-source (HEPT or Polywell) by some thirty years.

Almost at the same time, American physicist and inventor Philo T. Farnsworth conceived the same idea and proposed experiment at the ITT corporation [8]. Indeed, although his first patent for an apparatus developed on such a mechanism was only filed in January 11th, 1962 [6], the research on electrostatic confinement started more than thirty years before [9]. According to Robert L. Hirsch's personal correspondence, in the earlies 1930s Farnsworth was working on vacuum tubes -considering their possible use in electron televisions, whose first prototype he has patented in 1927- when he conceived the electrostatic confinement [9]. In truth, he noted the existence of a localized glow at the centre of a spherically symmetric, high-vacuum multipactor tube (same as shown in Fig. A.1): this phenomenon is today commonly known as "multipactor effect" [77]. He later reasoned that radially focused electron currents were producing a space charge, potential well in the hollow anode cavity: this well was confining and concentrating ions, which were produced from residual gas. While the operation of the multipactor tube has not been studied in detail, the concept of confinement in a dynamically produced potential well has received further consideration.

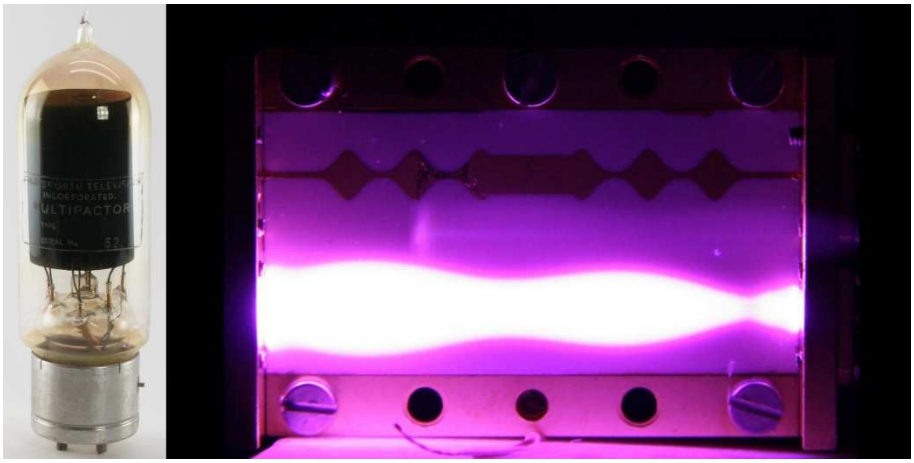

Figure A.1 (a) Example of multipactor tube, manufacture by Farnsworth Television Inc. on P.T. Farnsworth patent US2.141.837 [77]
(b) Glow discharge plasma engendered in a microstrip RF antenna, due to the multipactor effect.

In the mid-1950's Farnsworth suggested that the ion the mechanism of potential well formation -responsible for the ion constraint and consequent discharge phenomenon inside the multipactor- could be exploited in order to confine and focus highly energetic ions in a small volume: an appreciable number of nuclear fusion reactions could have then occurred. At the same time, W.C. Elmore *et al.* analysed a fusion device based upon particle confinement, in spherical potential wells produced by circulating

electrons [12]. Their system was given a spherical geometry and it operated on the assumption of purely radial motion of negative charge-carriers (i.e. electrons) toward the centre of the device itself. On the basis of "*Lawson criterion*" -a criterion for fusion reactors to produce net power-, they reported that such a system would require prohibitively high power inputs to be of thermonuclear interest, and, furthermore, it would probably be unstable [12]. Subsequently, J.L. Tuck expressed interest in a system where in ions played the role given to electrons in the previous model, but did not pursue the subject.

In the light of this theoretical study and Farnsworth's theory on multipactors, International Telephone and Telegraph (ITT) initiated a testing programme to investigate this technique of fusion-gas confinement, involving Robert L. Hirsch: his results were eventually published in 1967 in the (already cited) seminal paper "Inertial-Electrostatic Confinement of Ionized Fusion Gases" [9]. Supported by the ITT Corporation, Farnsworth and Hirsch constructed a device that used six inwardly directed ion guns mounted on a sphere, all injecting into a central cavity to produce 10^{10} neutrons per second in steady state operation, using Deuterium gas.

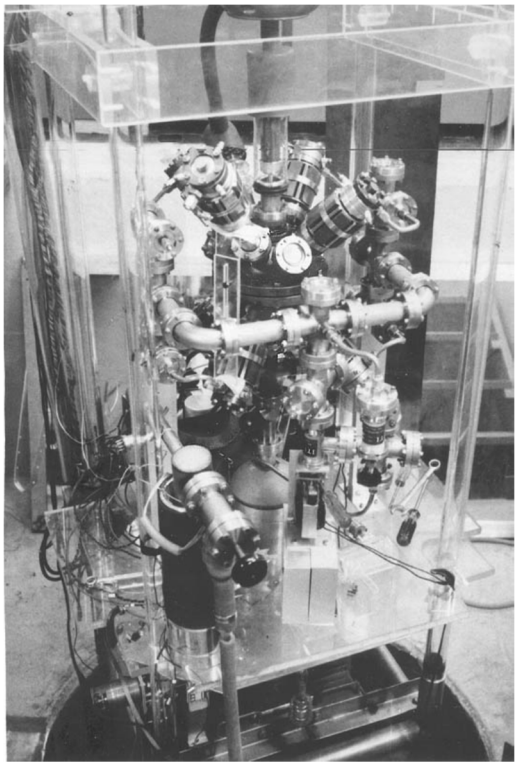

Figure A.2 Hirsch ITT experiment set-up, cutaway view [28].

On the theoretical side, the phenomena of space charge and particle trapping in potential wells was already well known, at that time. In the earlies 1910s, Clement D. Child had investigated space-charge effects in a plane-parallel diode -developing a functional relation between carried current and applied potential, nowadays known as "Child's law"-, after which Irving Langmuir and his co-worker studied other electrode configurations. The "*ITT Farnsworth Research Corporation"* group predicted the electrodes' central region to form multiple potential wells (that they first called "poissors"), developing the conceptual basis exposed in Chapter 2. Finally, Farnsworth and Hirsch's research efforts led to a series of patents for the first prototypes of fusors [6, 23, 34]. In Fig. A.3 the schematics of both Farnsworth's and Hirsch's fusor devices are provided.

Farnsworth-Hirsch fusor design proved itself able of firmly providing net fusion power and was thus, in this respect, a successful design (their fusion output has yet to be exceeded); nevertheless, the fusion energy gain reached by such a device was quite low, being in the order of magnitude of $\sim 3 \cdot 10^{-4}$ [9, 28].

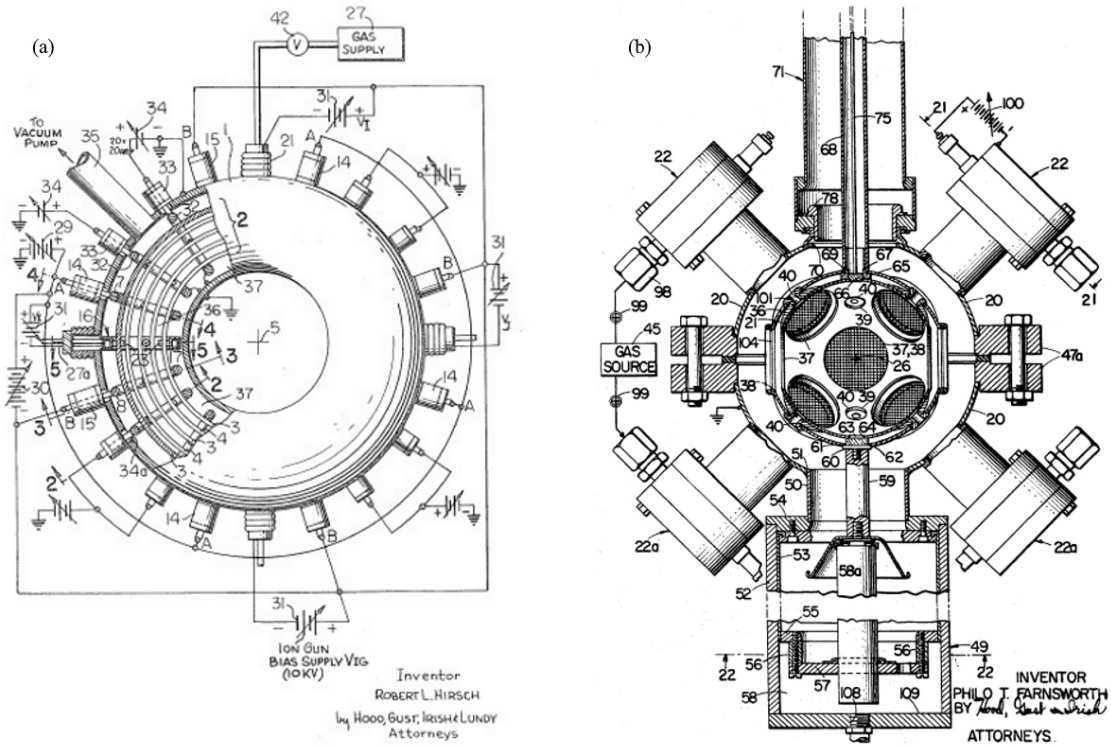

Figure A.3 (a) R.L. Hirsch's fusor, as filed US 3.664.920 patent [34]
(b) P.T. Farnsworth fusor, patented US 3386883 file [23].

Concurrently, in the USSR, interest in electrostatic confinement arose and O.A. Lavrent'ev -who published, in 1963, a paper where he took into consideration the case of symmetric ion and electron injection both in planar and spherically symmetrical devices- achieved great theoretical progresses. Lavrent'ev developed a one-dimensional kinetic model based on the resolution of Poisson's equation (see Chapter 2, Section 1, Eq. 2.1), for arbitrary charge-carriers distribution functions. His solutions exhibited potential wells for various distribution functions of interest, i.e., parabolic, Gaussian, and Maxwellian but he did not, however, carry his analysis so far as to detail the shapes of the potentials [9]. Lavrent'ev's kinetic model is one of the most commonly employed tool for the numerical simulation of a steady-state IEC device and will be thoroughly explained the third chapter of the present essay.

Beyond these theoretical endeavours, experiments languished until the late 1980s, when George H. Miley, in the Fusion Studies Laboratory at the University of Illinois (UIUC), tested the first IEC device employing a glow discharge as the main ion source, i.e. the GD design. The employment of such a design, rather than the ES tested on fusion research application, was motivated by the possibility of developing a marketable low-level neutron source for neutron activation analysis (NAA) applications. Miley's research group at UIUC developed simplified devices that are generally capable of producing 10^6 neutrons per second: the use of one of these IEC device for NAA identification of impurities in ores, by former Daimler-Chrysler Aerospace Corporation, in Germany, was the first commercial use of a fusing plasma [8]. On top of that, the Illinois group performed a large amount of experimental and theoretical work, including conceptualization of spacecraft systems relying on favourable power scaling arising from the poissor phenomenon [28].

On the wake of Miley's work at UIUC, the NASA Marshall Space Flight Center launched a research campaign aimed to attain the IEC scaling laws at higher input powers: in fact, the conceptual use of fusion reactors as power sources for spacecrafts relies on a highly favourable, non-linear power scaling with input current [28].

As far as IEC fusion research is concerned, it was carried on at the Fusion Technology Institute in the University of Wisconsin: this was focused on the possibility of enhancing the IEC fusion performance

by burning "advanced" fuels. These are loosely defined as any non deuterium–tritium (D–T) fuels, including deuterium–deuterium (D–D), deuterium–helium-3 (D–^{3}He), helium-3–helium-3 (^{3}He–^{3}He) and proton–boron (p–^{11}B). The latter is particularly suitable for possible fusion power-plants as, on one hand, it eliminates the need for tritium breeding and handling, whilst on the other the fusion reaction only yields energetic alpha particles (easily screened for safety purpose) without neutron production. While a proton-boron reactor thus represents the ideal solution, from an environmental and energy sustainability point of view, it is worth noting that the fusion of a p–^{11}B is only possible if highly non-Maxwellian plasma conditions are provided, reducing cyclotron radiation and Bremsstrahlung losses. Hence, inertial electrostatic confinement is one of the few confinement technique theoretically capable of burning p–^{11}B. In parallel, advanced IEC fusion research is conducted in Japan, namely at Kyoto, Kobe and Tokyo Institute of Technology, and in Australia, at Sidney University.

Regardless of all the effort put in the improvement of inertial electrostatic confinement, no progress has been registered yet as far as the fusion energy gain is concerned. Indeed the ratio of fusion power generated to electrical power input is still the major concern about IEC fusion system: while most experiments have been in the range of $Q = 10^{-7}$, no one has yet to exceed Hirsch's Q of $3 \cdot 10^{-4}$ [28].

Since 2009 [78], the Electric and Advanced Space Propulsion Research Group of the Institute for Space Systems in Stuttgart, Germany, launched a research campaign on inertial electrostatic confinement, on the belief of the IEC device being one of the most promising concepts, for the next generation of the high specific impulse electric thrusters [31]. Hence, the IRS research focused on propulsive GD-IEC devices operates in non-fusing regime: particular consideration was paid to the jet-extraction mechanism (see Chapter 2, Section 1, ¶ Operating modes), since its description is critical to the enhancement of the propulsive performance of an IEC device [44].

A.2 State of the art

¶ Multi-grid device

According to Carl C. Dietrich, from Massachusetts Institute of Technology, the primary limiter for IEC-based fusion is the extremely short energy confinement time, portrayed by the short charged particle confinement time in the system [29]. Under typical IEC operating parameters, electrons stream out from the central cathode and are collected on the outer anode, and ions typically make only about ten passes through the cathode before being lost by either colliding on one of the grid wires or undergoing a charge-exchange reaction with background gas in the system. In such a scenario, a charged particle is much more likely to be lost, as a result of its interaction with neutrals or gridded electrode, than to be involved in a fusion reaction.

Thomas J. McGuire identified the need to operate an IEC fusion device in a regime where the ion loss probability is within the fusion energy gain to input power ratio of ion fusion probability (a factor of order 10) in order to approach the breakeven condition, i.e. $Q = 1$ [28]. In order to do so, the system needs to be operated in ultra-high vacuum conditions, thus enhancing the ion-ion total cross-section; moreover, the ion trajectories should be confined in highly focused ion beams, avoiding ion collisions with the cathode grid.

In addressing the latter issue, Prof. Ray Sedwick, from University of Maryland, conceived the employment of multiple acceleration grids, acting like immersion lenses in particle accelerators. His concept design then employs three or more independently biased, concentric spherical grids, whose applied voltage is tailored to the required electrostatic potential layout. In the same way as the screen-accelerator grids in a common ion thruster, the multiple cathode grids in Sedwick's concept are designed to engender a suitable electric field, focusing the ion beam towards the IEC device centre. The space-charge effects, defocusing the resulting beams inside the cathode, can be reduced by the innermost grid by decelerating the ions before they reach the core (again, this concept resembles the acceleration-

deceleration design employed in common ion thrusters). Moreover, if the innermost grid is manufacture in a suitable material (e.g. Tungsten-Tantalum alloy) it could have a electron emission rate sufficient to the neutralisation of the incoming ion beams, thus eliding the space-charge defocusing effect in the core region.

McGuire numerically proved the validity of such a concept and showed that, by operating in an adequate vacuum condition and employing the most suitable ion focusing design, the typical ion confinement times would to be improved by three orders of magnitude – from 10 passes to 10,000 passes, dependent on the background pressure [29]. By adopting Sedwick's multi-grid design, the two major loss channel in inertial electrostatic confinement devices can thus be reduced, allowing for a drastic improvement in IEC efficiency.

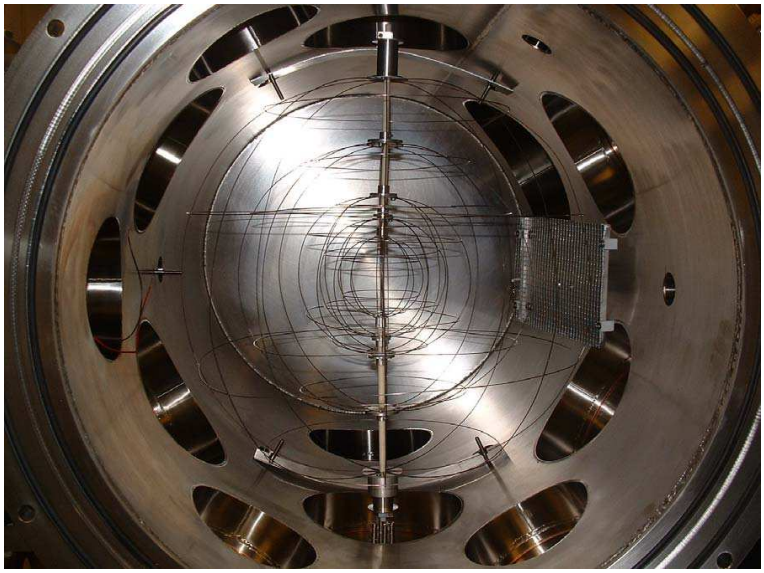

Figure A.4 Multi-grid IEC device in vacuum chamber [29].

¶ Periodically oscillating plasma sphere device

In 1998, D.C. Barnes and R.A. Nebel tackled the problem of large-amplitude spherical oscillations of an ion cloud in an IEC device. In the resulting publication, the stability of ion fluctuations of a Gaussian profile in a spherical, harmonic well was disclosed; moreover, they showed that the ion state forms a thermal equilibrium, in spite of the order of magnitude for density and temperature changes, during the oscillation period [79]. Hence, by introducing a harmonic oscillator potential, induced by a uniform electron background, a small ion cloud may undergo a self-similar collapse: a dynamic IEC behaviour results on account of the oscillating ion cloud. A device exploiting such an operating principle then is able of confining a fusing plasma thanks to the dynamic inception of a stable, virtual cathode [80]: this kind of plasma device was referred to as "periodically oscillating plasma sphere device" or "POPS".

Peculiarity of POPS concept is the capability of providing a different ion density distribution rather than the conventional ion focusing IEC (i.e. the fusor design): such an ion distribution resembles more a Maxwellian distribution and was proven stable through the harmonic potential oscillations, thus bypassing the stability issue hindering the multiple-well ion focusing in canonical IEC designs.

A key issue yet to be addressed, in order to assess the suitability of such a design to a fusion power plant, is the amount of plasma compression achievable by the potential oscillations [8].

¶ Gridless device

Pursuing the same objective -i.e. improving the system efficiency in order to achieve the breakthrough condition- a design, different from the multi-grid IEC proposed by McGuire and Dietrich, was conceived: namely a grid-less device. Grid-less inertial electrostatic confinement is, in a sense, a hybrid concept: involving magnetic field to play the role of the gridded electrodes in a canonical IEC, this devices are somewhere between inertial electrostatic confinement and magnetic confinement fusion systems, such as Tokamak (e.g. in Fig. A.5).

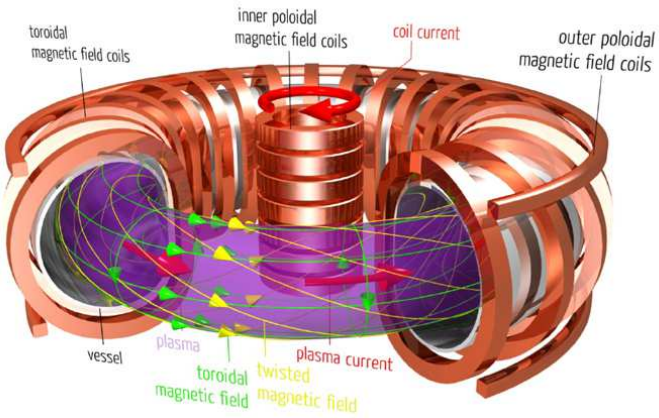

Figure A.5 Schematic of the average tokamak [81].

Several grid-less IEC designs have been proposed over the years, in particular two different concepts have been most delved into: Penning-traps and polyhedral magnetic cusps (commonly known as Polywell).

In the 1990s T.B. Mitchell *et al.* started a research campaign, at Los Alamos National Laboratory, focused on the development of a fusion reactor based on spherical focusing of ions in dense, non-neutral plasmas [82]. The specificity of such a project was embodied by the absence of the gridded cathode to generate the potential well responsible, accordingly to the physical mechanism detailed in the previous paragraph, for ion confinement and focusing. In place of the solid grid, their design involved a small (3[mm]radius) Penning trap to confine low-energy electrons, injected at a single pole of the sphere. Penning trap is a device invented by Nobel laureate Hans G. Dehmelt, which allows to trap (i.e. confine) a charged particle indefinitely, by means of the combination of an electric quadrupole and a magnetic field. Hence, this device is composed of electrodes in form of hyperbola of revolution (as shown in Fig. A.6.a) responsible for the generation of an electric quadrupole field, while a strong, uniform magnetic field is super-imposed along the axis of the trap. The resulting electromagnetic field is depicted in Fig. A.6.b.

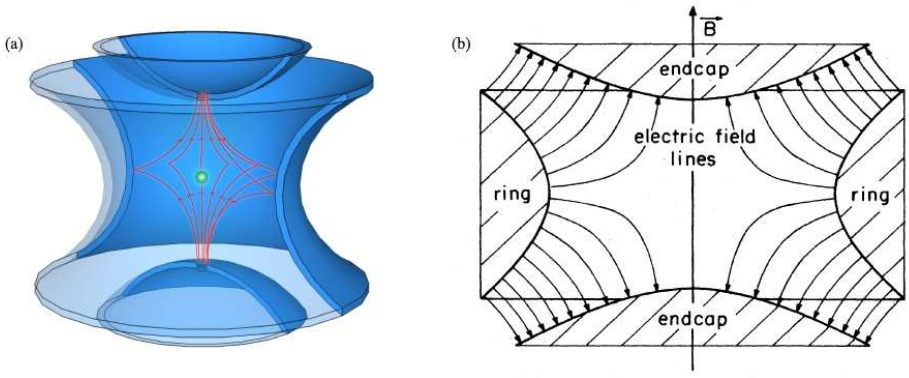

Figure A.6 Three-dimensional rendering and schematic of a Penning trap, employing magnetic and electric field to confine charged particles [83].

Electrons are initially introduced into the trap by applying a high voltage to the field emission point: this produces a beam of energetic electrons that collide with the very sparse residual gas atoms to produce slow electrons, which are then captured in the trap. Thus, electrons are confined by the device's electromagnetic field and their resultant motion consists of a fast circular cyclotron motion with a small radius carried along by a slow circular magnetron drift motion in a large orbit: the outcome is an epicyclical orbit in the *x-y* plane (Fig. A.7.a). In addition, the electrons oscillates harmonically along the *z*-axis perpendicular to the *x-y* plane, i.e. the axis of the magnetic field (Fig. A.7.b) [84].

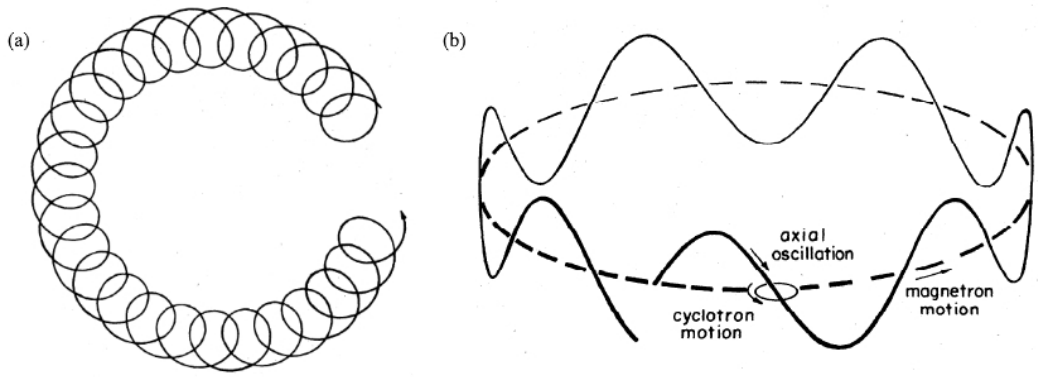

Figure A.7 Orbit of a charged particle in a Penning trap. The total motion is given by the superimposition of a slow magnetron circle motion (dashed line), an axial oscillation (resulting in the solid sinusoidal line) and the fast but small cyclotron circular motion about the particle's moving guiding centre [84].

Precisely when the trap parameters are adjusted to produce a spherical well, the system self-organizes into a spherical state through a bootstrapping mechanism, which produces a hysteresis [82].

Fascinated by an idea originally conceived by Lavrent'ev in 1951 [85], American physicist Robert W. Bussard -who spent much of his professional life in the field of nuclear fusion research, working along with Hirsch in the U.S. Atomic Energy Commission- started, in the mid-1980s, working on a new concept design for inertial electrostatic confinement: the Polywell. Bussard's Polywell (whose name comes from the contraction of "polyhedral" and "well") is based on the use of Magneto-hydrodynamically (MHD) stable, quasi-spherical, polyhedral magnetic fields to contain energetic electrons, which are injected to form a negative potential well [86]. These fields consist of point cusps arranged in an alternating pattern in a generally spherical geometry around the confinement region, such that they occupy the faces of polyhedra with an even number of faces around each vertex.

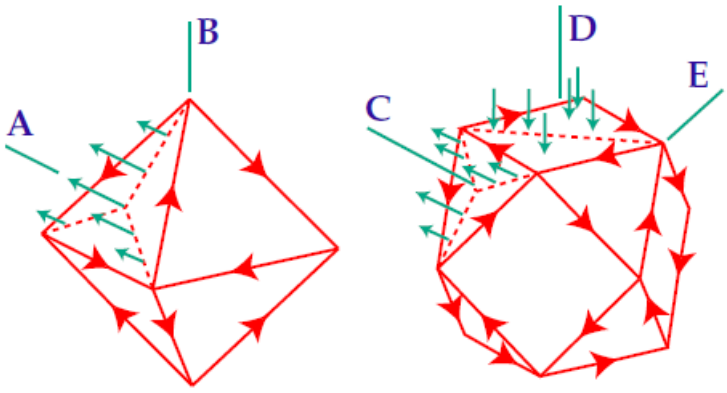

Figure A.8 Octahedral and truncated cube polyhedral geometries, showing face-centre magnetic fields (A, C, D), field direction on face-symmetry lines, and axes of null field (B, E). Arrows on polyhedron edges indicate direction of current flow in edge conductors to product desired fields [86]

he magnetically confined electrons play thus the same role as the gridded cathode plays in canonical IEC: they provide the potential well responsible for ions confinement and focusing. Beneficial features of such a design being the avoidance of IEC's losses, due to ions' collisions with the grid, and all the structural issues related to electrodes over-heating and sputtering.

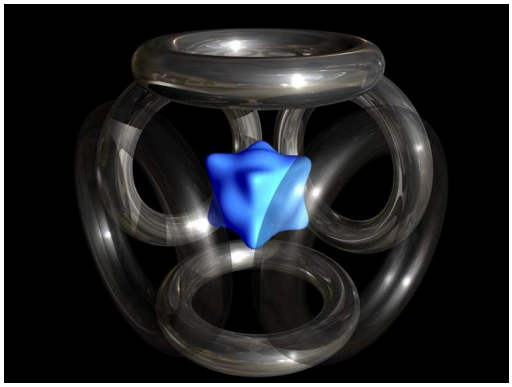

Figure A.9 Three-dimensional rendering for the magnetic cusp field, employed in the confinement of the injected electron population, from which a virtual cathode yields [87]

In 1987 Bussard started a research program (funded firstly by the Defense Threat Reduction Agency and later by DARPA) in order to deliver a first Polywell prototype for the U.S. Navy [28]: his efforts resulted in a patent registered in 1989 [88] and a scientific publications dating the same year [86]. In this very paper, Bussard provided a simple phenomenological model for his system, showing that::

1. Polywell design is proven stable against internal and global perturbations by virtue of the effects of both the external magnetic fields (in the order of magnitude of 1÷5 [kG]) and the large central azimuthally isotropic power flow due to conservation of transverse momentum in the recirculating ion flow.
2. Electron current recirculation ratios must be of the order of 10^5 for net fusion power operation.
3. Losses -mainly due to bremsstrahlung and synchrotron radiation- can be kept small relative to fusion power generation, and ion energy Maxwellianization –due to Coulomb scattering- might be contained into reasonable levels by operating the system at sufficiently large well depth [89].
4. Fusion energy gain, for the system, in the order of magnitude of 10÷100 seems feasible from several fusion fuels.
5. No zeroth-order impediments have yet been found to this highly speculative concept, nevertheless feasibility must be determined by study of more complex and detailed phenomena.

Energy/Matter Conversion Corporation, Inc. (EMC2), the company Bussard founded in 1985 to develop his concept, is at the moment searching for more funding in order to deliver a functioning fusion reactor based on Polywell design [90]. At the same time, Bussard's bewitching idea is been studied by several universities [91, 92] and organizations such as ProtonBoron.

Appendix B
Fundamentals of plasma simulation in an IEC device

B.1 Plasma modelling

¶ Kinetic model

For the purpose of the present thesis, a plasma can be regarded as a highly ionised gas, consisting of nuclei and electrons: due to its nature, a plasma is dominated by the electromagnetic interaction between the constituting particles and thus shows a collective behaviour [3]. The first plasma model, presented in the present appendix is the so-called "kinetic model", a microscopic description encompassing the motion of all the individual charged particles in the plasma [93]. Given the factual impossibility of describing the motion of each and every charged particle in a very large set, in most of the relevant cases plasmas need to be described as statistical ensembles, to whom the means of statistical mechanics apply. Hence, the kinetic description of a plasma entails recasting the unattainable description of the Newtonian motion of each particle in the considered plasma volume -under the body forces acting on it- in the Hamilton-Jacoby formulation. Each species (e.g. ions, electrons and neutrals) in the investigated plasma is thus described by means of a PDF over the phase space. The time-evolution of each distribution function in the phase space is described by Hamilton's equation or equivalently by Liouville's theorem, stating that for a quasi-closed system[28], the distribution is constant along the phase space trajectories of the system, as expressed by Eq. B.1.

$$\frac{\mathrm{d}f}{\mathrm{d}t} = \sum_{i=1}^{N} \left(\frac{\partial f_s}{\partial q_i} \dot{q}_\iota + \frac{\partial f}{\partial p_i} \dot{p}_\iota \right) = 0 \tag{B.1}$$

Where f_s, is the PDF for a particle in the "s" population

q_i, is the i-th generalised coordinate in the phase-space

p_i, is the conjugate momentum to the i-th generalised coordinate

N, is the total number of distinct particles in the "s" species.

From Liouville's theorem follows, at once, that every PDF in the phase space must be expressible in terms of a combination of the canonical coordinates (q_i, p_i), these combination are the mechanical invariants or integrals of the motion [94].

Defining $\vec{x}$ and $\vec{v}$ to be respectively the location and velocity vector for a particle in a Cartesian reference frame, and $\vec{a}$ to be the related acceleration, Eq. B.1 can be recast as follows:

$$\frac{\partial f}{\partial t} + \vec{v} \cdot \frac{\partial f}{\partial \vec{x}} + \vec{a} \cdot \frac{\partial f}{\partial \vec{v}} = 0 \qquad f = f(\vec{x}, \vec{v}, t) \tag{B.2}$$

[28] A quasi-closed system is a physical system occurring in weak interaction with the surrounding medium, i.e. such interaction does not destroy the system's structure.

If the effect of the particles' collisions can be neglected[29] with respect to the electromagnetic interaction, the acceleration term can be computed according to Lorentz's equation:

$$\vec{a} = \frac{\vec{F}}{m} = \frac{q}{m}\left(\vec{E} + \vec{v} \times \vec{B}\right) \tag{B.3}$$

Where $\vec{F}$, is the electro-magnetic force acting on a charge particle

$\vec{E}$, is the external electric field

$\vec{B}$, is the external magnetic field

$\vec{v}$, is the particle's velocity

m, is the particle's mass.

Therefore, under assumption of negligible scattering effects, the dynamics of a distribution function for a species in a plasma is depicted by the following equation, known as "Vlasov's equation":

$$\frac{\partial f}{\partial t} + \vec{v} \cdot \frac{\partial f}{\partial \vec{x}} + \frac{q}{m}\left(\vec{E} + \vec{v} \times \vec{B}\right) \cdot \frac{\partial f}{\partial \vec{v}} = 0 \tag{B.4}$$

Hence, Vlasov's equation expresses the conservation of the distribution function along the particles' trajectories in the phase space, under the action of an electromagnetic field. An important entailment of this fact is the above-mentioned possibility of choosing the distribution function, for the particle populations considered in the modelled plasma, to depend on any quantity that is constant along the particles' orbits [95]. In the second section of the present appendix an applicative example is given, namely the Lavrent'ev's method, where the ion and electron distribution functions are expressed as some functions of the physical quantities conserved in the motion of charged particles, that is total mechanical energy and angular momentum.

The kinetic description of a plasma, in terms of PDFs for the constituting particle populations, allows then for the mathematical definition of all the common physical quantities by taking the respective moment of the distribution function.

Number density

The number density for a population of particles in the plasma is determined as the zeroth-order moment of the respective distribution function, ad given in Eq. B.5.

$$n(\vec{x}, t) = \iiint f(\vec{x}, \vec{v}, t)\, \mathrm{d}\vec{v} \tag{B.5}$$

Mean velocity

The mean velocity of a given population of particles in the investigated plasma is determined as the first-order moment, i.e. the expectation value, of the distribution function, as in Eq. B.6.

$$\langle \vec{v} \rangle (\vec{x}, t) = \frac{\iiint \vec{v}\, f(\vec{x}, \vec{v}, t)\, \mathrm{d}\vec{v}}{n(\vec{x}, t)} \tag{B.6}$$

Is thus possible to define the relative velocity for a charged particle in the considered population, as the velocity deviation from the average value:

$$\overrightarrow{v_r}(\vec{x}, t) \doteq \vec{v} - \langle \vec{v} \rangle \tag{B.7}$$

[29] More advanced plasma descriptions entails the modelling of particles' collisions, determining the relaxation of the energy distribution over the phase space: e.g. Fokker-Planck equation introduces a source term in Eq. C.2, which takes into account binary Coulomb collisions [3].

Mean kinetic energy

The mean kinetic energy of a particle population is given in Eq. B.8 and is proportional to the second-order moment, i.e. the variance, of the distribution function (Eq. B.9).

$$\langle \mathrm{E} \rangle(\vec{x}, t) = \frac{m}{2} \frac{\iiint {v_r}^2 \, f(\vec{x}, \vec{v}, t) \, \mathrm{d}\vec{v}}{n(\vec{x}, t)} \tag{B.8}$$

$$\sigma^2{}_{\vec{v}}(\vec{x}, t) = \frac{\iiint {v_r}^2 \, f(\vec{x}, \vec{v}, t) \, \mathrm{d}\vec{v}}{n(\vec{x}, t)} \tag{B.9}$$

It is worth noticing that mean kinetic energy of a particle population is commonly referred to as its kinetic temperature, which do coincide with the thermodynamic temperature in the special case of a fully thermalised population, i.e. when the collisional processes have determined the complete relaxation to the Maxwell-Boltzmann distribution function.

Analogously, the moment-taking approach allows for the definition of all the relevant physical quantities such as the average stress tensor, the average and thermodynamic pressure, the entropy, *etc.* In conclusion, the possibility of defining the mechanical variables of a particle population, in the plasma, as the statistical average of the microscopic features of the particles' motion is the basis of the fluid description of plasmas.

¶ Two-Fluid plasma model

As above-shown, the most relevant plasma parameters can be defined as the velocity-space moments of the particle distribution functions, which represents the physical solution of the kinetic description for the modelled plasma. In a similar way, it is possible to formulate the conservation law for a number of physical quantities in a plasma, by taking the relating moments of plasma kinetic equation[30]: each conserved variable is thus identified by a specific function of the velocity (e.g. trivially, the unity for the conservation of the system mass) according to Eq. B.10.

$$\iiint \not{f}(\vec{v}) \left[\frac{\partial f}{\partial t} + \vec{v} \cdot \frac{\partial f}{\partial \vec{x}} + \frac{q}{m} \left(\vec{E} + \vec{v} \times \vec{B} \right) \cdot \frac{\partial f}{\partial \vec{v}} \right] \mathrm{d}\vec{v} = 0 \tag{B.10}$$

Where $\not{f}(\vec{v})$, is the relevant velocity function for the desired distribution moment.

This mathematical procedure allows for the definition of a set of fluid equations, i.e. partial differential equations for the average physical variables of the particle populations constituting the plasma. In the following, the conservation laws for the mass, linear momentum and energy of a generic species (denoted by the subscript "s") in the plasma, are presented.

Conservation of mass

Taking the zeroth-order moment of Vlasov equation the continuity equation, expressing the local conservation of the subsystem mass, yields:

$$\frac{\partial n_\mathrm{s}}{\partial t} + \nabla \cdot (n_\mathrm{s} \langle \vec{v_\mathrm{s}} \rangle) = 0 \tag{B.11}$$

Introducing the substantive derivative then, it is possible to recast Eq. B.11 in the Lagrangian form given in Eq. B.12; the latter expresses the evolution of the number density, along a phase-trajectory, due to convection.

[30] The most general form for the kinetic equation, expressing the invariance of the microscopic distribution function and taking into account the particle collisions as well as the electromagnetic interaction, is called "Klimontovich equation" [93], whose special form when the collisional term is neglected is the Vlasov's equation, given in Eq. C.4.

$$\frac{\mathrm{d}n_\mathrm{s}}{\mathrm{d}t} = -n_\mathrm{s}\,\nabla\cdot\langle\overrightarrow{v_\mathrm{s}}\rangle \tag{B.12}$$

According to Eq. B.12, in a reference frame moving with the flow velocity, variations in the local density are directly linked to the compression (or expansion) of the flow.

Conservation of momentum

Since the linear momentum of a particle in the modelled plasma is defined to be proportional to the velocity vector field -where the proportionality constant is the particle's mass-, the conservation law for the momentum is obtained by taking the first momentum of the kinetic plasma equation, multiplied by the respective species mass. Hence, Eq. B.13 expresses the conservation law for the generic species "s" in the plasma.

$$\iiint m\,\vec{v}\left[\frac{\partial f}{\partial t}+\vec{v}\cdot\frac{\partial f}{\partial\vec{x}}+\frac{q}{m}\left(\vec{E}+\vec{v}\times\vec{B}\right)\cdot\frac{\partial f}{\partial\vec{v}}\right]\mathrm{d}\vec{v} = \iiint m\,\vec{v}\,\mathcal{C}(f)\,\mathrm{d}\vec{v} \tag{B.13}$$

Where $\mathcal{C}(f)$, is the Coulomb collision operator on the average distribution function f, introducing the effect of the collisional processes, which determine the relaxation of the distribution function over the phase space [95, 93].

Eq. B.14, B.15 and B.16 respectively introduce the definition for the local stress tensor field, pressure tensor field and frictional force density:

$$\overleftrightarrow{\sigma_\mathrm{s}} = \iiint m_\mathrm{s}\left(\overrightarrow{v_{\mathrm{r,s}}}\,\overrightarrow{v_{\mathrm{r,s}}}-\frac{{v_{\mathrm{r,s}}}^2}{3}\overleftrightarrow{I}\right)\mathrm{d}\vec{v} \tag{B.14}$$

$$\overleftrightarrow{p_\mathrm{s}} = \iiint m_\mathrm{s}\,\overrightarrow{v_{\mathrm{r,s}}}\,\overrightarrow{v_{\mathrm{r,s}}}\,f_\mathrm{s}\,\mathrm{d}\vec{v} = p_\mathrm{s}\overleftrightarrow{I}+\overleftrightarrow{\sigma_\mathrm{s}} \tag{B.15}$$

Where p_s, is the kinetic pressure for the considered plasma species.

$$\overrightarrow{R_\mathrm{s}} = \iiint m_\mathrm{s}\,\overrightarrow{v_\mathrm{s}}\,\mathcal{C}(f_\mathrm{s})\,\mathrm{d}\vec{v} \tag{B.16}$$

Is thus possible to recast the conservation law in Eq. B.13 in its differential (or local) form as in Eq. B.17.

$$m_\mathrm{s}\,n_\mathrm{s}\,\frac{\mathrm{d}\langle\overrightarrow{v_\mathrm{s}}\rangle}{\mathrm{d}t} = n_\mathrm{s}\,q_\mathrm{s}\left(\vec{E}+\langle\overrightarrow{v_\mathrm{s}}\rangle\times\vec{B}\right)-\nabla\cdot\overleftrightarrow{p_\mathrm{s}}-\overrightarrow{R_\mathrm{s}} \tag{B.17}$$

Eq. B.17 then represents the average if Newton's second law of motion, over the entire distribution of particles in the "s" species. The left-hand term of Eq. B.17 is the inertial force per unit volume in the moving frame, while the right-hand side is the average contribution due to all the external forces acting on the particles in the considered species.

Conservation of energy

The last equation that is usually introduced for the fluid description of a particle species in the modelled plasma is obtained by taking the energy-related moment of the plasma kinetic equation. Hence, assuming the relevant velocity function to be the kinetic energy ($m\,v_s^2/2$), Eq. B.18 represents the conservation law for the subsystem energy:

$$\iiint m\,\frac{v^2}{2}\left[\frac{\partial f}{\partial t}+\vec{v}\cdot\frac{\partial f}{\partial\vec{x}}+\frac{q}{m}\left(\vec{E}+\vec{v}\times\vec{B}\right)\cdot\frac{\partial f}{\partial\vec{v}}\right]\mathrm{d}\vec{v} = \iiint m\,\frac{v^2}{2}\,\mathcal{C}(f)\,\mathrm{d}\vec{v} \tag{B.18}$$

The introduction of the local tensor fields defined in Eq. B.14, B. 15 and B.16, along with the definition of the local conductive heat flux and the collision-dissipated energy density (given in Eq. B.19 and B.20 respectively), allows for writing the differential form of the conservation law of energy, as in Eq. B.21.

$$\overrightarrow{\mathrm{q_s}} = \iiint m_\mathrm{s} \frac{v_{\mathrm{r,s}}^2}{2} \overrightarrow{v_{\mathrm{r,s}}}\ f_\mathrm{s}\, \mathrm{d}\vec{v} \tag{B.19}$$

$$\mathrm{Q_s} = \iiint m_\mathrm{s} \frac{v_{\mathrm{r,s}}^2}{2} \overrightarrow{v_{\mathrm{r,s}}}\ \mathcal{C}(f)\, \mathrm{d}\vec{v} \tag{B.20}$$

$$\frac{3}{2} n_\mathrm{s} \frac{\mathrm{d}T_\mathrm{s}}{\mathrm{d}t} = -n_\mathrm{s}\, T_\mathrm{s}(\nabla \cdot \langle \overrightarrow{v_\mathrm{s}} \rangle) - \nabla \cdot \overrightarrow{\mathrm{q_s}} - \overleftrightarrow{\sigma_\mathrm{s}} \colon \nabla \langle \overrightarrow{v_\mathrm{s}} \rangle + \mathrm{Q_s} \tag{B.21}$$

Where T_s, is the kinetic temperature of the plasma species.

According to Eq. B.21, the kinetic temperature of a plasma species increases, in the Lagrangian reference frame, due to a compressible flow, the divergence of the conductive heat flux and the dissipation due to both flow-gradient-induced stresses and collisional energy transfer [93]. Moreover, two important limiting cases can be presented, in which Eq. B.21 can be simplified in an algebraic form, representing a state equation for the considered plasma species, which typically provides closure to the differential problem:

- Isothermal limit, when the heat flux dominates the energy dynamics in the plasma and the temperature is therefore spatially uniform [95]

$$\begin{cases} p_\mathrm{s} = n_\mathrm{s}\, \mathrm{k}\, T_\mathrm{s} \\ T_\mathrm{s} = const. \end{cases} \tag{B.22}$$

- Adiabatic limit, when both heat conduction and convection are negligible

$$p_\mathrm{s} \propto {n_\mathrm{s}}^\gamma \tag{B.23}$$

Where γ, is the heat capacity ration for the plasma species.

The conservation laws for mass, momentum and energy are commonly employed in the context of Cauchy continuum mechanics and provide the motion equation in fluid dynamics; in the framework of plasma physics, Eq. B.12, B.17 and B.21 allows for definition of the two-fluid plasma model. This physical model depicts the plasma as a physical system whose average properties are determined in terms of two fluid subsystem, namely the ion and electron population. Hence, the plasma is described as a continuous medium composed of two distinct electromagnetically interacting ad oppositely charged fluids, each of whom is described by the fluid equations in Eq. B.12, B.17 and B.21. In addition, these equations are typically coupled with Maxwell's equations, describing the electromagnetic field interacting with the fluid components of the plasma.

B.2 Lavrent'ev's method for plasma simulation in an IEC device

¶ Mathematical definition of Lavrent'ev's method

The objective of the present appendix is to provide a sufficiently detailed physical and mathematical framework for the numerical plasma simulation presented in Chapter 3. Hence, in the following reference is made to one of the most widely employed mathematical approach for the simulation of the discharge plasma confined in an IEC device: Lavrent'ev's method. This simulation algorithm exploits the typical geometrical symmetry in IEC devices to develop a one-dimensional mathematical model, basing upon two-fluid equations for plasma description.

As shown in the Chapter 2, Section 1, the steady-state operation of an IEC device can be described by means of Poisson's equation, under the assumption of null external magnetic field and steady state operations:

$$\nabla^2 V = \frac{\rho}{\varepsilon_0} \tag{B.24}$$

The space-charge density in Eq. B.24 depends on the average space distribution of the charge carriers in the plasma; in particular, assuming a singly-charged ion population, the space-charge density can be defined with respect to the two-fluid model as the difference of the number density for the ion and electron number densities, multiplied by the elementary charge. The discharge plasma confined in an IEC device is thus described by the following set of equations:

$$\begin{cases} \dfrac{\mathrm{d}n_\mathrm{i}}{\mathrm{d}t} = -n_\mathrm{i}\,\nabla\cdot\langle\vec{v_\mathrm{i}}\rangle \\ m_\mathrm{i}\,n_\mathrm{i}\,\dfrac{\mathrm{d}\langle\vec{v_\mathrm{i}}\rangle}{dt} = n_\mathrm{i}\,q_\mathrm{i}\left(\vec{E}+\langle\vec{v_\mathrm{i}}\rangle\times\vec{B}\right) - \nabla\cdot\vec{p_\mathrm{i}} - \vec{R_\mathrm{i}} \\ \dfrac{3}{2}n_\mathrm{i}\dfrac{\mathrm{d}T_\mathrm{i}}{dt} = -n_\mathrm{i}\,T_\mathrm{i}(\nabla\cdot\langle\vec{v_\mathrm{i}}\rangle) - \nabla\cdot\vec{q_\mathrm{i}} - \vec{\sigma_\mathrm{i}}\colon\nabla\langle\vec{v_\mathrm{i}}\rangle + \mathrm{Q_i} \end{cases} \quad \begin{cases} \dfrac{\mathrm{d}n_\mathrm{e}}{\mathrm{d}t} = -n_\mathrm{e}\,\nabla\cdot\langle\vec{v_\mathrm{e}}\rangle \\ m_\mathrm{e}\,n_\mathrm{e}\,\dfrac{\mathrm{d}\langle\vec{v_\mathrm{e}}\rangle}{dt} = n_\mathrm{e}\,q_\mathrm{e}\left(\vec{E}+\langle\vec{v_\mathrm{e}}\rangle\times\vec{B}\right) - \nabla\cdot\vec{p_\mathrm{e}} - \vec{R_\mathrm{e}} \\ \dfrac{3}{2}n_\mathrm{e}\dfrac{\mathrm{d}T_\mathrm{e}}{dt} = -n_\mathrm{e}\,T_\mathrm{e}(\nabla\cdot\langle\vec{v_\mathrm{e}}\rangle) - \nabla\cdot\vec{q_\mathrm{e}} - \vec{\sigma_\mathrm{e}}\colon\nabla\langle\vec{v_\mathrm{e}}\rangle + \mathrm{Q_e} \end{cases} \tag{B.25}$$

$$\nabla^2 V = \frac{|q_e|}{\varepsilon_0}(n_\mathrm{i} - n_\mathrm{e})$$

Lavrent'ev's method consists, then, in the numerical resolution of Eq. B.24, given an educated guess for the charge-carrier populations' density inside the device. More specifically, an assumption for the PDF of total energy and angular momentum is required: the charge-carrier number densities are then obtained as the zeroth-order moment of the respective distribution functions. In the following, the mathematical form of the numerical simulation model will be retrieved from physical considerations; two different formulation, for the model, will be provided and the connection between them clarified.

Considering Poisson's equation for the electrostatic potential, given the typical symmetry for the device's geometry (being it spherical for S-IEC or axial for C-IEC), it is reasonable to choose a spherical or cylindrical coordinate system instead of a Cartesian one. For the purpose of the present thesis, the IEC device in IRS facility is spherical, thus adopting a spherical reference frame seems the most reasonable choice, without loss of generality

$$\begin{cases} r = \sqrt{x^2+y^2+z^2} \\ \theta = \dfrac{z}{\sqrt{x^2+y^2+z^2}} \\ \varphi = \tan^{-1}\dfrac{y}{x} \end{cases} \tag{B.26}$$

Laplace operator in spherical coordinates assumes, then, the form:

$$\nabla^2(\cdot) = \frac{1}{r^2}\frac{\partial}{\partial r}\left(r^2\frac{\partial(\cdot)}{\partial r}\right) + \frac{1}{r^2\sin\theta}\frac{\partial}{\partial\theta}\left(\sin\theta\frac{\partial(\cdot)}{\partial\theta}\right) + \frac{1}{r^2(\sin\theta)^2}\frac{\partial^2(\cdot)}{\partial\varphi^2} \tag{B.27}$$

If the finiteness of the electrode grids can be neglected so that they can be assumed to be homogeneous surfaces, than from the spherical symmetry of the problem a remarkable simplification in the mathematical form derives:

$$\frac{\partial(\cdot)}{\partial\theta}, \frac{\partial(\cdot)}{\partial\varphi} = 0 \tag{B.28}$$

Thus, Eq. B.24 is recast as

$$\nabla^2(\cdot) = \frac{1}{r^2}\frac{\mathrm{d}}{\mathrm{d}r}\left(r^2\frac{\mathrm{d}(\cdot)}{\mathrm{d}r}\right) \tag{B.29}$$

Hence, the steady-state electric field inside a spherical IEC is described by a second order ODE:

$$\frac{1}{r^2}\frac{\mathrm{d}}{\mathrm{d}r}\left(r^2\frac{\mathrm{d}V}{\mathrm{d}r}\right) = \frac{\rho}{\varepsilon_0} = |q_e|\frac{n_i - n_e}{\varepsilon_0} \tag{B.30}$$

In order to simplify the notation it is common, in literature, to normalise Eq. B.30 with respect to the reference quantities in Tab. B.1

Table B.1 Reference values for the normalisation of Poisson's equation

Physical quantity	Unit of measurement (SI)	Reference value
Radial position (r)	[m]	Cathode radius r_c
Electrostatic potential (V)	[V]	Cathode voltage V_c
Electric charge (q)	[C]	Elementary charge q_e $(or\ e)$

Let then the normalised quantities in Eq. B.36 be defined as:

$$\begin{aligned} \rho &\triangleq \frac{r}{r_c} \qquad normalized\ radius \\ \phi &\triangleq \frac{V}{V_c} \quad normalized\ potential \end{aligned} \tag{B.31}$$

By differentiating Eq. B.31, the following differential relations yields:

$$\begin{aligned} \mathrm{d}\rho &= \frac{\mathrm{d}r}{r_c} \\ \mathrm{d}\phi &= \frac{\mathrm{d}V}{V_c} \end{aligned} \tag{B.32}$$

Hence, the radial derivative is normalised as follows:

$$\frac{\mathrm{d}(\cdot)}{\mathrm{d}r} = \frac{\mathrm{d}(\cdot)}{\mathrm{d}\rho}\frac{\mathrm{d}\rho}{\mathrm{d}r} = \frac{\mathrm{d}(\cdot)}{\mathrm{d}\rho}\frac{1}{r_c} \tag{B.33}$$

Therefore, Poisson's equation for the normalised electrostatic potential inside a Spherical-IEC yields:

$$\frac{1}{\rho^2}\frac{\mathrm{d}}{\mathrm{d}\rho}\left(\rho^2\frac{\mathrm{d}\phi}{\mathrm{d}\rho}\right) = \frac{r_c^2}{V_c}|q_e|\frac{n_i - n_e}{\varepsilon_0} \tag{B.34}$$

It is then possible to define a quantity that, although not having any physical meaning, is dimensionally a number density and, along the lines the drove the normalisation, can be referred to as "cathode number density":

$$n_c \triangleq \frac{V_c}{|q_e|}\frac{\varepsilon_0}{r_c^2} \tag{B.35}$$

By substituting relation Eq. B.35 into Eq. B.34 the final form for the normalised Poisson's equation – that will serve as a mathematical model for the IEC operation- is determined as:

$$\frac{1}{\rho^2}\frac{\mathrm{d}}{\mathrm{d}\rho}\left(\rho^2\frac{\mathrm{d}\phi}{\mathrm{d}\rho}\right) = \frac{n_i - n_e}{n_c} \tag{B.36}$$

It is worth pointing out that only lesser differences arise in the mathematical formulation when a cylindrical symmetry in assumed in place of the spherical one:

$$\begin{cases} r = \sqrt{x^2 + y^2} \\ \varphi = \tan^{-1}\dfrac{y}{x} \\ z \end{cases} \tag{B.37}$$

In such a reference frame Laplace operator has then the form:

$$\nabla^2(\cdot) = \frac{1}{r}\frac{\partial}{\partial r}\left(r\frac{\partial(\cdot)}{\partial r}\right) + \frac{1}{r^2}\frac{\partial^2(\cdot)}{\partial \varphi^2} + \frac{\partial^2(\cdot)}{\partial z^2} \tag{B.38}$$

Assuming a cylindrical symmetry form the physical quantities inside the device:

$$\frac{\partial(\cdot)}{\partial \varphi}, \frac{\partial(\cdot)}{\partial z} = 0 \tag{B.39}$$

Hence the Laplacian in cylindrical coordinates results

$$\nabla^2(\cdot) = \frac{1}{r}\frac{\mathrm{d}}{\mathrm{d}r}\left(r\frac{\mathrm{d}(\cdot)}{\mathrm{d}r}\right) \tag{B.40}$$

The normalised Poisson's equation for the electrostatic potential inside a Cylindrical-IEC is finally derived as in Eq. B.41:

$$\frac{1}{\rho}\frac{\mathrm{d}}{\mathrm{d}\rho}\left(\rho\frac{\mathrm{d}\phi}{\mathrm{d}\rho}\right) = \frac{n_i - n_e}{n_\mathrm{c}} \tag{B.41}$$

Either way, the mathematical formulation attained (Eq. B.36 or Eq. 3.41) describes the electrostatic potential depending on the distribution for the charge-carrier populations inside the IEB.

The spatial distribution of ion and electron number densities, inside an IEC device, depend on the topology of the electrostatic field, according to Eq. B.42:

$$\vec{F} = q\vec{E} \tag{B.42}$$

Lavrent'ev's method requires thus the *a priori* assumption of the PDFs, for the charge-carrier population, over the phase space. The number density for charge-carrier populations can thus be determined as the zeroth moment of their respective distribution function as described in the previous section of the present appendix. Following the dissertation on Lavrent'ev's method in Ref. [15], the motion of charge particles inside the device can be described in terms of two constant of motion, namely:

- Total mechanical energy, in a conservative system this consists of the contribution of kinetic energy and electrostatic potential energy

$$\frac{1}{2}m_\mathrm{s}v_\mathrm{s}^2 + q_\mathrm{s}V(r) = E_\mathrm{s} = const. \tag{B.43}$$

Where m_s, is the mass of a particle in the "*s*" population

$\overrightarrow{v_\mathrm{s}}$, is the particle's velocity

$V(r)$, is the electrostatic potential at the radial position r, inside the IEC

E_s, is the particle's total energy (expressed in Volts)

The velocity vector of charge particle can be decomposed in two different components in a local reference frame:

$$\overrightarrow{v_\mathrm{s}} = v_{r,s}\hat{r} + v_{t,s}\hat{t} \tag{B.44}$$

Being $v_{r,s}$ the radial velocity (i.e. the velocity component parallel to the radial direction in the reference frame)

$v_{t,s}$ the transverse velocity (i.e. the velocity component in the plane perpendicular to the radial direction in the reference frame).

Eq. B.43 can then be recast as

$$\frac{1}{2}m_s v_{r,s}^2 + \frac{1}{2}m_s v_{t,s}^2 + q_s V(r) = E_s = const. \tag{B.45}$$

- Angular momentum

$$m_s r v_{t,s} = L_s = const. \tag{B.46}$$

Where L_s, is the particle's angular momentum.

Along the line of the normalisation previously introduced for Poisson's equation, both the particle's total energy and angular momentum can be normalised with respect to the reference values reported in Tab B.2.

Table B.2 Reference values for the normalisation of the particle's constants of motion.

Physical quantity	Unit of measurement (SI)	Reference value
Mechanical energy (W_s)	[V]	Cathode voltage V_c
Ion Angular momentum (L_i)	$[\mathrm{Kg \cdot m^2 \cdot s^{-1}}]$	$\sqrt{2m_i r_c^2(-q_i V_c)}$
Electron Angular momentum (L_e)	$[\mathrm{Kg \cdot m^2 \cdot s^{-1}}]$	$\sqrt{2m_e r_c^2(eV_c)}$

$$\begin{aligned} y_s &\triangleq \frac{W_s}{V_c} && \text{Normalized total energy} \\ \xi_i &\triangleq \sqrt{\frac{L_i^2}{2m_i r_c^2(-q_i V_c)}} && \text{Normalized ion angular momentum} \\ \xi_e &\triangleq \sqrt{\frac{L_e^2}{2m_e r_c^2(eV_c)}} && \text{Normalized electron angular momentum} \end{aligned} \tag{B.47}$$

By substituting Eq. B.47 in Eq. B.45, the radial velocity for both ions and electrons can be expressed as a function of their normalised mechanical energy and angular momentum, as well as of the normalized electrostatic potential inside the IEC:

$$\begin{cases} v_{r,i} = \sqrt{-2q_i\frac{V_g}{m_i}}\sqrt{\phi(\rho) - y_i - \frac{\xi_i^2}{\rho^2}} \\ v_{r,e} = \sqrt{2e\frac{V_g}{m_e}}\sqrt{y_e - \phi(\rho) - \frac{\xi_e^2}{\rho^2}} \end{cases} \tag{B.48}$$

It is remarkable that a domain for the particle's total energy and angular momentum can be determined on the basis of some physical consideration. Indeed, in order for the particle to stay inside the device a significant amount of time, its normalised mechanical energy must belong to the interval [0,1] and, since the square root's arguments must not be negative:

$$\begin{aligned} &y_i, y_e \in [0,1] \\ &y_i \le \phi(\rho) \le y_e \end{aligned} \tag{B.49}$$

Thus, the integration limits for the total energy of the particles in each species are given by Eq. B.50:

$$0 \leq y_i \leq \phi(\rho) \leq y_e \leq 1 \tag{B.50}$$

Analogously, the particle's normalised angular momentum must lie between zero and a maximum value, which can be retrieved by setting the particle's radial velocity equal to zero:

$$v_{r,s} = 0 \tag{B.51}$$

Eq. B.52 then expresses the integration limits for the angular momentum variable:

$$\begin{cases} 0 \leq \xi_i \leq \sqrt{\phi(\rho) - y_i} \\ 0 \leq \xi_e \leq \sqrt{y_e - \phi(\rho)} \end{cases} \tag{B.52}$$

Hence, once outlined the conservation laws that constrain the motion of a charge particle inside the device, it is possible to describe the particle's PDF in terms of its constants of motion (y_s, ξ_s).

Consider the case of ion injection inside an IEC, and let $g(\xi_i, y_i)$ be the ion's joint PDF for the aleatory variables y_i and ξ_i. That means the probability for an injected particle, anywhere in the system, to have –simultaneously- total mechanical energy in the interval $[y_i - \mathrm{d}y_i, y_i + \mathrm{d}y_i]$ and angular momentum in the interval $[\xi_i - \mathrm{d}\xi_i, \xi_i + \mathrm{d}\xi_i]$, is:

$$\mathrm{d}p(\xi_i, y_i) = g(\xi_i, y_i)\mathrm{d}\xi_i\mathrm{d}y_i \tag{B.53}$$

Thus, the total number of ions injected in the system can be calculated, by integrating $\mathrm{d}p(\xi_i, y_i)$ over the energy and angular momentum domains:

$$N_i = \int_0^\infty \int_0^\infty g(\xi_i, y_i)\mathrm{d}\xi_i\mathrm{d}y_i \tag{B.54}$$

Consider then a thin spherical shell with volume infinitesimal volume $\mathrm{d}V = 4\pi r^2\mathrm{d}r$: some of the injected ions will oscillate back and forth across this volume -due to the mechanism explained in Chapter 2, Section 1 ¶ Operating principle - with period of oscillation

$$\tau_i = 2\int_{r_{min}}^{r_{max}} \frac{1}{v_{i,r}(r)}\mathrm{d}r \tag{B.55}$$

Where r_{min} and r_{max} are found from equation of motion and the factor "2" accounts for the fact that a particle passes through the shell twice per each full period of oscillation. The fraction of time that an ion spends inside the shell volume is then:

$$\frac{\mathrm{d}t}{\tau_i} = \frac{2\ \mathrm{d}r}{\tau_i\ v_{r,i}}\ u(r - r_{min})\ u(r_{max} - r) \tag{B.56}$$

Where $u(\cdot)$, is Heaviside step function $u: \mathbb{R} \rightarrow [0,1]$

$$u(x) = \begin{cases} 0, & x < 0 \\ 1, & x \geq 0 \end{cases} \tag{B.57}$$

The differential density of injected ions inside the device is thus:

$$f_i(r, \xi_i, y_i)\mathrm{d}\xi_i\mathrm{d}y_i = \frac{[g(\xi_i, y_i)\mathrm{d}\xi_i\mathrm{d}y_i]\left[\frac{2\ \mathrm{d}r}{\tau_i\ v_{i,r}}\ u(r - r_{min})\ u(r_{max} - r)\right]}{4\pi r^2\mathrm{d}r} \tag{B.58}$$

Hence, the PDF for the ion population results:

$$f_i(r, \xi_i, y_i) = \frac{g(\xi_i, y_i)\left[\frac{2\ \mathrm{d}r}{\tau_i\ v_{r,i}}\ u(r - r_{min})\ u(r_{max} - r)\right]}{4\pi r^2\mathrm{d}r} \tag{B.59}$$

The ion number density as a function of the radial position inside the IEC is then obtained by integrating the distribution function[31]:

$$n_i(r) = \int_0^{\infty} \int_0^{\infty} f_i(r, \xi_i, y_i) \mathrm{d}\xi_i \mathrm{d}y_i \tag{B.60}$$

It is worth noting that the use of Heaviside step functions in Eq. B.58 and B.59 may be replaced by introducing the equivalent integration limit in Eq. B.50 and B.52.

$$n_i(r) = \int_0^{\phi} \int_0^{\xi_{max}} \frac{2\, g(\xi_i, y_i)}{4\pi r^2 \tau_i \sqrt{\left(-2q_i \frac{V_g}{m_i}\right)\left(\phi(\rho) - y_i - \frac{\xi_i^2}{\rho^2}\right)}} \mathrm{d}\xi_i \mathrm{d}y_i \tag{B.61}$$

Since τ_i is a complicated function of the unknown electrostatic potential inside the device –through the dependency of the radial velocity from the potential, expressed in Eq. B.48- it is of use to define a "current distribution function":

$$i_i(\xi_i, y_i) \mathrm{d}\xi_i \mathrm{d}y_i = 2q_i \frac{g(\xi_i, y_i) \mathrm{d}\xi_i \mathrm{d}y_i}{\tau_i} \tag{B.62}$$

The total ion current inside the IEC, typically referred to as "*circulating current*" (as it is the current carried by the circulating ions inside the micro-channel structures depicted in Chapter 2, Section 1, ¶ Operating modes), is thus given by the integral:

$$I_i = \int_0^{1} \int_0^{\sqrt{1-\phi}} |i_i(\xi_i, y_i)| \mathrm{d}\xi_i \mathrm{d}y_i \tag{B.63}$$

The circulating current can be related to the measured grid current, i.e. the ion current collected at the cathode (I_{IC}), through Eq. B.64:

$$I_i = \frac{2\gamma_e}{1 - {\gamma_e}^2} I_{\mathrm{IC}} \tag{B.64}$$

Where γ_e, is the *effective cathode grid openness*, which is related (depending on the IEC architecture) to the *geometric cathode grid openness*, defined as the ration between the open area of the grid and the surface area of the grid sphere [14]:

$$\gamma_0 \triangleq 1 - \frac{\sigma_0}{A} \tag{B.65}$$

Where γ_0, is the geometric openness

σ_0, is the cross-sectional area of the grid

A, is the surface area of the cathode sphere

$$A = 4\pi r_c^2 \tag{B.66}$$

According to [24], in ES devices effective grid openness do coincide with con the geometric one. In GD and AGD architectures, on the other hand, the cathode effective openness results smaller -due to

[31] Note that a useful proof of the soundness of the reasoning here exposed can be identify in the fact that, by integrating the ion density $n_i(r)$ over the device's radius, the total number of injected particles N_i is retrieved

$$\int_0^R n_i(r) \mathrm{d}r = \int_0^R \int_0^{\infty} \int_0^{\infty} \frac{g(\xi_i, y_i) \left[\frac{2\,\mathrm{d}r}{\tau_i\, v_{r,i}}\, u(r - r_{min})\, u(r_{max} - r)\right]}{4\pi r^2 dr} \mathrm{d}\xi_i \mathrm{d}y_i\, \mathrm{d}r == \int_0^{\infty} \int_0^{\infty} g(\xi_i, y_i) \mathrm{d}\xi_i \mathrm{d}y_i \equiv N_i \tag{B.61}$$

the electrostatic interaction of charge particles with the gridded electrode itself- and a suitable coefficient, called "grid absorption efficiency", is introduce in order to account for such an effect:

$$\eta \triangleq \frac{1-\gamma_e}{1-\gamma_0} = \frac{\sigma_c}{\sigma_0} \tag{B.67}$$

Where σ_c, is the cross-section for ion absorption by the cathode grid.

In Ref. [5], T. J. Dolan evaluates the effect of deflection of the injected particles towards nearby grid wires which, as previously stated, determines a decrease in the effective open area of the grid. Indeed an equation is given, in which the ratio between the effective and geometric openness is reported as a function of both the diameter and the spacing for the grid wires:

$$\frac{\gamma_e}{\gamma_0} = \left(1 - \frac{1}{16\pi\,(g-d)/g}\right)^2 \tag{B.68}$$

Where g, is the spacing between grid wire centres (for an equally spaced mesh)

d, is the grid wire diameter.

On the other hand, Miley *et al.* [32] have fitted empirical data to Paschen curves, obtaining typical values -for the grid absorption efficiency- in the order $\eta \approx 10^{-1}$.

Finally, under typical experimental circumstances, the measured electric current is the one flowing through the power supply (thus referred to as "Power-supply current"), which is related to the current flowing through the cathode -due to collected ions- by Eq. B.69

$$I_{IC} = \frac{I_{PS} - I_{h\nu}}{1+\delta} \tag{B.69}$$

Where I_{PS}, is the electric current measured in the power supply

$I_{h\nu}$, is the secondary photoelectric emission rate

δ, is the secondary electron emission coefficient.

With regards of the present essay, in order to simplify the calculation, the cathode grid effective openness will be assumed to be coinciding with the geometric one and the cathode sputtering effect will be neglected:

$$\begin{gathered}\gamma_e \cong \gamma_0 \\ I_{h\nu} \ll I_{IC}\end{gathered} \tag{B.70}$$

Hence, the cathode current is assumed to virtually correspond to the value measured in the power supply and the ion circulating current in the device can be determined from such a value:

$$I_i = \frac{2\gamma_e}{1-{\gamma_e}^2} I_{IC} \cong \frac{2\gamma_e}{1-{\gamma_e}^2} I_{PS} \tag{B.71}$$

It should be now manifest that the substitution in Eq. B.71 allows for the reduction in the number of unknown quantities in the mathematical model, provided that the circulating current is determined from the measurement of the current flowing through the power supply. Combining Eq. B.61-63 is thus possible to express the number density for the ion population as an integral function of the circulating current distribution function, as shown in Eq. B.72.

$$n_i(r) = \int_0^{\phi}\int_0^{\xi_{max}} \frac{i_i(\xi_i, y_i)}{4\pi r^2 \sqrt{\left(-2q_i\frac{V_c}{m_i}\right)\left(\phi(\rho) - y_i - \frac{\xi_i^2}{\rho^2}\right)}}\,d\xi_i\,dy_i \tag{B.72}$$

Along the same line of reasoning, the number density for the electron population in an IEC device can determined as the expectation value of electron probability density distribution over the phase space:

$$n_e(r) = \int_0^{\infty} \int_0^{\infty} f_e(r, \xi_i, y_i) \mathrm{d}\xi_i \mathrm{d}y_i \tag{B.73}$$

$$n_e(r) = \int_{\phi}^{1} \int_0^{\xi_{max}} \frac{2\, g(\xi_e, y_e)}{4\pi r^2 \tau_e \sqrt{\left(2e\frac{V_g}{m_e}\right)\left(y_e - \phi(\rho) - \frac{\xi_e^2}{\rho^2}\right)}} \mathrm{d}\xi_e \mathrm{d}y_e \tag{B.74}$$

In an analogous way, the be the electron's joint PDF for the aleatory variables y_e and ξ_e, can be conveniently rearranged in order to remove the electron characteristic oscillation period, by introducing the electron current distribution function:

$$i_e(\xi_e, y_e)\mathrm{d}\xi_e \mathrm{d}y_e = 2e\frac{g(\xi_e, y_e)\mathrm{d}\xi_e \mathrm{d}y_e}{\tau_e} \tag{B.75}$$

$$n_e(r) = \int_{\phi}^{1} \int_0^{\xi_{max}} \frac{i_e(\xi_e, y_e)}{4\pi r^2 \sqrt{\left(2e\frac{V_g}{m_e}\right)\left(y_e - \phi(\rho) - \frac{\xi_e^2}{\rho^2}\right)}} \mathrm{d}\xi_e \mathrm{d}y_e \tag{B.76}$$

As far as the electron current inside the device is concerned, it can be thought of as the electron space charge current into the anode:

$$I_e = \int_0^{1} \int_0^{\sqrt{\phi - 1}} |i_e(\xi_e, y_e)| \mathrm{d}\xi_e \mathrm{d}y_e \tag{B.77}$$

Such a current flows in one direction only and, although I_{PS} has other contributions, the net result is $I_e = I_{PS}$. Hence, the primary currents I_i and I_e anchor the steady-state one-dimensional model for the operation of a symmetric IEC device. Actually, substituting the expression obtained for both the ion and electron number density (Eq B.61 and B.76) in Poisson's equation (Eq. B.36), the non-dimensional electrostatic potential can be, at last, calculated -along the radial position inside the device, i.e. $\phi(\rho)$- by solving the following second order ODE:

$$\frac{1}{\rho^2}\frac{\mathrm{d}}{\mathrm{d}\rho}\left(\rho^2 \frac{\mathrm{d}\phi}{\mathrm{d}\rho}\right) = Q_i(\rho, \phi) - Q_e(\rho, \phi) \tag{B.78}$$

Where the space charge densities are expressed in terms of the respective species current distribution functions as follows:

$$\begin{cases} Q_i(\rho, \phi) = \displaystyle\int_0^{\phi} \int_0^{\sqrt{1-\phi}} \frac{h_i(\xi_i, y_i)}{\sqrt{\left(-2q_i\frac{V_c}{m_i}\right)\left(\phi(\rho) - y_i - \frac{\xi_i^2}{\rho^2}\right)}} \mathrm{d}\xi_i \mathrm{d}y_i \\ h_i(\xi_i, y_i) = \dfrac{\sqrt{m_i}}{4\pi\varepsilon_0\sqrt{(-2q_i V_c)}}\left(-\dfrac{i_i(\xi_i, y_i)}{V_c}\right) \end{cases} \tag{B.79}$$

$$\begin{cases} Q_e(\rho,\phi) = \int_{\phi}^{1}\int_{0}^{\sqrt{\phi-1}} \dfrac{h_e(\xi_e,y_e)}{\sqrt{\left(2e\frac{V_c}{m_e}\right)\left(y_e-\phi(\rho)-\frac{\xi_e^2}{\rho^2}\right)}}\mathrm{d}\xi_e\mathrm{d}y_e \\ h_e(\xi_e,y_e) = \dfrac{\sqrt{m_e}}{4\pi\varepsilon_0\sqrt{(2eV_c)}}\left(\dfrac{i_e(\xi_e,y_e)}{V_c}\right) \end{cases} \tag{B.80}$$

It is worth noting that an analogous result can be achieved by considering a Cylindrical-IEB. In this case, Poisson's equation is given in Eq. B.41, and the source term can be recast by introducing the quantities:

$$\begin{aligned} R_i(\rho,\phi) &= \frac{2r_c}{l}Q_i(\rho,\phi) \\ R_e(\rho,\phi) &= \frac{2r_c}{l}Q_e(\rho,\phi) \end{aligned} \tag{B.81}$$

Where l, is the length of the investigated cylindrical plasma.

Therefore, the normalised electrostatic potential along the radial direction in a cylindrical device is described by the following second order ODE:

$$\frac{1}{\rho}\frac{\mathrm{d}}{\mathrm{d}\rho}\left(\rho\frac{\mathrm{d}\phi}{\mathrm{d}\rho}\right) = R_i(\rho,\phi) - R_e(\rho,\phi) \tag{B.82}$$

The number density for both the charge-carrier populations inside the device can thus be determined as a function of $Q_s(\rho,\phi)$ and $R_s(\rho,\phi)$, for a spherical or cylindrical device respectively:

$$\begin{aligned} n_s(\rho) &= \frac{\varepsilon_0}{{r_c}^2}\left|\frac{V_c}{q_s}\right|\frac{Q_s(\rho,\phi)}{\rho^2}\ (S-SIEC) \\ n_s(\rho) &= \frac{\varepsilon_0}{{r_c}^2}\left|\frac{V_c}{q_s}\right|\frac{R_s(\rho,\phi)}{\rho}\ (C-SIEC) \end{aligned} \tag{B.83}$$

Eq. 3.78 and 3.81 represent the steady-state one-dimensional model for the simulation of a symmetric IEC device, as it was presented by Dolan *et al.* in Ref. [15]. In the present thesis, however, a different approach is preferred: specifically the notation from [14] is presented below and maintained throughout the present essay.

$$\begin{aligned} \varepsilon_s &\triangleq \frac{E_s}{V_c} && \text{normalized total energy} \\ \lambda_s &\triangleq \sqrt{\frac{L_s^2}{2m_s r_c^2\left|q_s V_c\right|}} && \text{normalized angular momentum} \end{aligned} \tag{B.84}$$

Where E_s, is the total energy of a particle in the "s" population.

B. Dobson and I. Hrbud solved Eq. B.36 by directly assuming the PDF, for the charge-carrier populations inside the device $f_s\left(\rho,\phi,\varepsilon_s,\lambda_s\right)$, instead of referring to the current distribution function introduced by Dolan *et al.* (as in Eq. B.78). As previously discussed, the latter approach directly accounts for the motion of the particles inside the IEC, being the distribution function only constrained by the assumption over the particle's constants of motion (i.e. its total energy and angular momentum). Nonetheless, given the dependency of the particle distribution function on the characteristic period of oscillation, according to Eq. B.58, the resolution of the resulting plasma model is not straightforward. A

possible solution consist in the introduction of a new physical quantity, which will be referred to as "*mono-energetic perveance*", defined according to R. L. Hirsch [9] as in Eq B.85[32]:

$$K_{\mathrm{s}} = \frac{I_{\mathrm{s}}}{|V_{\mathrm{c}}|^{\frac{3}{2}}}\sqrt{\frac{m_{\mathrm{s}}}{|2q_{\mathrm{s}}|}} \tag{B.86}$$

It is useful then to introduce the conservation laws for electric charge and total mechanical energy for both ions and electrons:

$$\begin{aligned} &I_{\mathrm{s}} = 4\pi r^2 \rho_{\mathrm{s}} v_{\mathrm{s}} && \text{(electric charge conservation law)} \\ &\frac{1}{2} m_i v_i^2 = |q_i V(r)| && \text{(ion energy conservation law)} \\ &\frac{1}{2} m_e v_e^2 = |e(V(r) - V_{\mathrm{c}})| && \text{(electron energy conservation law)} \end{aligned} \tag{B.87}$$

Where ρ_{s}, is the space charge induced a charge-carrier population

v_{s}, is the mean velocity for a particle in the "s" population

By comparing Eq. B.85 with Eq. B.87, it is possible to represent the mono-energetic perveance as a function of the normalized electrostatic potential:

$$K_{\mathrm{s}} = \frac{4\pi r^2 \rho_{\mathrm{s}} \sqrt{\phi}}{|V_{\mathrm{c}}|} \tag{B.88}$$

Following the reasoning in Ref. [14], is then appropriate to define a "general form" for the perveance, by normalising it with respect to a suitable normalisation factor for the distribution function, whose meaning will later be clarified:

$$k_{\mathrm{s}} \triangleq \frac{K_{\mathrm{s}}}{C_{\mathrm{s}}} \tag{B.89}$$

Such a general form for both ion and electron perveances allows for the definition of current-normalised densities $\hat{n}_{\mathrm{s}}$, corresponding to the integral values –over the mechanical energy and angular momentum- of the PDF, for the relative charge-carrier population:

$$\hat{n}_{\mathrm{s}} = \int\int f_{\mathrm{s}}(\rho, \phi, \varepsilon_{\mathrm{s}}, \lambda_{\mathrm{s}})\, \mathrm{d}\lambda_{\mathrm{s}}\, \mathrm{d}\varepsilon_{\mathrm{s}} \tag{B.90}$$

These densities are related to the Poisson densities by the normalised perveance, in the form expressed by Eq. B.91.

[32] According to Eq. B.86, the mono-energetic perveance is, to some extent, akin the proportionality constant in Child's law for space-charge limited current. That is the mathematical relation describing the dependence of space-charge limited current –i.e. the electric current carried by a single particle population (e.g. electrons)- between plain electrodes, from the applied voltage:

$$I_{\mathrm{SCLC}} = \frac{4}{9}\varepsilon_0 \sqrt{\frac{2|q|}{m}} \frac{V^{\frac{3}{2}}}{d^2} \tag{B.85}$$

Where I_{SCLC}, is the space-charge limited electric current

V, is the voltage applied between the electrodes

d, is the distance between the plain electrodes.

Actually, in his paper [2], Hirsch quoted the work from Langmuir and Blodgett who extended Child's law to the case of cylindrical, concentric electrodes.

$$\hat{n}_\mathrm{s} = {k_\mathrm{s}}^{-1}\frac{n_\mathrm{s}}{n_\mathrm{c}} \tag{B.91}$$

Introducing the current-normalised number densities, distinct solutions $\phi(\rho)$ of Poisson's equation are obtained for different values assigned to the perveance k_s (resulting from the operating values for both the electrodes voltage and the power supply current, through Eq. B.71 and B.85) resulting in density profiles:

$$n_\mathrm{s}(\rho) = n_\mathrm{c}\, k_\mathrm{s}\, \hat{n}_\mathrm{s}[\rho, \phi(\, k_\mathrm{s}, \rho)] = n_\mathrm{c}\frac{K_\mathrm{s}}{C_\mathrm{s}}\int\int f_\mathrm{s}(\rho, \phi, \varepsilon_\mathrm{s}, \lambda_\mathrm{s})\, \mathrm{d}\lambda_\mathrm{s}\, \mathrm{d}\varepsilon_\mathrm{s} \tag{B.92}$$

In Ref. [26] the derivation of the normalisation factors for the distribution function is outlined, assuming the particles, in a given population, to have same mechanical energy and pure radial motion. Eq. B.87, which represents the charge conservation law, is than rearranged in:

$$n_\mathrm{s} = \frac{I_\mathrm{s}}{4\pi r_\mathrm{c}^2 |q_\mathrm{s}| v_{r,s}} \tag{B.93}$$

Substituting this relation in Eq. 3.B.92 and coupling with Eq. B.89, the following equation results:

$$\frac{I_\mathrm{s}}{4\pi r_\mathrm{c}^2 |q_\mathrm{s}|} = n_\mathrm{c}\, k_\mathrm{s}\int\int f_\mathrm{s}(\rho, \phi, \varepsilon_\mathrm{s}, \lambda_\mathrm{s}) \cdot v_{r,\mathrm{s}}(\rho, \phi, \varepsilon_\mathrm{s}, \lambda_\mathrm{s})\, \mathrm{d}\lambda_\mathrm{s}\, \mathrm{d}\varepsilon_\mathrm{s} \tag{B.94}$$

Hence, recalling Eq. B.35 and B.85, is possible to bring up the normalisation factor as follows:

$$\frac{I_\mathrm{s}}{4\pi r_\mathrm{c}^2 |q_\mathrm{s}|} = \frac{\varepsilon_0}{{r_\mathrm{c}}^2}\left|\frac{V_\mathrm{c}}{q_\mathrm{s}}\right| \frac{\dfrac{I_\mathrm{s}}{4\pi\varepsilon_0 |V_\mathrm{c}|^{3/2}}\sqrt{\dfrac{m_\mathrm{s}}{|2q_\mathrm{s}|}}}{C_\mathrm{s}} \int\int f_\mathrm{s} \cdot v_{r,\mathrm{s}}\, \mathrm{d}\lambda_\mathrm{s}\, \mathrm{d}\varepsilon_\mathrm{s} \tag{B.95}$$

Where r_s, identifies the radius of the electrode having opposite polarity of the "s" charge carriers population (i.e. the cathode radius for ions ad the anode one for electrons).

Solving Eq. B.95 with respect to C_s, yields

$$C_\mathrm{s} = \frac{r^2}{{r_\mathrm{s}}^2}\sqrt{\frac{m_\mathrm{s}}{2|q_\mathrm{s} V_\mathrm{c}|}}\int\int f_\mathrm{s} \cdot v_{r,\mathrm{s}}\, \mathrm{d}\lambda_\mathrm{s}\, \mathrm{d}\varepsilon_\mathrm{s} \tag{B.96}$$

Hence, the normalisation factor for the ion distribution function can be evaluated in correspondence of the cathode grid while the normalisation factor for electrons is determined at the anode. This leads to the following equations:

$$\begin{aligned} C_i &= \sqrt{\frac{m_i}{2|q_i V_\mathrm{c}|}}\int\int f_i(1,1,\varepsilon_i,\lambda_i) \cdot v_{r,i}(1,1,\varepsilon_i,\lambda_i)\, \mathrm{d}\lambda_i\, \mathrm{d}\varepsilon_i \\ C_e &= \sqrt{\frac{m_e}{2|eV_\mathrm{c}|}}\int\int f_e(1,1,\varepsilon_e,\lambda_e) \cdot v_{r,e}(1,1,\varepsilon_e,\lambda_e)\, \mathrm{d}\lambda_e\, \mathrm{d}\varepsilon_e \end{aligned} \tag{B.97}$$

It is thus manifest that the normalization factors do not depend on the power supply current, but only on the used distribution function and its constraints: as a consequence, they results to be constant at any radial position inside the IEB.

¶ Probability distribution functions

Once exposed the physical line of reasoning that lead the development of the two-fluid one-dimensional model and the related mathematical formulation, it is well timed to expound in detail the "core" concept in such a simulation tool: the particle PDF.

Since, at any given time, each particle has a specific position and velocity, the instantaneous configuration of a large number of particles is described by the Hamiltonian mechanics by specifying the density of particles at each point $(\vec{x}, \vec{v})$ in phase-space $\mathcal{F}$ [62]. The function prescribing the instantaneous density of particles in phase space is called the *distribution function* $f(t, \vec{x}, \vec{v})$: hence, the number of particles having positions in the range $[\vec{x}, \vec{x} + \mathrm{d}\vec{x}]$ and velocities in the range $[\vec{v}, \vec{v} + \mathrm{d}\vec{v}]$, at a given time t, is $f(t, \vec{x}, \vec{v})\, \mathrm{d}\vec{x}\, \mathrm{d}\vec{v}$. The particle distribution function can thus be thought of as the probability that a randomly selected particle -in the population considered- located at $\vec{x}$, has velocity $\vec{v}$. It is plain to show then that, given a number of particle inside a control volume, the number density for the particle population -which is characterized by its distribution function over the phase space- can be obtained in the integral form in Eq. 3.87.

$$n(t, \vec{x}) = \iiint f(t, \vec{x}, \vec{v})\, \mathrm{d}\vec{v} \tag{B.98}$$

That is to say that the number density for a particle population is the zeroth-order moment of its probability density function.

The temporal evolution for the system is typically described in terms of Hamilton's equations -which refer to the system's Hamiltonian (i.e. the Legendre transform of the Lagrangian) - but an equivalent formulation can be obtained by taking advantage of Liouville's theorem. This theorem states that the distribution function is constant along the phase trajectories of the subsystem (i.e. a particle), also referred to as "*orbits*":

$$\left.\frac{df\left(t, \vec{x}(t), \vec{v}(t)\right)}{dt}\right|_{orbit} = \frac{\partial f}{\partial t} + \vec{v} \cdot \frac{\partial f}{\partial \vec{x}} + \vec{a} \cdot \frac{\partial f}{\partial \vec{v}} = 0 \tag{B.99}$$

In the present case, the physical system considered is composed of a number of charged particles, hence the acceleration term in Eq. B.99 can be expressed (assuming the external force acting on the single particle to be purely electromagnetic), by means of Lorentz's equation, as:

$$\vec{a} = \frac{q}{m}\left(\vec{E} + \vec{v} \times \vec{B}\right) \tag{B.100}$$

Eq. B.100 is then recast, assuming the form of the well-known Vlasov's equation, which, due to its simplicity, is the most-commonly studied equation in kinetic theory [3]:

$$\frac{\partial f}{\partial t} + \vec{v} \cdot \nabla f + \frac{q}{m}\left(\vec{E} + \vec{v} \times \vec{B}\right) \cdot \frac{\partial f}{\partial \vec{v}} = 0 \tag{B.101}$$

It is worth noting that the source term in such an equation is null only under the assumption of the plasma being hot enough for the collision to be neglected (indeed Liouville's theorem is valid only for closed systems [94]). When collisions with neutral species, possibly resulting in the creation of free charge particles (i.e. ionization), are to be considered, a collision term is introduced in Eq. B.101, whose mathematical form depends on the physical characterization of the collisional processes (e.g. *Krook collision term*, *Fokker-Planck equation, etc.*) [94]. It follows at once from Liouville's theorem that the distribution function must be expressible entirely in terms of combinations of those variables, which remain constant when the subsystem moves as a closed subsystem: such combinations are the *mechanical invariants* (or *constants of motion*). This conclusion is particularly relevant for the purpose of the present dissertation, as it allows to recast the distribution function over the phase space as a function of the charged particles' integrals of motions.

As pointed out by M. Ohnishi *et al.* [49] and H. Matsuura *et al.* [50], inertial electrostatic confinement fusion is a weak collisional system, where the collision frequency and fusion-reaction rate are small compared with the transit frequency in the potential well. The motion of a charged particle in such a system, assuming a spherical symmetry for the device, is represented by two constants of motion, namely

the total mechanical energy E and the angular momentum L. Therefore, the PDF for a particle in the IEC core plasma is an arbitrary function of the aforementioned quantities:

$$f(t,x,v) \longrightarrow f(t,E,L) \tag{B.102}$$

Then, considering a steady-state operating IEC and introducing the normalisation discussed in the previous section, along with the constraint over the mechanical energy and angular momentum for the particles in the system, the probability density function has the form employed in Eq. B.90. Each species of charged particles in the IEC core plasma is thus described by its distribution function over the total mechanical energy and angular momentum, while ρ and ϕ can be considered, for the calculation presented in the previous section, as parameters. As pointed out in the dissertation above, Lavrent'ev's method requires an *a priori* assumption of the distribution function for the charge-carrier populations, inside the device. On the basis of the theoretical explanation provided, it should be now clear that this operation is tantamount to assuming, *a priori*, a possible solution for Vlasov's equation (Eq. B.101) and, by solving Poisson's equation with the consistent source terms (Eq. B.36), determining the resulting potential profile inside the device.

Over the years, many different distribution functions, for the charge-carrier populations inside the SIEC, have been proposed. Robert L. Hirsch reports [9] that Lavrent'ev himself, in its seminal work "*Магнитная Ловушка*" ("Magnetic Traps"), solved Poisson's equation for "various distribution functions of interest, i.e. parabolic, Gaussian, and Maxwellian". Dolan *et al.* [15] used Heaviside step functions in order to simulate a rectangular profile for the particle distribution over energy and angular momentum. They also developed a simpler model, based on the assumptions of pure radial motion (i.e. null angular momentum) and Dirac delta distribution over total mechanical energy, which will therefore referred to as "mono-energetic". M. Ohnishi *et al.* [49] took into account the difference in the collisional frequency for the ions and electrons: while they assumed the ions to be mono-energetic, they employed an exponential form for electron distribution function, so to consider the thermalisation of the population due to the greater effect of the collisional processes. The same line of reasoning was adopted by H. Matsuura *et al.* [50] who assumed that "the weak Coulomb collision may slowly relax the distributions towards a Maxwellian process". Hence, they simulated "the distributions using the exponential function so that their shapes are close to those expressed by the Heaviside function". Finally, B. Dobson and I. Hrbud [14] compared the number density and electrostatic potential profiles for a number of different distribution functions, namely mono-energetic, rectangular, parabolic and thermal. They furthermore underlined that, although the distribution functions -assumed *a priori* as solution of Vlasov's equation (Eq. B.101) - do not account, through such an equation, for any collisional process, "these functions are very general and may be assigned mathematical forms which, physically, reflect collisional processes".

For the purpose of the present essay, three different distribution functions have been presented (see Chapter 3, Section 1, ¶ Particle distribution functions) and implemented in the simulation algorithm:

- Mono-energetic, i.e. the particles are assumed to have null angular momentum and Dirac delta distribution over the total mechanical energy
- Rectangular, i.e. the particles are assumed to have Heaviside step distribution over both the total mechanical energy and angular momentum
- Thermal, i.e. the particles are assumed to have an exponential form for the distribution function, accounting for the thermalising effect of Coulomb interactions between particles in a collisional plasma.

The underlying physical assumptions and the meaning, in the context of plasma physics, of these models have already been presented in the third chapter of the present text. Nonetheless, a detailed discussion about the mathematical steps, which lead from the assumed particle distribution functions to the final ordinary differential equation, was delayed for the sake of clarity. In the following, this issue will be tackled: recalling the assumed particle distribution functions, for each and every above-presented plasma model, these will be integrated to assess the mathematical expression for the particle number

densities and the respective normalisation factors so to assess the source term in the resulting Poisson equation.

Mono-energetic distribution function

As already observed, the mono-energetic plasma model describes the motion of a charged particle inside the IEC device in terms of conservation of its total mechanical energy in purely radial motion. The resulting distribution function over the phase space hence takes the form given in Eq. B.103.

$$f_{\mathrm{M,s}}(\rho,\phi,\varepsilon_{\mathrm{s}},\lambda_{\mathrm{s}}) = \frac{\delta(\varepsilon_{\mathrm{s}})}{\rho^2\sqrt{|\phi(\rho)-\varepsilon_{\mathrm{s}}|}} \tag{B.103}$$

The number density for both the charge-carrier populations is determined as the zeroth-order moment of such a PDF, as:

$$\hat{n}_{\mathrm{s}}(\rho,\phi) = \int_{\varepsilon_{mins}}^{\varepsilon_{max,s}} f_{\mathrm{M,s}}(\rho,\phi,\varepsilon_{\mathrm{s}})\mathrm{d}\varepsilon_{\mathrm{s}} \tag{B.104}$$

$$\begin{cases} \hat{n}_i(\rho,\phi) = \int_0^{\phi} f_{\mathrm{M},i}(\rho,\phi,\varepsilon_i)\mathrm{d}\varepsilon_i = \int_0^{\phi} \dfrac{\delta(\varepsilon_i)}{\rho^2\sqrt{|\phi(\rho)-\varepsilon_i|}}\mathrm{d}\varepsilon_i \\ \hat{n}_e(\rho,\phi) = \int_{\phi}^{1} f_{\mathrm{M},e}(\rho,\phi,\varepsilon_e)\mathrm{d}\varepsilon_e = \int_{\phi}^{1} \dfrac{\delta(\varepsilon_e)}{\rho^2\sqrt{|\phi(\rho)-\varepsilon_e|}}\mathrm{d}\varepsilon_e \end{cases} \tag{B.105}$$

As a result of the simplification introduced in this plasma model, ions have normalised total energy equal to zero while electrons have normalised energy equals to one, i.e. all the electrons the same energy as the electrostatic potential energy at the cathode:

$$\begin{cases} \varepsilon_i = 0 \\ \varepsilon_e = 1 \end{cases} \tag{B.106}$$

Moreover, it is possible to taking advantage of the property of Dirac's delta distribution in Eq. B.107, to remove the integral dependency of the number densities on the mechanical energy, as in Eq. B.108.

$$\int_{-\infty}^{+\infty} \delta(x)\,\mathrm{d}x = 1 \tag{B.107}$$

$$\begin{cases} \hat{n}_i(\rho,\phi) = \dfrac{1}{\rho^2\sqrt{\phi}} \\ \hat{n}_e(\rho,\phi) = \dfrac{1}{\rho^2\sqrt{\phi-1}} \end{cases} \tag{B.108}$$

The normalisation factors for the PDFs can be determined by substituting Eq. B.105 into Eq. B.97 and solving the resulting equation, an extremely simple result yields:

$$\begin{cases} C_i = \sqrt{\dfrac{m_i}{2|q_iV_{\mathrm{c}}|}}\displaystyle\int_0^{\phi} \frac{\delta(\varepsilon_i)}{\sqrt{1-\phi}}\sqrt{\frac{2|q_iV_{\mathrm{c}}|}{m_i}}\sqrt{\phi}\,d\varepsilon_i = 1 \\ C_e = \sqrt{\dfrac{m_e}{2|eV_{\mathrm{c}}|}}\displaystyle\int_{\phi}^{1} \frac{\delta(\varepsilon_e)}{\sqrt{\phi}}\sqrt{\frac{2|eV_{\mathrm{c}}|}{m_e}}\sqrt{\phi-1}\,d\varepsilon_e = 1 \end{cases} \tag{B.109}$$

Thus, the normalised number densities in the source term of Poisson's equation are obtained in the following form:

$$\begin{cases} n_i(\rho,\phi) = \dfrac{K_i}{\rho^2\sqrt{\phi}} \\ n_e(\rho,\phi) = \dfrac{K_e}{\rho^2\sqrt{\phi-1}} \end{cases} \tag{B.110}$$

Poisson's equation takes then the final form already introduce in Chapter 3, Section 1, ¶ Particle distribution functions:

$$\frac{\mathrm{d}^2\phi}{\mathrm{d}\rho^2} + \frac{1}{2\rho}\frac{\mathrm{d}\phi}{\mathrm{d}\rho} = \frac{1}{\rho^2 n_\mathrm{c}}\left(\frac{K_i}{\sqrt{\phi}} - \frac{K_e}{\sqrt{\phi-1}}\right) \tag{B.111}$$

Rectangular distribution function

The rectangular distribution function uses Heaviside's step function to model the dependence of the particles' distribution function over total mechanical energy and angular momentum, as in Eq. B.112.

$$f_{\mathrm{H,s}}(\rho,\phi,\varepsilon_\mathrm{s},\lambda_\mathrm{s}) = \frac{H(\lambda_{max}-\lambda_\mathrm{s})H(\varepsilon_{max}-\varepsilon_\mathrm{s})H(\varepsilon_\mathrm{s}-\varepsilon_{min})}{\rho^2\sqrt{|\phi(\rho)-\varepsilon_\mathrm{s}| - \dfrac{\lambda_\mathrm{s}^2}{\rho^2}}} \tag{B.112}$$

It is then useful to introduce the following definition of Heaviside unit step function, as the cumulative distribution function relative to a Dirac delta distribution:

$$H(x) \triangleq \int_{-\infty}^{x} \delta(s)\,\mathrm{d}s \tag{B.113}$$

The Lebesgue integral of an arbitrary continuous, compactly supported function $f(x)$, with respect to the measure induced by $\delta(x)$, satisfies:

$$\int_{-\infty}^{+\infty} f(x)\,\delta\{\mathrm{d}x\} = \int_{-\infty}^{+\infty} f(x)\,\delta(x)\,\mathrm{d}x = f(0) \tag{B.114}$$

Introducing the definition in Eq. B.112, is possible to express Dirac delta function as the derivative of Heaviside step function

$$\delta(x) = \frac{\mathrm{d}H(x)}{\mathrm{d}x} \tag{B.115}$$

Hence, Eq. B.114 is recast as

$$\int_{-\infty}^{+\infty} f(x)\,\delta\{\mathrm{d}x\} = \int_{-\infty}^{+\infty} f(x)\,\mathrm{d}H(x) \tag{B.116}$$

Finally, the following fundamental property, for the unit step function, is obtained:

$$\int_{-\infty}^{+\infty} f(x)\,h(x)\;\mathrm{d}x = f(x) \tag{B.117}$$

Such a property allows for the immediate integration of Eq. B.112 so to assess the particle number densities:

$$\hat{n}_\mathrm{s}(\rho,\phi) = \iint f_{\mathrm{H,s}}(\rho,\phi,\varepsilon_\mathrm{s},\lambda_\mathrm{s})\mathrm{d}\lambda_\mathrm{s}\mathrm{d}\varepsilon_\mathrm{s} = \int_{\varepsilon_{min,\mathrm{s}}}^{\varepsilon_{max,\mathrm{s}}}\int_0^{\lambda_{max,\mathrm{s}}} \frac{\mathrm{d}\lambda_\mathrm{s}}{\rho^2\sqrt{|\phi(\rho)-\varepsilon_\mathrm{s}| - \dfrac{\lambda_\mathrm{s}^2}{\rho^2}}}\mathrm{d}\varepsilon_\mathrm{s} \tag{B.118}$$

$$\begin{cases} \hat{n}_i(\rho,\phi) = \dfrac{1}{\rho^2}\displaystyle\int_0^{\phi}\int_0^{\rho\sqrt{\phi-\varepsilon_i}} \dfrac{\mathrm{d}\lambda_i}{\sqrt{\phi-\varepsilon_i-\dfrac{\lambda_i^2}{\rho^2}}}\mathrm{d}\varepsilon_i \\ \hat{n}_e(\rho,\phi) = \dfrac{1}{\rho^2}\displaystyle\int_{\phi}^{1}\int_0^{\rho\sqrt{\varepsilon_e-\phi}} \dfrac{\mathrm{d}\lambda_e}{\sqrt{\varepsilon_e-\phi-\dfrac{\lambda_e^2}{\rho^2}}}\mathrm{d}\varepsilon_e \end{cases} \tag{B.119}$$

From standard integration tables, the general solution for the integration of the rectangular distribution function over angular momentum, is determined in the form:

$$\int \frac{\mathrm{d}x}{\sqrt{c-ax^2}} = \frac{1}{\sqrt{a}}\sin^{-1}\left(\frac{ax}{\sqrt{ac}}\right) \tag{B.120}$$

In the present case, the following transformations hold:

$$\begin{cases} c = |\phi(\rho)-\varepsilon_{\mathrm{s}}| \\ a = \dfrac{1}{\rho^2} \\ x = \lambda_{\mathrm{s}} \end{cases} \tag{B.121}$$

Hence, by solving the integral form between the integration limits assigned for each and every of the charge-carrier populations, the following equations descend:

$$\begin{cases} \hat{n}_i(\rho,\phi) = \dfrac{1}{\rho}\displaystyle\int_0^{\phi}\sin^{-1}\left(\frac{\rho\sqrt{\phi-\varepsilon_i}}{\rho\sqrt{|\phi-\varepsilon_i|}}\right)\mathrm{d}\varepsilon_i \\ \hat{n}_e(\rho,\phi) = \dfrac{1}{\rho}\displaystyle\int_{\phi}^{1}\frac{1}{\rho}\sin^{-1}\left(\frac{\rho\sqrt{\varepsilon_e-\phi}}{\rho\sqrt{|\phi-\varepsilon_e|}}\right)\mathrm{d}\varepsilon_e \end{cases} \tag{B.122}$$

Since $\sin^{-1}(1) = \frac{\pi}{2}$, the integration of the resulting function over total mechanical energy is trivial:

$$\begin{cases} \hat{n}_i(\rho,\phi) = \dfrac{\pi\,\phi}{2\,\rho} \\ \hat{n}_e(\rho,\phi) = \dfrac{\pi(1-\phi)}{2\,\rho} \end{cases} \tag{B.123}$$

The normalisation factors for the rectangular distribution function is then determined as in Eq. B.124:

$$\begin{aligned} C_i &= \sqrt{\frac{m_i}{2|q_iV_{\mathrm{c}}|}}\int\int f_{H,i}(1,1,\varepsilon_i,\lambda_i)\cdot v_{i,r}(1,1,\varepsilon_i,\lambda_i)\,\mathrm{d}\lambda_i\,\mathrm{d}\varepsilon_i \\ C_e &= \sqrt{\frac{m_e}{2|eV_{\mathrm{c}}|}}\int\int f_{H,e}(1,1,\varepsilon_e,\lambda_e)\cdot v_{e,r}(1,1,\varepsilon_e,\lambda_e)\,\mathrm{d}\lambda_i\,\mathrm{d}\varepsilon_i \end{aligned} \tag{B.124}$$

Being,

$$v_{r,\mathrm{s}} = \sqrt{\left|2q_{\mathrm{s}}\frac{V_{\mathrm{c}}}{m_{\mathrm{s}}}\right|}\sqrt{|\phi(\rho)-\varepsilon_{\mathrm{s}}|-\frac{\lambda_{\mathrm{s}}^2}{\rho^2}} \tag{B.125}$$

Eq. B.126 is then obtained:

$$\begin{cases} C_i = \sqrt{\dfrac{m_i}{2|q_i V_c|}}\dfrac{1}{\rho^2}\displaystyle\int_0^{\phi}\int_0^{\rho\sqrt{\varepsilon_i-\phi}}\sqrt{\dfrac{2|q_i V_c|}{m_i}}\left.\dfrac{\sqrt{\phi-\varepsilon_i-\dfrac{\lambda_i^2}{\rho^2}}}{\sqrt{\phi-\varepsilon_i-\dfrac{\lambda_i^2}{\rho^2}}}\right|_{\rho,\phi=1} & \mathrm{d}\lambda_i\,\mathrm{d}\varepsilon_i = \dfrac{1}{\rho^2}\displaystyle\int_0^{\phi}\int_0^{\rho\sqrt{\varepsilon_i-\phi}}\mathrm{d}\lambda_i\,\mathrm{d}\varepsilon_i \\ C_e = \sqrt{\dfrac{m_e}{2|eV_c|}}\dfrac{1}{\rho^2}\displaystyle\int_{\phi}^{1}\int_0^{\rho\sqrt{\phi-\varepsilon_e}}\sqrt{\dfrac{2|eV_c|}{m_e}}\left.\dfrac{\sqrt{\varepsilon_e-\phi-\dfrac{\lambda_e^2}{\rho^2}}}{\sqrt{\varepsilon_e-\phi-\dfrac{\lambda_e^2}{\rho^2}}}\right|_{\rho,\phi=1} & \mathrm{d}\lambda_e\,\mathrm{d}\varepsilon_e = \dfrac{1}{\rho^2}\displaystyle\int_{\phi}^{1}\int_0^{\rho\sqrt{\phi-\varepsilon_e}}\mathrm{d}\lambda_e\,\mathrm{d}\varepsilon_e \end{cases} \tag{B.126}$$

Finally, the normalisation factors for the rectangular distribution function result as in Eq. B.127.

$$\begin{cases} C_i = \dfrac{1}{\rho}\displaystyle\int_0^{\phi}\sqrt{\varepsilon_i-\phi}\,\mathrm{d}\varepsilon_i = \dfrac{2\phi^{\frac{3}{2}}}{3\rho} \\ C_e = \dfrac{1}{\rho}\displaystyle\int_{\phi}^{1}\rho\sqrt{\phi-\varepsilon_e}\,\mathrm{d}\varepsilon_e = \dfrac{2(1-\phi)^{\frac{3}{2}}}{3\rho} \end{cases} \tag{B.127}$$

Therefore, the normalised number densities in the source term of Poisson's equation are obtained, in the following form:

$$\begin{cases} n_i(\rho,\phi) = \dfrac{3}{4}\pi\dfrac{K_i}{\sqrt{\phi}} \\ n_e(\rho,\phi) = \dfrac{3}{4}\pi\dfrac{K_e}{\sqrt{1-\phi}} \end{cases} \tag{B.128}$$

Poisson's equation takes then the final form already introduce in Chapter 3, Section 1, ¶ Particle distribution functions:

$$\frac{\mathrm{d}^2\phi}{\mathrm{d}\rho^2}+\frac{1}{2\rho}\frac{\mathrm{d}\phi}{\mathrm{d}\rho} = \frac{3}{4}\frac{\pi}{n_c}\left(\frac{K_i}{\sqrt{\phi}}-\frac{K_e}{\sqrt{1-\phi}}\right) \tag{B.129}$$

Thermal distribution function

The thermal distribution function introduces the effect of the collisional processes, assuming the mathematical form given in Eq. B.130.

$$f_{T,s}(\rho,\phi,\varepsilon_s,\lambda_s) = \frac{H(\lambda_{max}-\lambda_s)H(\varepsilon_{max}-\varepsilon_s)H(\varepsilon_s-\varepsilon_{min})\lambda_s e^{-\frac{|\phi-\varepsilon_s|}{\varepsilon_{r,s}}}}{\rho^2\sqrt{|\phi(\rho)-\varepsilon_s|-\dfrac{\lambda_s^2}{\rho^2}}} \tag{B.130}$$

The first step, required for the thorough definition of the thermal model, is the assessment of the radial and transverse kinetic temperature for both the ion and electron populations. This is achieved by assuming the mean kinetic energy of each population, in the thermal model, to equal the value given in the rectangular model, at any radial location and potential value. In the following, the calculation for the mean kinetic energy for both the rectangular and thermal distribution functions is presented. As far as the rectangular model is concerned, the following relation holds:

$$\bar{U}_{\mathrm{H,s}} = \frac{1}{\rho} \int_{\varepsilon_{min,s}}^{\varepsilon_{max,s}} |\phi - \varepsilon_{\mathrm{s}}| \int_{0}^{\rho\sqrt{|\phi-\varepsilon_{\mathrm{s}}|}} \frac{\mathrm{d}\lambda_{\mathrm{s}}}{\sqrt{\rho^2|\phi - \varepsilon_{\mathrm{s}}| - {\lambda_{\mathrm{s}}}^2}} \mathrm{d}\varepsilon_{\mathrm{s}} \tag{B.131}$$

From standard integral tables:

$$\int \frac{\mathrm{d}x}{\sqrt{a - x^2}} = \frac{1}{\sqrt{a}} \sin^{-1}\left(\frac{x}{\sqrt{a}}\right) \tag{B.132}$$

Thus, the integral over total mechanical energy results in

$$\int_{0}^{\rho\sqrt{|\phi-\varepsilon_{\mathrm{s}}|}} \frac{\mathrm{d}\lambda_{\mathrm{s}}}{\sqrt{\rho^2|\phi - \varepsilon_{\mathrm{s}}| - {\lambda_{\mathrm{s}}}^2}} = \frac{1}{\rho} \sin^{-1}\left(\frac{\lambda_{\mathrm{s}}}{\rho\sqrt{|\phi - \varepsilon_{\mathrm{s}}|}}\right)\Bigg|_{0}^{\rho\sqrt{|\phi-\varepsilon_{\mathrm{s}}|}} = \frac{\pi}{2\rho} \tag{B.133}$$

Hence,

$$\bar{U}_{\mathrm{H,s}} = \int_{\varepsilon_{min,s}}^{\varepsilon_{max,s}} \frac{\pi}{2\rho} |\phi - \varepsilon_{\mathrm{s}}| \, \mathrm{d}\varepsilon_{\mathrm{s}} \tag{B.134}$$

Again, from standard integral tables:

$$\int a|b - x| \, \mathrm{d}x = a|x|\left(b - \frac{x}{2}\right) \tag{B.135}$$

Since the substitution in Eq. B.136 holds, the mean kinetic energy for the ion and electron populations, in the rectangular plasma model, is given in Eq. B.137.

$$\begin{cases} a = \dfrac{\pi}{2\rho} \\ b = \phi \\ x = \varepsilon_{\mathrm{s}} \end{cases} \tag{B.136}$$

$$\begin{cases} \bar{U}_{\mathrm{H},i} = \dfrac{\pi}{4\rho}\phi^2 \\ \bar{U}_{\mathrm{H},e} = \dfrac{\pi}{4\rho}(1 - \phi)^2 \end{cases} \tag{B.137}$$

As far as the thermal model is concerned, the mean kinetic energy can be determined as the expectation value in Eq. B.138.

$$\bar{U}_{\mathrm{T,s}} = \frac{1}{\rho} \int_{\varepsilon_{min,s}}^{\varepsilon_{max,s}} |\phi - \varepsilon_{\mathrm{s}}| e^{-\frac{|\phi-\varepsilon_{\mathrm{s}}|}{\varepsilon_{r,s}}} \int_{0}^{\rho\sqrt{|\phi-\varepsilon_{\mathrm{s}}|}} \frac{\lambda_{\mathrm{s}} \, \mathrm{d}\lambda_{\mathrm{s}}}{\sqrt{\rho^2|\phi - \varepsilon_{\mathrm{s}}| - {\lambda_{\mathrm{s}}}^2}} \mathrm{d}\varepsilon_{\mathrm{s}} \tag{B.138}$$

From standard integral tables:

$$\int \frac{x \, \mathrm{d}x}{\sqrt{a - x^2}} = -\sqrt{a - x^2} \tag{B.139}$$

Introducing the change of variables in Eq. B.140, the angular momentum integral is solved as in Eq. B.141.

$$\begin{cases} a = \rho^2|\phi - \varepsilon_{\mathrm{s}}| \\ x = \lambda_{\mathrm{s}} \end{cases} \tag{B.140}$$

$$\int_0^{\rho\sqrt{|\phi-\varepsilon_{\mathrm{s}}|}} \mathrm{d}\lambda_{\mathrm{s}} \frac{\lambda_{\mathrm{s}}}{\sqrt{\rho^2|\phi - \varepsilon_{\mathrm{s}}| - {\lambda_{\mathrm{s}}}^2}} = -\sqrt{\rho^2|\phi - \varepsilon_{\mathrm{s}}| - {\lambda_{\mathrm{s}}}^2}\Big|_0^{\rho\sqrt{|\phi-\varepsilon_{\mathrm{s}}|}} = \rho\sqrt{|\phi - \varepsilon_{\mathrm{s}}|} \tag{B.141}$$

Hence, the mean kinetic energy in the thermal model takes the following form:

$$\overline{U}_{\mathrm{T,s}} = \int_{\varepsilon_{min,s}}^{\varepsilon_{max,s}} \mathrm{d}\varepsilon_{\mathrm{s}}\, |\phi - \varepsilon_{\mathrm{s}}|^{\frac{3}{2}} e^{-\frac{|\phi-\varepsilon_{\mathrm{s}}|}{\varepsilon_{r,s}}} \tag{B.142}$$

From standard integral tables:

$$\int |a-x|^{\frac{3}{2}} e^{-\frac{|a-x|}{b}} \mathrm{d}x = \begin{cases} -\frac{b}{2} e^{-\frac{a-x}{b}} \sqrt{a-x}[-2(a-x) - 3b] - \frac{3}{4} b^{\frac{5}{2}} \sqrt{\pi} erf\left(\sqrt{\frac{a-x}{b}}\right) \\ -\frac{b}{2} e^{-\frac{x-a}{b}} \sqrt{x-a}[-2(a-x) + 3b] + \frac{3}{4} b^{\frac{5}{2}} \sqrt{\pi} erf\left(\sqrt{\frac{x-a}{b}}\right) \end{cases} \tag{B.143}$$

By substituting the general integral solution in Eq. B.141, the solution in Eq. B.143 yields.

$$\begin{cases} \overline{U}_{\mathrm{T},i} = -\frac{\varepsilon_{r,\mathrm{i}}}{2} e^{-\frac{\phi-\varepsilon_{\mathrm{i}}}{\varepsilon_{r,\mathrm{i}}}} \sqrt{\phi - \varepsilon_{\mathrm{i}}}\left[-2(\phi - \varepsilon_i) - 3\varepsilon_{r,\mathrm{i}}\right] - \frac{3}{4}\, {\varepsilon_{r,\mathrm{i}}}^{\frac{5}{2}}\, \sqrt{\pi}\; erf\left(\sqrt{\frac{\phi - \varepsilon_{\mathrm{i}}}{\varepsilon_{r,\mathrm{i}}}}\right)\Big|_0^{\phi} \\ \overline{U}_{\mathrm{T},e} = -\frac{\varepsilon_{r,\mathrm{e}}}{2} e^{-\frac{\varepsilon_e-\phi}{\varepsilon_{r,\mathrm{e}}}} \sqrt{\varepsilon_e - \phi}\left[2(\varepsilon_e - \phi) + 3\varepsilon_{r,\mathrm{e}}\right] + \frac{3}{4}\, {\varepsilon_{r,\mathrm{e}}}^{\frac{5}{2}}\, \sqrt{\pi}\; erf\left(\sqrt{\frac{\varepsilon_e - \phi}{\varepsilon_{r,\mathrm{e}}}}\right)\Big|_{\phi}^{1} \end{cases} \tag{B.144}$$

Finally, the mean kinetic energy for both the ion and electron population is obtained in thermal model:

$$\begin{cases} \overline{U}_{\mathrm{T},i} = -\frac{\varepsilon_{r,\mathrm{i}}}{2} e^{-\frac{\phi}{\varepsilon_{r,\mathrm{i}}}} \sqrt{\phi}\left[2\phi + 3\varepsilon_{r,\mathrm{i}}\right] + \frac{3}{4}\, {\varepsilon_{r,\mathrm{i}}}^{\frac{5}{2}}\, \sqrt{\pi}\; erf\left(\sqrt{\frac{\phi}{\varepsilon_{r,\mathrm{i}}}}\right) \\ \overline{U}_{\mathrm{T},e} = -\frac{\varepsilon_{r,\mathrm{e}}}{2} e^{-\frac{\varepsilon_e-\phi}{\varepsilon_{r,\mathrm{e}}}} \sqrt{1 - \phi}\left[2(1 - \phi) + 3\varepsilon_{r,\mathrm{e}}\right] + \frac{3}{4}\, {\varepsilon_{r,\mathrm{e}}}^{\frac{5}{2}}\, \sqrt{\pi}\; erf\left(\sqrt{\frac{1 - \phi}{\varepsilon_{r,\mathrm{e}}}}\right) \end{cases} \tag{B.145}$$

In order to evaluate the particles temperature Eq. B.146 is thus used:

$$\begin{aligned} \overline{U}_{\mathrm{T},i} &= \overline{U}_{\mathrm{H},i} \\ \overline{U}_{\mathrm{T},e} &= \overline{U}_{\mathrm{H},e} \end{aligned} \tag{B.146}$$

Substituting the integral result for the mean kinetic energies, the following functional relations yield:

$$\begin{cases} \frac{3}{4}\, {\varepsilon_{r,\mathrm{i}}}^{\frac{5}{2}}\, \sqrt{\pi}\; erf\left(\sqrt{\frac{\phi}{\varepsilon_{r,\mathrm{i}}}}\right) - \frac{\varepsilon_{r,\mathrm{i}}}{2} e^{-\frac{\phi}{\varepsilon_{r,\mathrm{i}}}} \sqrt{\phi}\left[2\phi + 3\varepsilon_{r,\mathrm{i}}\right] = \frac{\pi}{4\rho}\phi^2 \\ \frac{3}{4}\, {\varepsilon_{r,\mathrm{e}}}^{\frac{5}{2}}\, \sqrt{\pi}\; erf\left(\sqrt{\frac{1 - \phi}{\varepsilon_{r,\mathrm{e}}}}\right) - \frac{\varepsilon_{r,\mathrm{e}}}{2} e^{-\frac{\varepsilon_e-\phi}{\varepsilon_{r,\mathrm{e}}}} \sqrt{1 - \phi}\left[2(1 - \phi) + 3\varepsilon_{r,\mathrm{e}}\right] = \frac{\pi}{4\rho}(1 - \phi)^2 \end{cases} \tag{B.147}$$

Resolution of Eq. B.147, at a specific radial position and for a given electrostatic potential, allows for the determination of the normalised kinetic energy related to the particle radial motion and, subsequently, the local temperature for each charge-carrier population inside the IEC.

The number density for both the charge-carrier populations is determined by integrating the thermal distribution functions over mechanical energy and angular momentum:

$$\hat{n}_{\mathrm{s}}(\rho,\phi)=\int_{\varepsilon_{min,s}}^{\varepsilon_{max,s}}\int_{0}^{\lambda_{max,s}}\mathrm{d}\lambda_{\mathrm{s}}\,\frac{\lambda_{\mathrm{s}}\cdot e^{-\frac{|\phi-\varepsilon_{\mathrm{s}}|}{\varepsilon_{r,s}}}}{\rho^{2}\sqrt{|\phi-\varepsilon_{\mathrm{s}}|-\frac{\lambda_{\mathrm{s}}{}^{2}}{\rho^{2}}}}\mathrm{d}\varepsilon_{\mathrm{s}}=\int_{\varepsilon_{min,s}}^{\varepsilon_{max,s}}\frac{e^{-\frac{|\phi-\varepsilon_{\mathrm{s}}|}{\varepsilon_{r,s}}}}{\rho^{2}}\int_{0}^{\rho\sqrt{|\phi-\varepsilon_{\mathrm{s}}|}}\frac{\mathrm{d}\lambda_{\mathrm{s}}\,\lambda_{\mathrm{s}}}{\sqrt{|\phi-\varepsilon_{\mathrm{s}}|-\frac{\lambda_{\mathrm{s}}{}^{2}}{\rho^{2}}}}\mathrm{d}\varepsilon_{\mathrm{s}} \tag{B.148}$$

From standard integral tables:

$$\int\frac{x}{\sqrt{a-\frac{x^{2}}{b}}}\,\mathrm{d}x\;=-b\sqrt{a-\frac{x^{2}}{b}} \tag{B.149}$$

In the present case, the following relations hold:

$$\begin{cases}a=|\phi-\varepsilon_{\mathrm{s}}|\\ b=\rho^{2}\\ x=\lambda_{\mathrm{s}}\end{cases} \tag{B.150}$$

Thus, the integration over angular momentum yields:

$$\int_{0}^{\rho\sqrt{|\phi-\varepsilon_{\mathrm{s}}|}}\frac{\lambda_{\mathrm{s}}\,\mathrm{d}\lambda_{\mathrm{s}}}{\sqrt{|\phi-\varepsilon_{\mathrm{s}}|-\frac{\lambda_{\mathrm{s}}{}^{2}}{\rho^{2}}}}=\rho^{2}\sqrt{|\phi-\varepsilon_{\mathrm{s}}|} \tag{B.151}$$

$$\int_{\varepsilon_{min,s}}^{\varepsilon_{max,s}}\frac{\sqrt{|\phi-\varepsilon_{\mathrm{s}}|}}{\rho^{2}}\rho^{2}e^{-\frac{|\phi-\varepsilon_{\mathrm{s}}|}{\varepsilon_{r,s}}}\,\mathrm{d}\varepsilon_{\mathrm{s}}=\int_{\varepsilon_{min,s}}^{\phi}e^{-\frac{\phi-\varepsilon_{\mathrm{s}}}{\varepsilon_{r,s}}}\sqrt{\phi-\varepsilon_{\mathrm{s}}}\,\mathrm{d}\varepsilon_{\mathrm{s}}+\int_{\phi}^{\varepsilon_{max,s}}e^{\frac{\phi-\varepsilon_{\mathrm{s}}}{\varepsilon_{r,s}}}\sqrt{\varepsilon_{\mathrm{s}}-\phi}\,\mathrm{d}\varepsilon_{\mathrm{s}} \tag{B.152}$$

From standard integral tables:

$$\int\sqrt{a-x}\,e^{-\frac{a-x}{b}}\,\mathrm{d}x\;=b\sqrt{a-x}\,e^{\frac{x-a}{b}}-\frac{\sqrt{\pi}}{2}b^{\frac{3}{2}}\,\mathrm{erf}\left(\sqrt{\frac{a-x}{b}}\right) \tag{B.153}$$

Hence, being

$$\begin{cases}a=\phi\\ b=\varepsilon_{r,s}\\ x=\varepsilon_{\mathrm{s}}\end{cases} \tag{B.154}$$

The following result yields from the integration in Eq. B.148:

$$\hat{n}_{\mathrm{s}}=\left[\varepsilon_{r,s}\sqrt{\phi-\varepsilon_{\mathrm{s}}}\,e^{-\frac{\phi-\varepsilon_{\mathrm{s}}}{\varepsilon_{r,s}}}-\frac{\sqrt{\pi}}{2}\varepsilon_{r,s}{}^{\frac{3}{2}}\,\mathrm{erf}\left(\sqrt{\frac{\phi-\varepsilon_{\mathrm{s}}}{\varepsilon_{r,s}}}\right)\right]_{\varepsilon_{min,s}}^{\phi}-\left[\varepsilon_{r,s}\sqrt{\varepsilon_{\mathrm{s}}-\phi}\,e^{\frac{\varepsilon_{\mathrm{s}}-\phi}{\varepsilon_{r,s}}}-\frac{\sqrt{\pi}}{2}\varepsilon_{r,s}{}^{\frac{3}{2}}\,\mathrm{erf}\left(\sqrt{\frac{\varepsilon_{\mathrm{s}}-\phi}{\varepsilon_{r,s}}}\right)\right]_{\phi}^{\varepsilon_{max,s}} \tag{B.155}$$

Finally, recalling the integration limit in Eq. B.155, the number density for each charge-carrier populations is derived as in Eq. B.156:

$$\begin{cases} \hat{n}_i(\rho,\phi) = \varepsilon_{r,i}{}^{\frac{3}{2}}\left[\frac{\sqrt{\pi}}{2}\mathrm{erf}\left(\sqrt{\frac{\phi}{\varepsilon_{r,i}}}\right) - e^{-\frac{\phi}{\varepsilon_{r,i}}}\sqrt{\frac{\phi}{\varepsilon_{r,i}}}\right] \\ \hat{n}_e(\rho,\phi) = \varepsilon_{r,e}{}^{\frac{3}{2}}\left[\frac{\sqrt{\pi}}{2}\mathrm{erf}\left(\sqrt{\frac{1-\phi}{\varepsilon_{r,e}}}\right) - e^{-\frac{1-\phi}{\varepsilon_{r,e}}}\sqrt{\frac{1-\phi}{\varepsilon_{r,e}}}\right] \end{cases} \tag{B.156}$$

The normalisation factors for the thermal distribution function are assessed by substituting the thermal distribution function and the respective radial velocity into Eq. B.97:

$$\begin{aligned} C_\mathrm{s} &= \int_{\varepsilon_{min,\mathrm{s}}}^{\varepsilon_{max,\mathrm{s}}} \int_0^{\rho\sqrt{|\phi-\varepsilon_\mathrm{s}|}} \mathrm{d}\lambda_\mathrm{s} \frac{\lambda_\mathrm{s}\, e^{-\frac{|\phi-\varepsilon_\mathrm{s}|}{\varepsilon_{r,\mathrm{s}}}}}{\rho^2}\,\mathrm{d}\varepsilon_\mathrm{s} = \frac{1}{\rho^2}\int_{\varepsilon_{min,\mathrm{s}}}^{\varepsilon_{max,\mathrm{s}}} e^{-\frac{|\phi-\varepsilon_\mathrm{s}|}{\varepsilon_{r,\mathrm{s}}}} \int_0^{\rho\sqrt{|\phi-\varepsilon_\mathrm{s}|}} \lambda_\mathrm{s}\,\mathrm{d}\lambda_\mathrm{s}\,\mathrm{d}\varepsilon_\mathrm{s} = \\ &= \frac{1}{\rho^2}\int_{\varepsilon_{min,\mathrm{s}}}^{\varepsilon_{max,\mathrm{s}}} \frac{\rho^2}{2}|\phi-\varepsilon_\mathrm{s}| e^{-\frac{|\phi-\varepsilon_\mathrm{s}|}{\varepsilon_{r,\mathrm{s}}}}\,\mathrm{d}\varepsilon_\mathrm{s} = \frac{1}{2}\int_{\varepsilon_{min,\mathrm{s}}}^{\varepsilon_{max,\mathrm{s}}} |\phi-\varepsilon_\mathrm{s}|\, e^{-\frac{|\phi-\varepsilon_\mathrm{s}|}{\varepsilon_{r,\mathrm{s}}}}\,\mathrm{d}\varepsilon_\mathrm{s} \end{aligned} \tag{B.157}$$

From standard integral tables:

$$\int |a-x| e^{-\frac{|a-x|}{b}}\,\mathrm{d}x = \begin{cases} be^{-\frac{a-x}{b}}(b+a-x) \\ -be^{-\frac{x-a}{b}}(b+x-a) \end{cases} \tag{B.158}$$

Introducing the change of variables in Eq. B.159, the normalisation factors are assessed as in Eq. B.160.

$$\begin{cases} a = \phi \\ b = \varepsilon_{r,\mathrm{s}} \\ x = \varepsilon_\mathrm{s} \end{cases} \tag{B.159}$$

$$\begin{cases} C_i = \frac{\varepsilon_{r,\mathrm{i}}}{2}\left[\varepsilon_{r,\mathrm{i}} - e^{-\frac{\phi}{\varepsilon_{r,\mathrm{i}}}}\left(\varepsilon_{r,\mathrm{i}}+\phi\right)\right]\Big|_{\phi=1} = \frac{\varepsilon_{r,\mathrm{i}}}{2}\left[\varepsilon_{r,\mathrm{i}} - e^{-\frac{1}{\varepsilon_{r,\mathrm{i}}}}\left(\varepsilon_{r,\mathrm{i}}+1\right)\right] \\ C_e = \frac{\varepsilon_{r,\mathrm{e}}}{2}\left[\varepsilon_{r,\mathrm{e}} - e^{-\frac{1-\phi}{\varepsilon_{r,\mathrm{e}}}}\left(\varepsilon_{r,\mathrm{e}}+1-\phi\right)\right]\Big|_{\phi=0} = \frac{\varepsilon_{r,\mathrm{e}}}{2}\left[\varepsilon_{r,\mathrm{e}} - e^{-\frac{1}{\varepsilon_{r,\mathrm{e}}}}\left(\varepsilon_{r,\mathrm{e}}+1\right)\right] \end{cases} \tag{B.160}$$

Therefore, the normalised number densities in the source term of Poisson's equation are obtained, in the following form:

$$\begin{cases} n_i = n_g K_i \dfrac{2\sqrt{\varepsilon_{r,\mathrm{i}}}\left[\frac{\sqrt{\pi}}{2}\ erf\left(\sqrt{\frac{\phi}{\varepsilon_{r,\mathrm{i}}}}\right) - e^{-\frac{\phi}{\varepsilon_{r,\mathrm{i}}}}\sqrt{\frac{\phi}{\varepsilon_{r,\mathrm{i}}}}\right]}{\left[\varepsilon_{r,\mathrm{i}} - e^{-\frac{1}{\varepsilon_{r,\mathrm{i}}}}\left(\varepsilon_{r,\mathrm{i}}+1\right)\right]} \\ n_e = n_g K_e \dfrac{2\sqrt{\varepsilon_{r,\mathrm{e}}}\left[\frac{\sqrt{\pi}}{2}\ erf\left(\sqrt{\frac{1-\phi}{\varepsilon_{r,\mathrm{e}}}}\right) - e^{-\frac{1-\phi}{\varepsilon_{r,\mathrm{e}}}}\sqrt{\frac{1-\phi}{\varepsilon_{r,\mathrm{e}}}}\right]}{\left[\varepsilon_{r,\mathrm{e}} - e^{-\frac{1}{\varepsilon_{r,\mathrm{e}}}}\left(\varepsilon_{r,\mathrm{e}}+1\right)\right]} \end{cases} \tag{B.161}$$

Poisson's equation takes then the final form already introduce in Chapter 3, Section 1, ¶ Particle distribution functions:

$$\frac{\mathrm{d}^2\phi}{\mathrm{d}\rho^2} + \frac{1}{2\rho}\frac{\mathrm{d}\phi}{\mathrm{d}\rho} = \left\{ K_i \frac{2\sqrt{\varepsilon_{r,\mathrm{i}}}\left[\frac{\sqrt{\pi}}{2}\ erf\left(\sqrt{\frac{\phi}{\varepsilon_{r,\mathrm{i}}}}\right) - e^{-\frac{\phi}{\varepsilon_{r,\mathrm{i}}}}\sqrt{\frac{\phi}{\varepsilon_{r,\mathrm{i}}}}\right]}{\left[\varepsilon_{r,\mathrm{i}} - e^{-\frac{1}{\varepsilon_{r,\mathrm{i}}}}\left(\varepsilon_{r,\mathrm{i}}+1\right)\right]} - K_e \frac{2\sqrt{\varepsilon_{r,\mathrm{e}}}\left[\frac{\sqrt{\pi}}{2}\ erf\left(\sqrt{\frac{1-\phi}{\varepsilon_{r,\mathrm{e}}}}\right) - e^{-\frac{1-\phi}{\varepsilon_{r,\mathrm{e}}}}\sqrt{\frac{1-\phi}{\varepsilon_{r,\mathrm{e}}}}\right]}{\left[\varepsilon_{r,\mathrm{e}} - e^{-\frac{1}{\varepsilon_{r,\mathrm{e}}}}\left(\varepsilon_{r,\mathrm{e}}+1\right)\right]} \right\} \tag{B.162}$$

Appendix C
Harmonic function and Potential theory

C.1 Laplace equation

¶ Definition and physical interpretation

The present appendix addresses the topic of harmonic functions and their mathematical properties: they represent a function space, which assumes great importance in many of the issues of steady-state equilibrium physics and, more precisely, represent the basis of potential theory.

A harmonic function u can be defined on an open, nonempty subset of the n-dimensional Euclidian space $\mathbb{R}^n$ -denoted as $\mathbb{U}$- as a $\mathcal{C}^2$class function, that satisfies Eq. C.1.

$$\nabla^2 u = 0 \tag{C.1}$$

Where $\nabla^2(\cdot)$ is the differential operator, known as "Laplace operator" or "Laplacian", defined as:

$$\nabla^2(\cdot) = \sum_{i=1}^{n} \frac{\partial^2(\cdot)}{\partial {x_i}^2} \tag{C.2}$$

Hence, Eq. C.1 is commonly referred to as "Laplace equation" and a harmonic function can be simply defined as a twice continuously differentiable function that is a solution to Laplace equation. The Laplacian is a linear, elliptic differential operator of the second order and its properties reflect on the related homogeneous equation. Indeed, due to the linearity of the Laplace operator, the linear combination of two (or more) harmonic functions is itself a solution to Laplace equation, i.e. harmonic: this property is commonly referred to as "superimposition principle". Laplace equation is one of the most important of all partial differential equations, appearing in a number of different physical contexts [74] and is thus one of the most studied and well-understood objects in mathematical physics. The typical interpretation of Laplace equation in this context is that it describes the steady-state equilibrium for the density of a physical quantity, represented by u. Remarkable examples of this concept are Fick's law of diffusion, Fourier's law of heat conduction and Ohm's law of electrical conduction, where the equilibrium variable u denotes the chemical concentration of the diffusing species, the temperature and the electrostatic potential, respectively. Therefore, assuming $\mathbb{V}$ to be a smooth sub-region of $\mathbb{U}$, if the physical quantity u is conserved over $\mathbb{V}$ and a steady-state assumption can be made, the conservation equation takes than the following form:

$$\int_{\partial \mathbb{V}} \left(\vec{F} \cdot \vec{v}\right) \mathrm{d}S = 0 \tag{C.3}$$

Where $\vec{F}$, is the flux density of u
$\vec{v}$, is the unit outer normal field
$\partial \mathbb{V}$, is the boundary surface of $\mathbb{V}$.

For the purpose of the present thesis, in particular, reference to the interpretation of Laplace equation, as describing the steady-state equilibrium for an electrostatic system, will be made: the equation -written for the electrostatic potential- follows directly from the conservation law for the electric potential energy in a system characterised by a time-invariant electric field. In the context of classical electrostatics, u is then a scalar field, representing the electrostatic potential ϕ over a compact subset of the three-

dimensional Euclidian space, $\mathbb{V} \subseteq \mathbb{R}^3$, and its flux density vector can be assumed to be proportional to the gradient field - i.e. to the electrostatic field $\vec{E}$- but pointing in the opposite direction:

$$\vec{F} = -\alpha \nabla\phi = \alpha \vec{E} \tag{C.4}$$

Where α is a positive constant, $\alpha \in \mathbb{R}^+$.

Applying Gauss-Green theorem, the outward flux of the electrostatic field can thus be expressed in terms of the divergence of the field itself over $\mathbb{V}$:

$$\oiint_{\partial\mathbb{V}} (\vec{F} \cdot \vec{v})\, \mathrm{d}S = \iiint_{\mathbb{V}} (\nabla \cdot \vec{F})\, \mathrm{d}V \tag{C.5}$$

Then, substituting Eq. C.4 and C.5 in Eq. C.3, the following yields:

$$\iiint_{\mathbb{V}} (\nabla \cdot \vec{E})\, \mathrm{d}V = 0 \tag{C.6}$$

Moreover, since no specific assumptions where made for the physical domain $\mathbb{V}$, the global equilibrium condition expressed in Eq. C.6 can be recast in a local form, as a Laplace equation for the electrostatic field (Eq. C.8):

$$\nabla \cdot \vec{E} = 0 \tag{C.7}$$

$$\Downarrow$$

$$\nabla^2\phi = 0 \tag{C.8}$$

Therefore, it is possible to conclude that, in the limit of steady-state assumption, the electrostatic field can be described in terms of its scalar potential ϕ, which is a harmonic function according to Eq. C.8 [96].

Hence, the concept of harmonic function is especially central in the context of classical physics: until the end of 19th Century, it was thought that every physical force was to be described in terms of elementary potential fields, which satisfied Laplace equation. This notion is the basis of what is known as "Potential theory" and, although nowadays it is well understood that elementary forces, in physics, are to be delineated by means of sets of non-linear equations (e.g. Einstein field equations, Yang-Mills equations, etc.), it still plays a significant role in equilibrium problems for homogeneous media.

¶ Harmonic function properties

The interest in potential theory, for the purpose of the present thesis, is related to the desire to assess the detailed topography of the electrostatic field engendered by the gridded electrodes in an IEC device (see Chapter 5). If the electromagnetic induction effects -due to the electric current flowing through the electrodes- are assumed to be negligible, the problem is reduced to the following Dirichlet boundary problem:

"*Absence of localised charges. The electrostatic field is generated by a system of conducting bodies* S_i $(i = 1 \dots N)$ *whose geometry and potential values* V_i $(i = 1 \dots N)$ *are known.*" [96]

This physical problem takes then the following mathematical form:

$$\begin{cases} \nabla^2\phi(x) = 0 & x \in \mathbb{V} \\ \phi(x) = \phi_{electrodes} & x \in \partial\mathbb{V} \end{cases} \tag{C.9}$$

Where $\partial\mathbb{V}$ represents the totality of the conductive wires in the IEC device electrodes. It is clear, then, that the solution to such a problem is to be found in the set of harmonic functions: such functions show a variety of properties, which prove themselves extremely useful to the solution of Eq. C.9. In the following the most relevant of these properties are illustrated.

Invariance

Given the linearity of the Laplace operator over $C^2(\mathbb{U})$, the linear combination of two or more harmonic functions is still a harmonic function. Two distinct mathematical properties yield from this fact. First, harmonic functions represent a function vector space. In addition, such a vector space is closed with respect to a vast set of transformations:

- Translations of harmonic functions are harmonic;
- Dilates of harmonic function are harmonic;
- Orthogonal transforms (i.e. rotations and reflections) of harmonic function are harmonic;
- If a function is harmonic over a plane domain (i.e. a compact subset of $\mathbb{R}^2$), and is transformed via a conformal map to another plane domain, the transformation is also harmonic.

Mean-value theorem

Assuming that u can be defined on an open, nonempty subset of the n-dimensional Euclidian space $\mathbb{R}^n$ -denoted as $\mathbb{U}$- as a C^2class to be a harmonic function over the open set $\mathbb{U} \in \mathbb{R}^n$, for every ball $\mathcal{B}(x,r) \subset \mathbb{U}$, the value of $u(x)$ equals both the average of u over the sphere $\partial\mathcal{B}$ and the average over the entire ball $\mathcal{B}$ [97]:

$$u(\vec{x}) = \int_{\partial\mathcal{B}(x,r)} u(x+\zeta r)\, \mathrm{d}S(\zeta) = \frac{1}{V\big(\mathcal{B}(x,r)\big)} \int_{\mathcal{B}(x,r)} u\ \mathrm{d}V \tag{C.10}$$

Where $V\big(\mathcal{B}(x,r)\big)$ is the volume measure of the ball of radius r, centred in x.

Regularity

The following regularity theorem directly descends from the mean-value property: if $u \in C(\mathbb{U})$ satisfies the mean-value theorem (Eq. C.10) for each ball $\mathcal{B}(x,r) \subset \mathbb{U}$, then $u \in C^\infty(\mathbb{U})$. Hence any harmonic function is naturally infinitely differentiable over its definition domain, although this might not hold over the domain boundary $\partial\mathbb{U}$, where u may not even be continuous [74].

Uniqueness

If a harmonic function u is continuous on the domain boundary $\partial\mathbb{U}$, another interesting property comes from the mean-value theorem, namely a strong maximum (and minimum) principle stating that any harmonic function attains its maximum (and minimum) value on the domain border. Moreover, if the domain is connected, this implies that u is constant over the closure of its domain. An important application of such a principle is that it establishes the uniqueness of the solution to certain Dirichlet problems for Poisson equation [74]. In particular, if $g \in C(\partial\mathbb{U})$ and $f \in C(\mathbb{U})$, then exists at most one solution $u \in C^2(\mathbb{U}) \cap C(\mathbb{U})$ for the boundary value problem in Eq. C.11.

$$\begin{cases} -\nabla^2 u = f & in\ \mathbb{U} \\ u = g & on\ \partial\mathbb{U} \end{cases} \tag{C.11}$$

This result can be easily extended to the case of interest, i.e. the Dirichlet problem for Laplace equation in Eq. C.9, by trivially choosing the source term function f to be equal to zero over the entire domain $\mathbb{U}$ [98].

Liouville's theorem

The previous results can then be extended over the entire Euclidian space, according to Liouville's theorem, stating that there are no nontrivial bounded harmonic functions over $\mathbb{R}^n$. Indeed, if $u\colon \mathbb{R}^n \to \mathbb{R}$ is harmonic and bounded, than u is constant.

From all the above mentioned properties follows that harmonic functions that arise in physics as solutions of steady-state equilibrium problems, are determined by their singularities and boundary conditions. Referring to the terminology of electrostatics, the singularities are considered to be point

charges (for isolated singularities) or charge distributions: due to such singularities, the harmonic solution to Dirichlet problem will be proportional to the electrostatic potential. Hence, given a physical problem, such as in Eq. C.9, the solution can be defined as the unique harmonic function determined by the singularities on the border of its physical domain.

C.2 Resolution of two-dimensional Laplace equation

¶ Analyticity of harmonic functions

When looking for a solution of Laplace equation over a two-dimensional manifold (e.g. the Euclidian plane $\mathbb{R}^2$), it is possible to employ a specific property of the equation itself to transpose the issue on the complex plane $\mathbb{C}$ and solve the equation by the means of complex analysis and conformal mapping. Assuming the function $f : \mathbb{R}^2 \rightarrow \mathbb{R}$ to be a solution of Laplace equation and considering a Cartesian reference system xy for the real plane, Eq. C.12 holds:

$$\frac{\partial^2 f}{\partial x^2} + \frac{\partial^2 f}{\partial y^2} = 0 \tag{C.12}$$

Since the set $\mathbb{C}$ can be simultaneously thought of as a one-dimensional complex vector space (i.e. the complex field) and a real two-dimensional vector space (considering Argand-Gauss plane to be the Euclidian plane), the harmonic function f can be easily seen as a real-valued function on the complex field. This leads to the introduction of a critical property for the solutions of Eq. C.12, establishing a close tie between harmonic functions and complex analytics functions (whose definition will be presented later on). To understand such a link, consider the complex change of variable $\xi, \eta: \mathbb{R}^2 \rightarrow \mathbb{C}$, defined as follows [99]:

$$\begin{aligned} \xi &= x + iy \\ \eta &= x - iy \end{aligned} \tag{C.13}$$

The inverse mapping is given by Eq. C.14:

$$\begin{aligned} x &= \frac{1}{2}(\xi + \eta) \\ y &= \frac{1}{2}(\xi - \eta) \end{aligned} \tag{C.14}$$

Thus, differentiating Eq. C.14 according to the chain rule, Eq. C.15 yields:

$$\begin{aligned} \frac{\partial(\cdot)}{\partial x} &= \frac{\partial(\cdot)}{\partial \xi} + \frac{\partial(\cdot)}{\partial \eta} \\ \frac{\partial(\cdot)}{\partial y} &= i\left(\frac{\partial(\cdot)}{\partial \xi} - \frac{\partial(\cdot)}{\partial \eta}\right) \end{aligned} \tag{C.15}$$

The differential relations allow then to recast Laplace equation as:

$$4\frac{\partial^2 f}{\partial \xi \partial \eta} = 0 \tag{C.16}$$

The general form for the solution of Eq. C.16 is

$$f = p(\xi) + q(\eta) = p(x + iy) + q(x - iy) \tag{C.17}$$

Where p and q are differentiable complex functions.

Noticing that the complex variables introduced in Eq. C.13 represent the canonical notation for a complex number ($z = x + iy$) and its complex conjugate ($\bar{z} = x + iy$), Eq. C.16 is recast as:

$$f = p(z) + q(\bar{z}) \tag{C.18}$$

Hence, if a real solution of the original Laplace equation over the Euclidian plane is required, an additional constraint is introduced: the sum of the two functions must have no imaginary part.

It is now appropriate to explain what does the requirement for the complex functions p and q to be differentiable, entail. A complex-valued function f might be thought of as the linear combination of two real-valued function over the two-dimensional Euclidian space $u, v : \mathbb{R}^2 \rightarrow \mathbb{R}$, as in Eq. C.19:

$$f(z) = f(x + iy) = u(x, y) + iv(x + iy) \tag{C.19}$$

Such a function is said to be "analytic" (or "holomorphic") at a point $z_0 = x_0 + iy_0$ of Argand-Gauss plane, if the derivative in Eq. C.20 exists and is unique, for a step Δz taken in any direction of the complex plane:

$$\left.\frac{\mathrm{d}f}{\mathrm{d}z}\right|_{z_0} = \lim_{\Delta z \to 0} \frac{f(z_0 + \Delta z) - f(z_0)}{\Delta z} \tag{C.20}$$

Considering the infinitesimal increment $\Delta z = \Delta x + i\Delta y$ to be taken parallel to the real and imaginary axis of the complex plane, Eq. C.21 and C.22 yield respectively:

$$\left.\frac{\mathrm{d}f}{\mathrm{d}z}\right|_{z_0} = \lim_{\Delta x \to 0} \frac{u(x_0 + \Delta x, y_0) - u(x_0, y_0) + i[v(x_0 + \Delta x, y_0) - v(x_0, y_0)]}{\Delta x} = \frac{\partial u}{\partial x} + i\frac{\partial v}{\partial x} \tag{C.21}$$

$$\left.\frac{\mathrm{d}f}{\mathrm{d}z}\right|_{z_0} = \lim_{i\Delta y \to 0} \frac{u(x_0, y_0 + \Delta y) - u(x_0, y_0) + i[v(x_0, y_0 + \Delta y) - v(x_0, y_0)]}{i\,\Delta y} = -i\frac{\partial u}{\partial y} + \frac{\partial v}{\partial y} \tag{C.22}$$

Therefore, it is possible to compare the corresponding members in Eq. C.21 and C.22. For the complex derivative in Eq. C.20 to be uniquely defined the following equivalences, commonly known as Cauchy-Riemann equations, must hold:

$$\begin{cases} \dfrac{\partial u}{\partial x} = \dfrac{\partial v}{\partial y} \\ \dfrac{\partial u}{\partial y} = -\dfrac{\partial v}{\partial x} \end{cases} \tag{C.23}$$

These relations can be differentiated once to give the following:

$$\begin{aligned} \frac{\partial^2 u}{\partial x^2} &= \frac{\partial^2 v}{\partial x \partial y} \quad & \frac{\partial^2 v}{\partial x^2} &= -\frac{\partial^2 u}{\partial x \partial y} \\ \frac{\partial^2 u}{\partial y^2} &= -\frac{\partial^2 v}{\partial y \partial x} \quad & \frac{\partial^2 v}{\partial y^2} &= \frac{\partial^2 u}{\partial y \partial x} \end{aligned} \tag{C.24}$$

Summing the corresponding terms of the second derivative for the functions u and v, two distinct equations, formally identical to Laplace equation in Eq. C.12, yield:

$$\frac{\partial^2 u}{\partial x^2} + \frac{\partial^2 u}{\partial y^2} = 0 \tag{C.25}$$

$$\frac{\partial^2 v}{\partial x^2} + \frac{\partial^2 v}{\partial y^2} = 0 \tag{C.26}$$

Hence, it is possible to conclude that the following statements are equivalent:

- $f : \mathbb{C} \rightarrow \mathbb{R}$ is holomorphic;
- Cauchy-Riemann equations for the component functions u and v hold;

- u and v are harmonic functions.

Therefore, the complex functions involved in the solution of Laplace equation, according to Eq. C.18, must be expressible as a combination of harmonic functions, in the form of Eq. C.19. Every analytic function on the Argand-Gauss plane provides, then, two solutions of a two-dimensional Laplace equation, usually referred to as "*conjugate harmonic*" functions. From Eq. C.23 is easily seen that:

$$\nabla u \cdot \nabla v = 0 \tag{C.27}$$

Hence, the curves $u = const.$ and $v = const.$, representing a set of solution for the Laplace system in Eq. C.25 and C.26, are perpendicular to each other.

$$u(x, y) = C_1 \tag{C.28}$$

$$v(x, y) = C_2 \tag{C.29}$$

Where $C_1, C_2 \in \mathbb{R}$.

Interpreting the original Laplace equation (Eq. C.12) on the Euclidian plane as describing the two-dimensional scalar field for the electrostatic potential ϕ, once a solution is found on the complex plane, a distinct physical meaning can be given to these curves. If u is the real component of the complex solution f, the curves over $\mathbb{R}^2$ represented by Eq. C.28 are the contour lines of equal electrostatic potential. On the other hand, the curves corresponding to the solution of Eq. C.29 represent the flux line of the corresponding electrostatic field [100].

¶ Complex variables

In the previous section, the close tie between analytic complex functions and harmonic functions was described and the two-dimensional Laplace equation was transposed on the complex plane. The present section is then focused on the resolution of Laplace equation by means of the mathematical tools provided by complex analysis.

Eq C.18 provided a representation form, for the solution of Laplace equation, by means of holomorphic functions. It is now necessary to assess the proper solution of the Dirichlet problem for Laplace equation (Eq. C.9), determining a mathematical formulation that takes into account the assigned boundary conditions. First of all, it is of use to further transpose the differential problem in an alternative reference frame: given the invariance of harmonic functions with respect to orthogonal transformations, in particular rotations, the expected solution is radial and the polar coordinate frame (Eq. C.30) is remarkably suitable for the problem at hand.

$$\begin{aligned} r &= \sqrt{x^2 + y^2} \\ \theta &= \tan^{-1}\frac{y}{x} \end{aligned} \tag{C.30}$$

Substituting Eq. C.30 in Eq. C.12, the following result yields:

$$\nabla^2 f = \frac{1}{r}\frac{\partial}{\partial r}\left(r\frac{\partial f}{\partial r}\right) + \frac{1}{r^2}\frac{\partial^2 f}{\partial \theta^2} = 0 \tag{C.31}$$

Is then possible to proceed and separate the variables r, θ: according to [74] the method of separation of the variables consists in the attempt to construct a solution to a given partial differential equation, as some sort of combination of functions of fewer variables. In case of Eq. C.31, the approach is thus to conjecture the existence of a solution f, in the form:

$$f = R(r)\,\Theta(\theta) \tag{C.32}$$

Where $R(r) :]0, +\infty[\rightarrow \mathbb{R}$ and $\Theta(\theta) : [0, 2\pi] \rightarrow \mathbb{R}$.

Introducing the resulting form for the solution of Eq. C.31:

$$\frac{1}{R}\left[r\frac{\partial}{\partial r}\left(r\frac{\partial R}{\partial r}\right)\right] = -\frac{1}{\Theta}\left(\frac{\partial^2\Theta}{\partial\theta^2}\right) \tag{C.33}$$

The right-hand side of Eq. C.33 is a positive constant m^2 so that the following ordinary differential equation results:

$$\frac{\partial^2\Theta}{\partial\theta^2} = -m^2\Theta \tag{C.34}$$

Whose solution has the periodic form given in Eq. C.35 and remembering that m must be an integer:

$$\Theta = \alpha\cos(m\theta) + \beta\sin(m\theta) \tag{C.35}$$

Considering the left-hand side of Eq. C.33, an analogous line of reasoning holds:

$$r\frac{\partial}{\partial r}\left(r\frac{\partial R}{\partial r}\right) = m^2R \tag{C.36}$$

The solution of Eq. C.37 can thus be express in the following form:

$$\mathrm{R} = Cr^l \tag{C.37}$$

Substituting Eq. C.34 and C.37 in Eq. C.33 the following yields:

$$l^2Cr^l = l^2R = m^2R \tag{C.38}$$

$$\Downarrow$$

$$l = \pm m \tag{C.39}$$

Hence, the general form for the function R is:

$$\begin{cases} R = \gamma r^m + \delta r^{-m} & (m = 0) \\ R = A + B\ln r & (m \neq 0) \end{cases} \tag{C.40}$$

Combining Eq. C.35 and C.40, the following mathematical form for the solution of Laplace equation results [99, 100]:

$$f(r,\theta) = A + B\ln r + \sum_m [\alpha_m\cos(m\theta) + \beta_m\sin(m\theta)](\gamma_m r^m + \delta_m r^{-m}) \tag{C.41}$$

Introducing the canonical representation for a complex number ($z = r\,e^{i\theta}$) the solution of Eq. C.12 can be recast as:

$$f = \Re\left\{A + B\ln z + \sum_m [\gamma_m(\alpha_m - i\beta_m)z^m + \delta_m(a_m + ib_m)z^{-m}]\right\} = \Re\{g(z)\} \tag{C.42}$$

Therefore, the required solution of Laplace equation can be obtained as the real part of the analytic function g over the complex domain.

C.3 Resolution of three-dimensional Laplace equation

¶ Fundamental solution

While the two-dimensional Laplace equation can be solved by transposing the problem to the complex field $\mathbb{C}$, as shown in the previous section, it is not possible to apply such a method to the resolution of higher-dimensional Dirichlet problems. Hence, to assess the three-dimensional structure of the electrostatic field engendered inside an IEC device, an alternative approach is required.

In the 1830s, British mathematician George Green conceived and developed the idea of exploiting the superposition principle for linear differential operators to obtain the solution of inhomogeneous, linear partial differential equations (such as Poisson equation, Eq. C.43), as the convolution of the source term $f(x)$ and the impulsive response $G(x,s)$, later called "Green's function" (see Eq. C.44).

$$Lu(x) = f(x) \tag{C.43}$$

Where L, is the linear differential operator defining the partial differential equation,
$f(x)$, is the source term of the differential equation.

$$u(x) = \int G(x,s)\, f(x)\, \mathrm{d}s \tag{C.44}$$

Where $G(x,s)$, is the Green's function for the L operator[33].
In modern mathematics, the concept of Green's function is reformulated in the frame of distribution theory and is replaced by the notion of generalised solution of a linear differential operator.

Distributions (or "generalised functions") are a mathematical object of peculiar importance, allowing for the extension of classical calculus to discontinuous functions, which would not be differentiable in a classical sense, provided that they are Lebegue-measurable (i.e. integrable). To provide a proper mathematical definition of distributions and their property, it is of use to define the test function space over an open subset of the Euclidian space. Consider $\mathbb{U}$ to be an open subset of $\mathbb{R}^n$, a test function $\varphi: \mathbb{U} \rightarrow \mathbb{R}^n$ is defined as a smooth function (i.e. of class C^∞) with a compact support over $\mathbb{U}$. The set of all the test functions, defined over $\mathbb{U}$, represents a vector space denoted as $\mathcal{D}(\mathbb{U})$: this is the foundation of the distribution space, as follows. Indeed, a distribution is defined as a continuous linear functional $T: \mathcal{D}(\mathbb{U}) \rightarrow \mathbb{R}$ which then linearly assigns, to each test function, a real scalar $T(\varphi)$. The whole set of the distributions defined over the test function space $\mathcal{D}(\mathbb{U})$ is itself a vector space, denoted as $\mathcal{D}^*(\mathbb{U})$, known as the dual space of $\mathcal{D}$. As aforementioned, distributions are a powerful mathematical object that allows for the extension of the classical concept of derivative (which, in this context, is referred to as "strong derivative") to non-differentiable functions, provided that they are integrable. Let u be a Lebegue-measurable function -$f \in \mathcal{L}^1(\mathbb{U})$-, u is said to be weakly differentiable with respect to the variable x_i ($i = 1 \dots n$) if there exists a function $g \in \mathcal{L}^1(\mathbb{U})$ so that, for any test function φ in $\mathcal{D}(\mathbb{U})$, Eq. C.45 holds [74]:

$$\int_{\mathbb{U}} f \frac{\partial \varphi}{\partial x_i} \mathrm{d}x = -\int_{\mathbb{U}} g_i \varphi \, \mathrm{d}x \tag{C.45}$$

The function g is the partial weak derivative of f and is commonly denoted as $\partial_i f$. Introducing the multi-index $\alpha \in \mathbb{N}_0^n$, the definition for the weak derivative $D^\alpha f$ of is f given as the unique function in $\mathcal{L}^1(\mathbb{U})$ that satisfies Eq. C.46 for any test function φ in $\mathcal{D}(\mathbb{U})$:

$$\int_{\mathbb{U}} (D^\alpha f)\, \varphi \, \mathrm{d}x = (-1)^{|\alpha|} \int_{\mathbb{U}} f (D^\alpha \varphi) \, \mathrm{d}x \tag{C.46}$$

It is worth to underline that, owing to the smoothness of the test functions employed in the definition in Eq. C.46, the weak derivative does coincide with the pointwise derivative (i.e. the strong derivative) for any continuously differentiable function over $\mathbb{U}$, but can also be defined for non-continuous functions, which thus would not be differentiable in correspondence of the discontinuity. The concept of weak derivative assumes, therefore, a key role in the description of discrete physical phenomena such as the electrostatics of point charges. Finally, the idea of weak differentiability for measurable functions allows for the definition of the weak solution of a differential problem: intuitively, the formulation in Eq. C.46 can be exploited to recast a partial differential equation in an integral form -called "weak" (or "integral", "global") formulation- requiring a solution in the sense of a distribution.

[33] A proper definition of the Green function will be given in the next subsection of the present chapter.

The above-presented theory allows to introduce the conception of a fundamental solution for a linear partial differential operator. According to [73] the following the definition can be given:

"The fundamental solution of a linear partial differential equation is a solution of a partial differential equation $\mathrm{L}u(x) = 0, x \in \mathbb{R}^n$*, with coefficient of class* C^∞*, in the form of a function* $F(x, x')$ *that satisfies, for fixed* $x' \in \mathbb{R}^n$*, the equation*

$$LF(x, x') = \delta(x - x') \tag{C.47}$$

Which is interpreted in the sense of the theory of generalised functions, where δ *is the delta-function*[34]*".*

An important conclusion coming from such a definition is that any partial differential equation with constant coefficient, or any elliptic equation, have a fundamental solution. In particular, for Laplace equation, the fundamental solution is defined in Ref. [74], as the function:

$$F(x, x') \doteq \begin{cases} -\dfrac{1}{2\pi}\log|x - x'| & (n = 2) \\ \dfrac{1}{n(n-2)V\big(\mathcal{B}(x,x')\big)}\dfrac{1}{|x - x'|^{n-2}} & (n \geq 3) \end{cases} \tag{C.48}$$

Where $V\big(\mathcal{B}(x,x')\big)$, is the volume of the ball centred in x' and passing through x.

It is worth noticing that the modulus term $|x - x'|$, introduced in both the forms for the fundamental solution of Laplace operator in Eq. C.17, formally reflects the rotational symmetry of Laplace operator (i.e. its invariance under transformations in the special orthogonal group $SO(n)$. Hence, the actual solution has a radial form, depending on the variable $r = |x - x'|$: trivial manipulation if Eq. C.1 allows to obtain the form, for the fundamental solution, reported in Eq. C.48.

¶ Green's function

As mentioned in the previous section, the concept of fundamental solution is a reformulation, in a more modern mathematical language, of the previous idea of Green's function, which further addresses the boundary conditions assigned to the linear partial differential equation. The core idea justifying the introduction of the fundamental solution for a linear differential operator, such as Laplace operator, is that the linearity of the operator, reflecting on the PDE, allows to express the solution of Poisson equation in terms of the convolution of its source term with the distribution itself. Consider the partial differential equation defined by the linear operator L in Eq. C. 43, denoting the convolution of the source term $f(x)$ and the fundamental solution $F(x, x')$ as $(F * f)$, it is possible to apply the differential operator to such a product as in Eq. C.49.

$$L(F * f) = (LF) * f \tag{C.49}$$

Taking advantage of the definition in Eq. C.47, the following yields:

$$L(F * f) = \delta(x) * f(x) \tag{C.50}$$

Since Dirac's delta-function is an identity element for the convolution operation, the left-hand side of Eq. C.50 is reduced to the source term in Eq. C.43:

$$L(F * f) = \int_{-\infty}^{+\infty} \delta(x - x')\, f(x')\ \mathrm{d}x' \equiv f(x) \tag{C.51}$$

[34] Note that Dirac's delta-function, whose definition is given in Eq. 3.29, is indeed a distribution. Incidentally, Paul Dirac was the first to introduce, in his formalism, an intuitive idea of distribution with his definition of the delta-function.

Comparing Eq. C.43 and C.51, it is clearly seen that the solution $u(x)$ can be expressed as the convolution of the fundamental solution for the differential operator and the source term:

$$u \equiv L(F * f) \tag{C.52}$$

Hence, considering Poisson equation with source term $f \in \mathrm{C}^{\infty}(\mathbb{R}^{n}\mathbb{R}^{n}), n \geq 3$:

$$-\nabla^2 u = f \tag{C.53}$$

Any bounded solution of such an equitation can be expressed as the convolution given in Eq. C.54 [74]:

$$u(x) = \int_{\mathbb{U}} F(x - x')\, f(x')\, \mathrm{d}x' + C \tag{C.54}$$

Where C, is the integration constant;
$x, x' \in \mathbb{U}$.

It is now necessary to address the problem of solving Poisson (or Laplace) equation when Dirichlet boundary conditions are prescribed, i.e. to tackle the differential problem in Eq. C.11: the idea is to combine the general representation formula (Eq. C.54) for the solution of Poisson equation and an auxiliary function introducing the boundary conditions. Let the function f^x, defined over $\mathbb{U}$ for fixed x, be the solution to the following Cauchy problem:

$$\begin{cases} \nabla^2 f^x = 0 & in\ \mathbb{U} \\ f^x(x') = F(x - x') & on\ \partial\mathbb{U} \end{cases} \tag{C.55}$$

The function f^x is called "corrector" and allows for the following definition of Green's function [74]:

$$G(x - x') \doteq F(x - x') - f^x(x') \tag{C.56}$$

It is worth to highlight that, according to the definition in Eq. C.47, Green's function for the Laplace operator given in Eq. C.56 is not a proper function over the Cauchy problem domain -indeed, in correspondence of the source point, Green's function is singular[35]-, but is rather a distribution in the sense depicted in the previous section of the present chapter. The following representation formula can be thus retrieved for the solution of Dirichlet problem for Poisson equation:

$$u(x) = -\int_{\partial\mathbb{U}} \frac{\partial G}{\partial \nu}(x - x')\, g(x')\, \mathrm{d}x' + \int_{\mathbb{U}} G(x, x')\, f(x')\, \mathrm{d}x' \tag{C.57}$$

Where ν, is the outer normal vector for the boundary surface $\partial\mathbb{U}$.

In case of a null source term, the representation formula for the solution of Laplace boundary problem yields [74]:

$$u(x) = -\int_{\partial\mathbb{U}} \frac{\partial G}{\partial \nu}(x - x')\, g(x')\, \mathrm{d}x' \tag{C.58}$$

Hence, the problem of assessing the three-dimensional topography of the electrostatic field engendered in an IEC device can be solved, for the assigned voltage value on the electrodes (i.e. the boundary value g), by a proper construction of Green's function G for the given domain. This is however a complex matter and can only be done when the problem domain has a simple geometry.

For the purpose of the present work, indeed, the typical electrode geometry is definitively too complex to determine the exact Green's function. A simple approach to overcome such an issue was

[35] The behaviour of Green's function for Laplace operator in correspondence of the source location x' closely resembles that of Dirac's δ distribution: it is real-valued for every point of the assigned domain, except for its origin, where it presents a singular behaviour, assuming an infinite value.

proposed to the author by Professor Ray Sedwick [75] from University of Maryland, College Park, and consist of describing the conductive wires, constituting the device electrodes, as a set of point charges each of whom inducing a spherical electrostatic potential over the surrounding space. This modelling for the electrostatics of an IEC device presents the great advantage of adopting, for each pointwise charge in the discretisation, an extremely simple form for Green's function, which coincides with the Laplace fundamental solution (see Eq. C.48) in the tree-dimensional case:

$$G(x, x') \doteq \frac{1}{4\pi\,|x - x'|} \tag{C.59}$$

Where x', represent here the location of each point charge.

The overall electrostatic potential resulting inside the device is thus obtained as the superimposition of the single contribution due to each charge in the electrode discretisation. For a detailed description of such a resolution method, the reader is referred to Chapter 5, Section 3, of the present essay.

References

[1] B. Palaszewski, "Electric Propulsion for Future Space Missions," [Online]. Available: https://www.grc.nasa.gov/WWW/K-12/DLN/descriptions/presentations/systemsengineering/SystemsEngPart1.ppt.. [Accessed 5th October 2017].

[2] R. G. Jahn, "The Province of Electric Propulsion," in *Physics of Electric Propulsion*, New York, McGraw-Hill Book Company, 1968, pp. 2-10.

[3] F. F. Chen, "Introduction," in *Introduction to plasma physics and controlled fusion*, New York and London, Plenum Press, 1974, p. 3.

[4] L. D. Landau and E. M. Lifshitz, "Molecular collisions," in *Course of Theoretical Physics Vol. 5, Statistical Physics Part 1*, Oxford, UK, Pergamon Press Ltd., 1980, p. 117.

[5] T. Dolan, "Magnetic electrostatic plasma confinement," *Plasma Physics and Controlled Fusion,* no. 36, pp. 1539-1593, 1994.

[6] P. T. Farnsworth, "Electric discharge device for producing interactions between nuclei". USA Patent 3.258.402, 28th June 1966.

[7] G. Miley, The Inertial Electrostatic Confinement Approach to Fusion Power, Boston, MA, USA: Springer, 1997.

[8] G. H. Miley and K. S. Murali, Inertial Electrostatic Confinement (IEC) Fusion Fundamentals and Applications, New York: Springer Science+Business Media, 2014.

[9] R. L. Hirsch, "Inertial-Electrostatic Confinement of Ionezed Fusion Gases," *Journal of Applied Physics,* no. 38, pp. 4522-4534, 1967.

[10] S. Murali, R. Nebel and P. J., "Carbon Nanotubes in IEC Fusion Reactors," *Transaction of the American Nuclear Society,* vol. 94, pp. 638-639, 2006.

[11] R. Bussard, "Some Physics Considerations of Magnetic Inertial Electrostatic Confinement: A New Concept for Spherical Converging Flow Fusion," *Fusion Technology,* vol. 19, pp. 1-21, 1991.

[12] W. Elmore, J. Tuck and K. Watson, "On the inertial-electrostatic confinement of a plasma," *Physics of Fluids,* vol. 2, pp. 239-246, 1959.

[13] W. Black and E. Klevans, "Theory of potential-well formation in an electrostatic confinement device," *Journal of Applied Physics,* no. 45, p. 2502, 1974.

[14] C. Dobson and I. Hrbud, "Electron density and two-channel neutron emission measurements in steady-state spherical inertial-electrostatically confined plasmas, with review of the one-dimensional kinetic model," *Journal of Applied Physics,* vol. 96, no. 1, pp. 94-108, 2004.

[15] T. Dolan, J. Verdeyen, D. Meeker and B. Cherrington, "Electrostatic-Inertial Plasma Confinement," *Journal of Applied Physics,* no. 43, p. 1590, 1972.

[16] K. Murali, "Systems and methods for acccelarting particles". Patent PCT/IB2012/054717, 2013.

[17] G. Miley and J. Juvedani, "Inertial Electrostatic Confinement (IEC) Neutron Sources," in *Proceedings of 16th International Symposium on Fusion Engineering*, Champaign, IL, USA, USA, 1995.

[18] T. Thorson, R. Durst, R. Fonck and L. Waiwright, "Convergence, electrostatic potential, and density measurements in a spherically convergent ion focus," *Physics of Plasmas,* vol. 4, no. 1, pp. 4-15, 1996.

[19] Y. Chan and G. Herdrich, "Inertial Electrostatic Confinement: Innovation for Electric Propulsion and Plasma Systems," in *35th International Electric Propulsion Conference*, Atalanta, GA, USA, 2017.

[20] M. Raadu, "The physics of double layers and their role in astrophysics," *Physics Reports,* vol. 178, no. 2, pp. 25-97, 1989.

[21] B. Song, R. Merlino and N. D'Angelo, "On the Stability of Strong Double Layers," *Physica Scripta,* vol. 45, pp. 391-394, 1992.

[22] B. Song, N. D'Angelo and R. Merlino, "Stability of a spherical double layer produced through ionization," *Journal of Applied Physics,* no. 25, pp. 938-941, 1992.

[23] P. T. Farnsworth, "Method and apparatus for producing nucleear-fusion reactions". USA Patent 3.386.883, 13th May 1966.

[24] S. Dibra, *Theoretical study of temperature in an inertial electrostatic confinement device,* Turin, Italy: Politecnico di Torino, 2015.

[25] C. Syring and G. Herdrich, "Experimental Discharge Characterization and Scaling of IEC Plasma Devices," in *33rd International Electric Propulsion Conference*, Washington, D.C., USA, 2013.

[26] D. Galla, "Simulation of the Electrostatic potential equation (Poisson equation) for an IEC device," Institute for Space System, University of Stuttgart, Stuttgart, Germany, 2014.

[27] D. C. B. Swanson and J. Verdeyen, "Potential well structure in an inertial electrostatic plasma confinement device," *Physics of Fluids,* vol. 19, p. 1939, 1973.

[28] T. J. McGuire, *Improved Lifetimes and Synchronization Behavior in Multi-grid Inertial Electrostatic Confinement Fusion Devices,* Cambridge, USA: Massachusetts Institute of Technology, 2007.

[29] C. C. Dietrich, "Improving Particle Confinement in Inertial Electrostatic Fusion for Spacecraft Power and Propulsion," Massachusetts Institute of Technology, Cambridge, USA, 2007.

[30] J. Roth, Industrial Plasma Engineering Vol. 1, Bristol, UK: Institute of Physics Publishing, 1995.

[31] H. Herdrich, B. A. G. R. Bauder U., M. Lau, D. P. M. Petkow, C. Syring and S. Fasoulas, "Advanced Plasma (Propulsion) Concepts at IRS," *Vacuum Journal,* vol. 88, pp. 30-38, 2013.

[32] G. Miley, Y. Gu, J. Demora, S. R. A., T. Hochberg, J. H. Nadler and R. Anderl, "Discharge characteristics of the spherical interial electrostatic confinement (IEC) device," in *XVIIth International Symposium on Discharges and Electrical Insulation in Vacuum*, Berkley, CA, USA, 1996.

[33] R. M. P. M. A. Meyer and S. K. Loyalka, "Experimental Observations of a Spherical Transparent Cathode Glow Discharge," *IEEE Transactions on Plasma Science,* vol. 36, no. 4, pp. 1881-1889, 2008.

[34] R. L. Hirsch, "Electrostatic containment in fusion reactors". USA Patent 3.664.920, 23rd May 1972.

[35] D. Meeker, J. Verdeyen and B. Cherrington, "Measurement of electron density in a cylindrical inertial electrostatic plasma confinement device," *Journal of Applied Physics,* vol. 44, no. 12, p. 5347, 1973.

[36] C. H. G. Syring, "Discharge and Operational Conditions of an Inertial Electrostatic Confinement Device," in *49th AIAA/ASME/SAE/ASEE Joint Propulsion Conference*, San Jose, CA, USA, 2013.

[37] Y. Chan, C. Syring and G. Herdrich, "Development of Inertial Electrostatic Confinement Devices for Space Propulsion in IRS," in *5th Space Propulsion Conference*, Rome, Italy, 2016.

[38] J. DeMora, R. Stubbers and R. Anderl, "Study of ion microchannels and IEC grid effects using the SIMION code," in *Proceedings of 16th International Symposium on Fusion Engineering*, Champaign, IL, USA, USA, 1995.

[39] Y. Gu and G. Miley, "Experimental study of potential structure in a spherical IEC fusion device," *IEEE Transactions on Plasma Science,* vol. 28, no. 1, pp. 331-346, 2000.

[40] R. Moses, "Enhancing IEC performance with focusing grids," in *Physics of Spherical Continuous Inertial Fusion Workshop*, Santa Fe, NM, USA, 1995.

[41] Y. Chan and G. Herdrich, "Characterization of an IEC Plasma Thruster Plume by a Nude-type Faraday Probe," in *35th International Electric Propulsion Conference*, Atlanta, GA, USA, 2017.

[42] Y. Chan and G. Herdrich, "Inertial Electrostatic Confinement: Innovation for Electric Propulsion and Plasma Systems," in *35th International Electric Propulsion Conference*, Atlanta, GA, USA, 2017.

[43] Y. Chan, F. Mazza and G. Herdrich, "Development of Free-space Potential Solver for 3D Grid IEC Configuration, IRS-17-IB09," Institute of Space Systems, University of Stuttgart, Stuttgart, Germany, 2017.

[44] G. Herdrich and C. P. M. P. D. Syring, "Kinetic modeling of the jet extraction mechanism in spherical IEC devices," in *33rd International Electric Propulsion Conference*, Washington, D.C., USA, 2013.

[45] G. Miley, H. Momota, L. Wu, M. Reilly, R. Burton, V. Teofilo, D. Dell, R. Dell and W. Hargus, "Space Probe Application of IEC Thrusters," *Fusion Science and Technology,* vol. 56, no. 1, pp. 533-539, 2009.

[46] R. Burton, H. Momota, N. Richardson, Y. Shaban and G. Miley, "Fusion Ship II - A Fast Manned Interplanetary Space Vehicle Using Inertial Electrostatic Fusion," in *Space Technology and Applications International Forum - STAIF*, Albuquerque, NM, USA, 2003.

[47] G. Miley and L. Wu, "Magnetically-Channeled IEC Fusion for Interplanetary Travel," in *43rd AIAA/ASME/SAE/ASEE Joint Propulsion Conference & Exhibit*, Cincinnati, OH, USA, 8th-11th July 2007.

[48] S. Murali, G. Emmert, J. Santarius and G. Kulchinski, "Effects of chamber pressure variation on the grid temperature in an inertial electrostatic confinement device," *Physics of Plasmas,* vol. 17, no. 10, 2010.

[49] M. Ohnishi, K. H. Sato, Y. Yamamoto and K. Yoshikawa, "Correlation between potential well structure and neutron production in inertial electrostatic confinement fusion," *Nuclear Fusion,* vol. 37, no. 5, pp. 611-619, 1997.

[50] H. Matsuura, K. Funakoshi and Y. Nakao, "Correlation between ion/electron distribution functions and neutron production rate in spherical inertial electrostatic confinement plasmas," *Nuclear Fusion,* vol. 43, no. 9, pp. 989-998, 2003.

[51] C. Dobson, *private communication,* 2017.

[52] Y. Chan, F. Mazza and G. Herdrich, "Evaluation and Development of Poisson Solver for IEC, IRS-17-IB07," Institute of Space Systems, University of Stuttgart, Stuttgart, Germany, 2017.

[53] W. Press, S. Teukolsky, W. Vetterling and B. Flannery, "Two Point Boundary Value Problem," in *Numerical Recipes in C*, New York, USA, Cambridge University Press, 1992, pp. 753-784.

[54] G. Herdrich, C. Syring, T. Torgau, Y. Chan and D. Petkow, "An Approach for Thrust and Losses in Inertial Electrostatic Confinement Devices for Electric Propulsion Applications," in *Joint Conference of 30th International Symposium on Space Technology and Science 34th International Electric Propulsion Conference and 6th Nano-satellite Symposium*, Hyogo-Kobe, Japan, 2015.

[55] A. Barkan and R. Merlino, "Confinement of dust particles in a double layer," *Physics of Plasma,* vol. 2, no. 9, pp. 3261-3265, 1995.

[56] C. Charles, "A review of recent laboratory double layer experiments," *Plasma Sources Science and Technology,* vol. 16, pp. 1-25, 2007.

[57] R. Stenzel and J. Urrutia, "Oscillating plasma bubbles. I. Basic properties and instabilities," *Physics of Plasmas,* vol. 19, no. 082105, pp. 1-10, 2012.

[58] ©. NASA/IMAGE, "NASA Earth Observatory," 11th September 2005. [Online]. Available: https://earthobservatory.nasa.gov/IOTD/view.php?id=6226. [Accessed 19th October 2017].

[59] ©. NASA/SDO, "NASA," 4th August 2017. [Online]. Available: https://www.nasa.gov/content/goddard/sun-release-m8.7-class-solar-flare-dec-17-2014. [Accessed 19th October 2017].

[60] ©. NASA/CXC/M.Weiss, "Max Planck Institut für Radioastronomie," [Online]. Available: https://www.mpifr-bonn.mpg.de/research/fundamental/neutronstars. [Accessed 2017 October 2017].

[61] G. Hairapetian and R. Stenzel, "Observation of a Stationary, Current-Free Double Layer in a Plasma," *Physical Review Letters,* vol. 65, no. 2, pp. 175-178, 1990.

[62] P. Bellan, "Basic concepts," in *Fundamentals of Plasma Physics*, Cambridge, UK, Cambridge University Press, 2008, pp. 4-6.

[63] E. Ahedo and M. Sánchez, "Theory of a Stationary Current-Free Double Layer in a Collisionless Plasma," *Physical Review Letters,* vol. 103, pp. 1-4, 2009.

[64] H. Schamel and S. Bajarbarua, "Analytical double layers," *Phys. Fluids,* no. 26, pp. 190-193, 1983.

[65] B. Scheiner, E. Barnat, S. Baalrud, M. Hopkins and B. Yee, "Theory and simulation of anode spots in low pressure plasmas," *Phys. Plasmas,* vol. 24, no. 11, 8th August 2017.

[66] M. Lennon, K. Bell, H. Gilbody, J. Hughes, A. Kingston, M. Murray and F. Smith, "Recommended Data on the Electron Impact Ionization of Atoms and Ions: Fluorin to Nickel," *J. Phys. Chem. Ref. Data,* vol. 17, no. 3, pp. 1285-1363, 1988.

[67] I. Langmuir, "The Effect of Space Charge and Residual Gases on Thermionic Currents in High Vacuum," *Phys. Rev.,* vol. 2, no. 6, pp. 450-486, 1913.

[68] E. Murphy and R. Good, "Thermionic Emission, Field Emission, and the Transition Region," *Phys. Rev.,* vol. 102, no. 6, pp. 1464-1473, 1956.

[69] I. Langmuir, "The Interaction of Electron and Positive Ion Space Charges in Cathode Sheaths," *Phys. Rev.,* vol. 33, no. 6, pp. 954-989, 1929.

[70] M. Raadu, "Relativistic effects in electrostatic double layers," in *Symposium on Plasma Double Layers*, Risø, Denmark, 1982.

[71] H. Hora, M. Gu, S. Eliezer, P. Lalousis, R. Pease and H. Szichman, "On the Surface Tension of Plasmas," *IEEE Trans. Plasma Sci.,* vol. 17, no. 2, pp. 284-289, 1989.

[72] F. R. S. Sir Geoffrey Taylor, "Disintegration of water drops in an electric field," *Proc. R. Soc. Lond. A,* vol. 280, pp. 383-397, 1964.

[73] A. Soldatov, "Encyclopedia of Mathmatics, Fundamental solution," 7th February 2011. [Online]. Available: http://www.encyclopediaofmath.org/index.php?title=Fundamental_solution&oldid=11510. [Accessed 22nd November 2017].

[74] L. Evans, "Four important linear partial differential equations," in *Partial Differential Equations, 2nd ed.*, Providence, RI, USA, American Mathematical Society, 1997, pp. 19-42.

[75] R. Sedwick, *private communitacion,* 2017.

[76] S. Marcuccio, A. Genovese and M. Andrenucci, "Experimental Performance of Field Emission Mircothrusters," *Journal of Propulsion and Power,* vol. 14, no. 5, pp. 774-781, 1998.

[77] P. T. Farnsworth, "Multistage multipactor". USA Patent 2.141.837, 1938 December 27th.

[78] Y. Chan and G. Herdrich, "Development of Inertial Electrostatic Confinement Devices for Space Propulsion in IRS," in *5th Space Propulsion Conference*, Rome, Italy, 2016.

[79] D. Barnes and R. Nebel, "Stable, thermal equilibrium, large-amplitude, spherical plasma oscillations in electrostatic confinement devices," *Physcs of Plasma,* vol. 5, p. 2498, 1998.

[80] R. Nebel, J. Park, W. Rellergert and M. Sekora, "Experimental and Theoretical Studies of Electrostatic Confinement on the Intense Neutron Source (INS-e) Device," *Physics of Plasmas,* vol. 10, p. 3841, 2003.

[81] "ideen2020," [Online]. Available: http://www.ideen2020.de/wp-content/uploads/slideshow-gallery/7_Tokamak3D_41.png. [Accessed 10th October 2017].

[82] T. Mitchell and M. B. D. Schauer, "Observation of spherical focus in an electron penning trap," *Physical Review Letters,* vol. 78, no. 1, pp. 58-61, 1997.

[83] "TRIUMF," 27th December 2012. [Online]. Available: http://www.triumf.ca/headlines/current-events/nobel-laureate-visits-triumf. [Accessed 10th October 2017].

[84] L. Brown and G. Gerald, "Geonium theory: Physics of a single electron or ion in a Penning trap," *Reviews of Modern Physics,* vol. 58, no. 1, pp. 233-311, 1986.

[85] O. Lavrent'ev, "Electrostatic and electromagnetic high-temperature plasma traps," *Annals of the New York Academy of Sciences,* vol. 251, pp. 152-178, 1974.

[86] R. W. Bussard, "Some Physics Considerations of Magnetic Inertial Electrostatic Confinement: A New Concept for Spherical Converging Flow Fusion," *Fusion Technology,* vol. 19, pp. 1-21, 1991.

[87] T. Greek, "Talk-Polywell.org," 21st September 2007. [Online]. Available: http://www.talk-polywell.org/bb/viewtopic.php?f=8&t=487&start=30. [Accessed 10th October 2017].

[88] R. W. Bussard, "Method and apparatus for controlling charged particles". USA Patent US4826646 A, 29th October 1989.

[89] R. W. Bussard and K. King, "Bremmstrahlung and synchrotron radiation losses in Polywell System," EMC2 Energy/Matter conversion corporation, Manassas,VA, USA, 1992.

[90] R. W. Bussard, "Should Google Go Nuclear? Clean, cheap, nuclear power...," 12th December 2006. [Online]. Available: https://www.youtube.com/watch?v=FhL5VO2NStU. [Accessed 5th October 2017].

[91] S. Cornish, D. Gummershall and J. Khachan, "The dependence of potential well formation on the magnetic field strength and electron injection current in a polywell device," *Physics of Plasmas,* vol. 21, 2014.

[92] J. Kollasch, C. Sovinec and J. Santarius, "Vlasov-Poisson calculations of electron confinement times in Polywell(TM) devices using a steady-state particle-in-cell method," in *55th Annual Meeting of the APS Division of Plasma Physics*, Denver, CO, USA, 2013.

[93] J. Callen, "Fundamentals of Plasma Physics, Plasma Descriptions I: Kinetic, Two-Fluid," 21st January 2003. [Online]. Available: http://homepages.cae.wisc.edu/~callen/chap5.pdf. [Accessed 15th December 2017].

[94] L. D. Landau and E. M. Lifshitz, Course of Theoretical Physics Volume 5, Statistical Phisics Part 1, Oxford, UK: Pergamon Press Ltd., 1980.

[95] P. Bellan, "Derivation of fluid equations: Vlasov, 2-fluid, MHD," in *Fundamentals of Plasma Physics*, Cambridge, UK, Cambridge University Press, 2008, pp. 30-61.

[96] C. Mencucci and V. Silvestrini, "Sistemi di conduttori e campo elettrostatico," in *Fisica II*, Napoli, Italia, Liguori Editore, S.r.l., 1988, pp. 96-99.

[97] S. Axler, B. P. and W. Ramey, Harmonic Function Theory, 2nd ed., NY, USA: Springer-Verlag New York Ink., 2001.

[98] G. Barton, "Poisson's equation: I. Introduction," in *Elements of Green's Functions and Propagation: Potentials, Diffusion and Waves*, Oxford, UK, Oxford Science Publications, 1989, pp. 92-94.

[99] E. Wilson, "UCL Department of Mathematics, Analytical Methods," [Online]. Available: http://www.ucl.ac.uk/~ucahhwi/LTCC/sectionF-complex.pdf. [Accessed 23rd November 2017].

[100] C. Williams, "Universiy of Exeter, Physics and Astronomy, Electromagnetic Fields," [Online]. Available: https://newton.ex.ac.uk/teaching/CDHW/EM/CW970317-2.pdf. [Accessed 23rd November 2017].

[101] R. G. Jahn, "Particle Collision in an Ionised Gas," in *Physics of Electric Propulsion*, New York, McGraw-Hill Book Company, 1968, pp. 64-67.

[102] S. Earnshow, "On the Nature of the Molecular Forces which Regulate the Constitution of the Luminiferous Ether," *Transaction of the Cambridge Philosophical Society,* vol. 27, pp. 97-112, 1842.

Acknowledgements

Desidero, in conclusione alla presente dissertazione, porgere i miei ringraziamenti a tutte quelle persone che hanno reso possibile il raggiungimento di questo traguardo.

In primo luogo, il mio sentito ringraziamento va al Prof. Lorenzo Casalino, relatore del presente elaborato di laurea, per avermi offerto la possibilità di collaborare con l'Università di Stoccarda, con ogni probabilità l'esperienza più formativa che io abbia vissuto negli anni trascorsi all'università.

Al Prof. Georg Herdrich va la mia più profonda riconoscenza per avermi accolto con disponibilità nel suo team di ricerca presso l'Institut für Raumfahrtsysteme dell'Università di Stoccarda: lì ho avuto modo di approfondire lo studio della propulsione al plasma, argomento per me affascinante più di ogni altro trattato nei miei studi, e di gettare le basi di quello che spero sia il mio futuro percorso di ricerca.

Il lavoro di tesi illustrato nel presente testo non avrebbe potuto in alcun modo essere svolto senza la collaborazione del dottorando Yung-An Chan, mio diretto supervisore all'Institut für Raumfahrtsysteme. Non soltanto le sue indicazioni, osservazioni e consigli sono stati fondamentali nello svolgimento della mia ricerca, ma la sua passione e il costante sforzo, teso ad approfondire la nostra comprensione della materia in esame, sono stati una chiara dimostrazione dell'essenza della ricerca scientifica e, in tal senso, una vera ispirazione.

Fondamentale allo svolgimento del lavoro di ricerca qui illustrato, infine, è stato il contributo del Dr. Christopher C. Dobson (NASA Marshall Space Flight Center), del Dr. Tom McGuire (Lockheed Martin Aeronautics Company), e del Prof. Raymond Sedwick (University of Maryland). Desidero dunque ringraziarli per le pazienti spiegazioni del proprio lavoro e per i preziosi consigli.

A tutti gli amici che hanno condiviso con me questi anni, vi ringrazio per il tempo trascorso insieme, per le risate e le discussioni che lo hanno reso più interessante.

Per la mia famiglia e per Alice, non ci sono parole per esprimere di quanto vi sia debitore e tutta la mia riconoscenza: mi avete permesso di andare avanti nei periodi più bui e di superare i momenti di sconforto, avete reso più felici i momenti migliori. A voi è dedicato questo lavoro, non potendo il linguaggio definire adeguatamente il sentimento.